Advancing Charge Selective Contacts for Efficient Monolithic Perovskite-Silicon Tandem Solar Cells

Lukas Kegelmann

Univ.-Diss.

zur Erlangung des akademischen Grades

Doktor-Ingenieur

(Dr.-Ing.)

in der Wissenschaftsdisziplin Experimentalphysik

eingereicht an der

Mathematisch-Naturwissenschaftlichen Fakultät

Institut für Physik und Astronomie

der Universität Potsdam

und durchgeführt am

Helmholtz-Zentrum Berlin für Materialien und Energie

Ort und Tag der Disputation: Potsdam-Golm, 25.01.2019

Betreuer:

Prof. Dieter Neher
Prof. Bernd Rech
Prof. Rutger Schlatmann

Promotionsausschuss:

Vorsitzender:

Prof. Matias Bargheer

Gutachter:

Prof. Dieter Neher
Prof. Bernd Rech
Prof. Emil List-Kratochvil
Prof. Reimund Gerhard
Prof. Giovanni Bruno

https://doi.org/10.25932/publishup-42642
https://nbn-resolving.org/urn:nbn:de:kobv:517-opus4-426428

Abstract

Hybrid organic-inorganic perovskites are one of the most promising material classes for photovoltaic energy conversion. In solar cells, the perovskite absorber is sandwiched between *n*- and *p*-type contact layers which selectively transport electrons and holes to the cell's cathode and anode, respectively. This thesis aims to advance contact layers in perovskite solar cells and unravel the impact of interface and contact properties on the device performance. Further, the contact materials are applied in monolithic perovskite-silicon heterojunction (SHJ) tandem solar cells, which can overcome the single junction efficiency limits and attract increasing attention. Therefore, all contact layers must be highly transparent to foster light harvesting in the tandem solar cell design. Besides, the SHJ device restricts processing temperatures for the selective contacts to below 200°C.

A comparative study of various electron selective contact materials, all processed below 180°C, in *n-i-p* type perovskite solar cells highlights that selective contacts and their interfaces to the absorber govern the overall device performance. Combining fullerenes and metal-oxides in a TiO_2/$PC_{60}BM$ (phenyl-C_{60}-butyric acid methyl ester) double-layer contact allows to merge good charge extraction with minimized interface recombination. The layer sequence thereby achieved high stabilized solar cell performances up to 18.0% and negligible current-voltage hysteresis, an otherwise pronounced phenomenon in this device design. Double-layer structures are therefore emphasized as a general concept to establish efficient and highly selective contacts.

Based on this success, the concept to combine desired properties of different materials is transferred to the *p*-type contact. Here, a mixture of the small molecule Spiro-OMeTAD [2,2',7,7'-tetrakis(N,N-di-p-methoxyphenylamine)-9,9'-spirobifluoren] and the doped polymer PEDOT [poly(3,4-ethylenedioxythiophene)] is presented as a novel hole selective contact. PEDOT thereby remarkably suppresses charge recombination at the perovskite surface, allowing an increase of quasi-Fermi level splitting in the absorber. Further, the addition of Spiro-OMeTAD into the PEDOT layer is shown to enhance charge extraction at the interface and allow high efficiencies up to 16.8%.

Finally, the knowledge on contact properties is applied to monolithic perovskite-SHJ tandem solar cells. The main goal is to optimize the top contact stack of doped Spiro-OMeTAD/molybdenum oxide(MoOx)/ITO towards higher transparency by two different routes. First, fine-tuning of the ITO deposition to mitigate chemical reduction of MoOx and increase the transmittance of MoOx/ITO stacks by 25%. Second, replacing Spiro-OMeTAD with the alternative hole transport materials PEDOT/Spiro-OMeTAD mixtures, CuSCN or PTAA [poly(triaryl amine)]. Experimental results determine layer thickness constrains and validate optical simulations, which subsequently allow to realistically estimate the respective tandem device performances. As a result, PTAA represents the most promising replacement for Spiro-OMeTAD, with a projected increase of the optimum tandem device efficiency for the herein used architecture by 2.9% relative to 26.5% absolute. The results also reveal general guidelines for further performance gains of the technology.

Kurzfassung

Hybride, organisch-anorganische Perowskite gelten als eine der vielversprechendsten Materialklassen für die photovoltaische Energieumwandlung. Dazu werden Perowskit-Absorber in Solarzellen zwischen *n*- und *p*-Typ Kontaktschichten angeordnet, die Elektronen oder Löcher selektiv zur Kathode bzw. Anode der Zelle transportieren. Ziel dieser Arbeit ist es, die ladungsselektiven Transportschichten in Perowskit-Solarzellen zu verbessern und Einflüsse der Grenzflächen- und Kontakteigenschaften auf die Zelleffizienz herauszustellen. Darüber hinaus werden die selektiven Schichten in monolithischen Perowskit-Silizium-Heterokontakt (SHK) Tandem-Solarzellen eingesetzt. Diese können höhere Wirkungsgrade als Einfachsolarzellen erzielen und erfahren zunehmende Aufmerksamkeit aus der Forschung. Hierfür müssen alle Kontaktschichten hochtransparent sein, um eine möglichst effiziente Lichtausnutzung im Tandem-Solarzellen-Design zu erzielen. Des Weiteren limitiert die SHK-Solarzelle die höchst mögliche Temperatur zur Abscheidung der selektiven Kontakte auf 200°C.

In einer Vergleichsstudie werden deshalb zunächst verschiedene elektronenselektive Kontaktmaterialien, die alle unter 180°C prozessiert werden, in *n*-*i*-*p*-Typ Perowskit-Solarzellen eingesetzt. Es zeigt sich hierbei, wie wesentlich die selektiven Kontakte und ihre Grenzflächen zum Absorber die Effizienz der Solarzellen bestimmen. Eine Kombination aus Fulleren und Metalloxid in einem $TiO_2/PC_{60}BM$ (Phenyl-C_{60}-Buttersäuremethylester) Doppelschichtkontakt ermöglicht dabei eine besonders gute Ladungsextraktion und stark reduzierte Grenzflächenrekombination. Die Materialzusammenstellung erreicht in der Studie hohe stabilisierte Solarzellenwirkungsgrade bis zu 18,0% und eine vernachlässigbare Strom-Spannungs-Hysterese, ein üblicherweise ausgeprägtes Phänomen in diesem Zellaufbau. Das Ergebnis stellt Doppelschicht-Strukturen als generelles Konzept zur Herstellung effizienter und hochselektiver Kontakte heraus.

Basierend auf diesem Erfolg wird das Konzept, Eigenschaften verschiedener Materialien miteinander zu kombinieren, anschließend auf den *p*-Typ Kontakt übertragen. Dazu wird ein neuartiger lochselektiver Kontakt vorgestellt, bestehend aus einer Mischung des kleinen Moleküls Spiro-OMeTAD [2,2‘7,7‘-tetrakis(N,N-di-p-methoxyphenylamin)-9,9‘-spirobifluoren] und dem dotierten Polymer PEDOT [poly(3,4-ethylendioxythiophen)]. PEDOT unterdrückt dabei bemerkenswerter Weiße die Ladungsträgerrekombination an der Perowskit-Grenzfläche, wodurch eine Erhöhung der Quasi-Fermi-Niveau-Aufspaltung im Absorber erzielt wird. Weiterhin wird gezeigt, dass die Zugabe von Spiro-OMeTAD in die PEDOT-Schicht die Lochextraktion an der Grenzfläche verbessert und folglich hohe Solarzellenwirkungsgrade von bis zu 16,8% ermöglicht.

Schließlich wird das gewonnene Wissen über die Bedeutung der Kontakt- und Grenzflächeneigenschaften auf monolithische Perowskit-SHK-Tandemsolarzellen angewandt. Das Hauptziel dabei ist die Optimierung des oberen Kontaktstapels, bestehend aus dotiertem Spiro-OMeTAD/Molybdän Oxid (MoOx)/ITO, hin zu verbesserter Transparenz. Zwei verschiedene Ansätze werden hierzu verfolgt. Erstens, durch Feinanpassung der ITO-Abscheidung kann eine chemische Reduktion von MoOx verringert und die Transmission von MoOx/ITO-Schichtstapeln um 25% erhöht werden. Zweitens: Durch Ersetzen des Spiro-OMeTAD mit alternativen, transparenteren Lochtransportmaterialien sollen parasitäre Absorptionsverluste vermieden werden. Als potentielle Lochkontakte werden dabei PEDOT/Spiro-OMeTAD-Mischungen, CuSCN und PTAA [Poly(triarylamin)] analysiert. Experimentelle Untersuchungen liefern optimierte Dicken der Lochkontakt und MoOx Schichten und dienen der Validierung optischer Simulationen der Schichtstapel. Dies erlaubt im Folgenden eine realistische Abschätzung der maximal erreichbaren Tandemsolarzelleneffizienzen. Dabei stellt PTAA den vielversprechendsten Ersatz für Spiro-OMeTAD dar, mit einer prognostizierten Erhöhung des erreichbaren Tandem-Solarzellenwirkungsgrad um 2,9% relativ auf 26,5% absolut. Die Ergebnisse stellen zudem einen Leitfaden zur weiteren Effizienzsteigerung der Tandemsolarzellen-Technologie dar.

Table of Contents

1. Introduction

> “Coal is coming — clean coal. We love clean coal. And it’s coming back.”
>
> *- Donald J. Trump, president of the United States of America, July 25th, 2017.*

This statement by Mr. Trump, made at the saluting of “American Heroes” in Ohio, is in a way remarkable. Of course, there is no clean coal. Mining coal harmfully impacts large landscapes and its combustion accounted for 70% of the total CO_2 emissions of the US energy sector in 2017.[1] The quote can instead be understood as political campaign rhetoric, aimed at coal miners struggling with declining demand. It, therefore, stands illustrative of the increasing pressure on fossil fuels by renewable energies pushing into the electricity market.

Today, photovoltaics (PV) is the fastest growing technology for power generation and surpassed the net growth of coal already in 2016.[2, 3] A transition to renewable energies is also urgently needed to tackle global greenhouse gas emissions. The anthropogenic climate change already decupled the occurrence of extreme heatwaves in Europe from twice a century to twice a decade.[4] The summer of 2018, during preparation of this thesis, marked the driest ever recorded in many European countries, including Germany.[5] The terrible consequences were harvest losses in the billions and the continent’s deadliest wildfires this century in Scandinavia and Greece. Yet, fossil fuels still cover about 75% of the worldwide electricity production while PV only contributes with around 1.5%.[2, 6] To further increase this share, progressing price reductions and efficiency enhancements for photovoltaic systems are highly desirable.

Silicon solar cells are currently dominating the photovoltaic (PV) market with a share of 95% and module prices below 0.4 €/W_P, benefiting from scale effects and a decades-long learning curve of the industry.[7] Today, the balance-of-system costs (BOS) which include inverters, construction, connection, and mounting structures, account for more than 50% of the overall PV system price.[2] As BOS costs (excluding inverters) are all area-dependent, a forceful lever to further reduce the levelized cost of electricity (0.04-0.12 €/kWh for PV in Germany 2018[8]) is to increase the cell efficiency and yield more power per module area without significant additional processing costs. However, although silicon-PV module efficiencies are still developing, lab scale record values at 26.7%[9] already approach their theoretical efficiency limit of 29.4%.[10]

Instead, combining silicon with a larger band gap semiconductor in a tandem solar call can reduce thermalization losses while maintaining broad spectral absorption, which raises the theoretical efficiency limit up to 45%[11, 12]. Perovskite semiconductors perfectly match this requirement and can even more be fabricated simply and cost-effectively from abundant materials via low-temperature, solution-based processing. Integrating perovskites into existing production lines of silicon solar cells is therefore expected to increase the module costs by only 15%.[13] The perovskite-silicon tandem technology might thus exhibit low market entry barriers and represents a promising approach in PV to further increase the solar cell efficiencies while simultaneously reducing the levelized cost of electricity. Prototype photovoltaic modules, the establishment of companies dedicated to upscale the technology as well as commissioning of first pilot and development lines signify first steps towards commercialization of perovskite-silicon tandem solar cells.[14, 15]

Hybrid organic-inorganic perovskites were first employed in single-junction solar cells in 2009[16] and since then are the shooting star in PV research. Their excellent optical and electrical properties inspired extensive investigation and development of this material class at an unprecedented pace. In 2018, quantum yields of light emitting diodes already exceeded 10%[17] and solar cell efficiencies rocketed to above 23% (Figure 1.1).[18] Perovskites thereby surpass record values of CdTe and Cu(In,Ga)Se_2 (CIGS)[9], the two major technologies in thin film photovoltaics[2]. Further, altering the perovskite composition allows tuning the band gap energy to around 1.7 eV, which perfectly matches silicon for tandem solar cell application. Silicon heterojunction (SHJ) solar cells are especially promising candidates for perovskite-silicon tandem devices, as they obtained record open-circuit voltages[19], superior infrared performance[20] and the highest efficiencies so far in silicon photovoltaics at 26.7%[9] (Figure 1.1).

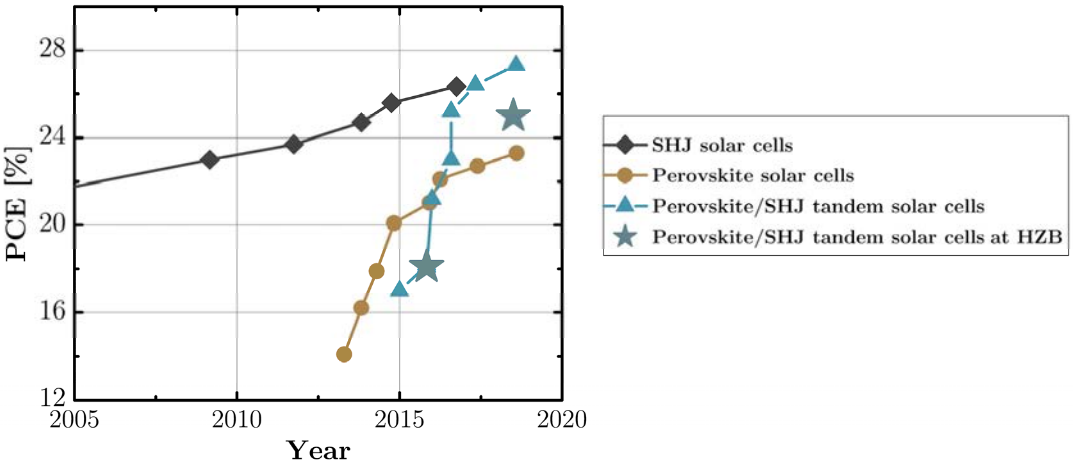

Figure 1.1: Rapid evolution of published or certified record efficiencies for perovskite and perovskite-silicon heterojunction (SHJ) tandem solar cells (two- and four-terminal) compared to highest values for SHJ single junction devices since 2005.[18] Stars mark perovskite-SHJ tandem solar cells realized at Helmholtz-Zentrum Berlin (HZB).[21, 22]

Indeed, record efficiencies of perovskite-silicon tandem solar cells already exceed the highest values for silicon single-junction devices (Figure 1.1). The current record, achieved with a SHJ bottom cell, amounts to 27.3%[23] and realistic estimates project efficiencies above 30% to be within reach[24, 25]. Two tandem architectures are generally distinguished: a mechanical stack of separately contacted perovskite and silicon solar cells (four-terminal), or their monolithic integration and series connection (two-terminal). The latter one thereby offers the potential advantages of fewer production steps, reduced parasitic absorption losses and less required wiring and power electronics on module level.

The monolithic design, however, also imposes process restrictions of the bottom cell on the manufacturing of the top cell. SHJ solar cells, for instance, are restricted to processing below 200°C. However, the best perovskite solar cells so far employ mesoporous TiO_2 as an electron selective contact, sintered at temperatures >450°C.[26, 27] Besides, the most commonly used hole selective contact, doped Spiro-OMeTAD [2,2‘7,7‘-tetrakis(N,N-di-p-methoxyphenylamin)-9,9‘-spirobifluoren], is highly absorptive and imposes severe optical losses in monolithic tandem solar cells.[21] Even more, the interfaces of perovskite thin films to adjacent layers were shown to determine the overall charge carrier collection from the absorber and thus require careful consideration.[28, 29] Contact layers, therefore, are decisive components which usually define the performance of perovskite solar cells. They need to tackle the main challenges of minimizing charge recombination losses at the interfaces while providing efficient carrier extraction.[28–30]

The presented work thus aims to advance contact layers in perovskite photovoltaics towards improved performances in monolithic perovskite-SHJ tandem solar cells. This requires low-temperature processing, high optical transmission and effective charge carrier extraction of the contact materials. Minimizing absorption losses thereby especially concerns the selective top contact, as light enters the tandem device through this layer, which is different for most perovskite single junction solar cells.

Motivated to develop efficient monolithic perovskite-silicon tandem solar cells, a variety of different planar, low temperature processed electron and hole selective contact materials are therefore examined here. The materials are first employed in opaque single-junction perovskite solar cells to analyze and understand the contact properties. Photoelectron spectroscopy measurements are utilized to investigate the energetics of the studied materials and photoluminescence characteristics provide insights into charge transport or recombination processes at the contact layer/perovskite absorber interface. Further, surface photovoltage spectroscopy and electron microscopy allow to determine the perovskite absorber quality grown on different contact materials. This enables a clear correlation of contact material and interface properties to solar cell parameters on the device level. Further, optical properties of the contact layers are determined by reflectance and transmittance measurements. Finally, these layers are integrated into complex monolithic tandem solar cells and their performance potential is examined. By combining experimental results with optical simulations, efficiency improvements in monolithic perovskite-SHJ tandem solar cells are evaluated. The design guidelines developed here might help to advance the tandem PV technology and in the long run contribute to further expand the harness of a truly clean source of energy: the Sun.

Outline of this work

The doctoral dissertation is structured as follows:

Chapter 2 provides the fundamentals to this theses. This includes the basic knowledge of solar cells and principle advantages of multi-junction devices. Further, a comprehensive introduction of the structural and physical properties of organic-inorganic perovskites is provided. Finally, the working principles and state of the art for perovskite, and SHJ single junction, as well as perovskite-SHJ tandem solar cells, are presented.

Chapter 3 describes the materials and methods utilized for the processing of solar cells. This includes opaque or semi-transparent single-junction as well as monolithic tandem solar cells. Besides, the experimental methods used to analyze the materials, the individual layers and the complete solar cells are described.

Chapter 4 presents the main part of the thesis as it summarizes the results based on three different concepts, all aiming to advance selective contact layers towards more efficient perovskite single junction and perovskite-silicon tandem solar cells.

Chapter 4.1 offers a comparative study of different electron selective contacts in planar, opaque *n-i-p* type perovskite solar cells. The energetic properties of the different materials, the perovskite absorber quality grown on top as well as charge extraction at their interface is investigated. Further, these results are used to identify dependencies between the electrical performances of solar cells and the *n*-type interface properties.

Chapter 4.2 introduces a mixture of dopant-free Spiro-OMeTAD and water-free PEDOT [poly(3,4-ethylene-dioxythiophene)] as novel hole selective contact in *n-i-p* type perovskite solar cells. The mixture is shown to suppress recombination losses at the absorber interface, enabling higher open circuit voltages and efficiencies in solar cells as compared to the generally used hole contact in this architecture, doped Spiro-OMeTAD.

Chapter 4.3 aims towards highly transparent top-contact layer stacks in monolithic perovskite-SHJ tandem solar cells with *n-i-p* type top cell architecture. Two regions of interest were identified: region (I) increasing the transparency-conductivity product of the MoOx/ITO top electrode. Region (II), alternative and more transparent selective hole contacts, replacing the typically used Spiro-OMeTAD. Determining the optical properties and minimum required layer thicknesses of the hole contacts allows to estimate their efficiency potentials in optical simulations. The viability of the simulations is further supported by experimental results.

Chapter 5 reviews the most important results as the conclusion of the presented work and provides an outlook as well as guidelines for further research. This concerns optimization of charge selective contact layers for perovskite single junctions, transparent top contacts for monolithic tandem integration as well as the tandem solar cell performance in general.

2. Fundamentals

The following chapter provides the core knowledge for the analysis and discussion of experimental data presented here. An overview of fundamental aspects of solar cells will elucidate the potential of tandem solar cells to evade thermalization losses and overcome efficiency limitations of the market-dominating single-junction architecture.

Further, hybrid organic-inorganic perovskites will be introduced at the current state of research. After presenting the general crystal structure, typical compositions and current drawbacks, mainly toxicity and stability, their exceptional optical and electronic properties will be highlighted. Reflection of these features in the rapid evolution of perovskite solar cells, common device structures, widely used materials as well as strategies for further performance enhancements will be discussed.

Finally, after introducing the basic architecture and working principle of silicon heterojunction solar cells, efficiency potentials and recent technological progress in perovskite-silicon (heterojunction) tandem solar cells will be elaborated.

2.1 Solar Cells – A Brief Introduction

The sun provides a sustainable source of energy for the next 5 billion years.[31] Proton-proton chain reactions within the core cause fusion of hydrogen to helium and direct conversion of mass to energy, following Einstein's relation $E=mc^2$.[32] This release of energy allows photoemission from excited atoms within the photosphere and radiation of light to earth.[31, 32] Remarkably, the amount of usable solar radiation received by earth exceeds the global power consumption on earth by three orders of magnitude.[33]

Light irradiated on a semiconductor can be directly converted to electricity by the photovoltaic effect, as discovered by Becquerel in 1839.[34] A first solar cell made from gold-coated selenium in 1885[35], as well as an initial silicon-based device in 1941[36], mark the cornerstones of photovoltaic (PV) research.

2.1.1 Solar Radiation and Spectrum

The sun can be regarded as a black body meaning that it absorbs all incoming light and emits radiation according to Planck's law [31]:

$$L_\lambda(\lambda, T) = \frac{2\pi hc^2}{\lambda^5} \frac{1}{e^{\frac{hc}{\lambda k_B T}} - 1}, \tag{2.1}$$

where L_λ is the spectral radiance in $\mathrm{W \cdot m^{-2} \cdot nm^{-1} \cdot sr^{-1}}$, h is the Planck constant, c is the speed of light in vacuum, k_B is the Boltzmann constant, T is the surface temperature of the black body and λ is the respective wavelength of the emitted photons. The spectral irradiance E_λ of the sun, regarded as a black body, onto earth can then be approximated from equation (2.1) by taking the radius of the black body (the Sun) r_{BB} and its distance to earth d_{BE} into account [31]:

$$E_\lambda(\lambda, T) = \left(\frac{r_{BB}}{d_{BE}}\right)^2 L_\lambda(\lambda, T). \tag{2.2}$$

The solar radiation can be calculated by integrating the spectral irradiance over wavelength, which amounts to 1360 $\mathrm{W/m^2}$ received by the earth orbit. [37] Its spectral distribution (AM0) is depicted in Figure 2.1 as compared to the irradiance from a black body with a surface temperature of the sun's photosphere (~5800 K), a radius of to the sun $r_{BB} \approx 7 \cdot 10^5$ km and $d_{BE} \approx 1.5 \cdot 10^8$ km equal to the sun's distance to earth [31]. Yet, Rayleigh scattering at molecules, Mie scattering at particles and parasitic absorption in the atmosphere e.g. from O_2, CO_2 or H_2O affect the spectral irradiance on the surface of the earth after the sun light has passed the atmosphere at a certain angle. The solar spectrum on earth for a zenith angle of 48.2° was defined as standard test condition illumination which corresponds to the light passing through 1.5 atmosphere heights or so-called Air Masses (AM).[37] For this case, the spectral irradiance taking both direct as well as diffuse sunlight into account (AM1.5G) is shown in Figure 2.1 as well. Integrating the spectral irradiance over the wavelength reveals a reduced solar radiation for AM1.5G of 1000 $\mathrm{W/m^2}$ as compared to AM0.[31]

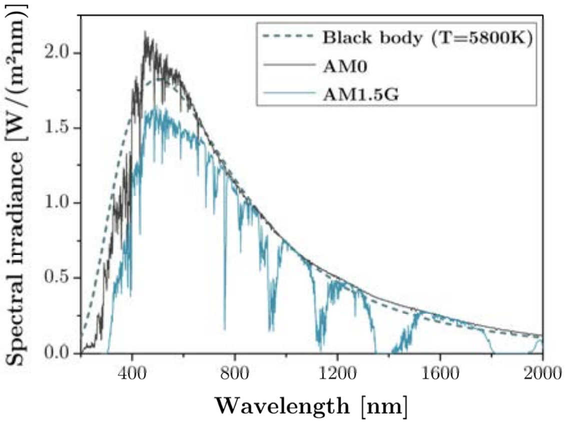

Figure 2.1: Spectral irradiance of the sun outside the atmosphere (AM0) and at the surface of earth for a solar zenith angle of 48.2° (AM1.5G) in comparison to black body radiation at 5800 K surface temperature. Data for AM0[38] and AM1.5G[39] were obtained from the National Renewable Energy Laboratory (NREL), black body irradiation was calculated according to eq. (2.2).

2.1.2 Charge Generation, Collection and Recombination

A solar cell directly converts incident light into electric power by the photovoltaic effect, meaning the generation of photocurrent and photovoltage.[34, 37] This requires the creation of free electron-hole pairs and their efficient collection at the respective contact while avoiding carrier losses due to different recombination processes.

Generation

The main generation process of electron-hole pairs in solar cells is the internal photoelectric effect. Accordingly, photons with energies higher than the band gap energy of the semiconductor can excite electrons into the conduction band of the material, leaving behind a hole in the valence band. After excitation, electron-hole pairs relax to the conduction and valence band edges (thermalization), most likely by transferring their excess energy to phonon modes.[31] Defect states within the forbidden band gap energy can also allow a stepwise reach of the charge generation energy by smaller portions from lower energy photons or even phonons.[10] However, under working solar cell conditions, this effect is negligible.

Due to their band structure as shown exemplarily for Si on the left in Figure 2.2, indirect semiconductors require not only a change in energy but also in momentum to excite electrons from the valence band maximum to the conduction band minimum. As the momentum of photons is negligible, this change in momentum is provided by the absorption or emission of phonons from or to the semiconductor, making the photon absorption less probable.[31] In contrast, direct semiconductors do not require a change in momentum on charge excitation, such as for $CH_3NH_3PbI_3$ perovskites with a band structure shown on the right in Figure 2.2 a), determined by *ab initio* calculations from Leguy et al.[40]

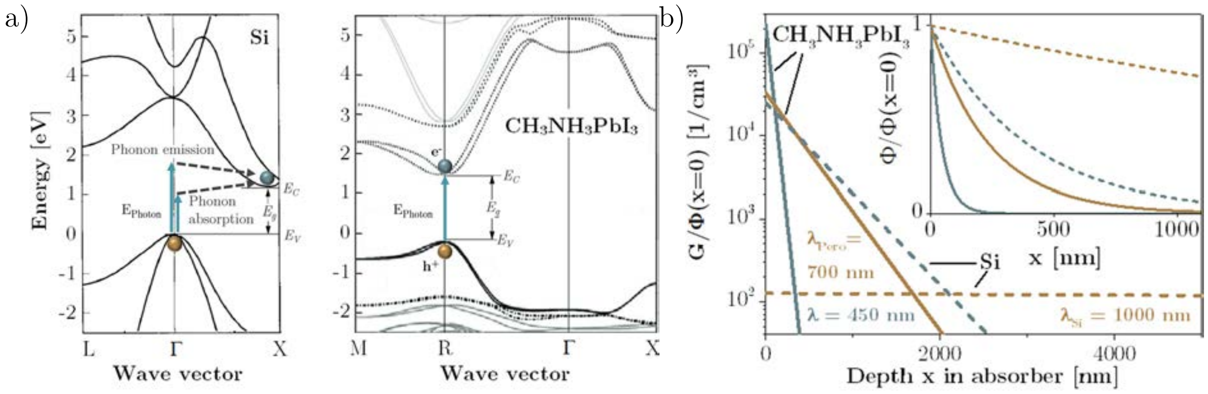

Figure 2.2: a) Energy band structure of Si [41] (left) and cubic $CH_3NH_3PbI_3$ perovskites along the relevant k-branches in the first Brillouin zone according to ab initio calculations by Leguy et al.[40] (right). Generation of free electrons (e^-) and holes (h^+) by photon absorption is indicated by a blue arrow for the direct semiconductor $CH_3NH_3PbI_3$ in comparison to the indirect semiconductor Si which requires additional absorption or emission of phonons (black arrows). E_C, E_V, E_G denotes conduction band minimum and valence band maximum energy as well as band gap energy, respectively. b) Generation rate of electron-hole pairs on excitation of Si and $CH_3NH_3PbI_3$ perovskite close to the band gap energy (λ=700 nm for perovskite and 1000 nm for Si) and far above it (λ=450 nm) as well as corresponding photon flux decays within the absorbers (inset), both normalized to the incident photon flux ϕ(x=0). Absorption coefficients for calculations were obtained from Green et al.[42] for Si and Guerra et al.[43] for $CH_3NH_3PbI_3$.

The onset of the absorption coefficient at the band gap energy is thus considerably sharper than for indirect semiconductors. According to Lambert-Beer law, the spectral (ϕ_λ) and total (ϕ) photon flux through a semiconductor declines proportional to its absorption coefficient α with[31]:

$$\Phi_\lambda(x,\lambda) = \Phi_\lambda(x=0,\lambda)e^{-\alpha(\lambda)\cdot x} = A\frac{E_\lambda(\lambda)\cdot\lambda}{hc}e^{-\alpha(\lambda)\cdot x} \tag{2.3}$$

$$and\ \Phi(x) = \int \Phi_\lambda(x,\lambda)d\lambda,$$

where x is the depth in the absorber, A is the illuminated area and E_λ the spectral irradiance. The spectral (G_λ) and total (G) generation rate of electron-hole pairs is then proportional to the decay of the photon flux [31]:

$$G_\lambda(x,\lambda) = -\frac{\eta_q}{A}\cdot\frac{\partial\Phi(x,\lambda)}{\partial x} = \eta_q\frac{E_\lambda(\lambda)\cdot\lambda}{hc}\alpha(\lambda)\cdot e^{-\alpha(\lambda)\cdot x} \tag{2.4}$$

$$and\ G(x) = \int G_\lambda(x,\lambda)d\lambda,$$

with η_q being a constant describing the photon-to-electron conversion efficiency. Assuming that every photon is converted to an electron-hole pair (η_q=1), the normalized decay of the photon flux as well as the charge generation rate is shown in Figure 2.2 b) on excitation of Si and $CH_3NH_3PbI_3$ perovskite with photon energies close to the band gap energy and far above it. These decays illustrate the stronger absorption of higher energy photons for both materials. Besides, it highlights the weaker absorption of the indirect semiconductor Si close to the band gap energy mentioned before as compared to the $CH_3NH_3PbI_3$ perovskite, which will also be further discussed in chapter 2.2.2. Thus, also charge generation rates are lower close to the surface and decay less strongly into the bulk of the absorber for indirect semiconductors which requires thicker films to reach high absorption and with that high photocurrents.

Irrespective of direct or indirect photoexcitation, the generated electron-hole pairs attract each other by Coulomb force due to their opposite charge. If their energy after excitation is insufficient to escape the attraction, a quasiparticle named exciton is formed as a bound state of an electron and a hole. Inorganic semiconductors such as Si usually have high relative dielectric constants (>10)[44] and well delocalized states, which effectively reduces the Coulomb attraction and leads to exciton binding energies lower than the thermal energy at room temperature ($k_BT \approx 25.7$ meV). Therefore essentially all generated electrons and holes are free particles in these materials. Organic semiconductors, on the other hand, typically exhibit a relative permittivity in the range of 2-4, together with strongly localized states and low mobilities.[45, 46] Their exciton binding energies therefore are much larger than k_BT which requires subsequent dissociation of excitons at a hetero-interface with energetic band offsets and complicates the photovoltaic process.[10] The role of excitons in hybrid perovskites was unclear in the beginning years of research and is known today to strongly depend on the perovskite composition. For $CH_3NH_3PbI_3$ i.e. exciton binding energies fall below k_BT[47], whereas for $CH_3NH_3PbBr_3$ they amount to around 40 meV[48]. Exciton binding energies in perovskites are further discussed in section 2.2.2.

Collection

After photogeneration, free electron-hole pairs have to be collected efficiently in order to provide electrical power. This requires a suitable combination of absorber thickness, which along with the absorption coefficient determines the overall charge generation, charge carrier mobility μ and charge carrier lifetime τ, which is limited by recombination processes as further elucidated below. Indirect semiconductors like Si, with several hundred micrometer thick absorbers, therefore have to provide substantially higher carrier mobilities and/or lifetimes as compared to thin film photovoltaics of direct semiconductors like GaAs. $CH_3NH_3PbI_3$ perovskites turned out to provide diffusion lengths L $(L=(\tau \cdot D)^{0.5}=(\tau \cdot \mu \cdot k_BT \cdot e^{-1})^{0.5})$[44] well exceeding typical film thicknesses in solar cells of usually below 1 µm.[49, 50] In these cases, charge collection strongly depends on their efficient extraction at the respective charge selective contact.

Charge collection is driven by electric fields or diffusion, both combined in the gradients of the quasi-Fermi levels.[10] Yet, these forces are not necessarily selective in illuminated semiconductors and charge carriers may be able to move towards both contacts where they are extracted.[51] This problem can be circumvented by using selective contacts; semipermeable membranes, which ideally exclusively transfer one carrier type. A necessity for this is a large difference in the conductivities of electrons and holes within the selective contacts.[10, 51]

The *pn*-homojunction as depicted in Figure 2.3 a) represents a typical implementation of this concept, where conductivities of majority and minority carriers differ by orders of magnitude in the respectively doped regions. However, while a large quasi-Fermi level splitting across the semiconductor under illumination enables high voltages, it also increases the minority carrier densities, as displayed in Figure 2.3 a) by the far reaching minority quasi-Fermi levels in the doped regions. As a consequence, also the conductivities of the minorities are increased, which counteracts the concept of a semi-permeable membrane and reduces the selectivity of the *p*- and *n*-doped regions.[10, 51] This is illustrated in Figure 2.3 a) by the slight drop in quasi-Fermi level splitting towards the surfaces of *n*- and *p*-type regions. A *pn*-junction is therefore ultimately not an ideal structure for solar cells, especially for enabling the highest photovoltages.

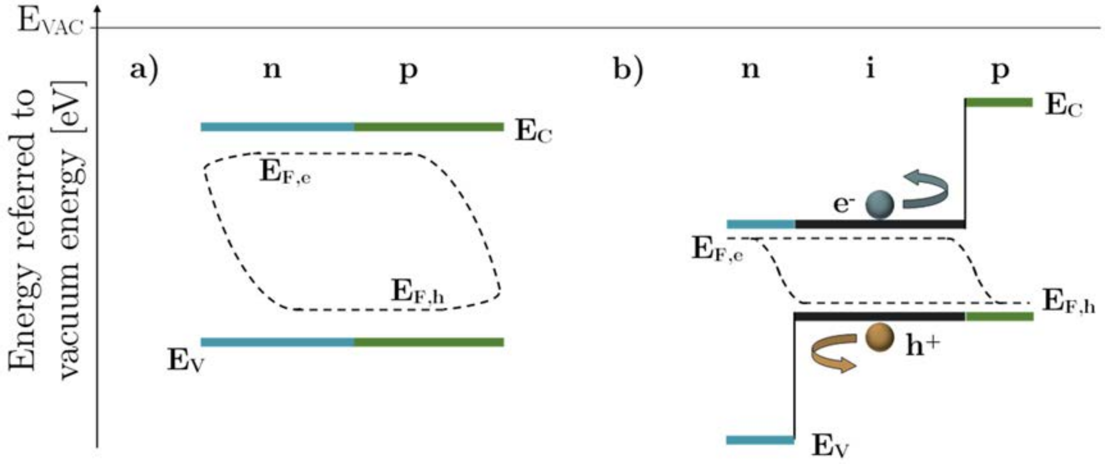

Figure 2.3: Band diagram and quasi-Fermi level splitting of a) a pn-homojunction and b) a double heterojunction structure under illumination. N, i and p mark n-type, intrinsic and p-type regions. E_C, E_V, $E_{F,h}$, $E_{F,h}$ denote conduction, and valence band energies, as well as quasi-Fermi energies of holes and electrons, respectively. Depiction following Würfel et al.[10]

Heterojunctions instead can create substantial differences in electron and hole conductivities. Conductivity is proportional to the charge carrier mobility and density.[10] Large energetic barriers for the undesired charge at the interfaces reduce the minority carrier density in the selective contact layer and thus its minority conductivity. The double heterojunction device structure shown in Figure 2.3 b) has no built-in electric field at all, but was confirmed in simulations by Würfel et al. to be capable to work as an ideal solar cell due to efficient blocking of holes (electrons) and conduction of electrons (holes) at the *n*-type (*p*-type) contact.[51] Both, the Si heterojunction as well as the hybrid perovskite solar cells used in this work employ heterojunctions for charge separation as further discussed in chapters 2.3 and 2.2.3, respectively.

Recombination

Charge carrier recombination represents the opposite process of generation and designates any process leading to annihilation of electron-hole pairs. A recombination event can be radiative by emitting a photon that could potentially be reabsorbed, or by a non-radiative process and concomitant energy dissipation most likely into phonon modes of the lattice. The entirety of charge recombination events can be subdivided in the fundamental mechanisms of (a) direct (or also called bimolecular) recombination which is typically a radiative process, (b) Auger recombination, (c) Shockley-Read-Hall recombination and (d) surface recombination, with (b),(c), and (d) being most likely non-radiative processes. Their principle recombination pathways are simplified in Figure 2.4 and further discussed in the following.

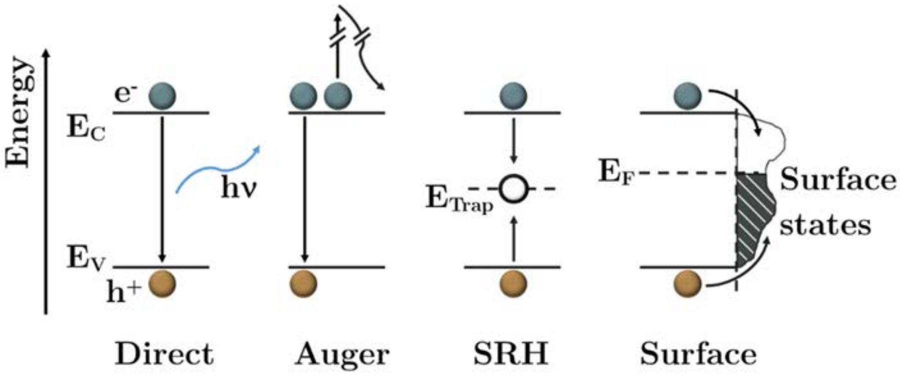

Figure 2.4: Simplified electron (e$^-$) – hole (h$^+$) recombination pathways for direct, Auger, Shockley-Read-Hall (SRH) and surface recombination. Adopted from [37].

Direct recombination typically is the inverse internal photoelectric effect, meaning annihilation of an electron-hole pair, under release of the excess energy (E_g) by the emission of a photon. It is therefore also often denoted as radiative or also as bimolecular recombination. As this process involves one electron and one hole, the radiative recombination rate (R_{rad}) increases with their respective densities (n, p) as $R_{rad} = \beta np$, where β is the radiative recombination rate constant.[37] Thus, the recombination rate depends on the carrier density to the power of two. Direct recombination is of minor importance in Si with β being in the order of 10^{-14}-10^{-15} cm^3/s[52] due to its indirect bandgap.[53] In perovskites on the other hand, β amounts to around 10^{-10}-10^{-11} cm^3/s[54] which is similar to GaAs with 10^{-10}-10^{-11} cm^3/s[52, 55].

Auger recombination describes an electron-hole pair that transfers its excess energy and momentum during annihilation to another charge carrier in the vicinity which subsequently releases the energy to phonon modes and relaxes to the band edge. Auger recombination hence is a three-particle process and its rate is proportional to n^2p (p^2n), the charge density to the power of three.[37] It is negligible in perovskites under one-sun illumination due to their direct bandgap and high radiative recombination rate[52] but represents a substantial recombination mechanism in Si semiconductors due to their indirect band gap and common doping levels in the order of 10^{15} cm^{-3} [53].

Both direct and Auger recombination are intrinsic processes and cannot be avoided.

Shockley-Read-Hall (SRH) recombination denotes the recombination of an excited electron-hole pair via a defect state (also called trap state) within the band gap. An ideal semiconductor is free of electronic states with energies in the forbidden band gap. However, in real photovoltaic absorbers, imperfections such as impurities or point defects (e.g. interstitials or vacancies) in the crystal can create states within this gap.[37, 53] Charge carriers can occupy those states and either be released to the conduction (for electrons) or valence (for holes) band or recombine with a carrier of opposite charge. As the re-emission rates reduce exponentially with the defect state getting closer to the middle of the band gap, it follows that mid-gap defect states act as more severe recombination centers than states close to the band edges.[56, 57] The recombination rate for SRH recombination is directly proportional to the carrier density, the trap state density and their capture cross-sections for electrons and holes, but also depends on the occupation of the traps.[44] For mid-gap traps in an intrinsic semiconductor, half of them is occupied with electrons, and the order of recombination becomes one.

Surface recombination designates SRH recombination across defect states at the surface of a semiconductor. As surfaces constitute an abrupt termination of the crystal symmetry, the substantial amount of non-saturated (dangling) bonds gives rise to high densities of electronic states with broad distribution in the forbidden band gap.[37] Besides, recombination through energetic states of layers interfacing the absorber surface and unintended extraction of electrons (holes) at the p-type (n-type) contact have been assigned as surface recombination losses.[52] Typically, surface recombination is described by a surface recombination velocity $s_{n,p}$ which is proportional to the trap state density and their capture cross-sections for electrons and holes. Surface recombination further is generally treated as a first order recombination process. Passivation of surface recombination was a key strategy to increase the efficiency in Si photovoltaics[58] and lead to the development of Si-heterojunction solar cells as further discussed in section 2.3. It also has turned out as a major obstacle in perovskite solar cells recently,[28, 52] chapter 4.2 discusses this in more detail and introduces a method to passivate surface recombination.

The combination of all aforementioned recombination processes determines the effective charge carrier lifetime of a semiconductor as [37]:

$$\frac{1}{\tau_{Total}} = \frac{1}{\tau_{Dir}} + \frac{1}{\tau_{Auger}} + \frac{1}{\tau_{SRH}} + \frac{1}{\tau_{Surface}} \quad and \quad \frac{1}{\tau_i} = \frac{\Delta n}{R_i(\Delta n, n_0)} \tag{1}$$

with τ_i being the lifetime, n_0 and Δn the intrinsic and excess charge carrier density, respectively, as well as R_i the recombination rate for direct (Dir), Auger, SRH and surface recombination, respectively. SRH and surface recombination losses depend on defect states in the material and are thus subject to absorber processing and handling conditions. They have to be minimized in order to maximize the charge carrier lifetime of a semiconductor. As an example, high-quality semiconductors under one-sun-equivalent excitation achieve lifetimes in the order of 0.01-1 µs for GaAs[44, 59], 1-10 µs for perovskite thin films[60, 61] and single crystals[50, 62] and >1 ms for crystalline Silicon[44].

2.1.3 Relevant Performance Parameters

An ideal solar cell under illumination can be described by an electrical equivalent circuit of a diode in parallel to a current source. The current output (I) for an external voltage (V) is then given by [12]:

$$I = I_0 \left[exp\left(\frac{q \cdot V}{k_B T}\right) - 1 \right] - I_{SC}. \tag{2.5}$$

Here, I_0 denotes the reverse dark saturation current and q the elementary charge. The short-circuit current I_{SC} is the photocurrent generated by the solar cell under illumination and can be determined by [12, 63]:

$$I_{SC} = q \int_0^{\infty} EQE_{PV}(E) \cdot \Phi_{AM1.5G}(E) dE, \tag{2.6}$$

where EQE_{PV} is the spectral photon-to-electron conversion efficiency of the solar cell and $\phi_{AM1.5G}$ is the photon flux under AM1.5G illumination. I_0, the reverse saturation current, represents charge recombination processes in dark and in thermal equilibrium of the solar cell with its environment. In this case, the solar cell has to emit radiation equal to the amount absorbed by black body radiation from its surrounding, i.e. from earth ($\phi_{BB,E}$), to be in detailed balance. I_0 can thus be expressed as [63]:

$$I_0 = \frac{q}{EQE_{EL}} \int_0^{\infty} EQE_{PV}(E) \cdot \Phi_{BB,E}(E) dE. \tag{2.7}$$

EQE_{EL} is the external electron-to-photon conversion efficiency, which equals one for the ideal case of pure radiative recombination in the solar cell. As such, we can determine the open circuit voltage V_{OC} from eq. (2.5) by setting I to zero and including eq. (2.6) and (2.7) as:

$$V_{OC} = \frac{k_B T}{q} \ln\left(\frac{I_{SC}}{I_0} + 1\right) = \frac{k_B T}{q} \ln\left(\frac{EQE_{EL} \cdot \int_0^{\infty} EQE_{PV}(E) \cdot \Phi_{AM1.5G}(E) dE}{\int_0^{\infty} EQE_{PV}(E) \cdot \Phi_{BB,E}(E) dE} + 1\right) \tag{2.8}$$

While I_{SC} is directly proportional to ϕ, V_{OC} only follows the illumination intensity by $ln(\phi)$. To maximize I_{SC} and minimize I_0, EQE_{PV} should therefore be as high as possible in the energy region where the solar flux dominates (typically above E_g) and as low as possible in the lower energy region where ϕ_{BB} dominates (typically below E_g). It can thus be deduced from eq. (2.8) that an efficient solar cell with both high I_{SC} and V_{OC} values requires a good spectral EQE_{PV} with a sharp onset at E_g as well as a high electroluminescence efficiency (EQE_{EL}) with minimal non-radiative recombination pathways.[12, 63] A good solar cell therefore also has to be an efficient light emitting device.

The electrical equivalent circuit corresponding to eq. (2.5) is often extended to better represent a real solar cell by [37]:

$$I = I_0 \left[exp\left(\frac{q \cdot (V - I \cdot R_S)}{n_{id} k_B T}\right) - 1\right] + \frac{V - I \cdot R_S}{R_P} - I_{SC} \tag{2.9}$$

Here, the diode ideality factor n_{id} equals one for the ideal case of solely radiative recombination in the solar cell and approaches two with increasing Shockley Read Hall recombination. Besides, the series resistance R_S in eq. (2.9) represents the ohmic charge transport losses for carriers on extraction from the solar cell, while the parallel resistance R_P resembles charge recombination losses via shunt paths in the solar cell, so-called "leakage currents".

Finally, the power output of a solar cell is given by the product of $I \cdot V$, which both depend on the external load connected to the cell. The working point in which $I \cdot V$ becomes maximal is denoted maximum power point (*MPP*). The power conversion efficiency (*PCE*) of a solar cell is therefore determined by the ratio between maximum electrical power output and incident light intensity (P_{light}) [37]:

$$PCE = \frac{P_{MPP}}{P_{light}} = \frac{I_{MPP} \cdot V_{MPP}}{P_{light}} = \frac{FF \cdot I_{SC} \cdot V_{OC}}{P_{light}} \; with\, FF = \frac{I_{MPP} \cdot V_{MPP}}{I_{SC} \cdot V_{OC}}. \tag{2.10}$$

The fill factor (*FF*) as defined in eq. (2.10) partially reflects the quality of the solar cell as it is reduced both by parallel as well as series resistance losses. The potential *FF* of a solar cell with

R_S=0 and R_P approaching infinity can be well approximated according to an empiric formula by Green [64]:

$$FF = \frac{v_{OC} - \ln(v_{OC} + 0.72)}{v_{OC} + 1} \; with \; v_{OC} = \frac{q \cdot V_{OC}}{n_{id} k_B T} \; for \; v_{OC} > 10. \tag{2.11}$$

Exemplary current density-voltage (*J-V*) characteristics of a solar cell in dark and under illumination are displayed in Figure 2.5 a). As depicted, an increase of R_S flattens the slope around V_{OC}, while a reduction of R_P raises the *J-V* gradient around J_{SC}, both leading to reduced *FF* and *PCE*. Plotting the corresponding dark *J-V* curves on a semi-logarithmic scale (Figure 2.5 b) further elucidates higher leakage currents in the low voltage regime (A) for reduced R_P. The influence of R_S, in contrast, is dominating in the region of higher voltages (B).

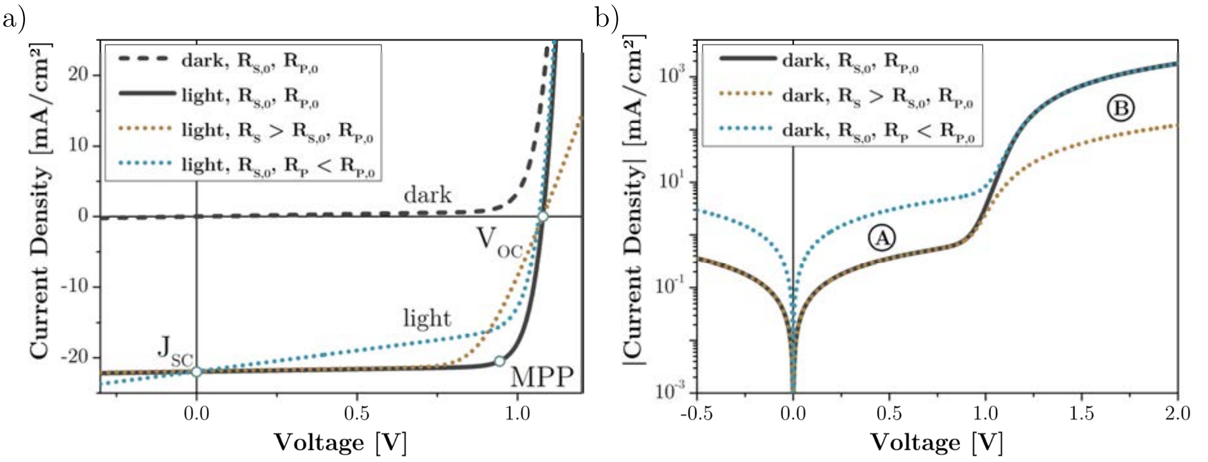

Figure 2.5: a) Current density-voltage (J-V) curves of an exemplary solar cell in dark and under illumination, as well as for increased series and reduced parallel resistance. b) Absolute values of the corresponding dark J-V characteristics on a semi-logarithmic plot and for an extended voltage range (-0.5 - 2 V). Note that J(0)=0 in all cases for dark conditions.

Transient phenomena, which are particularly pronounced in perovskite solar cells as described in section 2.2.3, can affect the power output of a device across an external load over time. It is therefore reasonable to perform MPP tracking measurement over minutes for a more precise determination of the efficiency. This is profoundly discussed in chapter 4.1 and the method for MPP tracking used in this work is presented in section 3.2.1.

2.1.4 Multi-Junction Solar Cells

As described in the previous chapter 2.1.2, the band gap energy of a semiconductor (E_g) imposes two substantial loss mechanisms in solar cells: (1) transmission: photons with energies $E_{Photon}<E_g$ are essentially not absorbed; (2) thermalization: for $E_{Photon}>E_g$ the excess energy of photogenerated charges is transferred as heat to the crystal lattice. Additionally, inevitable, yet less extensive loss processes, arise within the solar cell: The optical reciprocity theorem as first introduced by Kirchhoff[65], requires every absorber to also emit light (emission losses), which typically occurs via direct recombination. Besides, out of thermodynamic constraints, Carnot losses arise, as a solar cell can be regarded as heat engine with heat flowing from the hot Sun to the cold atmosphere, and the so-called Boltzmann losses due to the irreversibility in the direction of photon absorption versus emission.[11] Figure 2.6 a) depicts the proportionate distribution of those losses for the ideal power output of a single-junction solar cell under one sun-equivalent illumination. The maximum device efficiency for this case amounts to 33.77% for an E_g of 1.34 eV under AM1.5G illumination, as first elucidated by Shockley and Queisser[66] and later refined by others[67]. The spectral distribution of those losses and the power output is also presented in the bottom section of Figure 2.6 b).

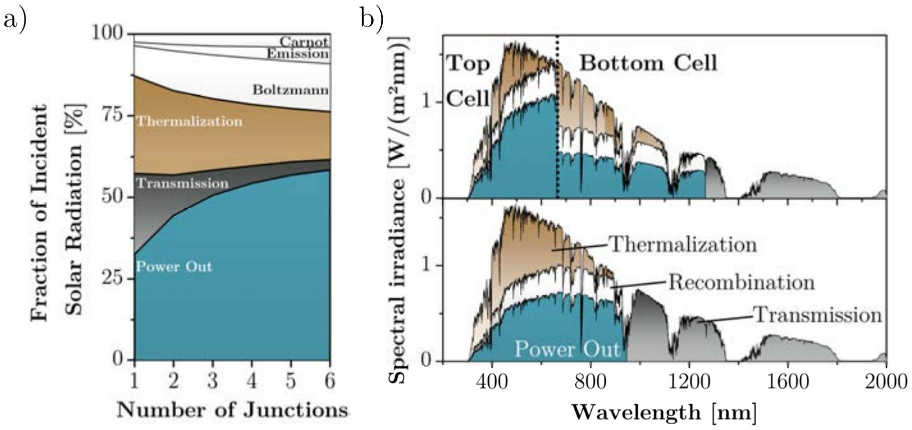

Figure 2.6: a) Fractional losses and maximum power output for the ideal band gap energies under one sun illumination in one to six junction solar cells. Adapted from [11]. b) Spectral distribution of thermalization, recombination and transmission losses as well as the maximum power output for an ideal single junction (bottom, E_g=1.34 eV) and an ideal two-junction tandem solar cell (top, E_{g1}=1.87 eV, E_{g2}=0.98 eV) under AM1.5G illumination. Calculated in reference to [11] and [12].

In order to reduce the vast transmission and thermalization losses, it is therefore beneficial to combine semiconductors with different E_g in a solar cell. Typically, n semiconductors with $E_{g1}>E_{g2}...>E_{gn}$, are arranged optically in series so that light enters the E_{g1} material first, as thermalization losses are smaller here than in lower E_g materials for the same E_{Photon}. All photons with $E_{Photon} < E_{g1}$ are then transmitted to the lower E_{g2} semiconductor and so forth. Also other concepts were demonstrated, such as spectral splitting systems which use dichroic mirrors to spectrally distribute the incoming light to the respective semiconductor according to the band gap.[68] Figure 2.6 a) delineates the reduction of thermalization and transmission losses for the optimum power output in multi-junction solar cells comprising two to six different semiconductors under one sun illumination. Additionally, the spectral distribution of losses and maximum power for an ideal two-junction device is illustrated in the top section of Figure 2.6 b). The reduction of transmission and thermalization losses raises the maximum achievable efficiency under one sun-equivalent excitation up to around 45, 50 and 53% for two-, three- and four-junction solar cells respectively.[11, 12] The current world-record for multi-junction solar cells with non-concentrated irridation is 38.8%, realized by Boeing-Spectrolab comprising five different band gap energies (2.17/1.68/1.40/1.06/0.73 eV).[9]

There are essentially two different structures that are used for multi-junction solar cells. Firstly, devices in which each of the subcells are contacted separately, whereby the cells function electrically independently of each other. They are simply mechanically stacked and share the incident light. This design offers the advantage, that every subcell can be operated for each illumination at its optimum working point. On the other hand, each subcell requires two electrodes which have to be highly transparent in the spectral range(s) of the underlying absorber(s). Besides, as every cell has to be connected individually, more electronic infrastructure is required, e.g. wiring or inverters, which increases the overall system costs.

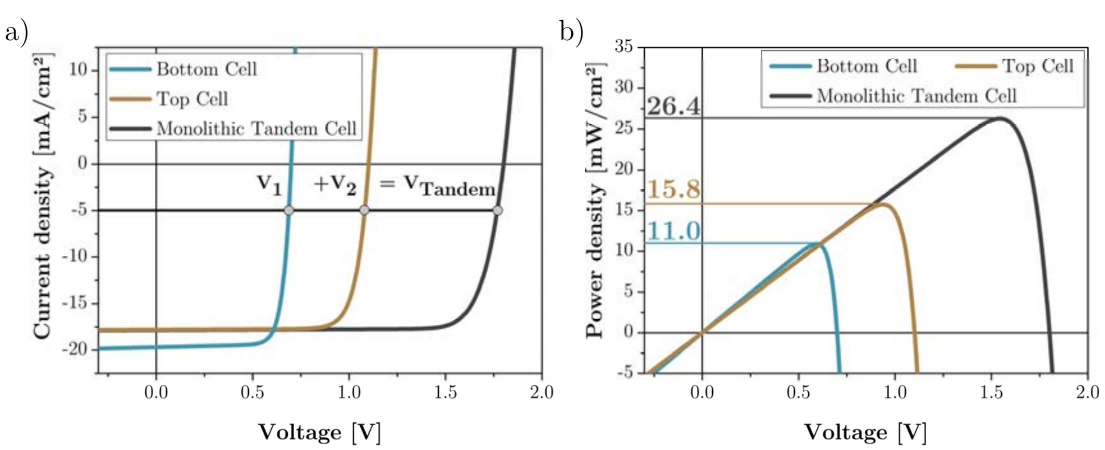

Figure 2.7: a) Current-voltage characteristics and b) corresponding power density output of independently contacted as well as series connected top and bottom cells in a two-junction tandem solar cell architecture.

Secondly, in monolithic multi-junction cells, all subcells are integrated directly on top of each other, which usually results in an electrical series connection of the cells. The series connection leads to an addition of the subcell voltages at each current density, as exemplarily illustrated for a two-junction tandem device in Figure 2.7 a). Yet, it also causes the complete tandem stack to be limited by the cell with the lowest current output, e.g. the top cell in the example of Figure 2.7 a). This can result in power losses, as illustrated in the corresponding Figure 2.7 b), where the peak power output of the series connected tandem cell is slightly lower than the sum of maximum power outputs for individually contacted subcells.

Multi-junction cells should thus be designed in a way that every sub cell generates the same current. Besides, by additional taps between the cells, a monolithic three- or more contact design can also be implemented, in which the subcells can be connected in parallel or operated independently at separate loads.[69]

A comparison of the expected annual power output between series and independently connected tandem solar cells under real-world conditions is presented in chapter 2.4, for the example of perovskite-Si tandem solar cells. Further in this work, the selective contacts in monolithic two-terminal tandem solar cells comprising Si and perovskite absorbers are investigated. A more detailed description of this tandem solar cell is presented in section 2.4.

2.2 Organic-Inorganic Perovskites

Today, the name perovskite designates one of the most versatile and chemically diverse families of crystals. With an ABX_3 stoichiometry crystallizing in a cubic, tetragonal or orthorhombic structure a broad range of properties can be achieved, e.g. from metallic[70] to semiconducting[71] and insulating[72]. Approximately 2000 perovskites are currently known.[73] They were first discovered as the mineral $CaTiO_3$ in the Ural Mountains by Rose in 1840 and named after the Russian mineralogist Lev Perovskii.[74] While already sparking some research interest in the early

20th century[75], the first perovskite structures with an organic ion at the A site were reported by Weber in 1978.[76] Later in the 1990s, such hybrid organic-inorganic perovskites were found by Mitzi et al. to exhibit semiconducting properties[71] and were utilized as thin film field-effect transistors[77] and light emitting diodes[78]. Ultimately, a first application of such hybrid perovskites as absorber in dye sensitized solar cells by Miyasaka et al. in 2009[16] and a breakthrough in the device design three years later started a real boom in this research field, as further elaborated in subchapter 2.2.3. Their superior optoelectronic properties even from cheap and simple wet-chemical deposition methods motivated an unparalleled rush in efficiencies. With more than 2000 publications on perovskite solar cells only in 2016,[79] the rapid gain of knowledge moreover patronized progress in other optoelectronic applications, such as efficient light emitting diodes[17], lasers[80] or X-ray detectors[81].

2.2.1 Structural Properties

As introduced, perovskites follow an ABX_3 crystal structure, illustrated for cubic symmetry in Figure 2.8. The crystal lattice is constituted by BX_6 octahedra which are constrained to the perovskite structure by the A ion.[82] Heteropolar (mixed ionic and covalent) bonds within the BX_6 sub-lattice thereby lead to strong orbital overlap (hybridization) between the two ions. The A-site species instead is bound less strongly in the lattice by van der Waals interactions.[83] Besides charge compensation and stabilization of the BX_6 octahedra, there seems to be no substantial hybridization of the organic (A-site) and inorganic (B-, X-site) ions in hybrid perovskites.[84]

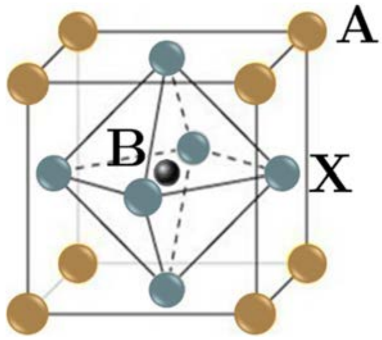

Figure 2.8: Schematic illustration of a cubic ABX_3 perovskite crystal.

Suitable combinations of ions to form a perovskite structure at room temperature can be predicted by an empirical condition according to Goldschmidt [85]:

$$0.71 < t < 1 \; with \; t = \frac{r_A + r_X}{\sqrt{2(r_B + r_X)}}, \tag{2.12}$$

where t is the Goldschmidt tolerance factor and r_i are the ionic radii of the A, B or X ions. For $0.9<t<1$, a cubic perovskite is formed at room temperature, such as $BaTiO_3$.

In hybrid organic-inorganic perovskites, X is a monovalent halide anion such as iodide (I^-), bromide (Br^-) or chloride (Cl^-). Further, B refers to a divalent metal cation, typically group 14 elements such as lead (Pb^{2+}) or tin (Sn^{2+}), but also other metals like strontium (Sr^{2+}) or barium (Ba^{2+})[86]. While Sn^{2+} readily oxidizes to its tetravalent counterpart,[52] lead-based perovskites are considered to be more stable in air and are most prominent in current hybrid perovskite research. Finally, the monovalent A cation represents an organic ion such as methylammonium $CH_3NH_3^+$

(MA^+), ethylammonium ($CH_3CH_2NH_3^+$), formamidinium $HC(NH_2)_2^+$ (FA) or guanidinium $CH_6N_3^+$ (Gua). Besides, also inorganic cations e.g. cesium (Cs^+), rubidium (Rb^+) or potassium (K^+) can be either alloyed into hybrid perovskites or utilized in fully inorganic perovskites. All aforementioned ions may also be blended to an extent, that the effective tolerance factor still holds the condition in eq. (4.1).[26, 87] This allows tailoring of the resulting optoelectronic properties, as further discussed in chapter 2.2.2. So far, the archetype for hybrid organic-inorganic perovskites is $CH_3NH_3PbI_3$. It exists in the tetragonal phase at room temperature and has phase transitions to orthorhombic at 162 K and cubic at 327 K.[88]

The ions in hybrid perovskites are supposed to form rather weak chemical bonds and establish a highly dynamic structure.[89] As a result, the activation energy (E_A) for ion migration within the material is rather low. For $CH_3NH_3PbI_3$, calculated values of E_A range from ~0.1-0.6 eV for I^-- , ~0.5-1.1 eV for MA^+- and 0.8 to >2 eV for Pb^+ -migration, with the general trend of $E_{A,I-} < E_{A,MA+} < E_{A,Pb+}$.[90] The large MA^+ cation is thereby expected to be more mobile than the smaller Pb^+ ion, due to rather weak binding of the organics in the inorganic sublattice of the perovskite.[83] The relatively open crystal structure at grain boundaries and surfaces further reduces E_A there by ~50%.[91] In comparison, the inorganic oxide perovskite $LaFeO_3$, which is known to be an efficient oxide ion conductor, exhibits E_A values for the ion migration between 0.5-2 eV.[92] Hybrid perovskites are therefore also regarded as ionic conductors, which can impact the solar cell performance as elaborated in chapter 2.2.3 and 4.1.

There are two major concerns towards hybrid perovskites, first the toxicity of the typically contained Pb or Sn. Due to the small material consumption in perovskite thin films, release of heavy metals e.g. from a broken solar cell to its surrounding is assumed to have a negligible impact on the environment.[93] However, even a minor toxic hazard could still adversely affect public perception and acceptance of the technology. Therefore, heavy metal-free hybrid perovskites are investigated with so-called double-perovskites as their most prominent example. Here, the the divalent B cation is replaced by alternating monovalent and trivalent cations such as Ag^+ and Bi^{3+} in an $A_2B'B''X_6$ crystal structure. Yet, inferior optical and electronic properties so far limit the applicability of double perovskites with solar cell device performances just above 1%.[94, 95]

The second main concern of hybrid perovskites is their long-term stability. The aforementioned weak bonds were calculated to result in low decomposition energy barriers e.g. ~0.1 eV in $CH_3NH_3PbI_3$.[96] Especially the organic cations are suspected to be sensitive to heat because of their volatile nature, already at temperatures as low as 85°C for MA^+.[97] Further, hybrid perovskites were shown to degrade readily upon exposure to moisture[98] or ultraviolet (UV) light[99]. Besides these intrinsic degradation mechanisms, also extrinsic processes can lead to harmful defects in optoelectronic devices, such as metal interdiffusion from electrodes.[100] On the other hand, hybrid perovskites were reported to be highly resilient towards proton radiation[101] and even possess self-healing capabilities by ion redistribution within the material.[101, 102] Hence, promising strategies to enhance the long-term stability of hybrid perovskites are effective protection against environmental impairments, for example by hydrophobic polymers atop the perovskite[103], or by barriers to maintain the (volatile) ions within the perovskite, e.g. by utilizing protective surfactants around perovskite grains[104] or barrier layers formed by metal oxides.[105]

Also altering the perovskite composition can enhance the stability, i.e. by substitution of MA^+ with more stable inorganic or with larger and therefore less volatile organic cations.[26, 106] FA^+, for example, is considered to be thermally more stable than MA^+,[106] yet $HC(NH_2)_2PbI_3$ ($FAPbI_3$) has a slightly too large Goldschmidt tolerance factor. It thus forms a non-perovskite and photo-inactive phase at room temperature (so-called δ-phase).[87] Partial substitution of FA with smaller cations like Cs was shown to reduce the tolerance factor and stabilize the perovskite structure at room temperature. CsFa based perovskites in combination with efficient barrier layers to avoid penetration or leakage of chemicals allowed perovskite solar cells to withstand 1,000-hour damp heat tests in dark at 85°C and 85% relative humidity.[107] Also these compositions can be used for concentrator PV at concentrations of ~10-50 suns.[108] Even larger organic cations than FA^+ often result in non-perovskite structures or perovskite compounds with reduced dimensionality, e.g. 2D layered perovskites, with typically poorer optoelectronic properties.[109, 110] However, mixed 2D/3D perovskite stacks have enabled long-term stable solar cells with carbon electrodes for >10,000 hours under illumination and in the presence of oxygen and moisture.[110]

2.2.2 Optical and Electrical Properties

The most prominent and extensively investigated hybrid perovskite is $CH_3NH_3PbI_3$ ($MAPbI_3$) because of its excellent optoelectronic properties. It is generally assumed to have a direct band gap of around 1.55 eV and exhibits a steep absorption edge, an overall high absorption coefficient and low sub-bandgap absorption[84] even in solution-processed thin films with rather high defect densities up to ~10^{16} cm^{-3} [49].

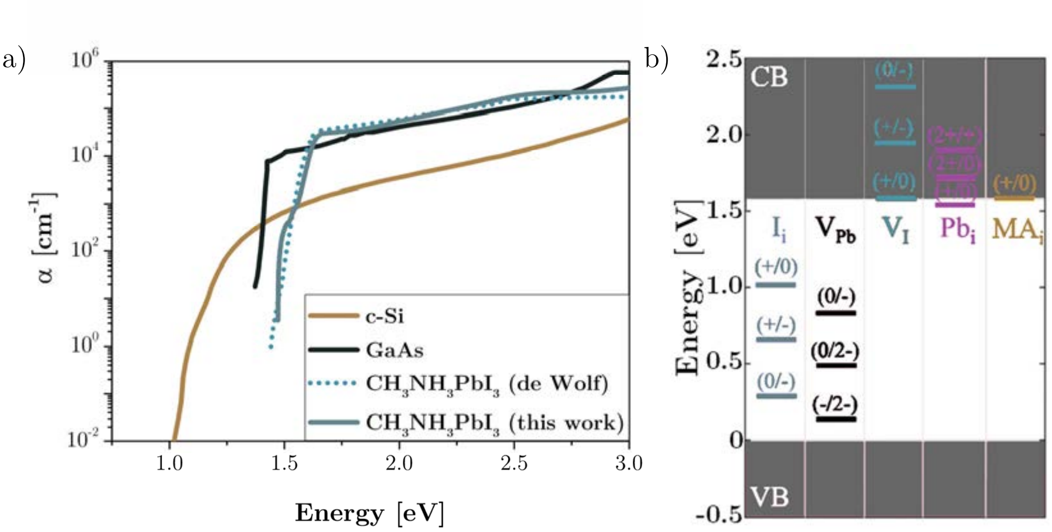

Figure 2.9: a) Absorption coefficient of crystalline Si[112], GaAs[112] and $CH_3NH_3PbI_3$[43, 112]. b) Energetic transition states of the most relevant point defects in $CH_3NH_3PbI_3$. Adapted with permission from [116].

The valence band maximum of $MAPbI_3$ is established by a mixture of I-5p and Pb-6s orbitals, while the conduction band minimum is determined by Pb-6p orbitals. Strong hybridization between the inorganic ions thereby results in low effective electron and hole masses (~0.15 times the free electron mass) along the octahedral framework.[83] Further, high probabilities of intra-atomic Pb-6s to Pb-6p transitions give rise to a strong absorption for $E_{Photon} \geq E_g$, exceeding for example GaAs.[96, 111] Figure 2.9 a) illustrates the absorption coefficients determined for $MAPbI_3$ thin films prepared in this work[43] and by de Wolf et al.[112], compared to the indirect crystalline

Si semiconductor and the direct semiconductor GaAs. Notably, the steep absorption edge below E_g over several decades of the herein solution-processed $MAPbI_3$ thin films corresponds to a low Urbach energy of around 15 meV[43]. This is in line with other reports[112, 113] and approaches the values for crystalline Si (11 meV)[112] or GaAs (7.5 meV)[114]. Minor electronic disorder for solution-deposited $FAPbI_3$ films has also been visualized by a shallow exponential band tail of states at the band gap with a characteristic energy of only 3 meV.[115]

Low Urbach energies and exponential band tails elucidate the pronounced defect tolerance often observed for solution processed hybrid perovskites.[52, 116] It has been argued that the most abundant point defects in perovskites, e.g. Pb-vacancies (V_{Pb}) and MA-interstitials (MA_i) in $MAPbI_3$, form states energetically close to the band edges and hence are less detrimental. Recent reports further suggest, that the only relevant point defect in $MAPbI_3$ to create trap states deep within the band gap is interstitial iodine (I_i), as illustrated in Figure 2.9 b). Note, that the reduction of charge neutral V_{Pb} by one or two electrons (0/- and 0/2- transitions) are thermodynamically unfavorable and therefore negligible.[116] However, the peculiar I^-/I^+ redox chemistry of iodine is assumed to substantially slow down electron trapping at I_i, leaving only short-lived hole traps as potentially detrimental defects.[116] Point defects within the bulk of perovskite crystals or grains thus appear to be less harmful. Instead, extended defects occurring at surfaces and grain boundaries are supposed to limit the overall electrical properties, making suppression of surface recombination vital in optoelectronic devices.[28, 117] Defect states also determine the native doping of a perovskite semiconductor. Calculations suggest a close to mid-gap Fermi-level position or mildly *p*-type doping for $MAPbI_3$ under stoichiometric crystallization conditions.[116] Yet, non-stoichiometric environments, e.g. I-rich/-poor or Pb-rich/-poor, can drastically change the formation energies of different defects.[116] Thus, the strength and type of doping in perovskite absorbers also depend on the manufacturing process.

Intrinsic effects to retard recombination of free carriers in perovskites have further been proposed, such as large polaron formation. Ultrafast molecular reorientation in the lattice is supposed to cause dynamical screening of free charges, which protects them from scattering at optical phonons or charged defects.[118] Also, localization of electrons and holes in spatially distinct regions of the inorganic sublattice was suggested to significantly reduce the overlap of their wave functions and thus their recombination probability.[119] Further, in contrast to the generally assumed direct band gap, a Rashba splitting effect has been controversially discussed in perovskites.[120, 121] According to this, the valence and conduction bands would split around the band gap and induce an indirect band gap with spin-forbidden transitions between the respective branches of the bands.[120] Both again would strongly hamper charge recombination. However, all aforementioned mechanisms would not only reduce non- but also radiative recombination rates. Yet, contrary studies found that radiative recombination of $MAPI_3$, similar to GaAs or Si, can be perfectly reproduced simply by the inverse of its absorption, following the Roosbroeck–Shockley relation.[121, 122] Charge recombination processes and potential mechanisms to protect free carriers from recombination in perovskites are thus still under debate.

As mentioned in chapter 2.1.2, radiative recombination rates R_{rad} for $MAPbI_3$ are on par to the best crystalline inorganic semiconductors, such as GaAs.[52, 54, 55, 123] Further, Auger recombination is expected to be negligible up to ~10^5 suns illumination.[124] Accompanied by the superior defect chemistry and possible protective effects for free carriers, long charge carrier lifetimes for $MAPbI_3$

in the order of 1-10 µs have been reported even for solution-processed perovskite thin films.[60, 61] These lifetimes exceed the values for GaAs[44, 59], and so far appear to be surface recombination limited.[28, 117, 124]

Carrier mobilities in $MAPbI_3$ for both electrons and holes were found to be in the order of 10-100 $cm^2V^{-1}s^{-1}$.[49, 117, 125] They are thus one to two orders of magnitude lower than electron mobilities in Si or GaAs.[44] The dominant scattering mechanism for carriers in perovskites is still under discussion. While some assume them to be acoustic phonon limited[126], other reports suggest prevalent scattering from longitudinal optical phonons via Fröhlich interactions between the BX_3 sub-lattice and free carriers.[127] Nevertheless, the carrier mobilities together with the long lifetimes enable large diffusion lengths above 10 µm in perovskite thin films and above 100 µm in single crystals.[49, 50] This well exceeds typical film thicknesses in optoelectronic devices (usually below 1 µm).

The low non-radiative recombination losses and high radiative recombination rates in $MAPbI_3$ perovskites also enable re-absorption of radiative emission within the perovskite material. Back-reflection of emitted photons into the perovskite absorber can lead to a substantial buildup of the free carrier density.[128]

Besides, a high dielectric constant of $MAPbI_3$ larger than 30[47] effectively screens the electric field between photo-excited electron-hole pairs. Therefore, $MAPbI_3$ exhibits small exciton binding energies of around 10 meV and below[28, 47, 48], which can be easily overcome by thermal energy at room temperature. Thus, basically all generated charges in $MAPbI_3$ are free carriers under one-sun illumination.

Apart from the archetype $MAPbI_3$, changing the perovskite composition usually alters the optical and electrical properties. For example, replacing I^- in $MAPbI_3$ with Br^- to obtain $MAPbBr_3$ increases the band gap from 1.55 to 2.4 eV, accompanied by a significantly increased exciton binding energy (~40 meV), ~3 times larger bimolecular and ~4 times higher Auger recombination rates.[48] Figure 2.10 a) exemplarily illustrates the successive increase in band gap energy for consecutive substitution of I^- with Br^- in $MAPb(I_{1-X}Br_X)_3$ perovskites.

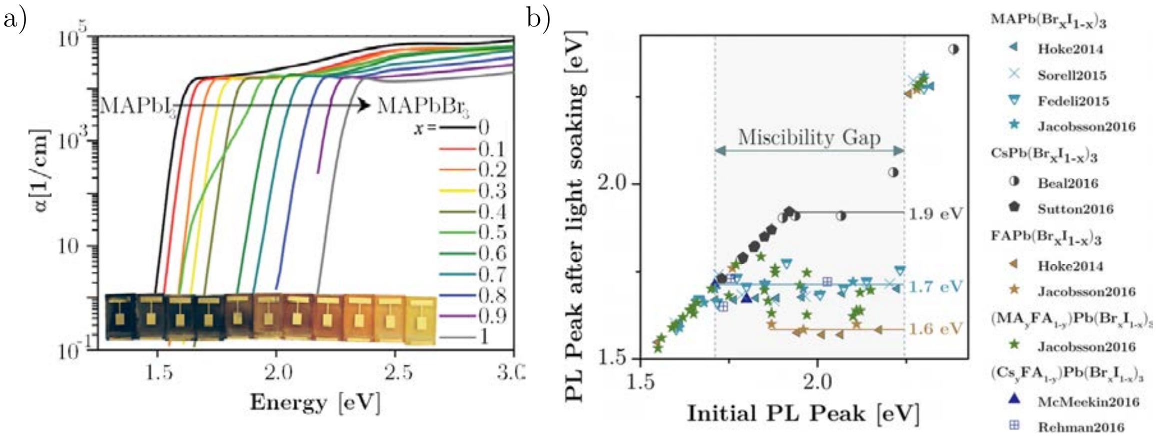

Figure 2.10: a) Absorption coefficients of perovskite compositions on substitution of iodine with bromine in $MAPb(I_{1-x}Br_x)_3$. Depiction following Hoke et al.[129] b) Photoluminescence (PL) emission peak energy after light soaking over the initial PL peak position for various reports of mixed bromide/iodide lead perovskite. Data was obtained from refs. [129–135]. MA and FA denotes methylammonium CH_3NH_3 and formamidinium $HC(NH_2)_2$.

Overall, the band gap can be tuned in hybrid perovskites throughout a wide spectral range from 1.2 eV for $FA_{0.75}Cs_{0.25}Sn_{0.5}Pb_{0.5}I_3$[136] up to 2.4 eV for $MAPbBr_3$[48, 137] and even 2.9 eV for $MAPbCl_3$[138]. The lower threshold of E_g for Pb-based perovskites is so far determined by $FAPbI_3$, slightly below 1.5 eV[87], while Pb-Sn mixtures allow band gaps down to 1.2 eV. [136] As discussed in chapter 2.1.4, the band gap of a semiconductor determines the maximum achievable efficiency of a solar cell, both in single- and multi-junction devices. Materials with an adjustable E_g therefore offer the advantage to provide the optimal band gap for various applications, e.g. as a top cell in tandem solar cells. However, E_g can so far not be seamlessly tuned throughout the whole spectral range. Between around 1.7 and 2.2 eV, compounds with alloyed bromide-iodide anions often exhibit photo-induced phase segregation.[129–135] As a result, lower band gap domains are created in the material, which act as traps and are predominantly emitting photoluminescence (PL) under excitation. The photo-induced phase segregation is illustrated in Figure 2.10 b) by the PL emission peak energies at the beginning of a PL measurement and after light soaking for various reports of mixed Br^-/I^- perovskites.[129–135] A miscibility gap between 1.7 and 2.2 eV, depending on the perovskite composition, is clearly distinguishable. While the driving force for this photo-induced phase segregation is still under debate[135, 139, 140], the onset of the miscibility gap also depends on the A site cations. $CH_3NH_3Pb(I_{1-X}Br_X)_3$ perovskites start to phase segregate at E_g~1.7 eV, whereas stable band gaps up to 1.9 eV can be obtained for $CsPb(I_{1-X}Br_X)_3$ compositions.[137] Note, that the absorption coefficients in Figure 2.10 a) were presumably measured in timescales faster than the occurrence of substantial photo-induced phase segregation, except for x=0.5.

2.2.3 Perovskite Solar Cells

Device architecture and evolution

Perovskite solar cells (PSC) originated from dye-sensitized solar cells (DSSC), as Miyasaka et al. first utilized $CH_3NH_3PbI_3$ quantumdots as a dye on a mesoporous TiO_2 electron contact in 2009 to realize a 3.8% efficient DSSC.[16] However, the liquid electrolyte used in this architecture as hole transport material quickly degraded the perovskite. Therefore, Grätzel et al.[141] and Snaith et al.[142] at the same time replaced the electrolyte with a solid hole selective contact in 2012, which enhanced both the device stability and the efficiency to 9.7% and 10.9%, respectively. This principle architecture still yields the highest solar cell efficiencies today. Yet, the TiO_2 is not sensitized with perovskite quantum dots anymore, but the good optoelectronic properties allow a thick absorber with a capping layer surmounting the TiO_2 matrix by several hundred nanometers. Typically, the transparent conductive oxides (TCO) SnO_2:F (FTO) or In_2O_3:Sn (ITO) as transparent front and metal contacts as opaque rear electrodes encompass the selective contact layers. The ensemble constitutes the so-called mesoporous *n-i-p* architecture, as schematically depicted in Figure 2.11 a). Note, that the perovskite absorber is generally assumed for simplification as intrinsically undoped and *i*-type. An analogous mesoporous *p-i-n* structure, as shown in Figure 2.11 b) has been demonstrated[143, 144], but is less common in PSCs, possibly due to the lack of experience with mesoporous *p*-type contacts in DSSCs, OPV or other fields of photovoltaic research.

The discovery of the high carrier lifetimes and mobilities, along with the low exciton binding energies in perovskites also motivated an alternative architecture with all planar contacts. Both planar *n-i-p*[30, 145] and *p-i-n*[146, 147] structured devices, as schematically drawn in Figure 2.11 c)and d), are widely used for PSCs and achieved efficiencies above 20%[145, 146]. Suitable contact layers, especially for the planar *p-i-n* structure, had partially been adopted from OPV, e.g. poly(3,4-ethylene-dioxythiophene):polystyrene sulfonate (PEDOT:PSS) as hole or phenyl-C61-butyric acid methyl ester (PCBM) as electron contact.

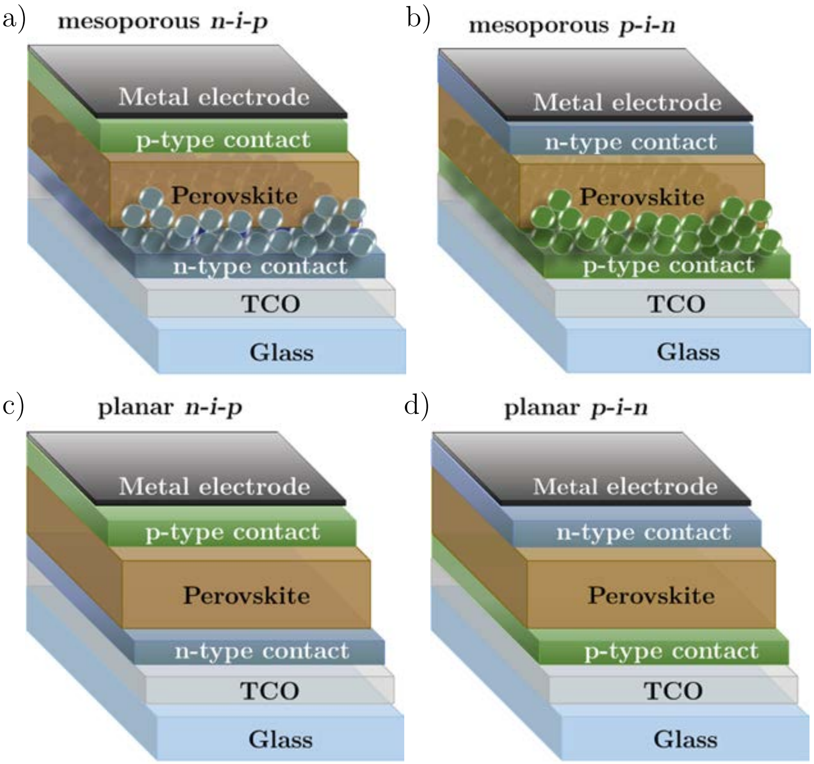

Figure 2.11: Schematic illustration of the mesoporous a) n-i-p and b) p-i-n as well as planar c) n-i-p and d) p-i-n architecture of perovskite solar cells.

The *n-i-p* architecture thereby typically outperforms *p-i-n* devices, mostly because of a smaller difference between E_g/e and V_{OC}, often denoted as the open circuit voltage loss ΔV_{oc}, with record ΔV_{oc} of 390 mV.[26, 29, 117, 148, 149] This has been attributed to high surface recombination and a rather low selectivity of the widely used fullerene *n*-type contacts in *p-i-n* devices.[29, 113] Recent advances to suppress interface recombination[29], e.g. by passivating surface defects[148] or introduction of an additional wide band gap perovskite heterojunction at the *n*-type contact[149], remedied this deficit in the *p-i-n* architecture and reduced the open circuit voltage loss ΔV_{oc} to 390 mV as well, with PCEs approaching 21%. However, ΔV_{oc} values of 400 mV and below, paired with highest FF >80% have up to now only been achieved in the mesoporous *n-i-p* structure.[26, 27, 117]

Materials

So far, PSC efficiencies >20% were often realized by perovskites with band gaps between 1.5-1.6 eV. Their chemical composition usually comprises Cs^+, Rb^+, FA^+ and/or MA^+ on the A-site, Pb^{2+} on the B site and Br^- and/or I^- as anion. Typical examples are $MAPbI_3$ (E_g ≈1.55 eV, PCE >20%)[104, 150], $Cs_{0.05}(FA_{0.83}MA_{0.17})_{0.95}Pb(I_{0.83}Br_{0.17})_3$ (E_g≈1.6 eV, PCE >21%)[151, 152] or $FA_{0.95}MA_{0.05}Pb(I_{0.95}Br_{0.05})_3$ (E_g ≈1.5 eV, PCE >22%)[27, 153]. Also, targeting the optimum E_g for single-junction solar cells (~1.3 eV) is possible by Pb-Sn mixed perovskites, which already surpassed 17% efficiency in $(FASnI_3)_{0.6}(MAPbI_3)_{0.4}$ solar cells with E_g=1.25 eV.[137, 154] Yet, the difference in the ideal PCEs for E_g~1.3 eV (~33%) and 1.5-1.6 eV (31-32%)[67] is minor as compared to the discrepancy between currently obtained and theoretical maximum efficiencies, which is mainly due to the V_{OC} loss as introduced above. Tuning the band gap therefore is rather not the main lever for further efficiency enhancements in perovskite single-junction solar cells at the moment.

Charge selective contacts were in general shown to have a substantial impact on the performance of perovskite solar cells.[155–157] As introduced in chapter 2.2.2, surface recombination often governs the optoelectronic properties of perovskite absorber and hence the solar cell efficiencies.[28] Therefore efficient suppression of surface recombination and highly selective charge extraction at the *p-i* and *i-n* heterojunction interfaces is essential in PSCs. Moreover, good charge extraction, carrier mobilities (ideally $>10^{-3}$ cm^2/Vs) and thermal and photochemical stability are required characteristics of contact materials.

Table 2.1: Typically used contact materials in different perovskite solar cell architectures and efficiency range of best reported devices (η). The transparent front contact in all cases is usually SnO_2:F (FTO) or In_2O_3:Sn (ITO). Spiro-OMeTAD denotes 2,2′,7,7′-tetrakis(N,N-di-p-methoxyphenylamine)-9,9′-spirobifluoren, PTAA labels poly(triaryl amine), PCBM is phenyl-C61-butyric acid methyl ester, BCP represents bathocuproine and PEDOT:PSS abbreviates poly(3,4-ethylene-dioxythiophene):polystyrene sulfonate. References as given.

	n-type contact	*p-type contact*	*Electrode*	*η*	*Refs.*
***n-i-p* mesop.**	TiO_2	doped Spiro-OMeTAD/PTAA	Au	>22%	[26, 27, 141, 153]
***n-i-p* planar**	SnO_2, TiO_2, PCBM	doped Spiro-OMeTAD/PTAA	Au	>21%	[30, 61, 158, 159]
***p-i-n* mesop.**	PCBM	NiO	Al	<10%	[143, 144]
***p-i-n* planar**	PCBM-BCP, C_{60}-BCP	PEDOT:PSS, NiO, undoped PTAA	Al, Ag, Cu	>21%	[29, 30, 148, 149, 155]

Typically used materials for *p*- and *n*-type selective contacts in the different architectures of PSCs are summarized in Table 2.1. Chemical structures of the organic materials are illustrated in Figure 2.12 a)-e). Besides the presented organic materials, bathocuproine (BCP) is often used to provide good electric contact between the fullerenes C_{60} or PCBM and the metal electrodes.[160] Further Figure 2.12 f) depicts ionization potentials and electron affinities of $CH_3NH_3PbI_3$ and the charge selective materials in Table 2.1, as well as the work functions of typically used electrode materials. As shown, a charge selective material ideally induces an energetic barrier at the perovskite interface in order to block one carrier type while conducting the other one, as introduced in chapter 2.1.2. The impact of different contact materials on the device performance is elucidated here in chapter 4.1 by a comparative study of low-temperature processed *n*-type contacts in planar *n-i-p* type PSCs. Further, chapter 4.2 presents mixtures of Spiro-OMeTAD and poly(3,4- ethylenedioxythiophene) (PEDOT) as a novel *p*-type contact which effectively suppresses surface recombination in planar *n-i-p* type devices.

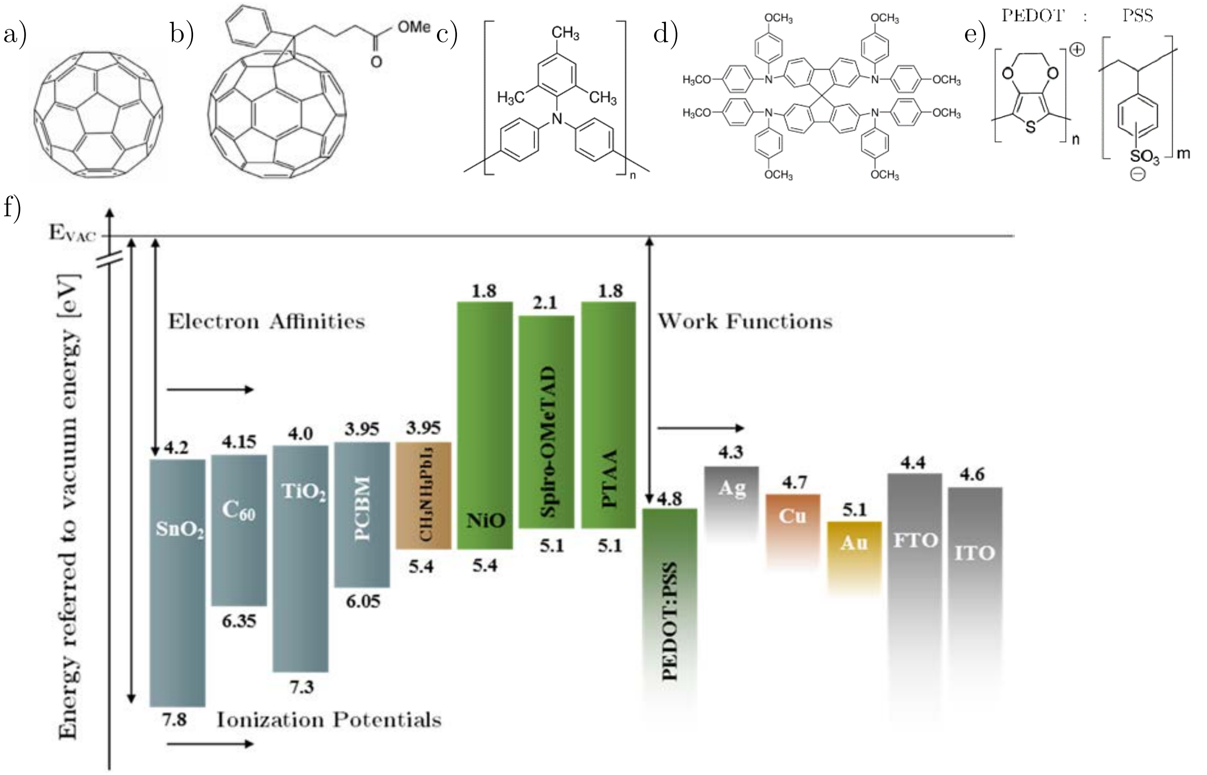

Figure 2.12: Chemical structures of the fullerenes a) C_{60} and b) phenyl-C61-butyric acid methyl ester (PCBM), as well as c) poly(triaryl amine) (PTAA), d) 2,2′,7,7′-tetrakis(N,N-di-p-methoxyphenylamine)-9,9′-spirobifluoren (Spiro-OMeTAD) and e) poly(3,4-ethylene-dioxythiophene):polystyrenesulfonate (PEDOT:PSS). f) Illustration of the energy levels for different electrode and charge selective materials related to $CH_3NH_3PbI_3$. For SnO_2, C_{60}, TiO_2, PCBM and In_2O_3:Sn (ITO) ionization potentials and work functions were determined by photoelectron spectroscopy, electron affinities by taking literature band gap values into account.[161–164] Further values for SnO_2:F (FTO)[165], $CH_3NH_3PbI_3$[166], NiO[144], Spiro-OMeTAD[167], PTAA[168], PEDOT:PSS[167], Ag[169], Cu[170] and Au[170] were obtained from literature.

Radiative efficiency limits

As introduced in chapter 2.1.4, thermodynamic constraints intrinsically limit the power conversion efficiency of a solar cell and require emission of an absorber when being in equilibrium with its environment. In the ideal case, solely radiative recombination occurs in the solar cell to achieve the required photon emission ($EQE_{EL} = 1$). The radiative efficiency limit of a solar cell is then, following eq. (2.6) and (2.8) in chapter 2.1.3, defined by its EQE_{PV} and converges the Shockley-Queisser Limit for the EQE_{PV} approaching a step-function of zero and one for photon energies $<$ and $\geq E_g$, respectively. Non-radiative recombination processes in the device reduce the EQE_{EL} and with that the achievable device efficiency.

For perovskite solar cells, apart from surface recombination, the exceptional defect tolerance and potential carrier protection effects enable low non-radiative recombination losses and a sharp onset of the absorption coefficient at the band gap, as discussed in the previous section 2.2.2. Radiative efficiency limits of PSCs, deduced from measured EQE_{PV} characteristics, are therefore already close to the Shockley-Queisser limit.[52] For PSCs with well-controlled surface recombination, highest EQE_{EL} of >1% under one-sun equivalent excitation were shown, which results in high V_{OC} values up to 1.24 V.[26] With the radiative limit for the V_{OC} being 1.33 V at

E_g≈1.6 V[52], this relates to a low potential loss <100 mV from non-radiative recombination or a V_{OC} of 93% referred to the radiative limit. PSCs thereby outperform most other PV technologies with Si reaching only 88% of its radiative V_{OC} limit as well as highest EQE_{EL} values for $Cu(In,Ga)Se_2$ (CIGS) of about 0.2% or for CdTe, a-Si and OPV of far below 10^{-3}%.[19, 171] Only GaAs achieves even lower non-radiative recombination losses, with demonstrated EQE_{EL} values above 20% and a record V_{OC} at 96-97% of the radiative limit (record V_{OC}=1.121 V for E_g≈1.42 eV and $V_{OC,rad}$≈1.158 V)[9, 67]. The main obstacle for further performance improvements in PSCs therefore is to reduce non-radiative losses, mainly from surface recombination, which consequently pushes the EQE_{EL} towards unity.

Device fabrication and upscaling

While the TCO is usually deposited by sputtering and the metal rear electrode is often thermally evaporated, all other layers in PSCs can potentially be processed simple and cheap e.g. by spin-coating. In contrast to the mesoporous TiO_2, which is often prepared via spray coating and subsequent annealing at 450°C [26, 141, 153], most planar contacts in Table 2.1 can be easily spin-coated and processed at temperatures below 150°C [30, 113, 145, 146, 155, 172]. Also thermally evaporated contact layers are widely used, especially C_{60} and BCP in the planar *p-i-n* structure. The perovskite absorber itself can be deposited via multiple methods, while wet-chemical spin-coating from solution is the most common procedure and realized the highest efficient PSCs so far.[106, 153, 173] However, the record efficiencies have always been measured on small active areas <0.2 cm². Besides, processing via spin-coating is not directly applicable to larger scale and volume preparations. Other techniques allowing high throughput and homogeneous coating of large areas might therefore become more relevant for upscaling efforts. Co-evaporation e.g. of MAI and PbI_2 to form $MAPbI_3$ perovskites has been successfully demonstrated with the highest efficiencies exceeding 20%.[150] Further, blade coating [174], slot-dye coating [175], screen [110] or ink-jet [176] printing of perovskites has been presented. PSCs produced by industrial-scale printing techniques so far obtained >17% efficiencies on 0.04 cm² [176] and 11.2% on 100 cm² active area with outdoor stability of over a year.[110] Overall, the low temperature processing allows short energy payback times of PSCs and deposition on substrates with limited thermal budget, such as flexible foils[177] or heterojunction solar cells[21, 178, 179], as used in this work.

Current-voltage hysteresis

An often observed phenomenon in perovskite solar cells is a slow transient response of the current output on perturbation of the external voltage. Current transients can be observed on the timescale of seconds to minutes after a change in bias. This results in a dependence of the J-V characteristics on the history of the device and the measurement parameters. Pre-biasing before as well as the voltage step size and the measurement time per voltage point during the J-V scan routine can significantly influence the determined current densities. As a result, the J-V curve can strongly differ for a scan from the voltages $V_1 \rightarrow V_2$ as compared to $V_2 \rightarrow V_1$. This phenomenon is exemplarily depicted in Figure 2.13 a) and has generally been designated as hysteresis.[180, 181] The transient response of a PSC was found to depend on the perovskite layer quality[182] and to be substantially governed by the charge selective contacts[30, 155, 157]. In general, *n-i-p* type perovskite solar cell architectures are more prone to exhibit hysteresis than *p-i-n* structured devices, which has been attributed to the widely used fullerene *n*-type contact in the *p-i-n* structure.[155, 183] The impact of fullerenes and the charge selective layer in general on efficiency and hysteresis in planar *n-i-p* type perovskite solar cells is elucidated in a comparative study presented in chapter 4.1.

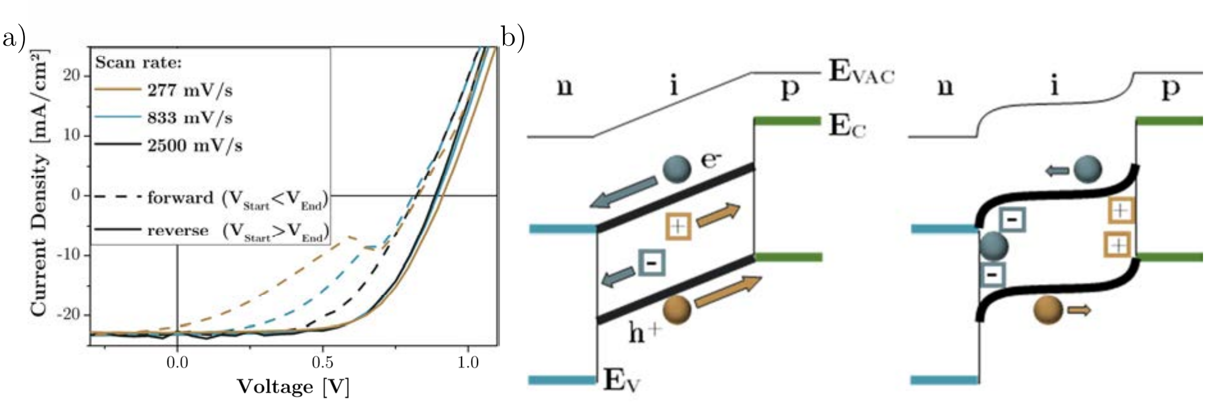

Figure 2.13: a) Current-voltage characteristics with exemplary depiction of the scan rate and scan direction dependence of a perovskite solar cell under illumination, also referred to as hysteresis. b) Schematic illustration of a perovskite solar cell under illumination and close to short-circuit conditions. The internal electric field initially drives charge carriers as well as mobile ions or their vacancies (symbolized by squares) towards the charge selective contacts (left). Right: subsequent accumulation of ions/vacancies and free charge carriers, e.g. in trap states, induces electrode polarization and (partially) compensates for the internal field. Depiction following ref.[90].

The origin of J-V-hysteresis is still under debate and different mechanisms have been proposed such as ferroelectric polarization[184], trapping of charge carriers at the perovskite interfaces[183] or ion migration[90, 185]. Possible ferroelectric effects can be induced by dipolar organic cations such as MA^+. External fields could force reorientation of the dipoles in order to compensate for the external bias. However, the orientation of MA^+ dipoles is assumed to occur within picoseconds[184], while transient J-V responses appear on much longer timescales.[180, 186]. Also, trapping of charge carriers was proposed as the origin of hysteresis.[183, 187] However, simulations revealed that trapping alone is not sufficient to cause J-V transients, but it rather amplifies hysteresis. As shown in chapter 4.1, similar accounts for the selective contact interface, where slow charge extraction or increased surface recombination losses intensify hysteresis. This also explains the reduced transient response observed for surface-passivated or high efficient perovskite solar cells.[181, 182]

Instead, the low activation energy for ion migration introduced in chapter 2.2.1 allows fast movement of mobile ions through the absorber. On external bias, ions and photogenerated free carriers were observed to drift towards the charge selective interfaces within few milliseconds and accumulate there.[188] This results in electrode polarization, and thus corresponds to capacitive charging-discharging dynamics during J-V scans.[185] It also changes the internal field within the absorber and concomitantly charge extraction or injection. The processes are exemplarily depicted in Figure 2.13 b) for the case of an illuminated perovskite solar cell under short-circuit conditions. Capacitive hysteresis effects in principle increase with the capacitance of the device and the scan speed. However, if the J-V sweep rate is too fast for the charging processes, hysteresis starts to decrease again with increased scan speeds as the response limit of the device capacitance is reached. Slower transients in the timescale of minutes, on the other hand, have been attributed to migration of slower ions, such as MA^+, which further induce modifications of the interface energetics.[184, 185]

2.3 Silicon Heterojunction Solar Cells

Crystalline Si (c-Si) has been investigated in photovoltaics since 1941, initiated by the Bell Laboratories New Jersey.[36] In 1954, the same facilities realized the first c-Si solar cell with a PCE of 6% using a diffused *p-n* homojunction.[189] Starting from this, intensive studies raised the efficiencies of Si photovoltaics (PV) up to 26.7% on lab-scale solar cells and 24.4% for complete modules in 2018.[9]

The increase in efficiency of c-Si solar cells within the last 30 years was strongly driven by passivation of surface recombination.[19, 58] Motivated by high recombination losses at the metal contacts in classical *pn*-homojunction c-Si solar cells, a-Si/c-Si heterojunctions were already investigated in the 1970s by Fuhs et al.[190] Decades of research eventually culminated in the development of the first modern Si heterojunction (SHJ) solar cell in 1991 with 18% efficiency.[191] SHJ devices utilize different layers of amorphous Si (a-Si) deposited on a c-Si wafer to provide well-passivated and highly selective heterocontacts at the Si surfaces. Today, the Si heterojunction (SHJ) architecture represents the most efficient technology in Si photovoltaics, with solar cells yielding the highest V_{OC} (750 mV) and PCE (26.7%) values for this semiconductor.[19, 192]

Amorphous silicon consists of Si atoms with sp^3-hybrid orbitals establishing a close range order. Yet, long-range order is not provided by a-Si as bond lengths and orientations between the silicon atoms are statistically distributed.[193] This entails a large number of unsaturated, so-called dangling, bonds which resemble defect states within the material. Therefore, hydrogen is incorporated in a-Si (a-Si:H) to saturate dangling bonds, typically in the order of 5-15 atomic-%. Dangling bonds, as well as the long range disorder, give rise to a large density of states in the band gap and exponential tails of the conduction and valence bands.[193] The optical band gap of a-Si thus depends on the material quality but is often considered to be around 1.7 eV. [193, 194] Further, a-Si:H layers can be intentionally doped by inclusion of donor or acceptor materials, typically phosphorus for *n*-type and boron for *p*-type doping similar to c-Si.[53, 193] Yet, as dopants also impose shallow defect states in the a-Si, *p*- or *n*-doped layers are significantly more prone to charge recombination losses than intrinsic amorphous Si films ((i)a-Si:H).[193] Layers of a-Si:H can be deposited by low-temperature processes (<200°C) such as chemical vapor deposition (CVD) with phosphine (PH_3) and diborane (B_2H_6) as gaseous precursors for *n*- and *p*- type doping, respectively.[193]

The schematic architecture of a typical SHJ solar cell is illustrated in Figure 2.14 a) and matches well with the structure of SHJ solar cells used in this work. The indirect band gap and weak absorption of c-Si requires a 100-200 µm thick absorber which is typically *n*-doped. Absorbers of inverse polarity have been shown but are assumed to be less suitable for high efficient solar cells, due to the superior defect tolerance of *n*-type c-Si.[195] Often, Si(100) wafers are used as they can be easily textured with micrometer high pyramids by anisotropic etching, typically with potassium hydroxide.[196] Pyramid structures on both surfaces drastically reduce reflection losses and efficiently retain light within the absorber, thereby outperforming e.g. ideal Lambertian light trapping schemes.[197] Yet, for tandem cells produced in this study, only the bottom surface is textured while the front surface remains planar to allow homogeneous deposition of the perovskite top-cell via spin-coating.

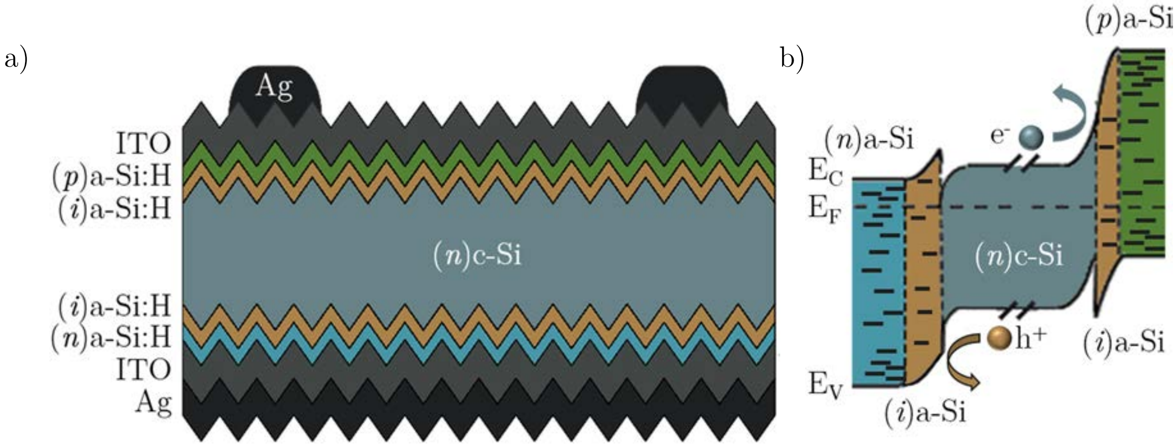

Figure 2.14: a) Schematic device structure of a silicon heterojunction solar cell.[195] b) Simplified band diagram of a (n)a-Si/(i)a-Si/(n)c-Si/(i)a-Si/(p)a-Si double heterojunction structure under short-circuit condition according to [195]. Dashes in a-Si layers indicate sub-band gap energy defect states.

Next, the c-Si surfaces are coated with (*i*)a-Si films on both sides. While *p*- or *n*-doped a-Si:H contacts in direct interface to c-Si lack passivation due to their high defect densities, (*i*)a-Si:H was found to passivate c-Si remarkably well.[193] The (*i*)a-Si:H chemically passivates dangling bonds on c-Si surfaces with Si or H from the a-Si thin film.[198] For carrier extraction, *n*- and *p*-doped a-Si:H layers are deposited as electron and hole selective contacts layers on top of the (*i*)a-Si. Due to the low conductivity and parasitic absorption of a-Si, the films are processed as thin as possible while maintaining their functionality, typically 5 nm for (*i*)a-Si and 10 nm for (*n*)/(*p*)a-Si.[193] A TCO layer, usually ITO, is deposited on the front side of the solar cell to serve as an anti-reflective coating and to provide lateral charge transport to a subsequently deposited metal grid. Also, the rear surface of the SHJ is covered with a TCO, typically again ITO, prior to a metal back-contact in order to reduce parasitic absorption by plasmons in the full area metal back contact.[199]

Charge excitation mainly occurs in the c-Si absorber, where the good surface passivation allows high carrier lifetimes of several milliseconds.[195] Free electrons (holes) can thus diffuse throughout the wafer as well as across the *n*-type (*p*-type) selective heterocontacts to the TCO electrode. As simplified depicted in Figure 2.14 b), the (*p*)/(*n*)a-Si:H layers impose energetic offsets as well as band bending at the c-Si interface to block the undesired carrier types. In contrary the opposite, desired charges face only smaller energetic barriers at the heterojunctions, which can be overcome by thermionic emission[200], tunneling or tunnel hopping[201, 202]. The exact mechanism of charge extraction in SHJ solar cells is still under debate. The desired band bending is thereby achieved by strong doping of the (*n*) and (*p*)a-Si:H layers in the order of 10^{19} cm^{-3}, as compared to 10^{15} cm^{-3} in the c-Si wafer. Additionally, hole extraction at the (*p*)a-Si:H/TCO contact is usually realized by tunnel-recombination processes with electrons from the typically *n*-type TCO.[195]

SHJ solar cells are limited to further processing below 200°C, otherwise hydrogen escapes from the a-Si:H layers and diminishes the passivation.[195] Therefore all deposition steps to develop a monolithic SHJ-perovskite tandem solar cell are restricted to low temperatures.

2.4 Perovskite-Silicon Tandem Solar Cells

Although the best commercially distributed modules with a PCE around 22%[203] still have potential for further improvements, record efficiencies for Si solar cells on lab scale already approach the theoretical limit of 29.4%[9, 10]. Overcoming this intrinsic limitation is enabled by multi-junction solar cells, as described in chapter 2.1.4, with the simplest structure being a two-junction or tandem device. Following the detailed balance considerations by Shockley and Queisser[66], the maximum efficiency in a tandem solar cell amounts to around 45%[11, 12]. Utilizing c-Si as the bottom cell, highest PCEs up to 45% are achievable for a top cell material with E_g~1.7 eV[12], as depicted in Figure 2.15 a). III-V semiconductors have been investigated as top cells in Si tandem devices, due to their tunable band gap and high efficiencies.[204] GaInP with E_g=1.81 eV mechanically stacked on a c-Si cell e.g. achieved a 32.5% tandem PCE.[204] However, production costs for III-V/Si tandems are expected to be an order of magnitude higher than for Si single-junction devices, rendering them uncompetitive for one-sun terrestrial power applications.[204] Perovskites on the other hand also provide tunable band gaps over a wide spectral range, high V_{OC} and PCE values in solar cells and even more potentially cheap manufacturing.

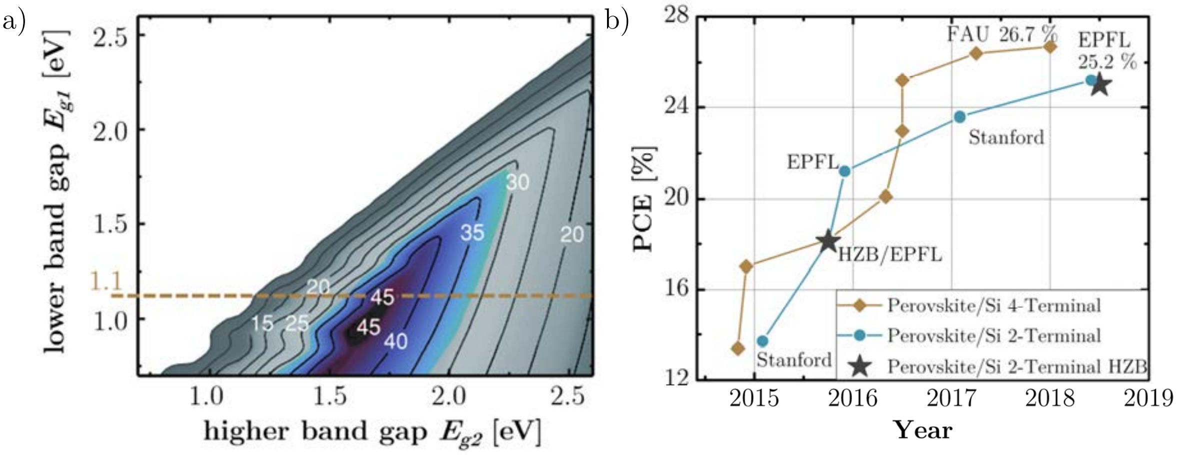

Figure 2.15: a) Theoretical maximum efficiency for two-junction solar cells depending on the band gaps of the top and bottom cell semiconductors. Adopted with permission from [12]. b) Historical development of the published efficiencies for two-terminal and four-terminal perovskite-Si tandem solar cells. Stanford, HZB, EPFL and FAU denotes Stanford University, Helmholtz-Zentrum Berlin, Ecole Polytechnique Fédérale de Lausanne and Friedrich-Alexander University Erlangen, respectively. Stars further mark monolithic tandem solar cells realized at Helmholtz-Zentrum Berlin. Values for four-terminal tandems were taken from [178, 205–211], for two-terminal devices from [21, 107, 212–214].

Both monolithic (two-terminal) as well as independently connected (four-terminal) perovskite-Si tandem solar cells were initially demonstrated about early 2015 with moderate efficiencies of around 13.5%, illustrated in Figure 2.15 b).[205, 212] One year later, Albrecht et al. realized a first monolithic tandem device comprising an SHJ bottom cell with above 18% stabilized and 19.9% reverse scan PCE.[21] From this point onward, the major focus was set on optical optimization of the tandem stack along with further improving the perovskite top cell performance. Duong et al. increased and stabilized the perovskite band gap at the theoretical optimum of 1.73 eV to realize a so far record efficient four-terminal tandem solar cell with 26.6% PCE.[210] Further, the perovskite top cells in the first monolithic tandem devices were *n-i-p* structured, with light entering the absorber through the highly absorptive Spiro-OMeTAD *p*-type contact.[21, 212, 215] A transition to the *p-i-n* design with the less absorptive C_{60} as *n*-type layer allowed a drastic reduction of parasitic absorption losses in the front contact and efficiencies above 23%.[22, 107, 216] Also, Sahli et al. replaced the (*p*)a-Si:H/TCO tunnel recombination junction typically used in SHJ solar cells by a recombination contact from highly *p*- and *n*-doped nanocrystalline Si. In turn, reflection losses of the SHJ bottom cell were reduced due to better suited refractive indices.[215] The same group further substantially minimized the reflection of monolithic tandem solar cells by utilizing not only rear but also front side textured SHJ bottom cells. By implementing only conformal coating processes, mainly thermal evaporation, the perovskite top cell was successfully deposited on the pyramidal structured Si surface resulting in a record 25.2% efficient monolithic tandem device with a high J_{SC} value close to 20 mA/cm².[214]

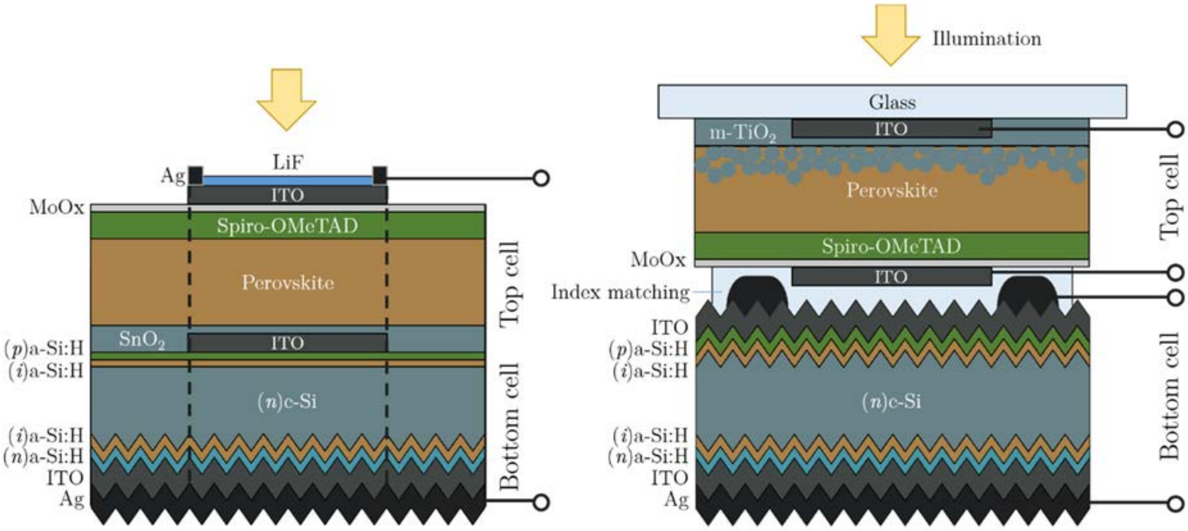

Figure 2.16: Schematic device structure of a monolithic[21, 213] (left) and four-terminal[178, 210] (right) perovskite-Si heterojunction tandem solar cell as utilized similarly in the indicated references.

The general device structure of the first reported perovskite-SHJ tandem solar cells[21, 213] is depicted on the left in Figure 2.16 and is similar to the design used in this work. The back contact of the bottom cell is identical to single-junction SHJ cells, with a textured Si surface to enhance light-trapping as discussed before (chapter 2.3). The front surface, on the other hand, is kept planar to allow homogeneous deposition of the perovskite top cell by the typically used spin-coating technique. The (*p*)a-Si/ITO top interface of the SHJ cell serves as a tunnel recombination contact and only has to provide vertical charge transport. It can thus be deposited substantially thinner to avoid parasitic absorption losses as compared to single-junction devices, where the TCO also laterally conducts current to the grid fingers. It is directly followed by the perovskite *n-i-p* device stack.

The limited thermal budget of the SHJ device however requires low temperature deposited, often planar, electron selective contacts, whereas the perovskite absorber, and typically used p-type contacts are usually processed at temperatures below 200°C. A systematic comparison of different low-temperature electron contacts in *n-i-p* type PSCs is presented in chapter 4.1. Next, a transparent top contact is usually realized by a sputter deposited TCO electrode. Additional buffer layers such as molybdenum oxide (MoOx)[207] or ITO nanoparticles[134] were introduced atop Spiro-OMeTAD to protect the organics from sputter induced damages. Finally, a metal grid is evaporated on the TCO for lateral charge transport as well as an anti-reflective layer such as LiF[21] or MgF_2[210] to reduce Fresnel reflection by better refractive index matching across the air-TCO transition. As indicated by the dashed lines in Figure 2.16, the active area of the monolithic tandem device is determined by the middle and top TCO electrodes, while the rear side contact usually completely covers the Si wafer.

A simpler realization of a tandem solar cell is the four-terminal design shown on the right in Figure 2.16. Here, standalone perovskite and SHJ solar cells are mechanically stacked on each other and can be processed without further constraints as compared to a single-junction device. Merely a transparent back contact is required for the perovskite top cell. MoOx/TCO stacks as typically used in the monolithic architecture[21, 207, 214], silver nanowires[211], thin metal layers[209] or even graphene[179] were demonstrated as transparent electrodes. However, only the first two realized complete top cells with high average transmission above 80% in the Si-related absorption range between 800-1200 nm wavelength.[210, 211] Finally, an index matching material such as silicon gel[210] can be inserted between the individual cells to avoid reflection losses at the intermediate contacts.

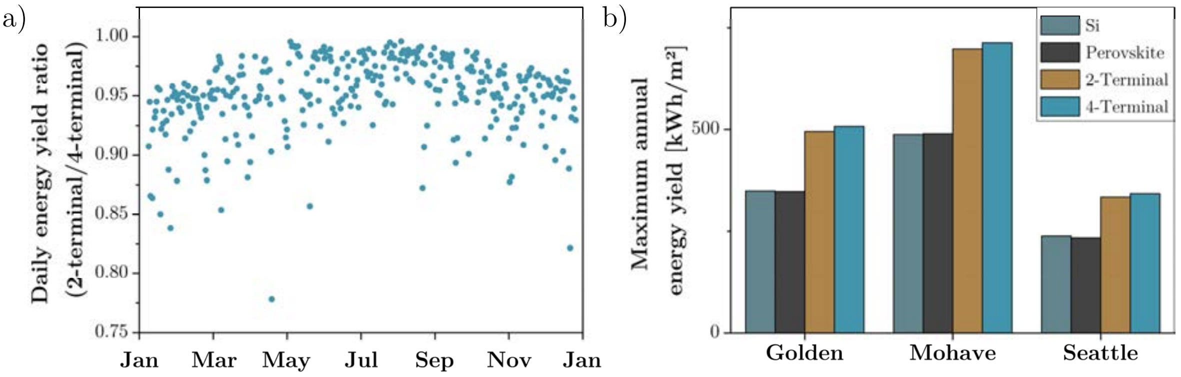

Figure 2.17: a) Simulated ratios of the daily power output between two- and four-terminal perovskite-Si tandem solar cells with real outdoor data from Newcastle, Australia.[217] b) Maximum annual energy yields of optimized devices for two- and four-terminal perovskite-Si heterojunction tandem solar cells as well as their respective single junction devices at different locations in the U.S.A. (Golden, California; Mohave, Arizona; Seattle, Washington). Data obtained from [25].

As introduced in chapter 2.1.4, monolithic tandem solar cells are always limited by the subcell with the lower current output. However, the incidence angle and spectral distribution of the solar irradiation is changing from dawn till dusk and throughout the year. Besides, the fraction of diffuse and direct sun light strongly depends on the weather conditions. Monolithic tandem solar cells will therefore only very rarely reach perfect current matching of the sub cells in real-world operation, which reduces the overall energy yield. Duck et al. simulated the power generation of two- and four-terminal perovskite-Si tandem solar cells for real outdoor data located in Newcastle, Australia. They predicted a seasonal dependence of the difference in power output between two- and four-terminal devices with an in average 4.5% lower energy yield for the monolithic tandem device (Figure 2.17 a). A comparable discrepancy around 2.5% was found by Höranther et al. in simulations for fully optimized two- and four-terminal tandem devices structured as shown in Figure 2.16 and multiple weather data sets (Figure 2.17 b). The results also suggest an up to

30% higher power production for perovskite-Si tandem solar cells as compared to their respective single-junction devices.[25]

3. Methods and Materials

In this chapter, solar cell fabrication methods and characterization techniques used in this work are elucidated.

The first section provides detailed descriptions of the device designs, the materials and the fabrication routines of planar *n-i-p* type perovskite solar cells. The devices are implemented as opaque or semi-transparent single junction or monolithic perovskite-silicon heterojunction tandem solar cells. Two different perovskite compositions are applied in this work: $CH_3NH_3PbI_3$ as utilized in the first results chapter 4.1 and $Cs_{0.05}((CH(NH_2)_2)_{0.83}(CH_3NH_3)_{0.17})_{0.95}Pb(I_{0.83}Br_{0.17})_3$ used for the remaining results in chapters 4.2 and 4.3. Optical measurements reveal a slightly larger band gap for the latter composition but excellent electronic quality for both absorbers with low Urbach energies ≤15 meV.

The second part further explains the working principles of characterization methods used in this work and provides detailed descriptions of the respective measurement setups.

3.1 Materials and Device Preparation

Planar *n–i–p* perovskite solar cells were prepared in this work as a layer stack of ITO/ETM/perovskite/HTM/electrode, fabricated either on glass substrates or on silicon heterojunction solar cells. Here, ETM/HTM is the electron/hole transport material and the electrode is either Au for opaque cells or molybdenum oxide (MoOx)/ITO(/LiF) in semi-transparent single junction or tandem devices.

The different device designs are illustrated in Figure 3.1. For single junction devices (Figure 3.1 a,b), intersection area between the ITO on glass and the top electrode, either Au as depicted or MoOx/ITO for semi-transparent devices, defines six different active areas of 4x4 mm^2 per sample, indicated by the dashed lines. For tandem solar cells, the ITO/Ag top contact stack defines the active area of 20x0.5 mm^2. The center of the top ITO matches the center of the (*p*)a-Si:H/ITO tunnel recombination junction between the two sub cells. Yet, the top ITO is slightly wider at dimensions of 20x0.6 mm^2 to allow connection to the Ag front grid at the longer edges, while maintaining an active area of 1 cm^2 (Figure 3.1 c, d). The rear contact is provided by the Ag metallization completely covering the wafer rear side.

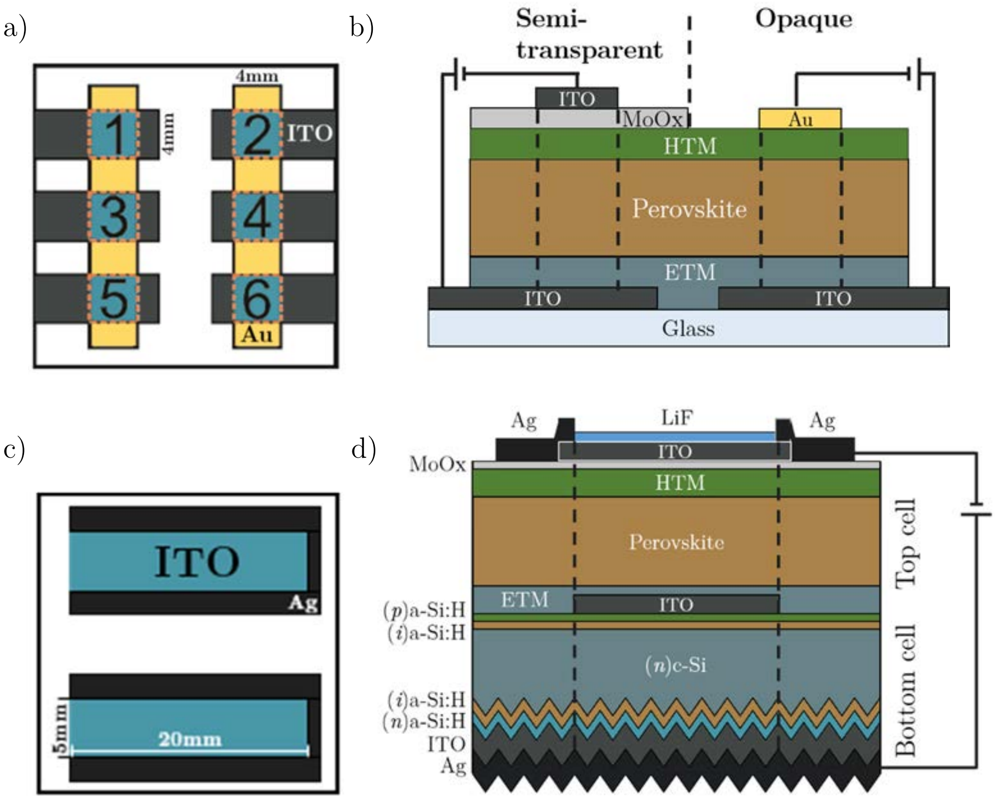

Figure 3.1: a) Schematic contact design of an opaque perovskite single-junction solar cell on glass/ITO in top-view. The ITO is structured in six independent stripes of 4 mm width. Their intersection area with 4 mm wide gold electrode stripes, perpendicular to the ITO, defines the active solar cell area to 16 mm^2. b) Schematic cross-section of the single junction device with either semi-transparent or opaque top contact. c) Schematic device and top contact structure of perovskite-silicon tandem solar cells. The visible ITO area defines the active tandem solar cell with 2x0.5 cm^2 whereas an Ag edge supports lateral charge transport. The contact area between ITO and Ag amounts to 1 mm at each side and exceeds the 2x0.5 cm^2 active area. d) Schematic cross-section of the tandem solar cell fabricated in this work. Dashed lines mark the active solar cell areas.

3.1.1 Substrate Cleaning

Patterned ITO coated glass substrates (R =15 Ω/sq.; Lumtec or Automatic Research) or soda lime glasses were cleaned sequentially for 15 min with detergent, acetone, and isopropanol in an ultrasonic bath.

3.1.2 Electron Selective Contact Deposition

Fullerene derivatives phenyl-C_{60}-butyric acid methyl ester (PCBM) (99.5%, Solenne BV) and 1',4'-Dihydro-naphtho[2',3':1,2][5,6]fullerene-C_{60} (ICMA) (>99%, Lumtec) were spin coated in a N_2 filled glovebox equipped with an MBraun SC-210 spin coater from 10 mg/mL solutions in anhydrous chlorobenzene (CBZ) at 2000 rpm for 30 s. Resulting film thicknesses were 30-40 nm. The samples were subsequently annealed at 100°C on a Präzitherm PZ28-2 hotplate for 10 minutes. Alternatively, 35 nm of C_{60} was thermally evaporated at a base pressure of 10^{-6} mbar and a crucible temperature of 385°C, which resulted in a rate of 0.2 Å/s. No further post-treatment was conducted after C_{60} evaporation.

A dispersion of TiO_2 nanoparticles and titanium diisopropoxide bis(acetylacetonate) (TiAcAc, 75 wt.-% in isopropanol; Sigma-Aldrich) in anhydrous ethanol (Sigma-Aldrich) was prepared following a reported synthesis procedure.[218] In brief, 0.25 mL of anhydrous $TiCl_4$ (99.9%; Sigma-Aldrich) was added dropwise whilst stirring to 1 mL of anhydrous ethanol and 5 mL of anhydrous benzyl alcohol (99.8%; Sigma-Aldrich). The solution was kept stirring at 80°C for 9 h, afterward cooled down to room temperature and mixed in a 1:9 volume ratio with diethyl ether to precipitate the TiO_2 nanoparticles. After centrifuging 10 mL samples of this mixture at 6000 rpm for 5 min, the precipitate was washed with acetone and redispersed in 20 mL of anhydrous ethanol. Finally, 5 µL of TiAcAc was added per 20 mL of the dispersion.

To deposit 30 nm of TiO_2 as an electron selective contact, the above described dispersion was spin coated two times on top of a sample at 1000 rpm for 40 s in ambient air. After a thermal annealing at 150°C on a Heidolph MR 3001K hotplate for 30 min, the complete procedure was repeated to double the final film thickness.

SnO_2 for samples in chapter 4.1 was prepared by spin-coating in ambient air with 4 mg of $SnCl_2 \cdot 2H_2O$ (>99.995%; Sigma- Aldrich) in 1 mL of anhydrous ethanol (Sigma-Aldrich) at 2000 rpm for 40 s and subsequently annealed at 180°C for 60 min. Alternatively, for chapters 4.2 and 4.3, a Tin(IV) oxide nanoparticle dispersion (15 % in H_2O; Alfa Aesar) was diluted 1:7 vol. with DI-H_2O and filtered through 0.45 µm PVDF filter prior to spin coating on the substrate at 4000 rpm for 30 s. After 20 minutes of annealing at 150°C on a Heidolph MR 3001K hotplate, the spin coating procedure was repeated and the samples were annealed again for 30 more minutes. Layer thicknesses in both cases amounted to around 20-30 nm.

3.1.3 Perovskite Absorber Preparation

A one-step, anti-solvent assisted spin-coating procedure was used to deposit perovskite absorbers in a N_2-filled glovebox equipped with an MBraun SC-210 spin coater. Thereby, an anti-solvent is poured on the rotating substrate during spin coating to supersaturate the liquid thin film and quickly initialize crystallization. Two different compositions and deposition protocols were utilized in this work:

(1) For $CH_3NH_3PbI_3$, 1.1 M CH_3NH_3I (Dyenamo) and 1.1 M PbI_2 (99.99%, TCI) were first dissolved in a cosolvent of -butyrolactone and dimethyl sulfoxide (DMSO) with 7:3 volume ratio and left stirring at 60°C for 12 h. Following a slightly modified published method[219], the precursor solution was then spin coated upon the samples in three consecutive steps. As illustrated in Figure 3.2, an initial step at 1000 rpm for 10 s spreads the solution over the substrate while the other steps at 2000 rpm for 20 s and 5000 rpm for 10 s thin down the liquid film. Finally, 37 s after the start of the spinning program, 150 µL of toluene are dropped onto the substrate (Figure 3.2 c). A subsequent annealing at 100°C for 10 min on a Präzitherm PZ28-2 hotplate completed the perovskite layer preparation (Figure 3.2 d). The final layer thickness of the absorber was 350 nm.

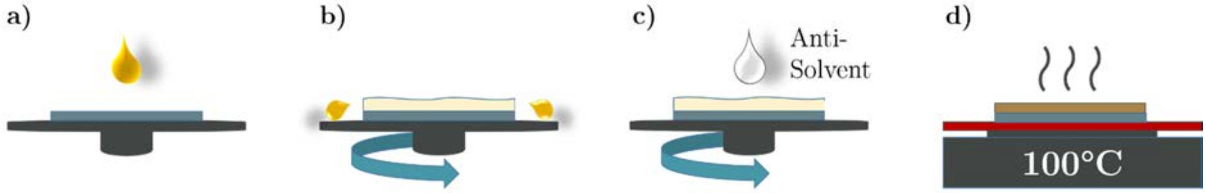

Figure 3.2: Schematic perovskite absorber deposition. a) Perovskite precursor solution is dropped onto the substrate. b) Start of the spin-coating program to spread the solution over the sample and thin down the liquid film. c) Several seconds before the end of the spin coating procedure, an anti-solvent is dispensed on the rotating substrate to supersaturate the liquid thin film and initialize perovskite crystallization. d) A final thermal annealing step at 100°C completes the perovskite crystallization process and evaporates residual solvents.

(2) $Cs_{0.05}(FA_{0.83}(MA)_{0.17})_{0.95}Pb(I_{0.83}Br_{0.17})_3$ perovskite compositions (so called "triple cation"), with FA being formamidinium ($CH(NH_2)_2$), were deposited following Saliba et al.[152] FAI (1 M, Dyenamo), PbI_2 (1.1 M, TCI), MABr (0.2 M, Dyenamo) and $PbBr_2$ (0.2 M, TCI) were dissolved in a 4:1 (v:v) mixture of anhydrous dimethyl formamide (DMF):DMSO. Further, 5 mol-% CsI from a 1.5 M stock solution in DMSO was added to the precursor solution. The perovskite solution was then spin coated onto the substrates in a two-step program at 1000 rpm for 10 s and 6000 rpm for 20 s. 30 s after the start of program, 150 µL of chlorobenzene was dispensed on the spinning substrate. Subsequently, the sample was annealed at 100°C on a Präzitherm PZ28-2 hotplate for 1 h. Here, absorber thicknesses between 500-600 nm were achieved.

For both perovskite absorbers prepared here, optical properties of thin films on quartz glass were determined by variable angle spectroscopic ellipsometry and transmittance/reflectance spectrophotometry as listed in Table 3.1. The low Urbach energies ≤15 meV highlight the superior quality of herein produced perovskite thin films.

Table 3.1 Band gap and Urbach energies for herein deposited perovskite absorbers of different composition, determined by variable angle spectroscopic ellipsometry and transmittance/reflectance spectrophotometry of thin films on quartz glass.[43]

Chemical composition	*Band gap energy*	*Urbach energy*
$MAPbI_3$	1.61 eV	15 meV
$Cs_{0.05}(FA_{0.83}(MA)_{0.17})_{0.95}Pb(I_{0.83}Br_{0.17})_3$	1.64 eV	14 meV

3.1.4 Hole Selective Contact Deposition

All hole transport materials were, similar to the perovskite absorber, deposited by spin-coating in an N_2 filled glovebox equipped with an MBraun SC-210 spin coater.

For 2,2‘7,7‘-tetrakis(N,N-di-p-methoxyphenylamin)-9,9‘-spirobifluoren (Spiro-OMeTAD; Merck), 36.2 mg of Spiro-OMeTAD was dissolved in 1 mL of CBZ, 8.8 µL of a bis(trifluoromethane) sulfonimide lithium salt (LiTFSI; Lumtec) stock solution (520 mg/mL in acetonitrile), 14.5 µL of a tris(bis(trifluoromethylsulfonyl)imide) (FK209; Dyenamo) stock solution (300 mg/mL in acetonitrile), and 14.4 µL of 4-tert-butylpyridine (Sigma-Aldrich). The Spiro-OMeTAD solution containing the doping agents was spin coated onto the samples at 1800 rpm for 30 s to form 150 nm thick layers.

Utilizing poly(3,4-ethylenedioxythiophene) (PEDOT) or PEDOT/Spiro-OMeTAD mixtures as HTM, the water-free dispersion Clevios P SB5 SCA 726-1 (Heraeus) was first filtered through a 0.45 µm PTFE filter. Next, the respective amount of Spiro-OMeTAD was added into the PEDOT dispersion and the entity was shaken at room temperature until complete dissolution. Finally, the mixtures were diluted with anisol to maintain similar film thicknesses of 100 nm. All PEDOT based HTMs were then prepared by spin coating at 4000 rpm for 30 s. Residual solvents were removed from the samples either by applying vacuum at 10^{-6} mbar base pressure overnight or by thermal annealing on a Präzitherm PZ28-2 hotplate at 120°C for 3 minutes.

10 mg of poly(tryaril amine) (PTAA; Sigma Aldrich) was dissolved at in 1 ml of toluene and 2.3 µL of a LiTFSI stock solution (520 mg/mL in acetonitrile as well as 2.0 µL of 4-tert-butylpyridine were added. A 50 nm thick layer was then spin cast from the solution at 4000 rpm for 30 s and the substrates were subsequently stored overnight in dry air (relative humidity below 10%).

CuSCN (99%; Sigma Aldrich) was dissolved with 20 mg/ml concentration in diethyl sulfide (98%; Sigma Aldrich) and spin coated at 6000 rpm for 30 s to achieve a layer thickness of 60 nm.

3.1.5 Top Electrode Deposition

Opaque solar cells were finalized by 80 nm of gold, thermally evaporated using an MBraun ProVap T5 at a base pressure of 10^{-6} mbar and a rate of 0.7 Å/s. Shadow masks were used to define the active areas of 16 mm^2.

For devices with transparent top contacts, 25 nm of MoOx were first evaporated using an MBraun ProVap T5 at a base pressure of 10^{-6} mbar with a rate of 0.6 Å/s.

For several experiments in chapter 4.3.2, buffer layers of ITO nanoparticles or SnO_2 were subsequently coated. The latter was prepared by thermal ALD in an Arradiance GEMStar reactor. TDMASn [Tetrakis(diethylamino)tin(IV)] was used as the Sn precursor and was held at 60 °C in a stainless steel container. Water was used as oxidant, and was delivered from a stainless steel container without intentional heating. The corresponding nitrogen-flow was set to 30 sccm for TDMASn and 90 sccm for watervapour. In between these pulses, the reactor was purged with

90 sccm nitrogen. One cycle of ALD deposition comprised subsequent injection of TDMASn (1 s), N_2 purge 1 (7.5 s), watervapour (0.2 s) and N_2 purge 2 (10 s) at a chamber- and door temperature of 100°C. ITO nanoparticles (<50 nm, 90% In_2O_3, 10% SnO_2; Sigma-Aldrich) were dispersed with 10 mg/ml in isopropanol, ultrasonicated for 10 mins or 1 h and subsequently spin coated on the MoOx surface in an N_2 filled glovebox equipped with an MBraun SC-210 spin coater at 5000 or 6000 rpm. A thermal annealing step at 80°C for 5 minutes concluded the deposition.

Next, ITO layers of different thickness were deposited by RF magnetron sputter deposition in a Roth & Rau MS200PVD sputter tool at a sputtering power of 70 W from a 2 inch ceramic target at room temperature. Shadow masks are used to define stripes of 4 mm width in semi-transparent solar cells, or for tandem devices rectangles of 2x0.6 cm^2 aligned to the center of the middle ITO stripes. For monolithic tandem solar cells 150 nm thick Ag stripes are evaporated at the edges of the ITO stripes to enhance lateral current transport and determine an active area of the ITO of 2x0.5 cm^2.

Finally, LiF is thermally evaporated at a base pressure of 10^{-6} mbar and a rate of 1 Å/s as an anti-reflection coating at the air/ITO interface.

3.1.6 Silicon Heterojunction Solar Cell Fabrication

The experimental details on the silicon heterojunction solar cell fabrication can be found elsewhere.[220] In brief, rear-side textured, front-side polished float zone n-type <100> oriented Si wafers with 4 inch diameter, 250 µm thickness, and a resistivity of 2-5 $\Omega \cdot \mathrm{cm}$ were used. The wafers were cleaned using the standard RCA process and the resulting oxides were removed by dipping in diluted hydrofluoric acid immediately before a-Si:H deposition. Intrinsic a-Si:H layers were deposited by standard PECVD processes using silane, SiH_4, as precursor gas. The *n*-type and *p*-type doped a-Si:H layers were prepared by adding PH_3 or B_2H_6 to the precursor gas, respectively. The back contact was formed by sputtering 140 nm of aluminum doped zinc oxide and 200 nm silver in a Leybold Optics A600V7 tool. On the front, 20 nm of ITO were deposited by RF magnetron sputter deposition in a Roth & Rau MS200PVD sputter tool at a sputtering power of 70 W from a 2 inch ceramic target at room temperature. Shadow masks define 18 stripes of 2x0.5 cm^2 on the wafers during sputtering. The 4 inch wafers are then broken in nine 2.5x2.5 cm^2 pieces with each substrate comprising two stripes of ITO.

3.2 Characterization Techniques

3.2.1 Current Density-Voltage Measurements

In current density-voltage (J-V) measurements, the current output of a solar cell in dark or under illumination is measured for varying externally applied voltages. In this work, measurements were conducted in air using a “Steuernagel Lichtechnik” sun simulator for the study presented in chapter 4.1 and a LED based class AAA Wavelabs Sinus-70 sun simulator in chapter 4.2 and 4.3. A spectrum mimicking AM 1.5g with an irradiance on the sample of 100 mW/cm^2 was adjusted by measuring the short circuit current of a calibrated, unfiltered silicon solar cell (Fraunhofer ISE) without mismatch correction. The silicon reference and the perovskite solar cells were temperature controlled to 25°C during measurement. The active area of 0.16 cm^2 was defined by the overlap of orthogonal ITO and gold patterns, both 4 mm in width. To avoid underestimations of the active area, J-V measurements of several single junction samples were additionally performed with 0.10 cm^2 shadow masks. As a result of the discrepancies in measured J_{SC} values between masked and unmasked devices, an area correction factor was derived which is included for all unmasked J-V scans. For all tandem cell measurements an aperture mask with 1 cm^2 size is used to define the active area and reduce edge effects. J-V curves of solar cells were scanned with a digital source meter (Keithley Model 2400 for single-junction and Model 2601B for tandem solar cells) in two consecutive sweeps in forward ($V_{Start}<V_{End}$) and reverse ($V_{Start}>V_{End}$) direction without pre-biasing of the device. The scan rate was varied between 277 and 2500 mV/s, with a standard scan speed of 833 mV/s. Measurements in N_2 atmosphere were performed as before but under the illumination of simulated AM 1.5G solar light from an Oriel class ABB solar simulator system, adjusted with the same unfiltered silicon reference cell without mismatch correction. For MPP tracking measurements, the power output of a device was continuously feedback controlled using a homemade software for all the sun simulators used herein. Starting at the voltage of the MPP of the reverse scan at 1666 mV/s, steps of +10 mV, 0 mV and -10 mV were added to the actual voltage and the current density of the device was traced at each operating point for 1 s (Figure 3.3). The bias point with the highest average power output during the last 0.5 s of each scan was then selected as the new MPP for the subsequent iteration. To measure the convergence of the MPP, after six iterations with similar MPP bias point, the voltage step increment is reduced by a factor of two (not shown in Figure 3.6).

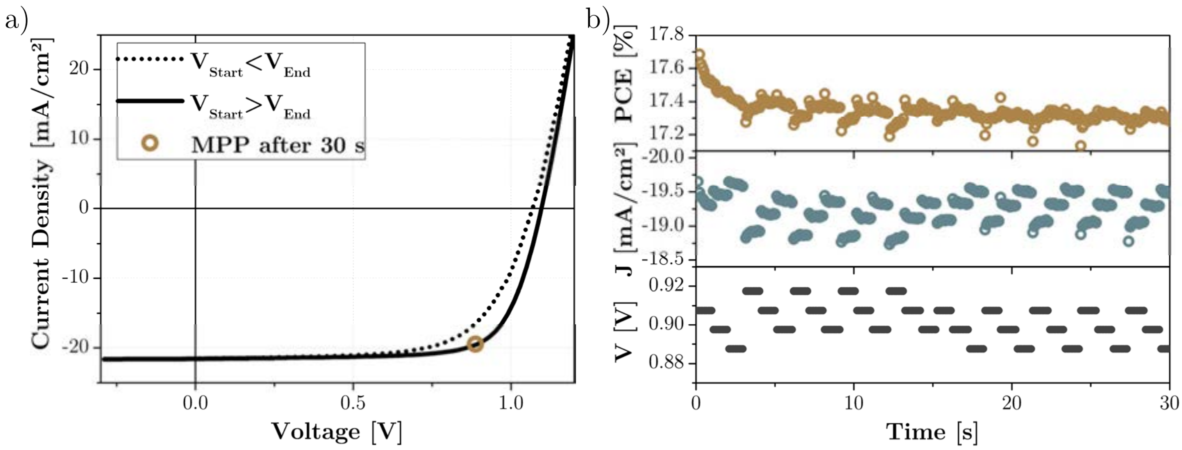

Figure 3.3: a) Exemplary current-voltage (J-V) characteristics of a perovskite solar cell in forward ($V_{Start}<V_{end}$) and reverse ($V_{Start}>V_{end}$) scan direction as well as maximum power point (MPP) after 30 s of MPP tracking. b) Corresponding MPP track with the herein used perturb-and-observe algorithm. The voltage applied to the device is altered around the MPP and the respective current density output of the solar cell is recorded. After each cycle, the MPP for the next iteration is determined by the voltage level achieving the highest power conversion efficiency ($PCE=J_{MPP} \cdot V_{MPP}/100$ mW/cm² under standard test conditions).

3.2.2 External Photovoltaic Quantum Efficiency

The external photovoltaic quantum efficiency (EQE_{PV}) describes the spectral incident photon-to-electron conversion efficiency of a solar cell, as introduced in chapter 2.1.3. Monochromatic light is radiated on the sample and the spectral current of the cell I_{Phot} generated by this excitation is measured. Knowing the spectral photon flux ϕ of the light source reaching the sample, the EQE_{PV} can be calculated with [37]:

$$EQE_{PV}(\lambda) = \frac{I_{Phot}(\lambda)}{q \cdot \Phi_{\lambda}(\lambda)}. \tag{3.1}$$

Further, the internal photovoltaic quantum efficiency (IQE_{PV}), which only accounts for photons actually being absorbed in the solar cell, can be obtained by calculating the spectral reflectance (R) and transmittance (T) out of the EQE_{PV} [37]:

$$IQE_{PV}(\lambda) = \frac{EQE_{PV}(\lambda)}{1 - R(\lambda) - T(\lambda)}. \tag{3.2}$$

EQE_{PV} is typically measured at short circuit conditions, but can also be determined under bias voltage. Further, a bias light can be utilized to increase the carrier density of a solar cell during EQE_{PV} measurements. Dependence of EQE_{PV} on the bias light intensity has often been observed in DSSC[221] or OPV[222], due to processes which vary non-linearly with the carrier density, e.g. direct recombination of carriers[222] or space charge effects[223]. However, both for Si as well as for perovskite solar cells[224], the I_{SC} scales linearly over a wide range of illumination intensities, as exemplarily shown for a herein produced perovskite solar cell in Figure 3.4 a). The photocurrent of the solar cell under one-sun illumination can then be calculated by integrating the product of $EQE_{PV} \cdot q \cdot \phi_{AM1.5G}$ over the absorption wavelength range of the examined semiconductor, as given in eq. 2.6.

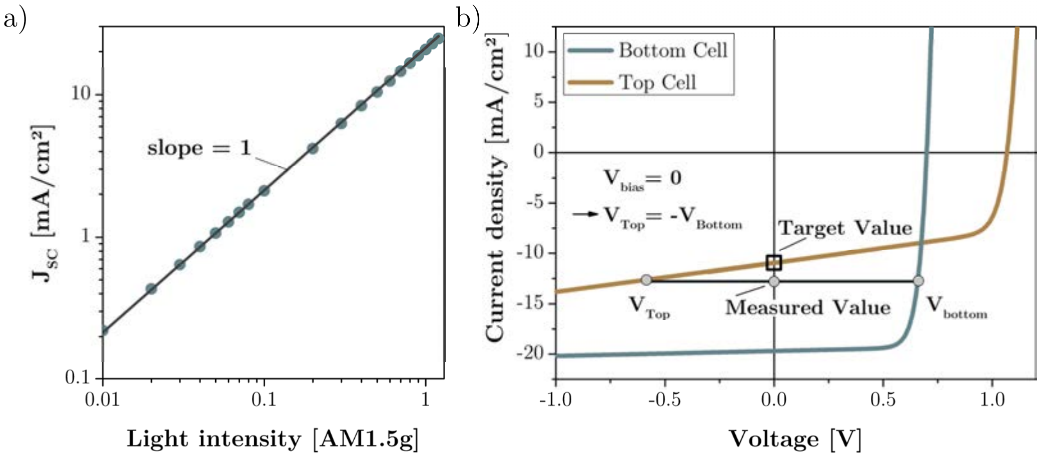

Figure 3.4: a) Linear dependence of short-circuit current density (J_{SC}) on illumination intensity as measured for a perovskite solar cell produced in this work. b) Exemplary illustration of overestimated J_{SC} values in EQE_{PV} studies on monolithic tandem solar cells without external bias voltage (V_{bias}). The voltage generated by the optically biased sub cell, here the bottom cell, causes the examined sub cell, here the top cell, to operate in reverse bias conditions. The measured currents of the top cell therefore exceed the target values. Instead, applying V_{bias} across the tandem solar cell similar to the open circuit voltage of the optically biased cell, allows the investigated sub cell to operate close to short circuit conditions.[225]

For monolithic tandem solar cells, EQE_{PV} of each sub cell can be measured individually. Yet, as the sub cells are electrically series connected, determining EQE_{PV} at short circuit conditions requires two prerequisites. First, the cell not under investigation has to be illuminated (optically biased), to enable a current flow in the entire circuit. Second, the voltage created by this illumination in the sub cell not under investigation has to be compensated by a bias voltage, in order to provide short-circuit conditions for the examined sub cell. During EQE_{PV} measurements, the optically biased cell operates close to its V_{OC}. Without external bias voltage, the tandem device is electrically shorted and this voltage close to V_{OC} would drop across the other sub cell. EQE_{PV} of the investigated cell would then be recorded not under short-circuit but under reverse bias conditions. This would lead to overestimation of the EQE_{PV}, especially for solar cells with low shunt resistances, as illustrated in Figure 3.4 b).[225]

EQE_{PV} was measured here for single-junction solar cells in nitrogen atmosphere using an Oriel Instrument's QEPVSI-b system with a Xenon arc lamp (Newport 300 W, 66902) chopped at 35.5 Hz and a monochromatic instrument (Newport Cornerstone 260) and a current-voltage Lock-in amplifier. The illumination beam size on the sample is 2.5 x 2.5 mm^2 and measurements were performed in a wavelength range from 300 to 850 nm with 10 nm steps, controlled by TracQ^{TM}-Basic software. The external quantum efficiency was measured without background illumination or applied bias voltage. Perovskite-silicon tandem solar cells instead were analyzed in air with a home-made EQE_{PV} measurement setup. A 75 watt xenon and a 100 watt halogen lamp were used as light sources for wavelengths below and above 770 nm, respectively. The monochromated light was mechanically chopped to 78 Hz and the measured signal was processed by a current-voltage Lock-in amplifier. The intensity of the lamp is checked with calibrated reference diodes. Bias light LEDs at wavelengths of 455 and 850 nm were used to selectively generate excess free carriers in the perovskite top or Si bottom cell, respectively. Further bias voltages of typically 0.7 V and 1.0 V were applied to compensate for the bias light generated photovoltage of the Si and perovskite sub cell, respectively.

3.2.3 Transient Photoluminescence

In transient photoluminescence (TRPL) measurements, an absorber is typically excited with a short light pulse to generate free charge carriers. After excitation, the number of photons emitted from radiative recombination events in the absorber are counted over time by a detector. The temporal decay of the signal thus gives implications about charge carrier dynamics, and can be influenced by e.g. efficient charge extraction from the perovskite or increased non-radiative recombination within the absorber and at its interfaces. The charge carrier density typically abates over time proportional to $\sim exp(-t/\tau)$, where the lifetime τ and the occurring recombination mechanisms can also depend on the carrier density.[124] At low carrier densities, SRH recombination is typically dominating and a monomolecular recombination lifetime can be extracted from the TRPL decay in this regime. Here, fully prepared perovskite solar cells were excited in air by a pulsed laser at 405 nm wavelength (LDH-P-C405, PicoQuant GmbH) and ca. 50 nJ/cm^2 fluence. The emission was recorded (650-850nm) with a TCSPC setup comprising a Becker&Hickl SPC-130 acquisition system and a PML-16-C-1 (modified Hamamatsu) multichannel detector, while filtering the excitation pulses (cut-off filter $<$ 450nm). No external bias was applied during the experiment.

3.2.4 Absolute Photoluminescence

Absolute photoluminescence (PL) measurements allow determination of the quasi-Fermi level splitting in an absorber under illumination from its PL emission. Assuming solely bimolecular recombination as radiative emission and optical constants and quasi-Fermi level splitting ΔE_F

being constant across the absorber depth, the spectral PL yield (Y_{PL}) outside the semiconductor can be assumed as [226]:

$$Y_{PL}(E) = \frac{2\pi}{h^3c^2}\frac{E^2a(E)}{e^{\frac{E-\Delta E_F}{k_BT}}-1} \quad or \quad \ln\left(\frac{Y_{PL}(E)h^3c^2}{2\pi E^2 a(E)}\right) = -\frac{E-\Delta E_F}{k_BT}, \tag{3.3}$$

where a is the absorptivity of the sample and T the temperature of the electrons, which is similar near room temperature to the sample temperature due to electron-phonon coupling. Determining the absolute number of photons being spectrally emitted (Figure 3.5 a) and further assuming that the absorptivity approaches unity well above the PL peak energy, allows to deduce T from the slope and ΔE_F from the intercept with the abscissa of a fit to the high energy tail of the absolute PL emission (Figure 3.5 b).

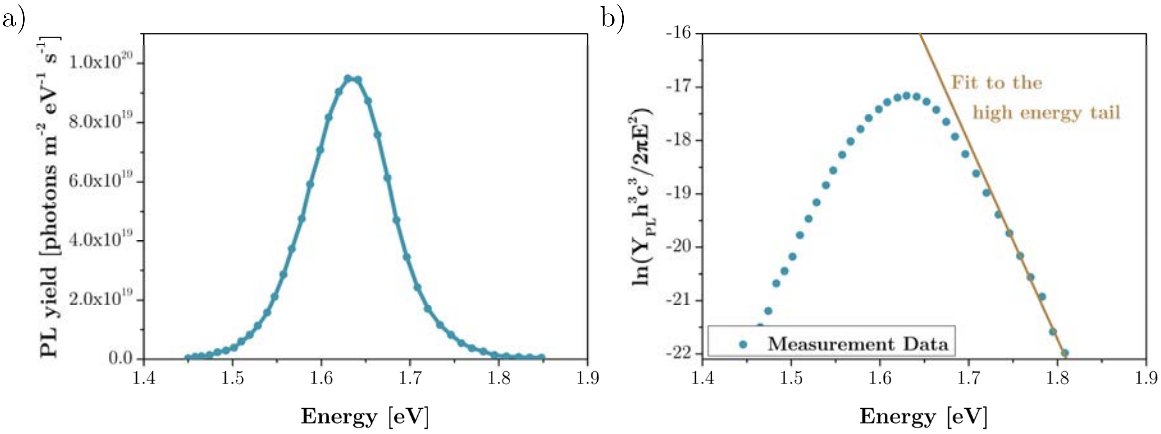

Figure 3.5 a) Absolute spectral photoluminescence emitted from a perovskite sample in this work. b) Corresponding recalculation of the data assuming an absorptivity of 1 above the PL peak position at 1.63 eV allows to linearly fit the high energy tail of the spectrum to determine the quasi-Fermi level splitting according to eq. (4.1).

Here, absolute PL measurements were performed on a temperature controlled stage at 300 K by excitation with two 450 nm light emitting diodes (LEDs) equipped with diffuser lenses. The intensity of the LEDs was adjusted to ~1 sun by illuminating a contacted perovskite solar cell at short circuit and matching the current density to the short circuit current density of the cell determined before under 1 sun illumination from a sun simulator (e.g. 22.2 mA/cm^2). The photoluminescence detection was performed with a CCD camera (Allied Vision) coupled with a liquid crystal tunable filter. The system was calibrated to absolute photon numbers.

3.2.5 Ultraviolet Photoelectron Spectroscopy (UPS)

Photoelectron spectroscopy in general gives insights into the electronic states of materials. Samples are illuminated by monochromatic light, causing emission of photoelectrons according to the external photoelectric effect. More specific, for photon energies $h\nu$ greater than the ionization energy IE of the examined material, electrons are excited above the vacuum edge and can be emitted with a kinetic energy $E_{kin} \leq h\nu - IE$.[227] The excitation depth in the material depends on the optical absorption properties of the specimen for the excitation energy according to Lambert-Beer's law given in chapter 2.1.2. However, inelastic scattering of photoelectrons excited deeper in the material often reduces their energy to below IE before leaving the sample surface.

Therefore the information depth of photoelectron spectroscopy is usually restricted to a few nanometers.[227, 228]

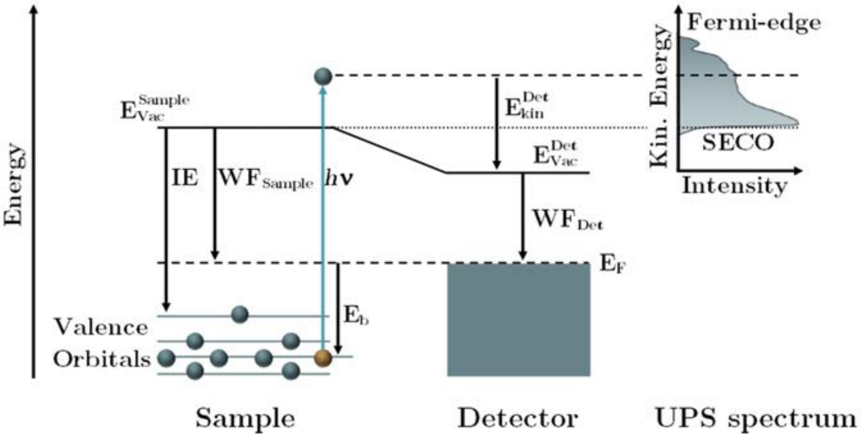

Figure 3.6: Schematic energy diagram of the essential energy levels for ultraviolet photoelectron spectroscopy (UPS) measurements on an arbitrary semiconductor. Note that the detector includes an energy dispersive analyzer. Grey circles mark electrons, the beige circle illustrates a hole after photoelectron excitation. IE, WF, hν, E_{Vac}, E_{kin}, E_F, E_b and SECO denote the ionization energy, work function, photon energy, vacuum energy level, kinetic energy, Fermi-level, binding energy and secondary electron cutoff, respectively. Depiction following refs. [227, 229, 230]

A distinction is made between X-ray and ultraviolet photoelectron spectroscopy. While the latter one typically illuminates samples with energies < 50 eV and provides information only about the valence electrons, soft X-ray excitation with energies in the order of 10^2-10^3 eV also allows probing of core electron levels.[227] Further, hard X-rays with energies of 10^4 eV enable excitation of electrons deep inside the sample with high kinetic energies, thus increasing the information depth to several tenths of nanometers.[228] In this work, mainly ultraviolet photoelectron spectroscopy (UPS) has been used to determine *IE* and the work function *WF* of different selective contact materials.

Here, a xenon high-pressure lamp with a monochromator at 6.5 eV and a He gas discharge lamp emitting photons with He(I)-line radiation at 21.2 eV are utilized as light sources. The spectrum of electron kinetic energies emitted from the sample in ultra-high vacuum is then collected by an energy dispersive analyzer and a detector. As illustrated in Figure 3.6, the measured kinetic energies (E_{kin}^{Det}) are referred to the vacuum energy of the detector. Detector and sample are electrically connected to align their Fermi-levels. By knowing the work function of the detector (WF_{Det}), the electron binding energy E_b in the sample relative to the Fermi-level can then be calculated as [229]:

$$E_b = h\nu - WF_{Det} - E_{kin}^{Det}. \tag{3.4}$$

Note, that $E_b + WF_{sample} \geq IE$. The work function WF_{sample} of the examined material is revealed by the signal edge from electrons, which have no kinetic energy with respect to the studied layer, also referred to as secondary electron cutoff (SECO). Subsequently, the lower limit of E_b, and thus *IE,* can be determined by the onset of the UPS signal at high kinetic energies of the photoelectrons, often denoted as Fermi-edge.

The ultraviolet photoelectron spectroscopy (UPS) measurements utilized in this work were performed in an UHV system at base pressures of 1×10^{-9} mbar. He-UPS measurements with an excitation energy of 21.2 eV were conducted to determine the ionization potentials. Since He-UPS is very surface sensitive and contaminations such as adsorbates could influence the work function of the samples, we additionally performed measurements with 6.5 eV excitation energy using a Xe-XBO-lamp with double grating monochromator. The work function was determined by fitting a Boltzmann sigmoid function to the secondary electron cut-off, whereas the ionization potential was identified by extrapolating the leading edge of the valence band or HOMO spectrum. All electron contacts characterized by UPS were prepared as described for the solar cell preparation in a glass/ITO/ETM structure. After deposition, all substrates were exposed to air for few minutes during the transport to the UHV system.

X-ray photoelectron spectroscopy (XPS) measurements were performed in a UHV chamber with a base pressure in the range of $5 \cdot 10^{-10}$ mbar, employing non-monochromatized Mg K_α excitation at 1253.6 eV and using a ScientaOmicron Argus CU electron analyzer. The analysis of the XPS elemental core level spectra was done using the software FITYK[231]. The spectra were fit simultaneously using Voigt profiles with coupled Gaussian and Lorentzian line widths including a linear background.

3.2.6 Surface Photovoltage

Modulated surface photovoltage (SPV) measurements were carried out in air with a fixed capacitor arrangement. Light from a halogen lamp was chopped at a frequency of 8 Hz and monochromated by a quartz prism to provide spectral measurements in an energy range from 1.4-1.8 eV. As illustrated in Figure 3.7, the samples were illuminated through a quartz cylinder partially covered with SnO_2:F (FTO) as a reference electrode while an about 10-30 µm thick mica sheet was used as a dielectric spacer to the perovskite surface. The respective perovskite sample was connected via the ITO front electrode. A high impedance buffer and a double phase lock in amplifier (EG & G, 7260 DSP) were used to record the modulated signals as an in-phase and a phase shifted by 90° signal. The tail slope parameter E_T were obtained by fitting the in-phase SPV signals at the leading edge below the band gap energy with an exponential expression reported elsewhere.[62]

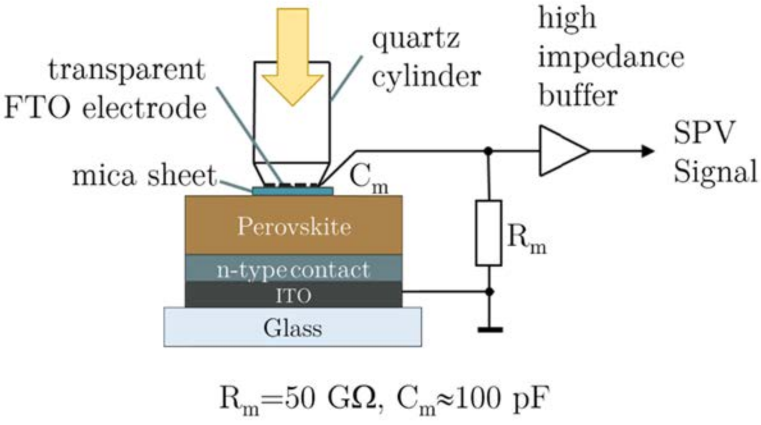

Figure 3.7: Schematic structure of the surface photovoltage measurement setup.

3.2.7 Atomic Force Microscope

Atomic force microscopes (AFM) utilize nanometer thin measurement tips (cantilever), typically from Si, SiO_2 or Si_3N_4, to probe a sample surface. When approaching the surface, forces such as mechanical contact forces, van der Waals forces, or electrostatic forces between the tip and the sample lead to a deflection of the cantilever.[232] Measuring this deflection allows to determine the surface topography of a sample with resolutions down to the atomic scale. There are in principle three different modes of measurements, contact, tapping and non-contact mode. The first and simplest method, the contact mode, brings the cantilever in contact to the substrate and measures the topography by dragging it across the sample. This can however easily damage the sample and the cantilever. In tapping mode, the cantilever is instead oscillating just above the substrate surface and only touching touches it periodically. This remedies lateral forces between the cantilever and surface during measurement. Further, in non-contact mode, the cantilever oscillates in distances of 10-100 nm above the sample surface to measure long-range forces like magnetic, electrostatic or van der Waals forces. This allows to image the surface topography while leaving the sample surface untouched and keeping the cantilever tip sharp.[232] In this work, AFM measurements were performed in tapping mode on a 10 x 10 μm^2 scan area using a Park Systems XE-70 instrument.

3.2.8 Scanning Electron Microscope

In a scanning electron microscope (SEM), an electron beam is radiated onto a sample with a spot size of a few nanometers and kinetic energies in the order of 10^2-10^5 eV. The electrons penetrate several hundred nanometers to micrometers into the material, depending on the electron energy, the atomic number and the density of the investigated sample. Besides reflection of high-energy electrons from elastic scattering, Auger electron and x-ray emission, the incident electron beam also causes emission of secondary electrons from the specimen by inelastic scattering. These secondary electrons can be selectively detected due to their comparably low kinetic energy. Changes in the angle or the composition of the sample surface usually alter the emission spectrum of secondary electrons. Scanning with the electron beam across a surface and detecting the intensity of secondary electron emission at each point thus allows to create an image of the sample surface with a resolution down to few 1-10 nm.[233]

Here, SEM pictures were recorded with the secondary electron detector of a Hitachi S-4100 SEM at 5kV acceleration voltage and 30k or 50k magnification for top view or cross section images respectively. Top view images were processed with “GNU Image Manipulation Program” software to optimize edge detection and grain size determination via the software “Gwyddion”.

3.2.9 Optical Measurements and Simulations

Absorption profiles of perovskite-silicon heterojunction tandem solar cells or layer stacks on glass were calculated with the MATLAB-based program GenPro4[234]. The program can determine reflection, transmission and absorption for layer stacks, either with both coherent and incoherent layers and can include surface textures for the interfaces.

For optically flat interfaces, the reflection and the layer transmittance can be calculated from the Fresnel equation and Lambert-Beer law.[31] However, depending on their incidence angle, photons can reflect at interfaces multiple times and travel a complicated path within a layer stack (left in Figure 3.6 a). GenPro4 therefore uses the net-radiation method[235] to determine reflection and transmission at each interface within the investigated system. For each wavelength, the method summarizes all possible photon paths in each layer to four distinct photon fluxes at every interface: approaching and leaving fluxes both from the top and bottom side. As illustrated in the right of Figure 3.6 a), the four fluxes can be defined as [236, 237]:

$$\begin{aligned} q_i^a &= \tau_i \cdot q_{i-1}^d \\ q_i^b &= r_i \cdot q_i^a + t_i \cdot q_i^c \\ q_i^c &= \tau_{i+1} \cdot q_{i+1}^b \\ q_i^d &= t_i \cdot q_i^a + r_i \cdot q_i^c \end{aligned} \tag{3.5}$$

Here, r_i and t_i are reflection and transmission coefficients from Fresnel equations and τ_i denotes transmittance of a layer according to Lambert-Beer. This reduces the complexity of the system to a set of linear equations with four times the number of interfaces. The system of equations can then be solved by standard numerical techniques to obtain the values of every flux. The absorption of a layer can then be calculated by the sum of fluxes entering minus the fluxes leaving the layer.

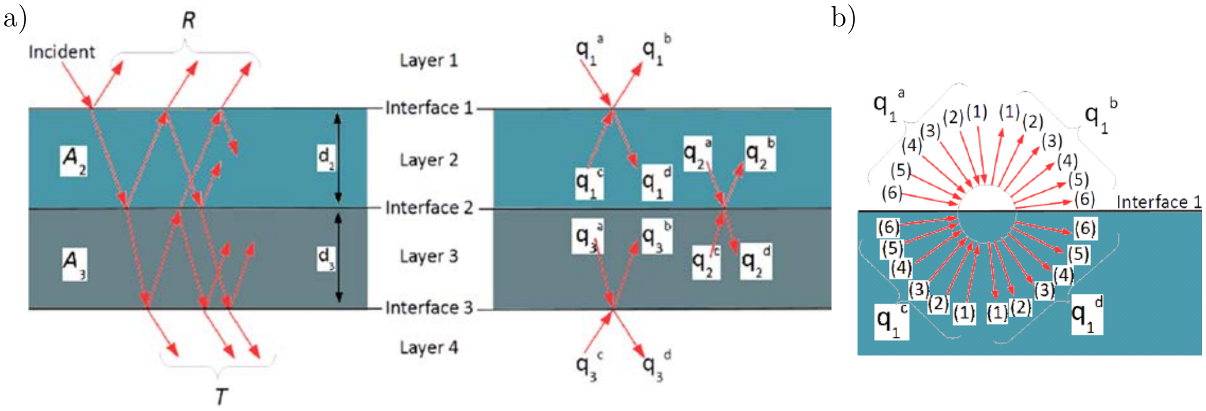

Figure 3.8: a) Illustration of the net-radiation approach. Left depicts the actual path of photons in a layer stack, right their summarization to four fluxes at each interface, thereby simplifying calculation of the absorption, reflection and transmittance profiles of the layer stack. b) Extension of the net-radiation method to multiple angle intervals for textured surfaces. Illustrations following Santbergen[237].

Layers can be treated coherently or incoherently in the simulation. For the tandem solar cells, c-Si was treated incoherently due to its large thickness of 180 µm, which clearly exceeds the coherence length of sunlight (~1 µm).[236] The same accounts for the 1 or 1.1 mm thick glass substrates in the case of single junction solar cells or single layers of a material coated on glass. Besides, an infinite layer of air is assumed as the incoherent top material of each system. All other layers have thicknesses below 1 µm and are thus treated as coherent thin films. Further, a surface texture of random pyramids is utilized for the rear Si contact in perovskite-Si tandem solar cells. For coherent layers, interferences must further be taken into account of the net-radiation method. In these cases, the simple photon fluxes in eq. (3.5) are replaced by complex amplitudes of electromagnetic waves, so at each interface the resulting amplitude and the phase of the electric field is determined.

A layer's transmittance is further determined by the change in complex amplitude according to [236]:

$$\tau_i(\lambda) = \exp\left(i \cdot \frac{2\pi N_i d_i}{\lambda}\right), \tag{3.6}$$

where N_i is the complex refractive index and d_i the thickness of the respective layer. From the resulting complex amplitude of the electric field at each interface, the energy flux or Poynting vector is given by the real part of the product of electric and complex conjugated magnetic field strength at the interface.[236]

Next, for textured surfaces, the reflected and transmitted light is distributed through the layers over a range of angles. The net-radiation method can in these cases be extended, by dividing the range of propagation angles into angular intervals. This is exemplarily shown in Figure 3.8 b) for a subdivision into six angular intervals. The program actually uses 30 divisions with an angular width of 3° each. For each interval, matrices similar to eq. (3.5) are determined, utilizing a ray-optics model with standard ray-tracing technique. Subsequently numerical solving of the set of equations allows to determine reflection, transmittance and absorption of the investigated system.[237]

Along with the absorption profiles A, the corresponding current densities J under AM1.5G illumination are calculated for each layer following:

$$J_i = -e \int_{300}^{1200} A_i \Phi_{AM1.5G}(\lambda) d\lambda. \tag{3.7}$$

For perovskite-silicon tandem solar cells, layer thickness optimizations are performed in chapter 4.3.3 to achieve a maximum short-circuit current J_{SC} of the tandem device. Due to the series connection of the monolithically integrated sub cells, J_{SC} is determined by the sub cell with the lower achievable current density.

A variety of complex refractive index spectra (n, k) were taken from literature: LiF[238], ITO[24, 239], Spiro-OMeTAD[240], PTAA[234], MoOx[241], SnO_2[242], doped and intrinsic a-Si:H layers[24, 239], c-Si[42] and Ag[243]. Optical data for perovskite were taken for $CH_3NH_3PbI_3$ from ref.[112] and for the so called "triple cation" composition (described in more detail in section 3.1), the same data was shifted by 20 nm to fit the larger band gap energy.

For all other layers, optical data were determined by their reflectance and transmittance measurements. Reflectance and transmittance measurements were performed with a Perkin Elmer LAMBDA 1050 UV—VIS spectrometer, equipped with an integrating Ulbricht sphere and calibrated from a Fraunhofer ISE certified white standard. Thereby, light from deuterium (UV) and tungsten lamps is monochromated between 250-1200 nm in 5 nm steps and radiated onto a sample which is either placed in front of (transmittance) or directly behind (reflectance) the Ulbricht sphere, at which a detector is attached. For transmittance measurements, the rear opening of the sphere is covered with the white standard. A reference beam and detector constantly measures the illumination intensity at each wavelength and allows determination of the overall light being transmitted or reflected into the Ulbricht sphere. Absorption was partially calculated here by 1-reflection-transmission and the corresponding current density under AM1.5G illumination calculated according to eq (4.1).

To determine the optical constants from reflectance and transmittance, a MATLAB based APCSA software was utilized.[244] This requires knowledge about the layer thickness of the material of interest as well as *n, k* for all other layers in the analyzed system. Here, layers were coated on 1 mm thick glass and their thickness was determined by scanning electron microscopy cross section images. The software then approximates the complex refractive index spectrum of the investigated material by combining the transfer-matrix-method[245] with a simulated annealing algorithm[246] to minimize the deviation of computed from the measured reflection and transmission.

3.2.10 Lateral Conductivity

Lateral conductivity of thin films on glass was determined by a homemade mercury two point probe setup following Abowitz et al52 in combination with a Keithley model 237 voltage source measure unit. The setup forms two mercury contacts in moulds attached to the investigated sample surface and performs a J-V scan from -1 to 1 V. From the dimensions of the moulded mercury electrodes and the distance between them as well as the sample layer thickness, the corresponding specific resistivity of the investigated material can be calculated.

4. Results and Discussion

4.1 Double-Layer Selective Contacts in Perovskite Solar Cells for Improved Device Performance and Reduced Hysteresis

The following chapter is based on the peer-reviewed article: “It Takes Two to Tango - Double-Layer Selective Contacts in Perovskite Solar Cells for Improved Device Performance and Reduced Hysteresis” by Lukas Kegelmann, C.M. Wolff, C. Awino, F. Lang, E.L. Unger, L. Korte, T. Dittrich, D. Neher, B. Rech and S. Albrecht published in ACS Applied Materials&Interfaces (2017), vol. 9 (20), pp. 17245-17255.

It presents a comparative study of different planar, low-temperature processed electron transport materials (ETM) commonly utilized as *n*-type contact in opaque single-junction perovskite solar cells. The examined ETMs range from the inorganic metal oxides titanium dioxide (TiO_2) and tin oxide (SnO_2) to different organic fullerene derivatives as well as their combination in metal-oxide/fullerene double-layer stacks. The systematic comparison allows to identify correlations between the ETM properties and the performance and hysteresis of planar *n-i-p* type perovskite solar cells as well as principle benefits of double-layer electron contact system combining benefits from the individual layers. Deposition temperatures of all examined ETMs below 180°C further render the investigated materials applicable to perovskite-silicon heterojunction tandem solar cells which was the main motivation for this work.

4.1.1 Introduction

TiO_2 is the most commonly used *n*-type contact in mesoporous *n-i-p* type PSC, and allowed the highest efficiencies above 22% so far.[26, 153, 155] Yet, it typically requires high sintering temperatures >450°C which deteriorates substrates with limited thermal budget such as flexible foils[177] or silicon heterojunction (SHJ) bottom cells.[21, 213] Therefore low temperature processable, typically planar electron selective contacts are required to enable monolithic perovskite-SHJ tandem solar cells.

Planar contacts thereby can face drawbacks as compared to the mesoporous architecture, e.g. a lack of templated perovskite nucleation and growth or reduced contact area to the absorber. Planar, low temperature deposited TiO_2 for example has been utilized before in PSCs, but revealed poor charge extraction and more pronounced photocurrent hysteresis as compared to the mesoporous counterpart.[156, 157]

It was shown, that high efficiencies >20% and negligible hysteresis can be achieved in planar *n-i-p* devices by optimizing the surface energetics and/or charge extraction properties of the *n*-type contact.[61, 145] A widely used alternative to compact TiO_2 layers is SnO_2 due to its wide band gap, high electron mobility and appropriate conduction band position.[247] Insufficient electron extraction from perovskite absorbers to metal oxide ETMs can also be remedied by carefully adjusting the metal oxide surfaces, e.g. by chlorination to passivate interfacial defects[61] or different plasma treatments to adjust the Fermi-level alignment to the absorber[248]. Besides metal oxides such as TiO_2 or SnO_2, also fullerene *n*-type contacts are utilized and not only show good charge extraction properties[172] but are also supposed to passivate defects at the perovskite interface.[187] Both can reduce recombination losses and hence improve device performance and suppress photocurrent hysteresis.[181] Also double-layer electron contacts such as TiO_2/C_{60}-monolayers[157], TiO_2/PCBM[172] or SnO_2/PCBM[249] are reported. However, in these cases the electron selective materials interfacing the perovskite are the same as for C_{60} or PCBM single-layer *n*-type contacts, so the necessity of the metal oxide in double-layer contacts remains unclear. In monolithic perovskite-SHJ tandem solar cells, single-layers of SnO_2 deposited by ALD[21] or the fullerenes C_{60}[215] or PCBM[178, 213] were so far employed as low temperature ETMs underneath the perovskite absorber.

However, it lacks methodical analysis to identify fundamental differences between these contact systems. In this chapter, within a comparative study, the influence of different low-temperature deposited organic and inorganic electron transport materials (ETM) on the performance and hysteresis of planar *n-i-p* PSCs is thoroughly investigated. The general device design comprises glass/ITO/ETM/perovskite/Spiro-OMeTAD/Au with Spiro-OMeTAD [2,2‘7,7‘-tetrakis(N,N-di-p-methoxyphenylamin)-9,9‘-spirobifluoren] being the hole transport material. Examined ETMs span a broad range from the inorganic metal oxides titanium dioxide (TiO_2) and tin oxide (SnO_2) fabricated according to reported protocols,[218, 247] to the organic fullerene C_{60} and its derivatives PCBM and ICMA (1’,4’-Dihydro-naphtho[2’,3’:1,2][5,6]fullerene-C_{60}). To the best of our knowledge, ICMA has been used here for the first time as ETM in perovskite solar cells. The fullerene derivative was utilized before in organic photovoltaics[250] and has a comparable chemical structure but different energy levels as compared to C_{60} or PCBM.[162]

To elucidate the role of the underlying metal oxide in double-layer ETMs, TiO_2 and SnO_2 are utilized in a metal oxide/PCBM structure and compared to PCBM single-layer ETMs in PSCs (glass/ITO/metal oxide/PCBM/perovskite/Spiro-OMeTAD/Au constitutes the extended device stack). Note that cathode buffer layers between PCBM and the electrode are often used in inverted *p-i-n* devices to increase the shunt and decrease the series resistance of the devices.[155] However, their utilization in the *n-i-p* architecture has hitherto not been examined in detail.

In order to isolate the impact of the ETM properties on device characteristics, all processing steps beside the ETM layer are kept unmodified. Additionally, the $CH_3NH_3PbI_3$ perovskite absorber is prepared by a “One-Step” spin coating method with anti-solvent drip[219] which results in a perovskite morphology unaffected by the underlying substrate, as shown by scanning electron microscopy in Figure 4.2 a). Further, surface photovoltage spectroscopy measurements indicate comparable perovskite absorber qualities on all ETMs except TiO_2 which shows a more prominent influence of defect states, see Figure 4.2 b) and c). This enables to establish an unambiguous relation between device performance and ETM contact properties.

In addition, transient photoluminescence and current-voltage measurements at different scan speeds reveal faster and less pronounced hysteretic responses as well as higher stabilized efficiencies for devices with fullerene compared to metal oxide ETMs. This is in line with numerous other reports focusing on the optimization of the charge selective material interfacing the perovskite.[61, 145] Beyond these findings, the study in this chapter further shows that an additional interlayer not in direct contact to the perovskite absorber can have major beneficial effects. By depositing metal oxides between the ITO electrode and a fullerene electron selective contact, hysteresis is successfully reduced and the power output strongly improves by ca. 30% on average and up to a stabilized champion device efficiency of 18.0%.

While the solar cells based on different single-layer ETMs vary in their scan rate dependence of the hysteresis, devices with metal oxide/fullerene double-layer ETMs exhibit a scan rate independent transient response. This indicates that the double-layer contact design resolves transient charge carrier extraction effects which otherwise result in hysteresis. Supported by photoelectron spectroscopy, the improved efficiencies are related to reduced recombination losses throughout the electron contact and suggest minimized shunt paths, improved hole blocking properties and enhanced charge transport from the fullerene to the electrode to be the root causes for these enhancements.

4.1.2 Results and Discussion

In this chapter, the effect of different electron transport materials (ETMs) on perovskite solar cell characteristics is analyzed in a planar *n-i-p* superstrate structure as shown in Figure 4.1 a). Various ETMs that are processed at temperatures below 180°C, are coated onto ITO covered glass substrates followed by the perovskite layer, Spiro-OMeTAD as a hole selective contact and a gold electrode. Further, the device structure is extended to a double-layer electron contact design by using a metal oxide and a fullerene derivative (PCBM) as depicted in Figure 4.1 b). The ETMs investigated cover the inorganic metal oxides titanium dioxide (TiO_2) and tin oxide (SnO_2) as well as the organic fullerene C_{60} and its derivatives PCBM and ICMA.

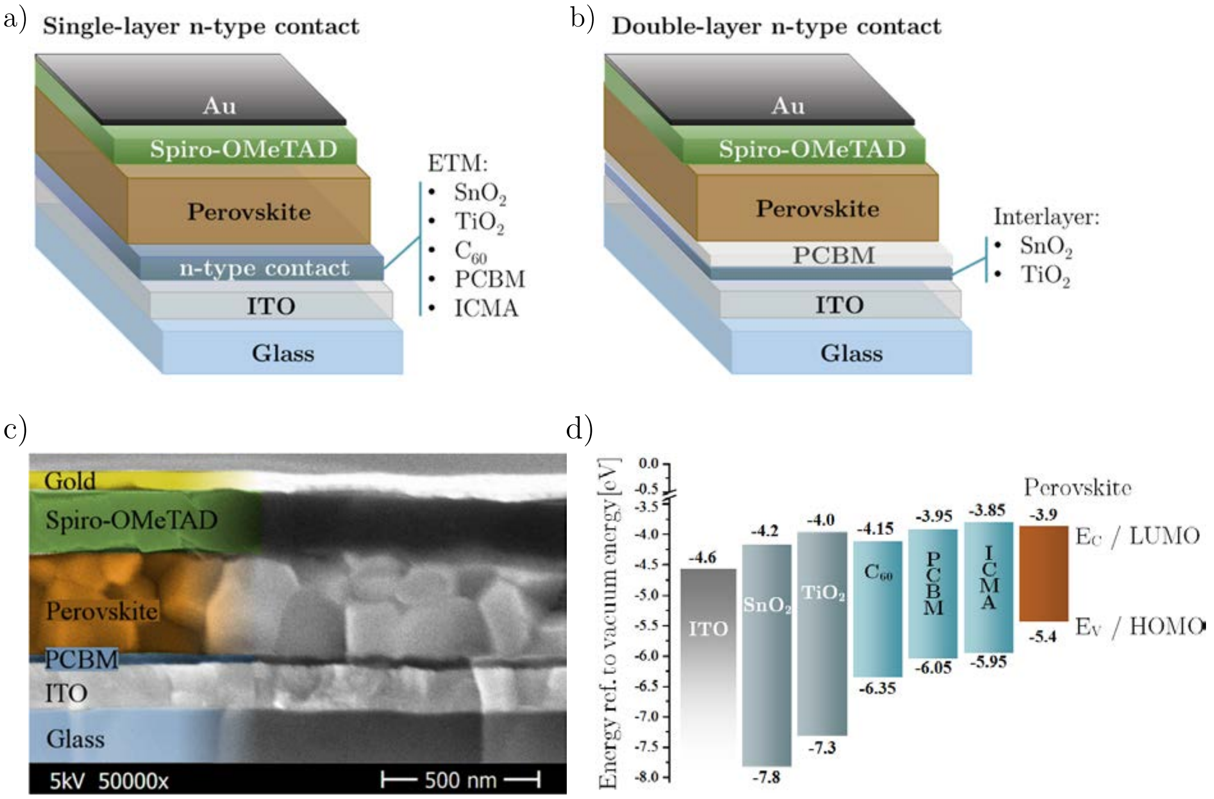

Figure 4.1: Schematic illustration of the device architecture with a) single-layer and b) double-layer electron contact structure. c) SEM cross section image of a perovskite solar cell with PCBM as single-layer electron transport material (ETM). d) Energy level scheme of the studied materials. Valence band (E_V) and HOMO energies were determined by UPS, conduction band (E_C) and LUMO levels are estimated by subtracting reported band gap values from the measured E_V or HOMO data.[161–164] Perovskite energy levels were obtained from literature.[166]

A scanning electron microscope (SEM) image presented in Figure 4.1 c) shows the cross section of a representative perovskite solar cell used in this study with a single-layer electron contact of PCBM. The device stack of ITO/PCBM/$CH_3NH_3PbI_3$/Spiro-OMeTAD/gold is clearly distinguishable with layer thicknesses around 150 nm, 30-40 nm, 350 nm, 200 nm and 80 nm, respectively. It can also be seen that most grains of the perovskite absorbers do not span the complete film thickness and horizontal grain boundaries are visible. The layer thicknesses of PCBM and all other ETMs used in this study have been optimized for the single-layer ETM design towards good surface coverage and minimum series resistance. These optimized thicknesses were then used in the single- as well as in the double-layer electron contact design in order to maintain the electro-optical properties of each layer and provide good comparability of the different device structures.

As described in chapter 2.1.2, an electron transport material has to efficiently extract electrons and block holes from a photoactive absorber to be highly selective. To identify the positions of the respective energy levels of the valence bands (E_V) and highest occupied molecular orbitals (HOMO), ultraviolet photoelectron spectroscopy (UPS) was applied here. The respective energies of the conduction bands (E_C) and lowest unoccupied molecular orbitals (LUMO) were approximated by subtracting reported band gap energies of the materials from the E_V/HOMO values.[161–164] The results are depicted in Figure 4.1 d) along with energy levels of $CH_3NH_3PbI_3$ obtained from literature.[166]

As displayed in Figure 4.1 d), the ETMs used in this study provide a diverse range of energy levels. The wide band gap metal oxides have an around 2 eV larger ionization energy than the perovskite absorber which should lead to distinct extraction barriers for holes at the interface. Fullerenes on the other hand have more than 1 eV lower ionization energies than the metal oxides and therefore also the hole blocking probability should be notably decreased as compared to the metal oxides. This is in line with other reports suggesting reduced selectivity of perovskite/fullerene heterocontacts.[113] The approximated electron affinities of the ETMs as displayed in Figure 4.1 d) are graduated over around 300 meV between -3.85 to -4.2 eV. A 200 meV difference in E_C values is distinguishable between the metal oxides SnO_2 and TiO_2, which can have significant influence on the device performance.[161] Besides, two of the fullerenes used in this study have comparable electron affinities as the two metal oxides, namely C_{60} (-4.15 eV towards -4.2 eV of SnO_2) as well as PCBM (-3.95 eV towards -4.0 eV of TiO_2). All aforementioned materials are supposed to have higher electron affinities than the perovskite absorber and should therefore not have energetic barriers for electrons being extracted from the perovskite into the ETM. ICMA however has the lowest electron affinity of approximately -3.85 eV which could induce a small electron extraction barrier when interfacing the perovskite. ICMA therefore seems to be less suitable as an ETM for perovskite solar cells but the exact band alignment at the perovskite interface remains unclear. Besides, it provides the potential to support previous reports that charge extraction barriers lead to not only reduced efficiency but also increased hysteresis in planar perovskite solar cells.[161]

Additionally, the energy levels for the double-layer ETM architecture were analyzed. UPS measurements revealed no substantial differences with only 50 meV higher ionization energies for PCBM layers deposited on TiO_2/SnO_2 (double-layer ETM) compared to PCBM on ITO (single-layer ETM) (Table S1 in the appendix, chapter 7.1). Therefore we suppose that any changes in device performance between the PCBM single and the TiO_2/PCBM double-layer are not significantly affected by energy level differences.

The numerous ETMs used in this study thus cover a wide range of material and surface properties. When comparing solar cells made on different ETMs, it has to be considered that topography and chemical properties of the underlying surface can significantly influence the perovskite absorber grown on top.[147] The "One-Step" deposition method used here with anti-solvent drip during spin coating first leads to a transparent intermediate phase layer. Perovskite nuclei are formed in the bulk or the surface of this preliminary film or at the ETM/film interface and grains afterwards grow from these nuclei during thermal annealing.[251] Differences in the surface roughness or the chemical properties of the underlying layer usually change the interfacial energies and thereby the nucleation dynamics on top of it.

Changes in the surface energies also influence the wetting properties and contact angles of the precursor solution on the substrate. The polar perovskite precursor solution used here showed good wetting properties with small contact angles on top of the polar metal oxide surfaces, but significantly larger values on the non-polar fullerenes PCBM and ICMA (see Figure S2 in the appendix, chapter 7.1). The contact angle on the evaporated C_{60} was considerably smaller than on the aforementioned spin coated fullerene derivatives which might be related to the different deposition method or the distinctly higher root-mean-square surface roughness of around 16 nm for C_{60} versus 4 nm for PCBM (Table S 2).

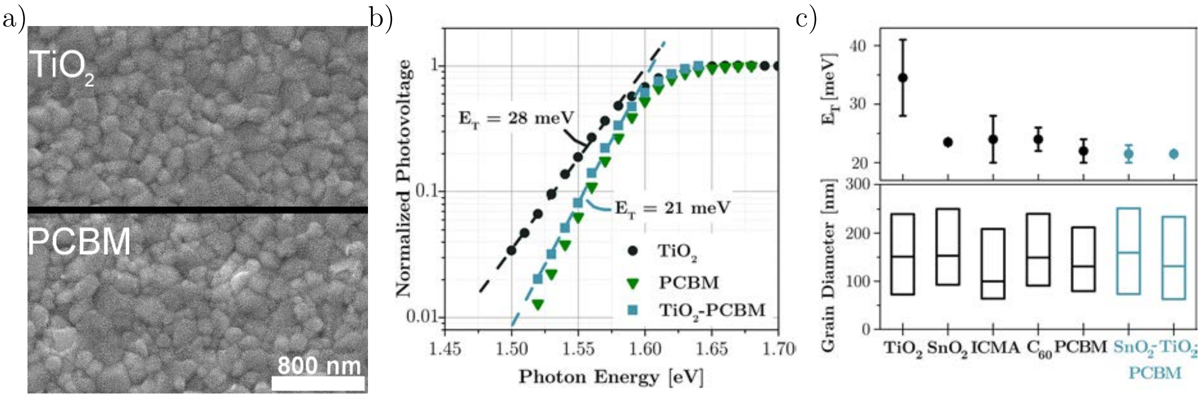

Figure 4.2: a) Top view scanning electron microscopy (SEM) images of perovskite absorbers on substrates coated with TiO_2 (top) and PCBM (bottom). b) Surface photovoltage (SPV) spectra and fits to the tail slope parameter E_T of perovskite absorbers on substrates with TiO_2 and PCBM single- as well as TiO_2/PCBM double-layer electron transport material (ETM). c) Top panel: tail slope parameter E_T from SPV measurements of perovskite absorbers grown on different ETM coated substrates. The error bar is defined by the standard deviation. Bottom panel: box plot diagram of the grain size distribution for perovskite surfaces on different underlying ETM determined from SEM micrographs.

Despite these large differences in contact angles and thereby interfacial energies, SEM top view images of annealed perovskite absorber surfaces on the various ETMs did not show significant differences in grain sizes as exemplarily shown in Figure 4.2 a) for TiO_2 and PCBM coated substrates. The grain size distribution from these top view images is depicted as a box plot in the lower panel of Figure 4.2 c), revealing an average perovskite grain diameter for all samples of around 150 nm with slightly lower values for ICMA based devices. Besides that, SEM cross section images revealed a prominent appearance of horizontal grain boundaries as described before. Note that solar cell efficiencies above 20% have been demonstrated for evaporated perovskite layers with even smaller grains by elaborate contact optimization.[150] Both, the unaffected grain size when being processed on different ETMs and the appearance of horizontal grain boundaries, indicate that a significant amount of perovskite nuclei are formed not at the ETM surface but within the bulk or at the surface of the intermediate phase film. The nucleation dynamics on the ETM surface thus seem to only partially contribute to the overall film formation. This finding is supported by previous reports, showing that an anti-solvent treatment can induce crystallization at the surface of a precursor liquid.[252] Therefore the perovskite film formation protocol applied here is highly useful for studying the differences in device performance when using different ETMs as the coarse film morphology seems to be independent of the specific ETM used.

In order to characterize the absorber quality in more detail, surface photovoltage (SPV) measurements were performed to determine the electronic disorder of perovskite layers on different ETMs. Disorder in an absorber causes exponential tails in the absorption spectra appearing near the band gap energy. The tail slope parameter E_T is used to characterize these exponential tails. Small E_T values indicate higher electrically ordered absorbers with low sub-bandgap trap densities near the band edge and therefore reduced recombination losses which is in general beneficial for the device performance. In order to compare the quality of the absorber deposited on the different ETMs, E_T was measured for several batches of perovskite layers on glass/ITO/ETM substrates by spectral dependent modulated SPV measurements.

As an example, Figure 4.2 b) shows the spectra of the modulated photovoltage amplitude for perovskite layers on a TiO_2 and a PCBM single- as well as on a TiO_2/PCBM double-layer ETM. The values of E_T amounted to 28, 20 and 21 meV, respectively. The mean tail slope parameters averaged over typically 3 samples each for perovskite layers on every ETM are depicted in Figure 4.2 c). Excluding the samples on TiO_2, average E_T values ranged between 22 and 24 meV and lowest values for each ETM of around 20 meV were achieved. Perovskites coated onTiO_2 showed higher values of the tail slope parameter with an average and lowest E_T of 35 and 28 meV, respectively. Therefore, the electronic disorder was comparable if the perovskite was coated onto PCBM, irrespective of the presence of an additional TiO_2 layer in between ITO and the fullerene. However, the relatively large value of E_T for $CH_3NH_3PbI_3$ deposited on TiO_2 indicates a substantial density of shallow traps at the interface, possibly in the TiO_2, which allows excitation of charge carriers from the perovskite valence band into TiO_2 defect states at the interface.

Summarizing the UPS, SEM and SPV data highly diverse material properties and energy levels of the used ETMs but rather similar perovskite absorbers on top were shown, as the coarse morphology and the perovskite tail slope parameters E_T (despite for bare TiO_2 samples) were found to be comparable. Because also the remaining top contact layers of the solar cells are identical, we can correlate differences in solar cell parameters to variations of the ETM. Hence, transient photoluminescence (TRPL) measurements were utilized to study the charge carrier dynamics for perovskite solar cells with different ETMs in the single- and double-layer design. The TRPL signal stems from radiative recombination of excited charge carriers in the absorber and can therefore be quenched by either efficient charge extraction from the perovskite or increased non-radiative recombination within the absorber and at its interfaces as introduced in chapter 2.1.2.

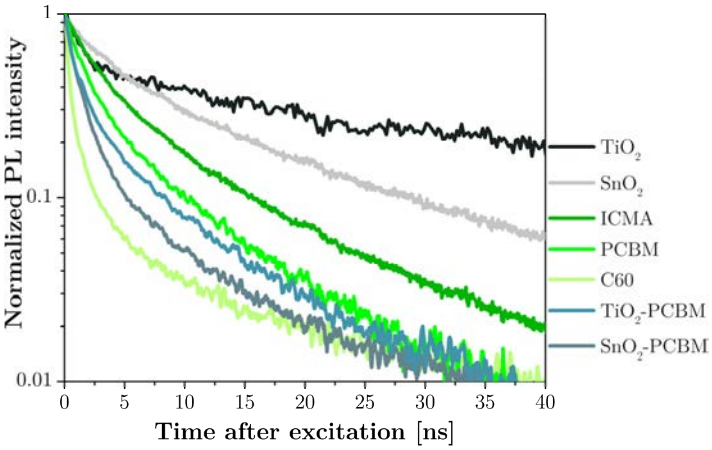

Figure 4.3: Normalized transient photoluminescence (TRPL) decays for perovskite solar cells with different electron transport materials (ETMs) measured without applying external bias.

As shown in Figure 4.3, fullerene ETM layers quench the photoluminescence signal stronger than metal oxide interfaces, which is in agreement to previous reports that C_{60} and its derivatives provide good electronic coupling to and efficient electron transfer from perovskite absorbers.[172, 253] As mentioned before, poor charge extraction of TiO_2 on the other hand was suggested elsewhere[157] and seems to be confirmed by the slow decline of the corresponding TRPL signal in Figure 4.3 (black line). However, TRPL decay might not be sufficient to identify charge extraction, as non-radiative interface recombination attenuates the signal similarly.

Interestingly, within the fullerenes as well as within the metal oxides, the TRPL decay seems to be faster for higher electron affinities of the ETM, cf. Figure 4.1 d). SnO_2 for example shows a faster TRPL decay and has a higher electron affinity by around 200 meV than TiO_2. Also within the group of fullerenes, C_{60} with the highest and ICMA with the lowest electron affinity exhibited the strongest and weakest TRPL quenching, respectively. Lower lying LUMOs or conduction bands of the ETMs might lead to stronger electrostatic driving forces for charge extraction at the interface to the perovskite absorber.

When progressing from the PCBM only to the double-layer ETM architecture, a comparable decay was observed for a TiO_2 interlayer and a slightly faster one for SnO_2. The stronger quenching for the latter device design is interesting, as UPS measurements did not reveal significant deviations in the energetics of PCBM only, SnO_2/PCBM or TiO_2/PCBM surfaces (Table S1) and also the electronic coupling to the perovskite should be in all three cases dominated by PCBM molecules.

However, different structural ordering of the PCBM molecules when being processed either directly on ITO or on ITO/TiO_2 cannot be excluded, and this could influence the device performance. Still, no significant differences in charge extraction properties are indicated by TRPL for the double-layer compared to the PCBM single-layer ETM design.

To further characterize the influence of the distinct ETMs on device characteristics, the electrical properties of perovskite solar cells are examined. More than 90 different devices were prepared and investigated in multiple batches over several weeks to achieve reliable trends and avoid stochastic variations by hidden or hardly controllable process parameters, such as the chemical composition or the temperature and humidity of the atmosphere during preparation. Current density-voltage (J-V) scans and maximum power point (MPP) tracking measurements of the devices under illumination were performed and the results are shown in Figure 4.4 a)-c).

J-V characteristics under illumination in forward ($V_{Start}<V_{End}$) and reverse ($V_{Start}>V_{End}$) scan direction are exemplarily shown in Figure 4.4 a) for devices based on TiO_2 and PCBM single- as well as TiO_2/PCBM double-layer ETMs. The maximum power point (MPP) after 60 s of MPP tracking measurements for each sample is also depicted. Note that the kinks partially observed in the forward J-V curves at current densities around 6 mA/cm^2 are an artifact from the autorange mode of the measurement source meter and are discussed in more detail in the appendix, chapter 7.1. The devices displayed are representative for the according ETM design as they possessed J-V parameters close to the respective average values. A significant reduction of photocurrent hysteresis and improved stabilized efficiency is observed when replacing TiO_2 with PCBM and even more for the double-layer contact design of the two materials. Also the champion device of this study depicted in Figure 4.4 b) was achieved on the TiO_2/PCBM double-layer ETM. The inset shows the MPP tracking measurement with the power output stabilizing at 18.0% within seconds and retaining this efficiency for minutes. The average device parameters under illumination for all ETMs used in this study are displayed in Figure 4.4 c) and are presented together with the champion device parameters in Table 4.1.

Figure 4.4 c) shows the power conversion efficiency (PCE) averaged separately for reverse and forward scans over all samples at 1666 mV/s sweep rate with circles marking the power output after 60 s of MPP tracking. The data points are averaged over at least 10 devices per ETM. Regarding the single-layer structure, it can clearly be seen that the metal oxide ETM solar cells show high efficiencies between 14 and 16% in the reverse scans only, with very moderate values below 9% when measured in forward direction. During MPP tracking, the PCE adversely approaches the one of the forward scan and drops to an average of 7.0 and 10.5% for TiO_2 and SnO_2 based devices respectively. This is in agreement to previous reports, showing a continuous decline in the photocurrent transients for planar perovskite solar cells with TiO_2 or SnO_2 ETMs.[161, 172]

Devices with fullerene single-layer ETMs on the other hand show lower PCEs in the reverse scan than the metal oxides but the power output stabilizes closer to the MPP of the backward than of the forward sweep. ICMA based samples provided an average PCE after 60 s MPP-tracking of 11.9%, devices incorporating C_{60} and PCBM gave the best efficiencies for the single-layer structures at 12.9 and 12.7%, respectively. The results shown here reiterate, that MPP tracking is one of the most reliable ways to truly compare device performances. Interestingly, the standard deviations of the J-V characteristics for solar cells with TiO_2 are comparable to devices with other ETMs. The large spread of E_T values observed in SPV is therefore not reflected in a wide variance of device performances. Yet, the trap density of TiO_2 at the perovskite interface, which can also influence E_T as discussed before, was shown to have minor effects on the solar cell parameters.[157] The high standard deviation of E_T might therefore also be related to variations of the trap densities at the TiO_2 layer surfaces.

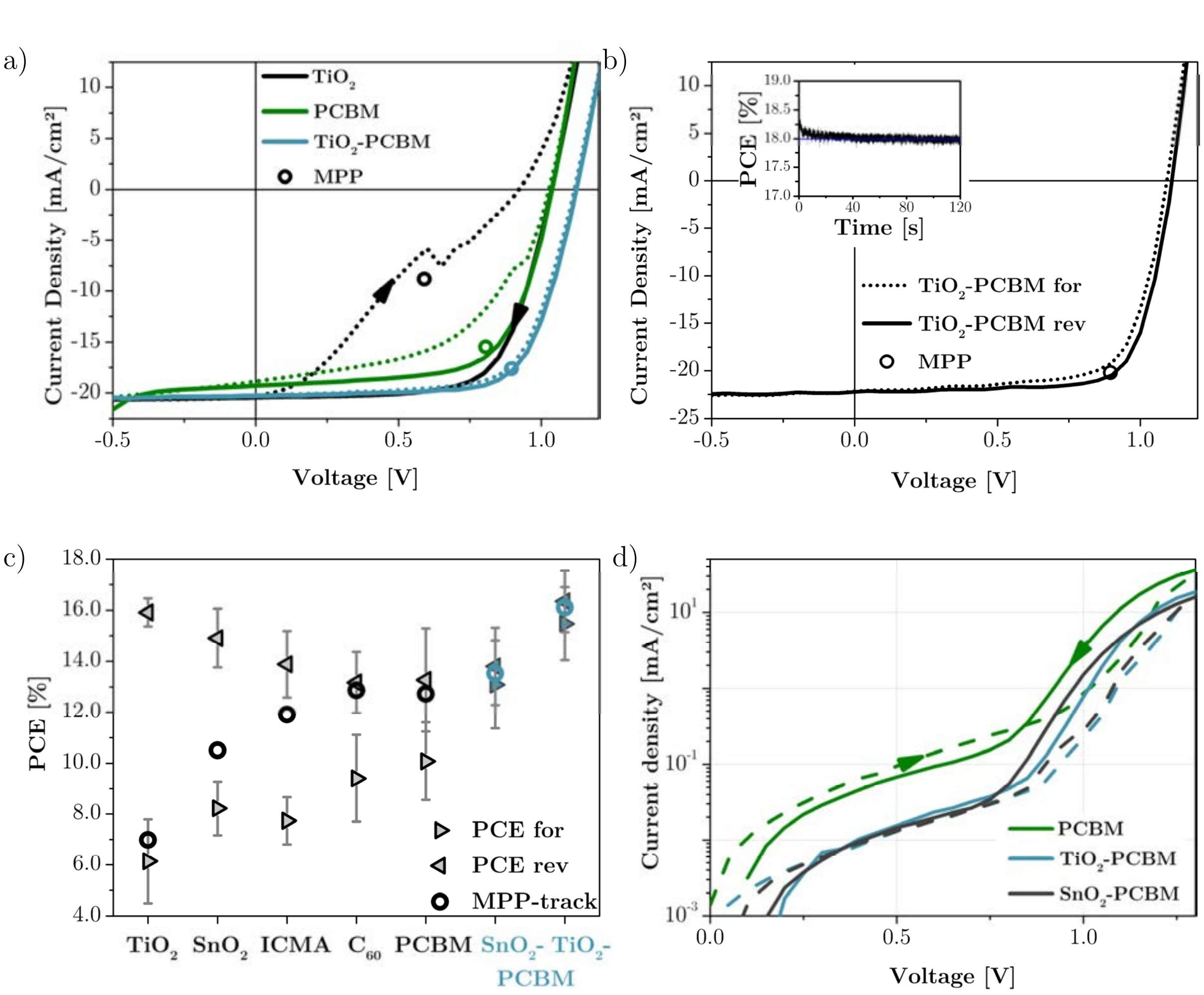

Figure 4.4: a) Current-voltage characteristics under illumination for perovskite solar cells with TiO_2 and PCBM single- as well as the corresponding TiO_2/PCBM double-layer ETM structure at 1666 mV/s scan speed. Circles mark the maximum power point (MPP) after 60 s of MPP tracking measurements. The depicted devices possessed J-V parameters (J_{SC}, FF, V_{OC}, H) close to the respective average values. b) Champion device current voltage characteristics measured under illumination at 1666 mV/s scan speed with 0.1 cm²aperture mask using a TiO_2/PCBM double-layer ETM. The inset shows the power conversion efficiency (PCE) during MPP tracking with the circle marking the corresponding stabilized MPP in the J-V-plot. c) Efficiency calculated from the forward and reverse scans at 1666 mV/s scan rate as well as after 60 s of MPP tracking measurements for perovskite solar cells under illumination with different ETMs averaged over all devices. d) Current voltage characteristics in the dark for perovskite solar cells with PCBM single- as well as the TiO_2/PCBM or SnO_2/PCBM double-layer ETM structure at 1666 mV/s scan speed.

When comparing solar cells with double- and PCBM single-layer ETM design, it can be seen that a SnO_2 interlayer only slightly improved the average efficiencies after 60 s of MPP-tracking to 13.5%. On the contrary, TiO_2 based double-layers significantly boosted the PCE to 16.1% averaged over 16 devices and up to 18.0% for the champion device of this study. The TiO_2 interlayer improved all device parameters (J_{SC}, FF, V_{OC}), whereas the SnO_2/PCBM based devices only showed higher J_{SC} but comparable FF in the reverse scan and even lower V_{OC} values as compared to the PCBM single-layer solar cells (Table 4.1). Comparing the solar cells with double-layer ETMs to their respective metal oxide single-layer equivalents clearly reveals a stabilization of the power and an improved efficiency during MPP tracking by the interfacial fullerene layer.

These observations are completely in line to previous reports showing enhanced and more stable solar cell efficiencies by interface modifications of metal oxide ETMs with fullerenes.[156, 172] However, the study presented here also puts the two different double-layer electron contacts in contrast with each other, revealing the aforementioned improved device parameters with TiO_2/PCBM as compared to SnO_2/PCBM electron contacts.

One enhancement of the double-layer ETM design is an increase in the shunt resistance of the device as shown by the reduced current density at low voltages in dark J-V scans as depicted exemplarily in Figure 4.4 d). It is reasonable to assume that the inserted metal oxide layer hampers direct contact between the perovskite absorber and the ITO electrode through pinholes in the PCBM layer. Additionally, as the wide band gap metal oxides have significantly higher ionization potentials than the fullerenes, they might support the hole blocking properties and increase the selectivity of the electron contact in the double-layer architecture.

Although the aforementioned arguments are applicable for both metal oxides, significant improvements in efficiency were only obtained for TiO_2 interlayers. As the electron affinities of TiO_2 and PCBM are comparable (Figure 4.1 d), the resultant double-layer structure potentially forms an energetically more favorable contact than the SnO_2/PCBM double- or ITO/PCBM single-layer ETM design. This would result in reduced recombination losses and improved charge extraction which is in agreement to the enhanced V_{OC}, FF and J_{SC} values of the TiO_2/PCBM devices as compared to not only the PCBM single- but also the SnO_2 double-layer structure (Table 4.1).

For a more detailed analysis of transient effects, the hysteresis index H of each current density-voltage (J-V) scan given by equation (4.1) is calculated following a reported approach[254], where $J_{for}(V)$ and $J_{rev}(V)$ are the current densities during forward and reverse sweep respectively.

$$H = \frac{\int_0^{V_{oc}} J_{rev}(V)dV - \int_0^{V_{oc}} J_{for}(V)dV}{\int_0^{V_{oc}} J_{rev}(V)dV} \tag{4.1}$$

It has been shown that hysteresis can be governed by multiple transient processes occurring on different timescales and thus strongly depends on the sweep rate, or more accurately the delay time, of the current-voltage scan.[180] We therefore determined the hysteresis index for a range of sweep rates from 277 to 2500 mV/s to provide better insights into the hysteretic dynamics of the different architectures used here.

The H indices for each single and double-layer ETM and scan speed shown in Figure 4.5 present the average values over at least 10 devices of the respective contact design. It can clearly be seen that a simple comparison of this index at one sweep rate is not informative. At the fastest scan speed for example, devices with a TiO_2 single-layer show less hysteresis than those with PCBM while it is vice versa for the slowest sweep rate. The comparison of H indices over a broader range of measurement speeds on the other hand captures significant deviations in the dynamics of the hysteresis between samples with metal oxide and fullerene single-layer ETMs. A strong hysteresis effect at slow scan speeds declining for faster sweep rates can be observed for devices with metal oxide ETMs while the fullerene based solar cells in contrast show the smallest hysteresis at 277 mV/s sweeps and an increase of the hysteretic response with higher sweep rates.

As explained in chapter 2.2.3, J-V hysteresis occurring within seconds has been attributed before to capacitive charging-discharging effects. These capacitive hysteresis effects thus in principle increase with the capacitance of the device and the scan speed. Yet, if the J-V sweep rate is too fast for the charging processes, hysteresis diminishes again with increased scan speeds as the response limit of the device capacitance is reached.[185]

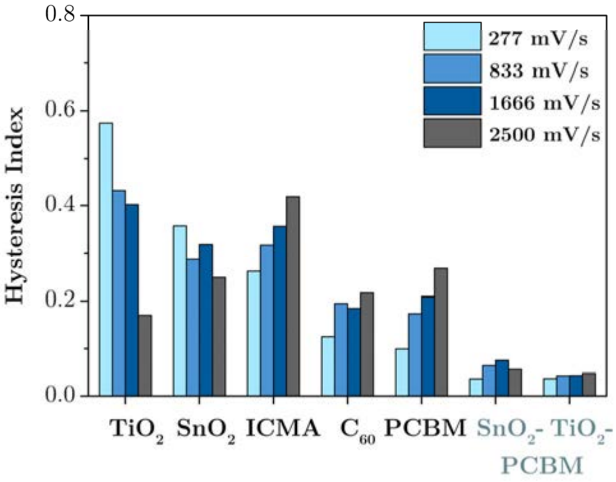

Figure 4.5: Hysteresis index (equation 1) calculated for different scan rates and averaged over all devices (typically ≥10) of the respective ETM.

The results shown in Figure 4.5 indicate that pronounced hysteresis occurs on much longer timescales for devices with metal oxide ETMs and the underlying processes are too slow to respond to the faster scan speeds. Slow processes are also observed for these devices during MPP tracking measurements, where the power output does not reach a stable value even after several minutes (see inset in Figure S3 a). It is unclear though if the same slow process is the origin of both transient behaviors observed or if there are multiple interplaying phenomena. For solar cells incorporating fullerenes on the other hand, the increase of H with the scan speed reveals much faster hysteresis that can still respond at the highest sweep rate performed here. The devices also reached a stable PCE within seconds and showed no significant reduction in efficiency over several minutes of MPP tracking (see inset in Figure S3 b).

Assuming that the longer PL lifetime originates in slow charge extraction of the metal oxide ETMs it is supposed to result in a large device capacitance due to increased electron accumulation at the ETM/perovskite interface. This is consistent with the response limit of the hysteresis processes being at slower scan speeds compared to devices incorporating fullerene ETMs with better charge extraction properties and therefore potentially lower capacitance values.[185] Also when comparing the magnitude of the hysteresis in the studied scan range for the fullerene ETMs, solar cells with C_{60} and ICMA electron contacts with the fastest/slowest charge extraction implied by TRPL also show the lowest/highest H values respectively.

Moreover as mentioned before, fullerenes are supposed to passivate defect states at the perovskite interface.[187] Previous reports even suggest that fullerenes can diffuse along the absorber grain boundaries, thereby passivating further defects and hampering ion migration.[255] As a result, charge recombination and interfacial ion accumulation is reduced, leading to further minimized capacitive effects and hysteresis. This is also in agreement to the stable power output over minutes during MPP tracking of devices with fullerene ETMs, revealing negligible interface modifications by slow processes such as slow ion migration.[185] However, the still apparent hysteresis at fast scan speeds is in contrast to the case of *p-i-n* devices incorporating fullerene electron contacts, which often show negligible current-voltage hysteresis.[155, 251] One possible explanation for this discrepancy could be the reduced contact area in a planar *n-i-p* compared to the *p-i-n* structure where PCBM is suspected to penetrate deeper into the perovskite absorber through pinholes and grain boundaries during processing,[183] which can even lead to graded heterojunction interfaces between perovskite and PCBM.[256]

In comparison, the double-layer ETM structures show strongly differing transient properties as compared to the metal oxide or fullerene single-layer devices. The magnitude of the hysteresis index in the studied scan speed range is dramatically reduced when the double-layer is utilized. Additionally, the dependence of H on the sweep rate is significantly smaller and hardly observable for solar cells incorporating TiO_2/PCBM electron contacts. Also during MPP-tracking, the power output stabilizes quickly and retains a high efficiency throughout the measurements (see inset in Figure S3 c)).

A reduction of the device capacitance was shown already by impedance spectral analysis for solar cells with TiO_2/PCBM compared to PCBM only electron contacts.[156] This observation seems to be confirmed here also for devices incorporating SnO_2/PCBM ETMs, as hysteresis is significantly reduced for all solar cells with double-layer ETM structure. However, TRPL decays did not imply significant differences in the charge extraction dynamics for the PCBM single- and the double-layer ETM devices. Also the interfacial fullerene passivation effects discussed before are supposed to be similar for these solar cells.

Instead, the improved shunt resistance of the double-layer ETM solar cells shown before reduces recombination losses at the perovskite interface. As charge recombination at the interface can amplify hysteresis, as explained in chapter 2.2.3, the suppressed transient effects in double-layer ETM devices can at least partially be attributed to the reduced losses over shunt paths. Interestingly, hysteresis is strongly suppressed for both double-layer ETMs as compared to the PCBM single-layer ETMs, although only the TiO_2/PCBM contact structure enables a significant improvement in solar cell efficiency. Still, as the shunt resistance is improved for both double-layer ETMs, the recombination losses limiting the efficiency of the SnO_2/PCBM based devices seem to occur not at the perovskite interface, but across the electron contact e.g. at the ITO/SnO_2 interface or within the SnO_2 layer. As these recombination losses presumably not influence the perovskite interface directly, they are also not supposed to contribute to hysteresis processes in the active layer. Indeed we have previously identified larger hysteresis on ITO/SnO_2 as compared to FTO/SnO_2 contacts in planar perovskite solar cells, indicating the electron extraction across the ITO/SnO_2 interface might be limited.[21]

Table 4.1: Parameters extracted from current voltage characteristics under illumination including standard deviations corresponding to Figure 4.4 b) and c) averaged over at least 10 devices per electron transport material (ETM) measured at 1666 mV/s scan speed in forward and reverse scan direction together with the stabilized power output from maximum power point (MPP) tracking after 60 seconds (PCE_{MPP}).

ETM	*Scan Dir.*	*J_{SC} [mA/cm^2]*	*FF [%]*	*V_{OC} [V]*	*PCE [%]*	*PCE_{MPP} [%]*
TiO_2	Forward	22.1 ± 0.6	29.5 ± 7.2	0.94 ± 0.04	6.1 ± 1.6	7.0 ± 1.8
	Reverse	22.3 ± 0.6	67.8 ± 1.4	1.05 ± 0.01	15.9 ± 0.5	
SnO_2	Forward	21.9 ± 0.8	37.3 ± 4.3	1.01 ± 0.07	8.2 ± 1.1	10.5 ± 0.9
	Reverse	22.2 ± 0.9	62.4 ± 4.7	1.08 ± 0.03	14.9 ± 1.2	
ICMA	Forward	18.7 ± 1.5	40.4 ± 5.8	1.03 ± 0.03	7.7 ± 0.9	11.9 ± 0.9
	Reverse	20.0 ± 1.2	64.7 ± 2.5	1.07 ± 0.02	13.9 ± 1.3	
C_{60}	Forward	19.4 ± 1.2	47.3 ± 8.3	1.03 ± 0.04	9.4 ± 1.7	12.9 ± 1.2
	Reverse	19.9 ± 1.3	62.9 ± 4.1	1.05 ± 0.02	13.2 ± 1.2	
PCBM	Forward	18.4 ± 1.9	51.5 ± 7.1	1.07 ± 0.03	10.1 ± 1.5	12.7 ± 1.8
	Reverse	19.0 ± 2.1	64.6 ± 3.6	1.08 ± 0.04	13.3 ± 2.0	
SnO_2 - PCBM	Forward	20.1 ± 1.1	62.1 ± 5.3	1.04 ± 0.05	13.1 ± 1.7	13.5 ± 1.6
	Reverse	20.3 ± 1.1	64.7 ± 3.3	1.04 ± 0.04	13.8 ± 1.5	
TiO_2 - PCBM	Forward	21.4 ± 1.2	65.5 ± 4.3	1.10 ± 0.03	15.4 ± 1.5	16.1 ± 1.1
	Reverse	21.5 ± 1.0	68.5 ± 2.4	1.11 ± 0.03	16.4 ± 1.3	
TiO_2-PCBM champion[1]	Forward	22.17	71.4	1.09	17.3	18.0
	Reverse	22.23	74.6	1.11	18.4	

[1] measured with 0.1 cm^2 aperture mask.

4.1.3 Conclusions

In summary, the perovskite properties and device performances have been analyzed in planar *n-i-p* type perovskite solar cells for a variety of different electron selective contacts including single- and double-layer electron transport materials (ETM). The metal oxides TiO_2 and SnO_2 as well as fullerene derivatives such as C_{60}, PCBM and ICMA were utilized. Furthermore, the contact structure was extended to a double-layer design with a metal oxide/PCBM stack as ETM. Scanning electron microscopy (SEM) images showed that the used perovskite fabrication process results in absorber layers with rather similar grain growth. In line to that, surface photovoltage measurements indicated comparable absorber qualities on all ETMs except TiO_2 where a strong influence of defect states was observed. On this basis, we could directly correlate the device performance and photocurrent hysteresis over a broad range of scan speeds to the ETM and its contact properties. When comparing fullerene to metal oxide ETM based devices, transient photoluminescence studies implied faster charge extraction and current-voltage (J-V) measurements revealed less pronounced hysteresis and better performances. However, only double-layer ETM structures lead to negligible photocurrent hysteresis and highest device efficiencies. A champion stabilized PCE of 18.0% was achieved by the combination of TiO_2 and PCBM as electron contact. J-V measurements indicate strongly reduced recombination losses for the TiO_2/PCBM contact design and we surmise multiple causes for these effects, as summarized in Figure 4.6: (I) reduction of shunt paths through the fullerene to the ITO layer, (II) improved hole blocking by the additional wide band-gap metal oxide and (III) decreased charge transport losses due to an energetically more favorable contact. The latter arguments are supported by photoelectron spectroscopy measurements. The demonstrated improvements are independent of the contact polarity or the architecture. This implies that double-layer or even multi-layer selective contacts could be a general design guideline for perovskite solar cells.

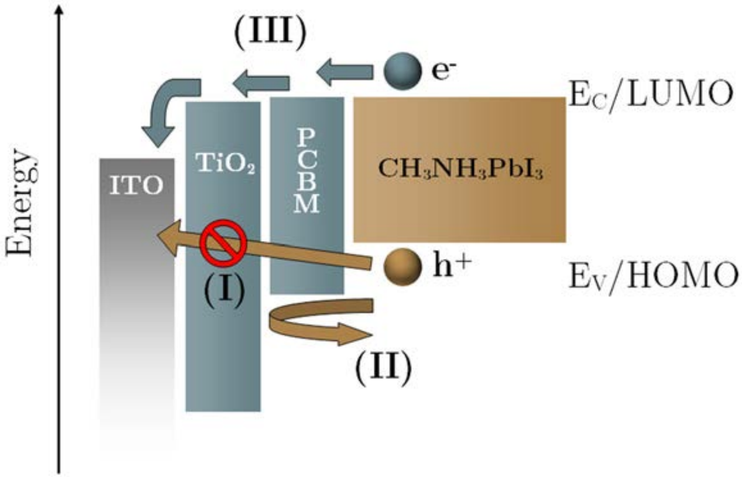

Figure 4.6: Schematic illustration of beneficial effects on charge extraction by the TiO_2 layer in TiO_2/PCBM double-layer electron contacts: (I) reduction of shunt paths through the PCBM, (II) improved hole blocking and (III) decreased charge transport losses due to an energetically more favorable contact to the ITO electrode. E_{VAC}, E_C, E_V, LUMO and HOMO denote vacuum energy level, conduction and valence band energies as well as lowest unoccupied and highest occupied molecular orbital, respectively.

4.2 Mixtures of PEDOT and Spiro-OMeTAD as Novel, Passivating Hole Contact

This chapter has been published as a peer-reviewed article under the title: "Mixtures of Dopant-Free Spiro-OMeTAD and Water-Free PEDOT as a Passivating Hole Contact in Perovskite Solar Cells" by Lukas Kegelmann, P. Tockhorn, C. M. Wolff, J. A. Márquez, L. Korte, T. Unold, W. Lövenich, D. Neher, B. Rech and S. Albrecht in ACS Applied Materials&Interfaces (2019), vol. 11 (9), pp. 9172–9181.

Mixtures of pristine Spiro-OMeTAD and water-free, pH-neutral PEDOT, doped with a sulfonated co-polymer, are introduced in this study as a novel hole selective contact for planar *n-i-p* type perovskite solar cells. The combination of the two contact materials provides a dual function for device operation: 1) selective hole extraction and 2) suppression of non-radiative recombination losses at the perovskite/hole contact surface.

PEDOT thereby not only provides sufficient conductivity in the mixed hole contact but also serves as a surface passivation layer at the perovskite interface. The sulfurous polymers might thereby chemically passivate vacancies at the perovskite surface by formation of S-Pb bonds. Yet, despite its comparably high conductivity, hole extraction of PEDOT from the perovskite absorber is rather poor. This presumably relates to an enrichment of the insulating co-polymer, used to dope the PEDOT, at the absorber interface. Adding Spiro-OMeTAD to the PEDOT layer instead substantially enhances hole extraction from the absorber while maintaining suppressed surface-recombination losses by the PEDOT.

As a result, the quasi-Fermi level splitting in the perovskite absorber is increased from 1.22 eV without hole contact to 1.24 eV with mixed PEDOT/Spiro-OMeTAD layers atop. This effect is outstanding for contact layers in perovskite photovoltaics, which generally enhance surface recombination losses.[29, 30, 113] It allows high V_{OC} values up to 1.19 V and stabilized efficiencies up to 16.8% for devices comprising the mixed hole contact, thereby outperforming solar cells with the standardly used doped Spiro-OMeTAD as *p*-type layer in the study.

4.2.1 Introduction

As discussed before, the impressive progress of organic-inorganic halide perovskite solar cells within the last few years is unparalleled in photovoltaic research. Concentration of research activities for this new material class raised the power conversion efficiencies (PCE) of this technology to above 22%.[9] However, highly-efficient perovskite solar cells already reach internal quantum efficiencies close to 100% and their fill factors (FF) are approaching the theoretical maximum.[106, 153, 224] Hence, the device parameter with the largest potential for further improvements is the open circuit voltage (V_{OC}).[106] It was shown before that surface recombination losses mainly govern the charge carrier lifetime in perovskite thin films and thus lower the V_{OC} in solar cells.[28, 257] Therefore, increasing efforts are made to mitigate surface recombination,[61, 117, 258–260] e.g. insertion of KI into the perovskite solution was shown to passivate surfaces and grain boundaries in the resulting absorbers and enabled solar cells with a record low potential loss between the band gap energy and $e \cdot V_{OC}$ of 0.39 eV.[117] Also blending passivating polymethyl methacrylate (PMMA) into the electron contact material in *n-i-p* type devices enabled to push the V_{OC} up to 1.18 V.[261]

For 2,2‘7,7‘-tetrakis(N,N-di-p-methoxyphenylamin)-9,9‘-spirobifluoren (Spiro-OMeTAD), which is the most commonly used hole transport material (HTM) in *n-i-p* type perovskite solar cells, high efficiencies around 22% were demonstrated.[26, 152] Yet, the dopants that are required to provide sufficient conductivity of Spiro-OMeTAD were found to act as charge recombination centers at the perovskite interface.[257] This alongside with dopant-accelerated degradation of perovskite solar cells[262, 263] and overall high material costs for Spiro-OMeTAD strongly motivated a pursuit for alternative HTMs.[264–267] Amongst them, poly (3, 4-ethylenedioxythiophene) (PEDOT) as an inexpensive, conductive and solution-producible HTM, being a frequently used HTM in organic PV[45] was employed in perovskite solar cells.[167, 268–271] For example, water-based poly (3, 4-ethylenedioxythiophene):polystyrene sulfonate (PEDOT:PSS) has been extensively used in the *p-i-n* architecture but the devices generally suffer from high surface recombination and thus low V_{OC} values.[106, 155, 272] As polar solvents degrade the perovskite absorber, water-free PEDOT formulations have been developed and utilized recently as HTM in *n-i-p* type solar cells allowing promising efficiencies up to 18.5% and V_{OC} values around 1.1 V.[268, 271]

Here, for the first time, mixtures of dopant-free Spiro-OMeTAD and water-free PEDOT are introduced as HTM in *n-i-p* structured perovskite solar cells. The approach aims to mitigate surface recombination induced by the dopants of Spiro-OMeTAD while maintaining sufficient conductivity via the conductive PEDOT. In addition, the required amount of the highly expensive Spiro-OMeTAD is drastically reduced and instead partially replaced by the cost-effective PEDOT polymer. The low temperature deposition further allows application in monolithic perovskite-silicon heterojunction tandem solar cells.

As discussed in detail in the following section, lateral conductivities of these mixed HTMs are found to be similar to the ones of doped Spiro-OMeTAD layers. The photoelectron spectroscopy studies reveal a superposition of states from both PEDOT and Spiro-OMeTAD at the intermixed thin film surfaces. Remarkably, transient and absolute photoluminescence measurements imply an enhanced charge carrier lifetime and quasi-Fermi level splitting when water-free PEDOT or mixtures with dopant-free Spiro-OMeTAD are coated on a bare perovskite absorber. This indicates suppressed surface recombination by the PEDOT and enables high V_{OC} values of up to

1.19 V in complete solar cells, thereby outclassing the open circuit voltages obtained for doped Spiro-OMeTAD as HTM in this study. Further, to the best of our knowledge, a V_{OC} of 1.19 V constitutes the lowest potential loss reported so far for perovskite solar cells utilizing PEDOT as HTM (around 410 mV open circuit voltage loss for an absorber bandgap of around 1.6 eV).[268, 273–275] Furthermore, the transient and absolute photoluminescence studies suggest that blending dopant-free Spiro-OMeTAD into the PEDOT enhances charge extraction at the perovskite interface while maintaining the surface passivation effect of the PEDOT. This is reflected in the resulting solar cells by increased fill factors and high stabilized efficiencies of up to 16.8%. The herein introduced mixtures of dopant-free Spiro-OMeTAD and water-free PEDOT therefore represent an efficient hole contact with intrinsic passivation effect at the perovskite interface which provides an exceptional feature as compared to the commonly used doped Spiro-OMeTAD.

4.2.2 Results and Discussion

To be applicable on the water- and PH-sensitive perovskite absorber, PEDOT and a sulfonated block-co-polymer as dopant were dispersed in anisole and pH-neutralized with butylamine. This water-free PEDOT formulation was provided by Heraeus. Additionally, 0 – 75 wt.-% of dopant-free Spiro-OMeTAD with respect to the total solid content mass of the resulting formulation was dissolved in the water-free PEDOT dispersion prior to deposition of the mixed HTMs.

Figure 4.7 a) depicts the complete layer stack of the herein prepared solar cells, comprising ITO/SnO_2/perovskite/HTM/Au, with the so-called “triple-cation” perovskite being $Cs_{0.05}(FA_{0.83}MA_{0.17})_{0.95}Pb(I_{0.83}Br_{0.17})_3$ as introduced by Saliba et al. (FA = formamidinium, $CH(NH_2)_2$; MA = methylammonium, CH_3NH_3).[152] The HTM in the layer stack is either pure water-free PEDOT, mixtures of dopant-free Spiro-OMeTAD and water-free PEDOT or as a reference system, Spiro-OMeTAD doped with 4-tert-butyl-pyridine, lithium bis(trifluoromethylsulphonyl) imide (Li-TFSI) and tris(bis(trifluoromethylsulfonyl)imide)) (FK209). The individual layers of an exemplary solar cell can be identified in the cross-section scanning electron microscopy image in Figure 4.7 b) with respective layer thicknesses of 150/30/550/100 nm for ITO/SnO_2/perovskite/mixture of 60 wt.-% dopant-free Spiro-OMeTAD and 40 wt.-% water-free PEDOT.

Note, that the excellent properties of TiO_2/PCBM the double layer ETM developed within the thesis and demonstrated in the previous chapter 4.1 cannot be utilized here. The underlying fullerene dissolves during processing of the “triple-cation” perovskite absorber which was chosen for the HySPRINT Innovation lab baseline after the work to chapter 4.1. finished. The “triple-cation” composition is more robust and does not employ high boiling point solvents such as γ-butyrolactone (GBL) that might interfere with other processes in the glove-box. However, it contains the solvent dimethyl formamide which dissolves fullerenes more efficiently. SnO_2 is therefore chosen as replacement because of its chemical resilience and better performance as compared to TiO_2 (c.f. chapter 4.1.2). Yet, during the period of this thesis, the solar cell FF was partially limited when employing SnO_2 as electron selective contact as further discussed below.

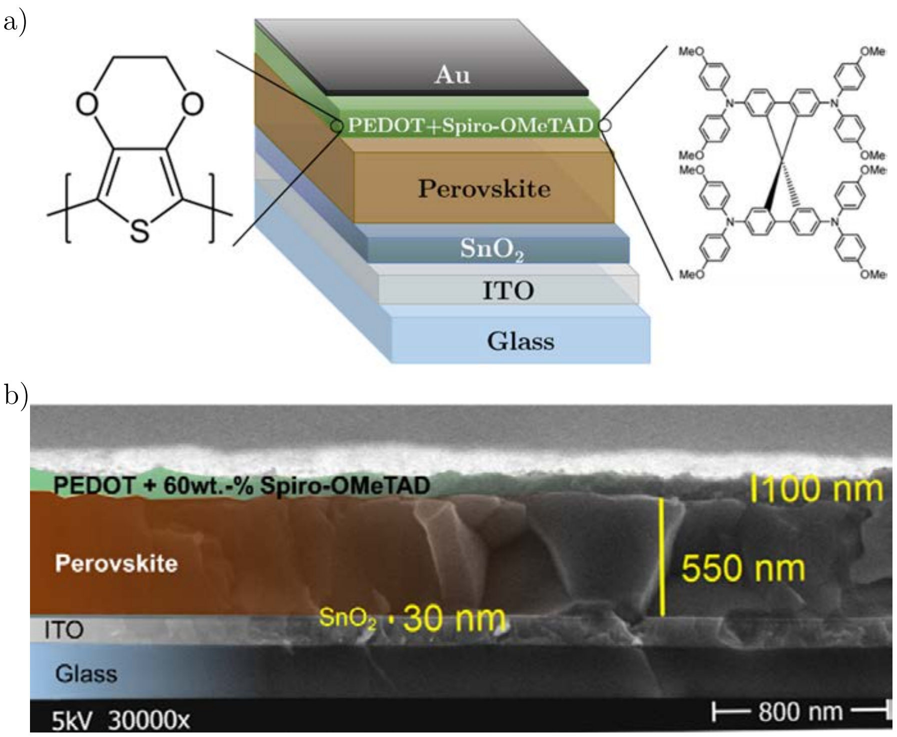

Figure 4.7: a) Schematic of the solar cell design used in this study as well as the chemical structures of PEDOT (left) and Spiro-OMeTAD (right). b) Cross-section scanning electron microscopy image of a solar cell produced here with 40:60 wt.-% PEDOT:Spiro-OMeTAD mixture as HTM.

All layers except the ITO and Au electrodes were fabricated by spin-coating, including the mixed Spiro-OMeTAD/PEDOT layers. Yet, it has to be considered that mixtures of chemicals with different surface energies can undergo phase separation during layer deposition due to repulsive interactions between the materials.[276] It was e.g. reported that mixtures of Spiro-OMeTAD and poly(3-hexylthiophene) (P3HT) show vertical phase separation during film formation because of the strong difference in surface energies between the hydrophilic small molecule Spiro-OMeTAD and the hydrophobic polymer P3HT.[277] However, the counter-ion in the water-free PEDOT dispersion used here is a co-polymer with a hydrophilic PSS center and hydrophobic ends that forms micelles by itself. As a result the PEDOT:counter-ion complex coordinates as a core shell particle in organic solvents with a polar, PEDOT-rich center and a hydrophobic shell. Given the amphiphilic nature of this complex, it is assumed that the hydrophilic Spiro-OMeTAD will associate with the PEDOT complex without phase-separation.

Lateral conductivity measurements were performed to characterize the mixed PEDOT and Spiro-OMeTAD layers electrically. As presented in Figure 4.8, PEDOT thin films fabricated from the pure water-free PEDOT dispersion achieved a specific conductivity of around $3.5 \cdot 10^{-3}$ S $\cdot$ cm^{-1}. Blending dopant-free Spiro-OMeTAD into the PEDOT dispersion linearly decreases the lateral conductivity of the resulting thin films with increasing concentration of Spiro-OMeTAD. For layers coated from a PEDOT dispersion with 50 wt.-% Spiro-OMeTAD for example, the conductivity with respect to the pure PEDOT thin film is reduced by nearly one order of magnitude, from $3.5 \cdot 10^{-3}$ S $\cdot$ cm^{-1} to $5 \cdot 10^{-4}$ S $\cdot$ cm^{-1}.

In comparison, reported values for layers of dopant free Spiro-OMeTAD are in the order of 10^{-8} S $\cdot$ cm^{-1} and 10^{-3} S $\cdot$ cm^{-1} for well-doped films.[278] The specific conductivities achieved in this study for mixed layers of dopant-free Spiro-OMeTAD and water-free PEDOT therefore are on par to the one of well-doped Spiro-OMeTAD which highlights their potential to be utilized as HTM in perovskite solar cells.

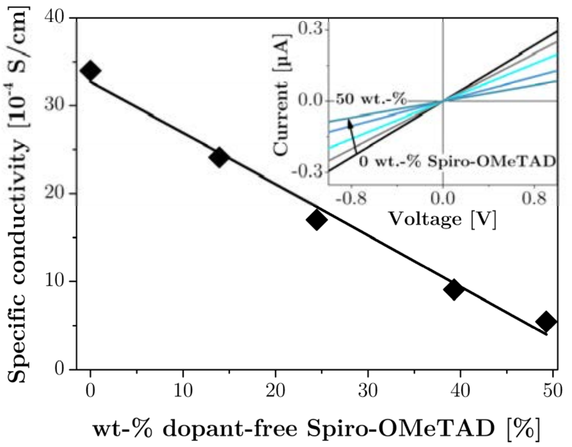

Figure 4.8: Lateral specific conductivity of thin films cast from water-free PEDOT dispersions containing different amounts of dopant-free Spiro-OMeTAD. The inset shows the lateral current-voltage characteristics of the different thin films.

In order to gain insights into the energetics at the HTM surfaces, ultraviolet photoelectron spectroscopy (UPS) measurements with 6.5 eV excitation energy were conducted. The thin films were deposited on glass/ITO substrates from solutions of dopant-free Spiro-OMeTAD, dispersions of water-free PEDOT and their mixtures. As displayed in Figure 4.9 a), layers of pure water-free PEDOT revealed a work function (i.e. Fermi-level relative to the vacuum energy) of 4.3 eV. Comparable values have been measured before on layers of pristine PEDOT.[279] Notably, the workfunction of doped, acidic PEDOT:PSS film was reported to be substantially larger, which was attributed to an enrichment of PSS at the PEDOT:PSS surface and the formation of surface dipoles[279]. This mechanism might thus not be functional here. Also neutralizing the PEDOT formulation was shown to before to reduce the work function by 0.7eV from pH of 1.7 to 7.[280] Blending 15 or 25 wt.-% of dopant-free Spiro-OMeTAD into the PEDOT dispersion increases the work function of resulting films by 20 and 50 meV, respectively. At the other extreme, dopant-free Spiro-OMeTAD on ITO has a Fermi-level position of 4.45 eV below the vacuum energy. Note, that the work function of un-doped organic semiconductors can strongly depend on the substrate energetics.[281] Turning to the ionization energy (IE), the spectrum of water-free PEDOT has no clear leading edge: occupied states are visible in the whole energy range up to the Fermi level ($E_{\mathrm{bind}} = 0$) as observed for water-based PEDOT:PSS,[282, 283] confirming a high degree of doping in the water-free PEDOT. The situation is different for pure dopant-free Spiro-OMeTAD samples, with IE = 5.1 eV. This is comparable to previously reported values.[167, 278, 284]

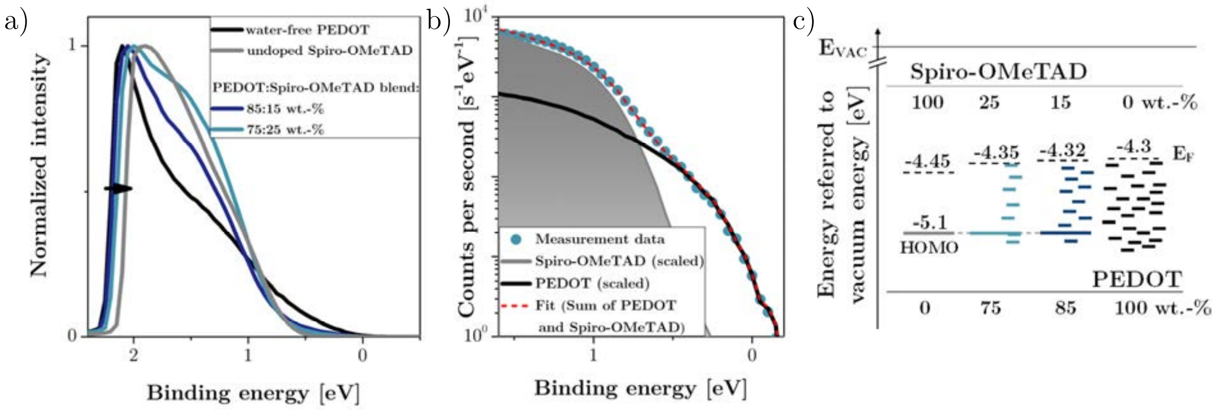

Figure 4.9: a) Photoelectron spectroscopy measurements for thin films of pure water-free PEDOT, pure dopant-free Spiro-OMeTAD and two blends. b) Semi-logarithmic depiction of the Fermi edge in a) for the 75:25 wt.-% PEDOT:Spiro-OMeTAD mixed film and a fit to the measurement by the sum of the scaled spectra for pure PEDOT and Spiro-OMeTAD. The excellent agreement between sample data and fitted spectrum indicates the presence of energetic states from PEDOT above the HOMO level of Spiro-OMeTAD in mixed thin films. c) Schematic representation of the resulting energy level diagrams.

Examining the Fermi edge of the two blends in Figure 4.9 a) indicates a superposition of the spectra of the two pure samples. Indeed, the leading edges of the mixed layers can be well approximated by weighted sums of the spectra for pure Spiro-OMeTAD and PEDOT, as exemplarily shown in Figure 4.9 b) and further elucidated in the appendix, chapter 7.2. States of the PEDOT seem to be apparent above the highest occupied molecular orbital (HOMO) level of Spiro-OMeTAD in the mixed film energetics, as illustrated in the simplified energy level diagram in Figure 4.9 c. The analysis shows that both PEDOT and Spiro-OMeTAD are present at the surface of the mixed layer, ruling out a strict vertical phase separation of PEDOT and Spiro-OMeTAD in the mixtures which is in line to the initial assumption.

In the following, processes occurring at the interface between different HTMs and the perovskite surface are examined by transient and steady-state photoluminescence measurements (PL). Transient PL (TRPL) of a bare perovskite absorber layer on glass yielded a slow bi-exponential decay of the PL signal with a high lifetime of the longer (second) component of around 470 ns (Figure 4.10 a). This matches well with previously reported lifetimes for similar perovskite compositions utilized in >20% efficient solar cells[61, 224] and thus implies a high quality of the “triple-cation” absorber thin films produced in this study. When doped Spiro-OMeTAD is coated onto the perovskite absorber, the TRPL signal decay is drastically accelerated and the second component lifetime is reduced to 70 ns. A reduction of the TRPL lifetime is generally observed when charge transport layers are brought in contact with the perovskite absorber and stems from enhanced non-radiative recombination at the interface or charge extraction into the selective contact materials.[61, 113, 158, 285, 286] Remarkably, for a layer stack of pure water-free PEDOT on perovskite, the observed TRPL signal abates slower than for the bare perovskite absorber with an increase of the lifetime of the second bi-exponential component to 570 ns. As the perovskite thin film was prepared identical in both cases, this implies reduced surface recombination of the absorber layer with PEDOT atop but might also be indicative of a poor charge extraction into the HTM. On addition of 25 wt.-% dopant-free Spiro-OMeTAD to the PEDOT dispersion, the TRPL signal of the resulting perovskite/HTM stack decays faster again with a second component lifetime of 200 ns. Therefore, blending Spiro-OMeTAD into the PEDOT layer seems to either promote non-radiative recombination at the perovskite interface and/or facilitate charge transport to the hole contact. Note that the 200 ns lifetime for the PEDOT/Spiro-OMeTAD mixtures as HTM is still higher than for doped Spiro-OMeTAD that are typically used as HTM.

To disentangle surface recombination from charge extraction, the steady-state absolute PL yield (APLY) was investigated for perovskite absorbers plus the respective hole transport layers on glass. As in this measurement samples are kept under constant illumination and open circuit, charge transport to the contact layers saturates quickly and an equilibrium of the PL emission is established which is limited by non-radiative recombination.[226, 287] The high energy tail of the PL emission can then be used to calculate the chemical potential of electrons and holes in the absorber also referred to as quasi-Fermi-level splitting (QFLS).[226, 287] In a solar cell, the QFLS of the absorber also represents the maximum achievable product $e \cdot V_{OC}$ for the respective illumination conditions. Here, a bare perovskite layer on glass achieved a QFLS of 1.22 eV for around 1 sun illumination intensity as depicted in Figure 4.10 b). For the ideal case of solely radiative charge recombination, a maximum QFLS around 1.33 eV can be obtained for the bandgap of the perovskite composition used in this study (~1.6 eV).[288] Accordingly, approximately 110 meV are lost in the absorber layer on glass due to non-radiative recombination. Doped Spiro-OMeTAD interfacing the perovskite further increases these non-radiative recombination losses and reduces the QFLS in the absorber to around 1.17 eV. The deposition of water-free PEDOT on the perovskite absorber on the other hand remarkably elevates the QFLS by around 20 meV up to 1.24 eV. This again indicates a reduction of non-radiative recombination losses by the PEDOT and is in line with the retarded TRPL decay as compared to the bare perovskite layer discussed above. As the perovskite absorber itself was again prepared similar with or without HTM, it is reasonable to attribute a decrease of non-radiative recombination to reduced surface recombination. Interestingly, this high QFLS of around 1.24 eV is maintained when dopant-free Spiro-OMeTAD is added into the PEDOT thin film. Spiro-OMeTAD therefore does not seem to introduce additional non-radiative recombination pathways and the reduced TRPL lifetime observed above for PEDOT/Spiro-OMeTAD mixtures is most likely attributable to enhanced charge extraction at the interface. The large QFLS values of 1.24 eV obtained for perovskite layers with PEDOT or PEDOT/Spiro-OMeTAD mixtures as HTMs therefore outperform the ones for doped Spiro-OMeTAD as HTM in this study. Further, they appear capable to provide small potential losses below 0.4 eV at the given absorber bandgap of around 1.6 eV.[152] This is on level with the best values reported so far in complete perovskite solar cells (0.39 eV) and underlines the potential of the contact systems introduced here.[26, 117]

Note, that thin films from acidic PEDOT or block-co-polymer dispersions significantly reduced the QFLS as compared to pH-neutralized PEDOT on perovskite layers, see Figure S 7 in chapter 7.2. This highlights the importance of using pH-neutral PEDOT formulations when being applied on top of the sensitive perovskite absorber to achieve high open circuit voltages.

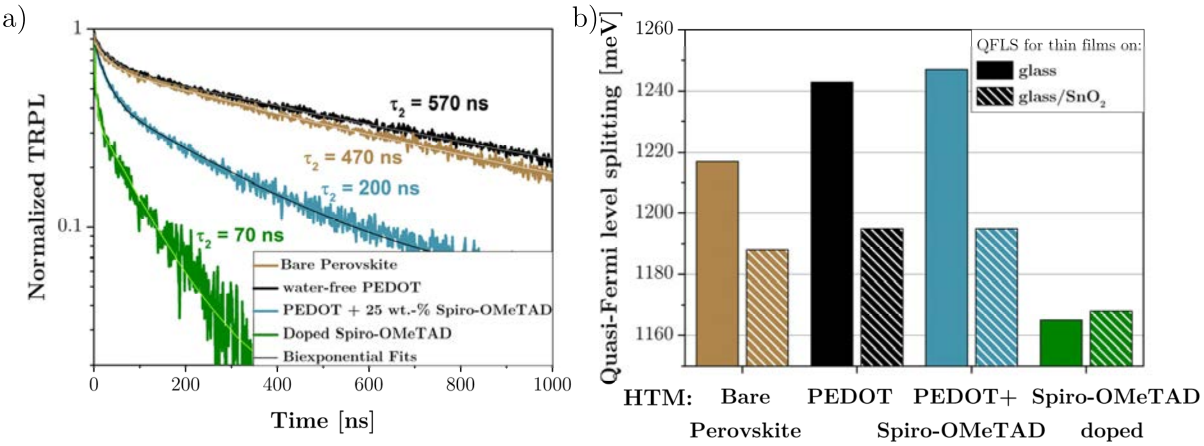

Figure 4.10: a) Transient photoluminescence decays and b) quasi-Fermi level splitting (QFLS) from absolute photoluminescence measurements for bare perovskite absorbers as well as perovskite/HTM layer stacks on glass or glass/SnO_2, with HTM being PEDOT, PEDOT & Spiro-OMeTAD mixtures or doped Spiro-OMeTAD. Lifetimes in a) refer to the second components of bi-exponential fits to the measured decays.

In addition, the absolute PL measurements were also conducted for samples including the electron selective contact SnO_2 utilized here, as this layer stack is closer to the final solar cell device geometry. With SnO_2 as the electron selective contact being deposited prior to the perovskite absorber, the QFLS without additional HTM is reduced significantly to around 1.19 eV. Likewise in combination with water-free PEDOT or mixtures of the latter one with dopant-free Spiro-OMeTAD as HTM atop the perovskite, the QFLS is equally decreased with SnO_2 as ETM to around 1.19 eV. The metal-oxide hence seems to impose substantial surface recombination at the perovskite interface and limit the highest V_{OC} achievable in a solar cell with these contact layers to a maximum value of around 1.19 V. In case of doped Spiro-OMeTAD as HTM in the layer stack, the QFLS is further reduced to 1.165 eV which is similar to the value achieved without SnO_2. Therefore, in this case, the QFLS is apparently limited by the non-radiative losses at the doped Spiro-OMeTAD interface as discussed before.

So in brief, combined TRPL and APLY measurements indicate reduced surface recombination and superior QFLS of up to 1.24 eV when water-free PEDOT is deposited on perovskite thin films. As mixtures of Spiro-OMeTAD and PEDOT maintain this high QFLS but reveal a faster TRPL decay as compared to pure PEDOT layers on perovskite, it seems that the addition of dopant-free Spiro-OMeTAD to PEDOT does not increase surface recombination but rather facilitates charge extraction at the interface.

Finally, planar *n-i-p* type perovskite solar cells were produced with different HTMs as introduced before and schematically depicted in Figure 4.7 a). The current-voltage (J-V) characteristics of the solar cells achieving the highest V_{OC} for each HTM in this study are depicted in Figure 4.11 a). Out of 30 solar cells with doped Spiro-OMeTAD as hole contact, the device with the highest V_{OC} of 1.13 V in the reverse scan (1.10 V in forward scan) was also the best performing one for this HTM with 15.7% power conversion efficiency (PCE) after 60 s of maximum power point (MPP) tracking. Short-circuit current density (J_{SC}) of the device was 22.2 mA/cm^2 and the FF was 64% in both forward and reverse scan. When doped Spiro-OMeTAD is replaced by water-free PEDOT, the open circuit voltage is enhanced to a maximum value of 1.17 V in the reverse scan (1.14 V in forward scan, out of 18 samples). Accompanied by a J_{SC} of 21.7 mA/cm^2 and a FF of 51% in the reverse scan (21.6 mA/cm^2 J_{SC} and 46% FF in forward scan) this allowed a PCE of 12.0% after 60 s of MPP tracking.

Eminently, adding 25 wt.-% dopant-free Spiro-OMeTAD to the water-free PEDOT further pushed the V_{OC} of the resulting solar cell up to 1.19 V in the reverse (1.17 V in the forward) J-V scan. Besides the enhancement in V_{OC}, the FF of the most efficient devices was raised from around 50% for pure PEDOT to 63% (56%) in the reverse (forward) J-V scan for the PEDOT/Spiro-OMeTAD mixtures as HTM. This is in line with the improved charge extraction on Spiro-OMeTAD addition to PEDOT implied by TRPL measurements. As a consequence, the PCE was enhanced to 14.6% after 60 s of MPP tracking.

As shown in Figure 4.11 b), the highest V_{OC} values obtained for solar cells with different HTMs match the trend observed in the QFLS from APLY measurements. Doped Spiro-OMeTAD as HTM and SnO_2 as ETM resulted in a low QFLS of 1.17 eV and an even lower maximum V_{OC} value for the reverse J-V scan in complete solar cells of 1.13 V. The deviation of the V_{OC} from the QFLS implies additional non-radiative recombination losses when ITO and Au electrodes encompass the SnO_2/perovskite/Spiro-OMeTAD stack. Additional losses can occur e.g. at the selective contact/electrode interface, by direct contact between the electrodes and the perovskite absorber via pinholes in the selective layers or due to energetic misalignment.[29]

Yet, the overall efficiency of solar cells including PEDOT as HTM was so far strongly limited by the FF. To overcome this limitation, the post-deposition treatment of the PEDOT based hole contacts has been optimized and a thermal annealing step of the solar cells for 3 minutes at 120°C was introduced. As a result and illustrated in Figure 4.11 c), the average FF of solar cells with water-free PEDOT was successfully raised to the level obtained for doped Spiro-OMeTAD as HTM in this study. Even more, mixtures of dopant-free Spiro-OMeTAD and water-free PEDOT as HTM in perovskite solar cells allowed even higher FFs of around 70%. In a series of ca. 18 solar cells per HTM, the FF enhanced with increasing concentrations of dopant-free Spiro-OMeTAD in PEDOT up to 60 wt.-% and subsequently dropped again. This confirms the enhanced charge extraction as implied by the combination of TRPL and APLY for mixtures of Spiro-OMeTAD and PEDOT as HTM. For very high concentrations of the dopant-free Spiro-OMeTAD in PEDOT, the decreasing conductivity depicted in Figure 4.8 might reduce the FF again. Finally, the post-deposition annealing enabled a solar cell with 16.8% stabilized efficiency during MPP tracking with a mixture of 60 wt.-% dopant-free Spiro-OMeTAD and 40 wt.-% water-free PEDOT as HTM, shown in Figure 4.11 d). This exceeds the best solar cell with Spiro-OMeTAD as HTM in this study (15.7%). The V_{OC} of 1.15 V for the champion device of this study was lower than the highest value achieved for non-annealed PEDOT/Spiro mixtures before, which correlates with a slight reduction of the QFLS observed for post-annealed PEDOT on perovskite layers by around 250 meV (Figure S 7, chapter 7.2). Yet, both the V_{OC} of solar cells with annealed PEDOT/Spiro-OMeTAD mixtures as HTM as well as the QFLS for perovskite/annealed PEDOT layer stacks still outmatch the values for doped Spiro-OMeTAD as HTM in this study. Additionally, post-deposition annealing of the mixed PEDOT/Spiro-OMeTAD thin films increased the FF of the champion device to 69% (65%) in the reverse (forward) J-V scan while the J_{SC} stayed rather constant at 21.2 mA/cm^2 which matches well within less than 5% mismatch to the calculated J_{SC} from external quantum efficiency (EQE_{PV}) measurements of a comparable device as shown in Figure S 8 chapter 7.2.

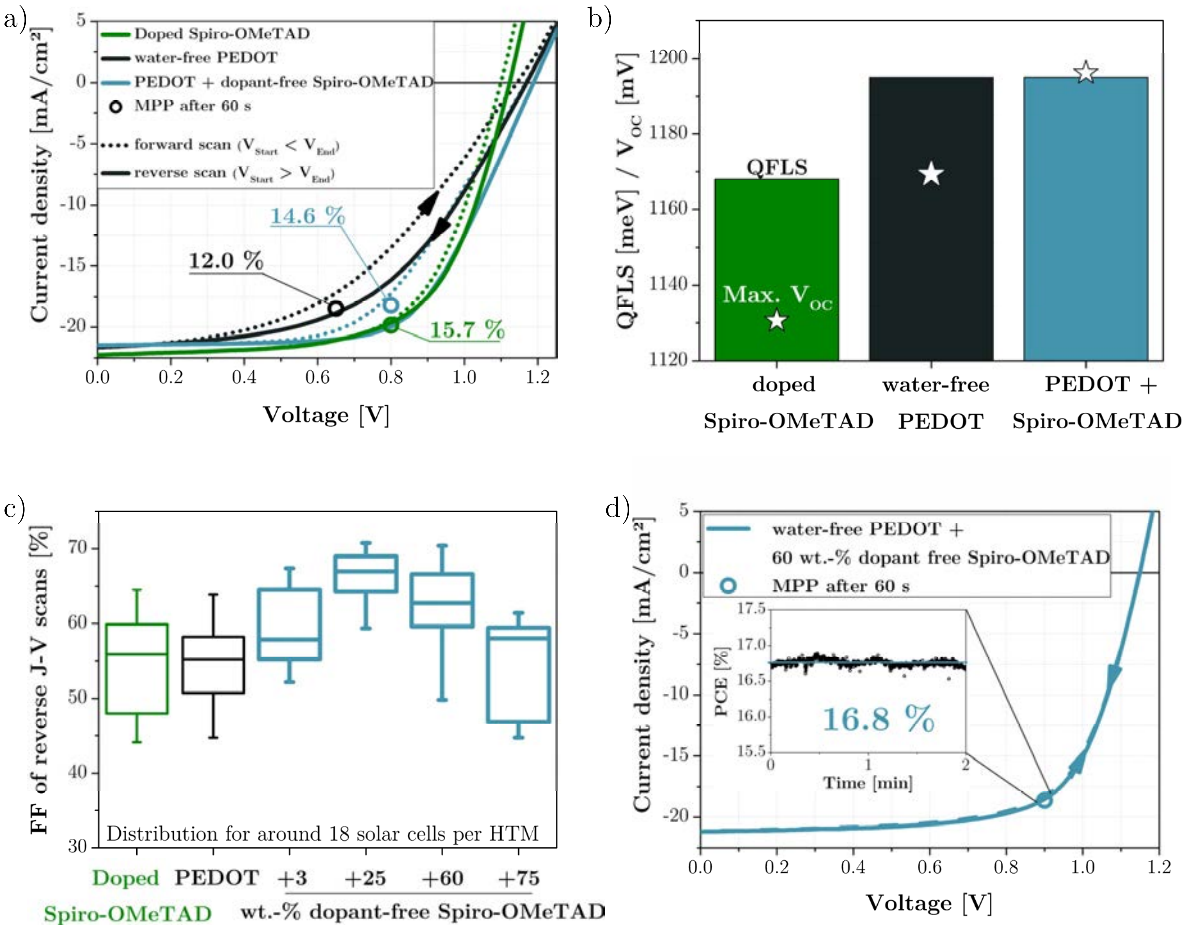

Figure 4.11: a) Current-voltage characteristics under illumination in forward and reverse scan for non-annealed layers of doped Spiro-OMeTAD, PEDOT or PEDOT & dopant-free Spiro-OMeTAD mixtures as HTM. The shown devices achieved the highest open circuit voltages in this study for the respective HTM. b) The quasi-Fermi level splitting (QFLS) from absolute photoluminescence measurements for the different HTMs compared to the maximum achieved V_{OC} values. c) Distribution of fill factors from reverse current-voltage scans at similar scan rate for solar cells with doped Spiro-OMeTAD as HTM as well as post-deposition annealed layers of PEDOT and PEDOT/Spiro-OMeTAD mixtures as HTM. d) Forward and reverse scan current-voltage characteristics of the champion solar cell in this study with a post-deposition annealed mixture of 40 wt.-% water-free PEDOT and 60 wt.-% dopant-free Spiro-OMeTAD as HTM. The inset shows the maximum power point track of the device confirming a stabilized efficiency of 16.8% for 120 sec of MPP tracking.

Moreover, the water-free PEDOT, as well as mixtures with dopant-free Spiro-OMeTAD, have also been implemented here as an HTM in *p-i-n* type perovskite solar cells. The device stack and J-V-results are depicted in the appendix 7.2, Figure S 9. Interestingly, the resulting solar cells revealed very low V_{OC} values of around 0.9 V as compared to 1.1 V when PTAA was employed as HTM. The discrepancy in V_{OC} between *n-i-p* and *p-i-n* architectures could e.g. stem from a substrate dependence of the absorber growth and properties.[147] Besides, the PEDOT thin film itself or its interfaces could be different at top or bottom or could be changed by the subsequent perovskite and contact layer depositions. It was e.g. shown before that solvents and especially solutions containing MAI or MABr can significantly alter PEDOT:PSS films when being spin-coated on top by forming MA-PSS or Br-/I-PEDOT bonds.[289]

The low FF in solar cells with pure PEDOT as HTM is rather surprising regarding the high conductivity of PEDOT. Besides, UPS measurements indicated a high density of energetic states for PEDOT layers up to 4.3 eV below the vacuum energy level. These states would be located deep within the band gap of the perovskite and could therefore impose harmful recombination sites.[113] However, PEDOT as HTM is shown above to even increase the QFLS and TRPL lifetimes of the perovskite absorber, which strongly implies reduced surface recombination. Unfortunately, the actual energetics at the buried perovskite/HTM interface are unknown and might differ from the ones probed at the HTM surface by UPS.

The core-shell structure of the PEDOT:co-polymer complex leads to a thin enrichment of the counter-ion at the film surfaces.[290] Passivation as well as the poor charge extraction might thus mainly be governed by the co-polymer interfacing the absorber. This coincides with the observed enhancement of the QFLS when only the pH-neutral co-polymer is coated on a perovskite layer (appendix 7.2, Figure S 7). Suppressed surface recombination has also been shown for PEDOT:PSS-Si interfaces.[291] Besides, previous reports suggest that polymers can chemically passivate defect states at perovskite surfaces e.g. by formation of S-Pb bonds.[259, 260, 292] Note, that both PEDOT as well as the co-polymer are sulfurous. However, the exact mechanisms occurring here are subject to further studies.

While QFLS and the average V_{OC} were similar for solar cells with water-free PEDOT as compared to Spiro-OMeTAD/PEDOT mixtures as HTM, faster TRPL decays and significantly enhanced FFs were observed. This implies improved charge extraction for increasing amounts of dopant-free Spiro-OMeTAD in the water-free PEDOT. The trend is supported by a concomitant reduction of current-voltage hysteresis, as shown more detailed in Figure S 10, which has been attributed before to reduced charge accumulation at the interface.[181] Enhanced hole extraction with addition of Spiro-OMeTAD to PEDOT might be related to a better electronic coupling of the small molecule to the perovskite surface as compared to the larger polymer. Also potential extraction barriers at the PEDOT/perovskite interface, e.g. by the co-polymer enrichment at the HTM surfaces discussed before, might be circumvented by additional Spiro-OMeTAD interfacing the absorber.

As a result, mixtures of water-free PEDOT and dopant-free Spiro-OMeTAD as HTM in perovskite solar cells were shown to combine the benefits of reduced non-radiative recombination losses and high V_{OC} by the PEDOT as well as good charge extraction and FF via the Spiro-OMeTAD.

4.2.3 Conclusions

For the first time, mixtures of dopant-free Spiro-OMeTAD and water-free, doped PEDOT were employed as HTM in perovskite solar cells (PSCs). Lateral conductivity measurements revealed similar conductivities for these mixtures as reported for doped Spiro-OMeTAD. UPS studies on thin films of Spiro-OMeTAD and PEDOT suggest a superposition of the energetic states of the two pure species, thereby excluding perfect vertical phase segregation of the two components.

Remarkably, while contact layers typically reduce the luminescence of perovskite absorbers, time-resolved and absolute photoluminescence (PL) measurements revealed the opposite when the water-free PEDOT is deposited atop a perovskite film, namely an enhancement of PL lifetimes and quasi-Fermi level splitting (QFLS). PEDOT, as well as PEDOT/Spiro-OMeTAD mixtures therefore have a dual function as hole selective contacts and passivation layers reducing non-radiative recombination losses at the perovskite surface (Figure 4.12). As a result, high QFLS of 1.24 eV were realized for a perovskite/HTM stack associated with high V_{OC} values of up to 1.19 V in complete solar cells. This exceeds the V_{OC} values obtained for doped Spiro-OMeTAD in this study and marks the lowest potential loss reported so far for PSCs containing PEDOT as HTM.

The enhancement in V_{OC} for solar cells with PEDOT as HTM as compared to Spiro-OMeTAD, however, was accompanied by decreased fill factors (FF). Both might be attributed to an enrichment of the insulating co-polymer, used to dope the PEDOT, at the perovskite surface. Blending dopant-free Spiro-OMeTAD into the PEDOT and optimizing the HTM deposition moreover enhanced charge extraction at the perovskite/HTM interface (Figure 4.12 b), c) and improved the FF of the resulting solar cells from 60% to above 70% for the best devices. As a result, 16.8% stabilized efficiency was realized in a solar cell with 40 wt.-% PEDOT and 60 wt.-% Spiro-OMeTAD as HTM.

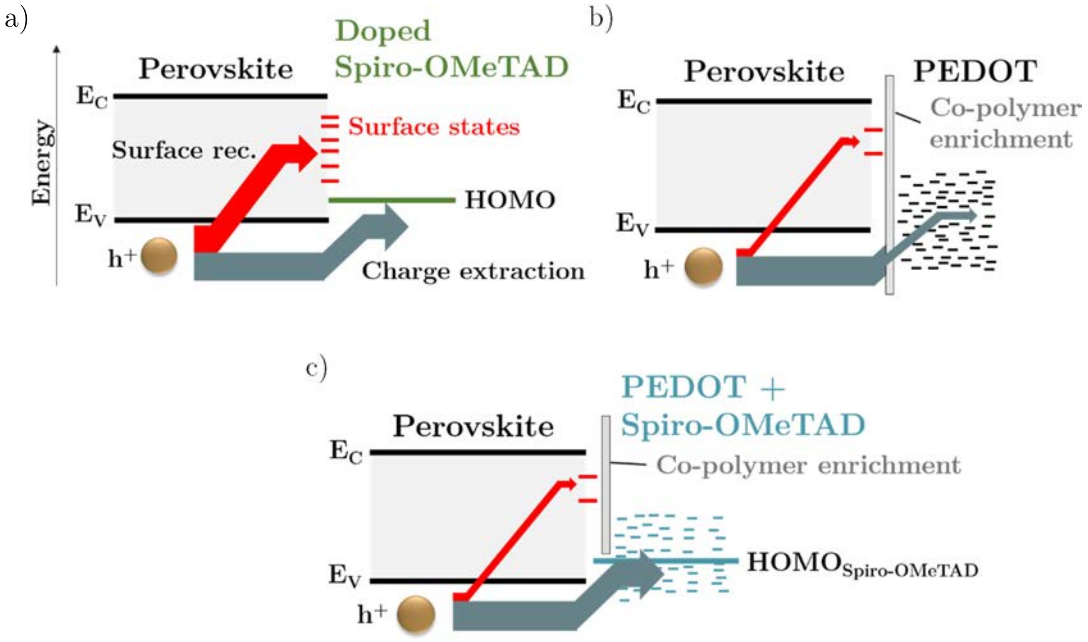

Figure 4.12: Simplified energy level diagram of the perovskite/HTM interface, illustrating charge extraction and surface recombination for HTM being a) doped Spiro-OMeTAD, b) PEDOT or c) PEDOT/Spiro-OMeTAD mixtures. E_C, E_V and HOMO denote conduction and valence band energies as well as highest occupied molecular orbitals, respectively.

4.3 Optical Top Contact Optimization in Monolithic Perovskite-Silicon Heterojunction Tandem Solar Cells

The following chapter considers advancements in the optical optimization of monolithic perovskite-silicon heterojunction tandem solar cells with *n-i-p* top cell architecture. For this very young tandem architecture, with first reports being published in the beginning year of this thesis, the two scientific regions of interest covered here are the molybdenum oxide (MoOx)/ITO top electrode and the Spiro-OMeTAD *p*-type top contact.

In the first region of interest, the MoOx layer is shown to suffer from sputter-induced damages by the ITO deposition, which increases the absorptivity of the layer stack. Interlayers of SnO_2 and ITO nanoparticles are introduced here to successfully avoid this sputter damage. Employing these interlayers in solar cells partially allowed to increase the V_{OC} values and reduce hysteresis, but also hampered charge transport and reduced the overall device efficiency. An optimized ITO deposition protocol is instead introduced to moderate the sputter induced damage of MoOx and increase the overall layer stack transmission while remaining the pristine MoOx/ITO interface. Further, small agglomerates of ITO nanoparticles between MoOx and ITO are shown in monolithic perovskite-silicon tandem solar cells to reduce current-voltage hysteresis and enhance the overall efficiency.

To optimize and analyze the second region of interest, optical parasitic losses of Spiro-OMeTAD are estimated for optimized perovskite-silicon heterojunction solar cells from optical simulations. Furthermore, alternative, more transparent *p*-type selective contacts are utilized and investigated in a combined experimental and simulative approach towards their potential to enhance the tandem device efficiency. Constraints to the respective layer thicknesses are derived from experimental results and first proof-of-concept tandem solar cells are realized with alternative hole contacts. The combined experimental and simulative approach allows realistic projections of the maximum achievable currents in tandem solar cells by numerical simulations. As a result, more transparent contact materials are expected to reduce the absorption losses in the *p*-type contact by a maximum of 90%, and enhance the efficiency by around 3% relative. This would enable the herein investigated tandem devices with *n-i-p* top cell to develop on par with and even exceed its currently more efficient *p-i-n* top cell counterpart.

4.3.1 Introduction

The rapid efficiency enhancements for perovskite-silicon tandem solar cells in the last three years were strongly driven by improved light management, as elucidated in chapter 2.4. The perovskite top cell is thereby impaired by optical losses for wavelengths below around 780 nm occurring at the top contact layer stack, here HTM/molybdenum oxide (MoOx)/ITO/LiF as shown in Figure 4.13. The bottom cell is affected similarly for the wavelength regime between ~780-1200 nm and by all layers atop the Si absorber. Further, also reflection and parasitic absorption occurs in the back contact for the wavelength regime between 1000-1200 nm, where absorption of Si becomes very low (see chapter 2.1.2). Within the top-cell stack, SnO_2, and perovskite are highly transparent for wavelengths above 780 nm and the a-Si and ITO recombination junction layers are only 5-10 and 20 nm thin, respectively. Thus, the parasitic absorption losses for the Si bottom cell are dominated by the top contact rather than by the layers between the perovskite and Si absorber. Reduction of parasitic absorption in the HTM/MoOx/ITO/LiF layer stack and optimization of layer thicknesses to enable efficient current matching of the sub cells are thus the main strategies to further improve the device performance of this tandem architecture and are therefore followed in this chapter in detail.

It is has been reported before and is also shown here in detail, that a MoOx/ITO layer stack, as used for the top electrode in tandem solar cells (region I in Figure 4.13), is more absorptive over the whole spectrum than expected from their respective single layers.[293] The Ar^+ ion bombardment during ITO sputtering is assumed to impose oxygen vacancies in the MoOx and thus increase its absorption.[293, 294] Previous reports addressed this issue by applying CO_2 plasmas to pre- or re-oxidize MoOx layers before or after Ar plasma exposure.[293] However, the effect of this treatment was minor with MoOx/TCO layers still being about twice as absorptive above 500 nm wavelengths as expected from their single layers.[293] Here instead, SnO_2 and ITO nanoparticles are first employed as interlayers between the MoOx and the ITO to successfully avoid sputter damage on the MoOx. As a result, the transparency of the MoOx/ITO layer stack is increased, allowing up to 1.6 mA/cm^2 more absorption in the tandem solar cell. Employing these interlayers in solar cells revealed the best results for 2 nm of SnO_2 with higher V_{OC} values and reduced hysteresis, however, due to lower FF a 1% absolute lower PCE as compared to a device without interlayer. Further, depositing the ITO at high deposition rates is shown to reduce the overall sputter damage on MoOx, presumably due to shorter exposure of the MoOx surface to Ar^+ ions. This is confirmed by a 25% increased optical transmittance and decreased appearance of reduced Mo-states in x-ray photoelectron spectroscopy, as compared to standardly deposited MoOx/ITO layer stacks. Further, small agglomerates of ITO nanoparticles as buffer layers do not improve the optical properties, but are found to enhance the device performance and reduce hysteresis. Applying the nanoparticles in monolithic perovskite-silicon tandem solar cells resulted in high open circuit voltages of 1.83 V, which is the highest value yet reported in perovskite-silicon tandem solar cells. Additionally, a higher perovskite top cell EQE_{PV} as compared to a device without interlayer is achieved. Consequently, the tandem efficiency is raised from 19.8% without ITO nanoparticles to 21.4% with the interlayer, or from 17.7 to 18.0%, respectively, when referencing to the integrated J_{SC} value from EQE_{PV} measurements.

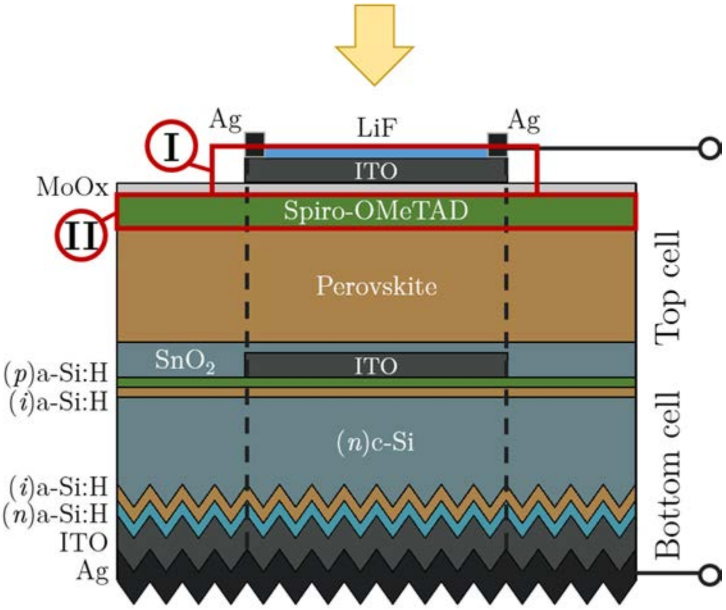

Figure 4.13: Schematic device structure of the monolithic tandem solar cells with a front contact (emitter) silicon heterojunction bottom and a *n-i-p* type perovskite top cell established in this study. Indicated sections I and II mark the herein identified regions of interest for optical improvements developed in this work.

Further, for the two-terminal solar cell architecture used here with *n-i-p* type PSCs, parasitic absorption in the Spiro-OMeTAD *p*-type contact (region II in Figure 4.13) is a crucial loss mechanism. Simulations by Jäger et al. expect the HTM to account for around 25% of the overall optical losses (reflection and parasitic absorption) in a device with optimized film thicknesses.[24, 173] Tandem solar cells with the highest efficiencies so far circumvent these losses by employing the *p-i-n* PSC architecture, which typically utilizes less absorptive and much thinner contact layers of C_{60} as ETM and NiO or PTAA as HTM.[22, 107, 214, 216] However, highest single-junction performances and typically higher V_{OC} values are still achieved in the *n-i-p* design, as discussed in chapter 2.2.3. Also, front-emitter SHJ bottom cells on *n*-type Si wafers, as utilized here, were assumed to outperform their rear-emitter and/or *p*-type wafer counterparts as *p*-type wafers are more prone to surface recombination losses and a front emitter benefits from stronger illumination, which improves charge transport through the a-Si.[295] Therefore, replacing the highly absorptive Spiro-OMeTAD with a more transparent HTM in the *n-i-p* architecture is a promising approach to further enhance tandem solar cell efficiencies.

Here, PTAA, PEDOT/Spiro-OMeTAD mixtures and CuSCN are investigated as alternative *p*-type contacts in *n-i-p* perovskite-silicon tandem solar cells. Although doped Spiro-OMeTAD is still the most frequently used HTM, PTAA and CuSCN provide high transmittance over a wide spectral range[24, 296] and were utilized by others in supremely efficient PSCs (>20%).[153, 267] Besides, mixtures of PEDOT and Spiro-OMeTAD, introduced in the previous chapter, allow to drastically reduce the amount and thus parasitic absorption of Spiro-OMeTAD in the HTM. Further, high device efficiencies were demonstrated utilizing PEDOT/Spiro-OMeTAD mixtures in section 4.2, exceeding the ones for reference solar cells with Spiro-OMeTAD as HTM.

To analyze the different HTMs utilized here, optical properties of PTAA, PEDOT/Spiro-OMeTAD mixtures, CuSCN, and doped Spiro-OMeTAD are first acquired from literature or are determined from experiments. Optical simulations by the software GenPro4, as described in detail in the methods chapter 3.2.9, proof to reproduce the reflection and transmission properties of experimentally deposited HTM thin films. Next, the minimum required thickness for each individual HTM in single-junction PSCs to still provide electrical functionality and enable minimized parasitic absorption is determined. 150, 50, 50 and 60 nm are revealed as ideal thicknesses for doped Spiro-OMeTAD, PTAA, PEDOT/Spiro-OMeTAD mixtures and CuSCN on application in single junction solar cells, respectively. Spiro-OMeTAD thereby suffers from high pinhole densities[297] and thus requires thicker layers to provide sufficient perovskite surface coverage. Further, the required MoOx thickness as a sputter protection layer is found for all HTMs to amount to 25 nm, following MoOx thickness variations in semi-transparent single-junction PSCs. However, the CuSCN/MoOx interface appears to be electrically disturbed and causes low FF in solar cells. This is confirmed in monolithic perovskite-SHJ tandem solar cells, where devices with CuSCN as HTM suffer from deteriorated charge extraction and subsequently very low performances. Besides that, Spiro-OMeTAD showed the best tandem device performance in the HTM comparison at 17.3% PCE stabilized as compared to PTAA (~10%) and PEDOT/Spiro-OMeTAD mixtures (12.4%), which both obtained lower V_{OC} and FF values and require further electrical optimization.

To determine the optical potential in more detail, the achievable J_{SC} of herein prepared perovskite-SHJ tandem solar cells (Figure 4.13) is numerically maximized for the different employed HTMs by adjusting the top-cell in the simulation. Thicknesses of LiF, the top ITO as well as the perovskite films are thereby optimized in optical simulations, constrained to experimentally realizable and relevant thickness ranges. The results imply similar parasitic absorption losses of 2.6 mA/cm^2 for Spiro-OMeTAD and PEDOT/Spiro-OMeTAD mixtures as HTM in perovskite-Si tandem solar cells but a reduction to 1.1 mA/cm^2 for PTAA and even 0.3 mA/cm^2 for CuSCN.

The determined maximum J_{SC} values are further combined with expected tandem V_{OC} and FF values, to estimate the achievable PCEs to: 25.8, 26.5, 25.6 and 26.7% when employing Spiro-OMeTAD, PTAA, PEDOT/Spiro-OMeTAD mixtures or CuSCN as top cell HTM, respectively. The inferior contact between CuSCN and MoOx identified before, clearly hampers the realization of this optimized efficiency of 26.7%. PTAA, estimated at an only 0.2% absolute lower maximum PCE, is therefore found here to be the most promising material to replace Spiro-OMeTAD and increase the PCE in monolithic perovskite-SHJ tandem solar cells.

4.3.2 Top Electrode Optimization (Region I)

The *n-i-p* perovskite top-cells are so far highly limited by photocurrent generation as discussed before. Thus improving light management by less parasitic absorption and employing anti-reflection schemes are highly relevant to further enhance the performance. This subchapter focuses on the optical optimization of the top electrode, comprising a MoOx layer to protect the organic materials below from sputter damage and an ITO electrode, used for lateral charge transport to the Ag front contact.

To enable more transmission into the tandem absorbers, fine tuning of the ITO bulk properties to reduce its absorptance or replacing it with a more transparent TCO such as In_2O_3:Zn[207] are viable approaches, and are subject to ongoing studies in our group. Several comparison measurements (data not shown) revealed better electrical properties for ITO over In_2O_3:Zn as top contact material. Therefore throughout this work, standardly deposited ITO as described in chapter 3.2 has been utilized and TCO optimization is not discussed herein.

To achieve better light trapping in the device and/or anti-reflection effects at the ITO/air interface, textured foils can be applied, but typically require index matching liquids which harm the perovskite sub cell.[21] Therefore, a flat layer of LiF has been employed here as the sole anti-reflection coating. Its low refractive index of around 1.4 matches well with the optimium for minimum Fresnel reflection of $(n_{air} \cdot n_{ITO})^{0.5} \approx (1 \cdot 1.8\text{-}2.2)^{0.5} \approx 1.34\text{-}1.48$. Its effect is exemplarily shown for a perovskite-silicon heterojunction tandem solar cell produced here in Figure 4.14. As depicted in Figure 4.14 a), reflection is substantially reduced by the LiF coating over the complete spectrum and allows a maximum additional current under standard test conditions (STC) of up to 0.9 mA/cm² for the perovskite and 1.9 mA/cm² for the Si sub cell, respectively. This gain is displayed concomitantly in the *EQE_{PV}* of the sub cells, with the integrated J_{SC} values increasing by 0.8 and 1.4 mA/cm² in perovskite and silicon.

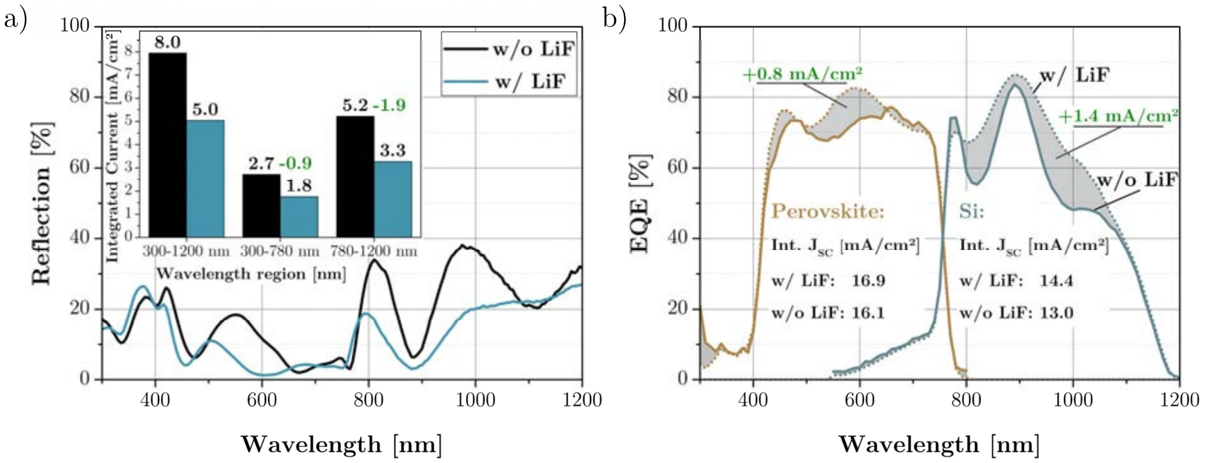

Figure 4.14: a) Spectral reflection and b) *EQE$_{PV}$* and integrated short-circuit current densities J_{SC} of the subcells for a monolithic perovskite-silicon heterojunction tandem solar cell with and without LiF anti reflection coating on the top electrode.

Further, previous reports suggested, that Ar^+ ion bombardement of MoOx during sputter deposition of ITO can result in enhanced absorptance of the layer stack.[293] To validate if and to which extend this effect as well occurs for the herein used deposition tools and procedures, the

MoOx/ITO layer stack as well as the two individual layers were deposited seperately on glass to determine their respective reflectance and transmittance. Aimed layer thicknesses were 25 nm for MoOx and 150-160 nm for ITO. Optical simulations with the software GenPro4, as described in chapter 3.2.9, were first performed for the single layers of ITO and MoOx on glass to validate the agreement between measurement and simulation and determine the corresponding layer thicknesses.

As displayed on the left and in the middle of Figure 4.15, the simulation results match well with the measured optical data for layer thicknesses of 23 nm for MoOx and 165 nm for ITO on glass, which is well within the expected range. However, utilizing these layer properties in simulations for glass/MoOx/ITO samples reveals similar reflectance but pronounced discrepencies in transmittance and absorptance between measurement and simulation (Figure 4.15 right). The experimentally determined absorptance (calculated from 1-reflectance-transmittance) significantly exceeds the expected value from simulations over the complete wavelength range. This is in line to previous reports and has been attributed to a sputter-induced increase of oxygen vacancies in the MoOx.[293] For AM1.5G illumination, the additional parasitic absorption loss amounts here to around 1.6 mA/cm^2 and is evenly distributed over the absorption regimes of perovskite (~300-760 nm) and Si (~760-1200 nm) with about 0.8 mA/cm^2 each. Thus, it potentially strongly impacts the photocurrent generation in the monolithic tandem cell.

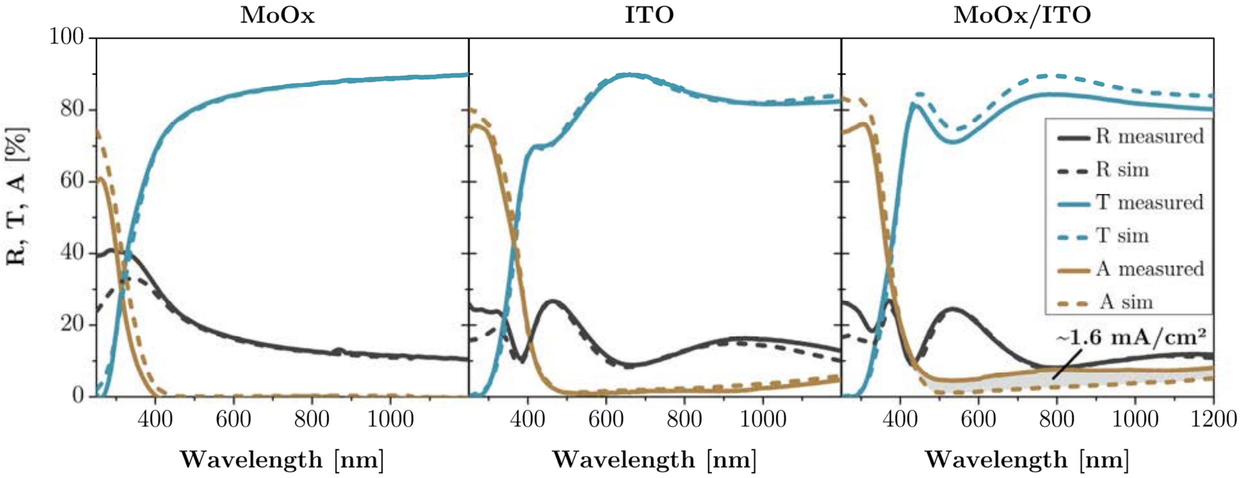

Figure 4.15: Measured and simulated spectral reflectance, transmittance and absorptance of glass/MoOx (left), glass/ITO (middle) and glass/MoOx/ITO (right) layer stacks. Absorptance (A) was calculated from reflectance (R) and transmittance (T) as 1-R-T.

To avoid reduction of MoOx during the sputter deposition of ITO, thin interlayers are introduced here as buffers between the metal oxides.[134] ITO nanoparticles with nominally <50 nm particle size dispersed in isopropanol at 10 mg/ml concentration and sonicated for about 10 minutes are spin coated on MoOx layers. Besides, 8, 17 and 25 cycles of SnO_2 prepared by atomic layer deposition (ALD) are utilized as interlayers, which is expected to correspond to 1, 2 and 3 nm thin layers, respectively. As depicted in Figure 4.16 a), while 8 cycles of SnO_2 by ALD even slightly increase the absorption of the overall layer stack, 17 and 25 cycles are sufficient to provide sputter protection of the MoOx and mitigate creation of oxygen vacancies. The parasitic absorption is reduced by a maximum of around 1.5 mA/cm^2 in total under one-sun illumination for 25 cycles of SnO_2 as interlayer (0.9 mA/cm^2 in the Si and 0.6 mA/cm^2 in the perovskite absorption range). Further, ITO nanoparticles spin coated at 4000 and 6000 rpm atop MoOx also successfully remedy deterioration of transmittance for the overall layer stack by the subsequent ITO sputter process (Figure 4.16 b). Here, parasitic absorption was even reduced by a maximum of 1.8 mA/cm² for ITO NP spin coated as a buffer layer at 6000 rpm with around 0.8 mA/cm² enhancement for the perovskite and 1 mA/cm² for the Si related wavelength range. Note that this improvement exceeds the value expected from Figure 4.15 by 0.2 mA/cm². However, additional interlayer also alter the interference pattern throughout the layer stack and thus potentially the absorption in the different materials. Besides, also overall absorption of the glass/MoOx/ITO stack is around 0.6 mA/cm² higher in Figure 4.16 as compared to Figure 4.15, which might originate from a less transparent or thicker ITO layer.

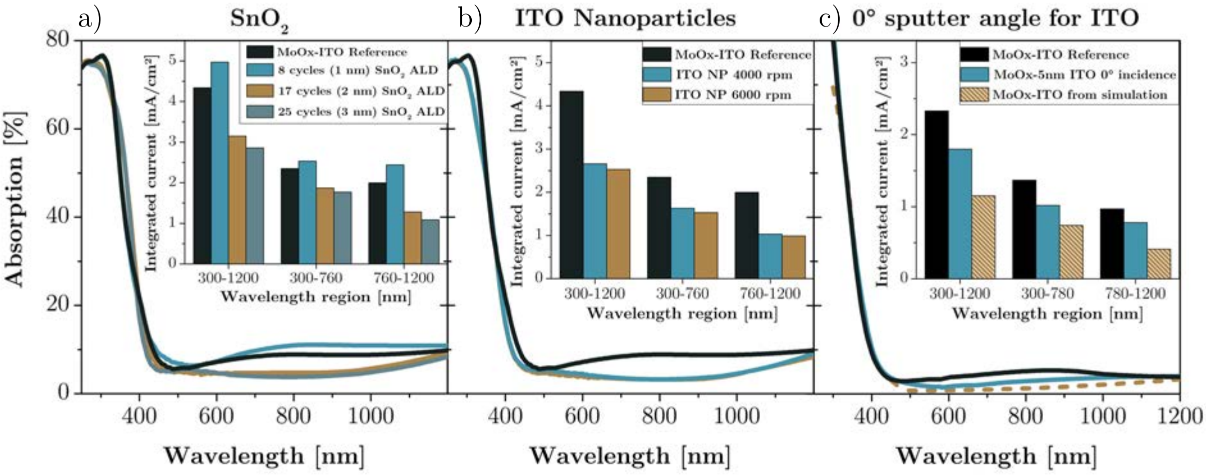

Figure 4.16: Spectral absorptance calculated from 1-reflectance-transmittance for layer stacks of glass/MoOx/buffer/ITO with buffer being: a) 8, 17 and 25 cycles atomic layer deposited SnO_2 which is expected to reveal 1, 2 and 3 nm thick layers, respectively; b) ITO nanoparticles spin coated from dispersion at 4000 and 6000 rpm. c) Spectral absorptance for MoOx-ITO layer stacks on glass with ITO being deposited as usual (reference) and with an initial static sputter deposition at 0° incidence angle. Beige line represents the absorption expected from simulations according to the measured absorption of the respective single layers. The insets further display the integrated current losses arising from the respective absorption curves under AM1.5G illumination.

However, scanning electron microscopy (SEM) images reveal non-uniformal coating of the MoOx by ITO nanoparticles. Instead, large agglomerates are visible on the sample surface as depicted in Figure 4.17 a) and the total thickness of the layer stack apart of the agglomerates was found to be similar to the sum of the ITO and MoOx layers (Figure S 14). Longer ultrasonication of the ITO dispersion leads to a shift in size distribution towards smaller ITO nanoparticle agglomerates in the MoOx/buffer/ITO structure, as exemplarily shown in Figure 4.17 b) for a one hour sonicated dispersion.

As a consequence, also the optical properties of the layer stack change. Surprisingly, in the case of smaller agglomerates and higher surface coverage, the overall absorption of the glass/MoOx/ITO nanoparticles/ITO configuration is increased as compared to without the interlayer. As shown in Figure 4.17 c) and d), dilution of the one hour sonicated ITO nanoparticle dispersion results in less surface coverage of the small agglomerates, less parasitic absorption but in all cases lower transmittance than for the glass/MoOx/ITO reference sample. Parasitic absorption of the ITO nanoparticles thus is significantly more pronounced for interlayers with smaller as compared to larger agglomerates (c.f. Figure 4.16 b) potentially due to the higher surface coverage. Further, the mechanism to protect MoOx from sputter induced damage might rather depend on the size than on the surface coverage of the ITO nanoparticle agglomerates on MoOx.

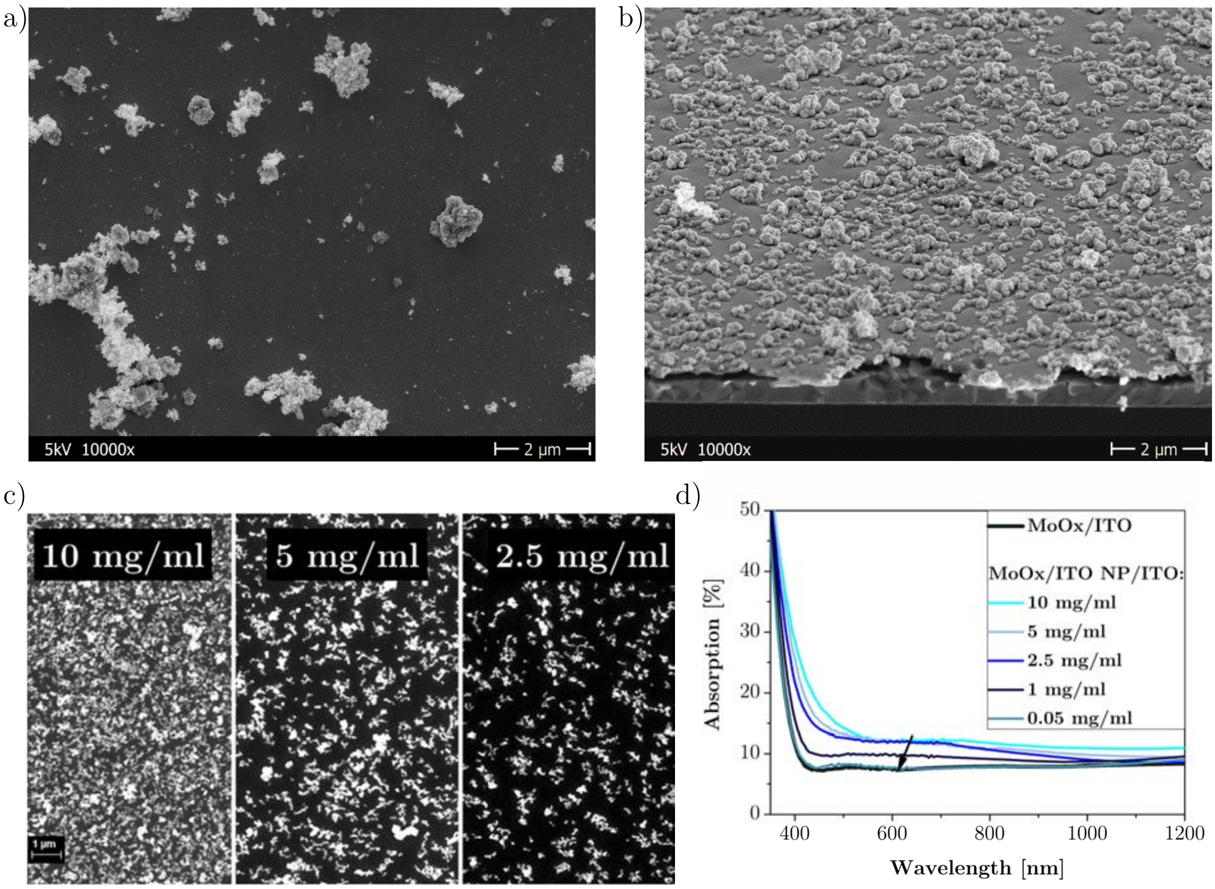

Figure 4.17: Scanning electron microscopy (SEM) images of MoOx/ITO nanoparticles/ITO layer stacks for 10 mg/ml dispersions of ITO nanoparticles in isopropanol ultrasonicated for around a) 10 minutes and b) 1 hour. c) SEM top view images of MoOx/ITO nanoparticle stacks on glass from 1 hour sonicated ITO nanoparticle dispersions with different concentrations and d) respective absorption spectra after subsequent ITO deposition, calculated from 1-reflection-transmission.

A potentially beneficial effect of large sized agglomerates could be shielding of the MoOx from Ar^+ bombardment during sputtering at high incident deposition angles.[294] In general, the samples rotate within the sputter chamber and transit the plasma and the deposition cone underneath the ITO target once per cycle. Therefore the incidence angle of particles and their fluxes are changing during the period, as simplified illustrated in Figure 4.18 a). As samples start the sputter deposition far apart from the target, particles initially hit the sample at high incidence angles while the substrate rotates towards the deposition center. Large agglomerates might shield this initial bombardment, whereas at low incidence angles (substrate underneath the target), high deposition rates of ITO quickly cover the MoOx surface.

To investigate the influence of the deposition angle on the MoOx/ITO stack transmittance, another experiment was conducted without any ITO nanoparticles as extra buffer layer. Instead, 5 nm of ITO was first sputtered statically on a glass/MoOx sample directly underneath the target (0° incidence angle). Next, 100 nm of ITO were deposited as usual (rotating substrate carrier) together with a reference sample of the identical glass/MoOx layer stack. As shown in Figure 4.16 c), the reference sample obtained an about twice as high absorption as expected from simulations (2.3 vs. 1.2 mA/cm^2). The specimen pre-treated with low-incidence angle deposited ITO in contrast revealed only an around 50% increased parasitic absorption at 1.8 mA/cm^2. To further analyze this difference, x-ray photoelectron spectroscopy (XPS) measurements of MoOx samples covered with around 2 nm of ITO at high and low deposition angles are compared. These measurements seem to confirm the optical observation: in comparison to a pristine MoOx surface, both ITO covered samples revealed pronounced contributions from Mo 3d doublets at lower binding energies in the XPS signal (Figure 4.18 b). Following Choi et al.[298], these contributions arise from reduction of Mo^{6+} to more absorptive lower oxidation states of Mo^{5+} and Mo^{4+}. However, low angle as compared to high angle deposited ITO revealed lesser shares of Mo^{5+} and Mo^{4+} states. Chemical reduction of the metal oxide therefore still seems to occur but is less pronounced with for low incidence angles of ITO sputtering. The higher deposition rate of ITO directly below the target reduces the exposure time of MoOx to Ar$^+$ ion bombardment before being covered with a protective TCO layer. This might also moderate the overall creation of oxygen vacancies in the MoOx.

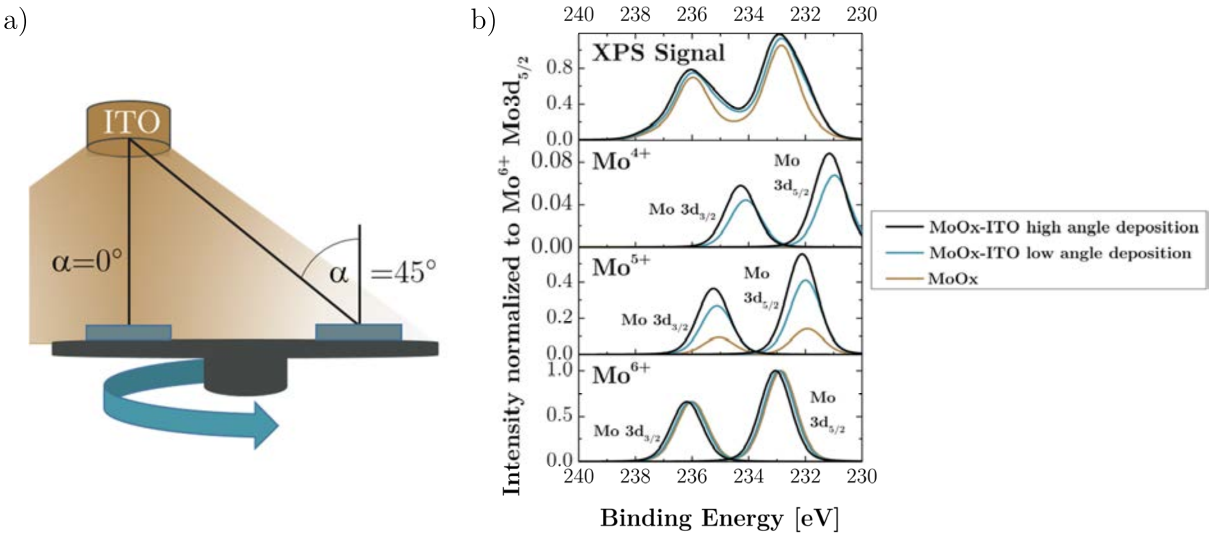

Figure 4.18: a) Simplified illustration of the ITO sputter deposition process with substrates rotating on a sample carrier below the ITO target. Further, low and high sputter incidence angles are illustrated for different positions of the substrates on the sample carrier. b) X-ray photoelectron spectroscopy results of a bare MoOx substrate (reference) as well as two MoOx layers with 2 nm of ITO being deposited atop at high and low sputter incidence angles. Measured signals can be fitted by multiple peaks of Mo^{6+}, Mo^{5+} and Mo^{4+} states according to ref.[298] All intensities are normalized to the determined peak intensity of the Mo^{6+} Mo 3d$_{5/2}$ spectrum.

After optical characterization of the different interlayers from ALD SnO$_2$ and ITO nanoparticles as well as from understanding of sputter damage with more Mo^{5+} and Mo^{4+} states, the interlayers are now analyzed with respect to their impact on the device performance. In the following, semi-transparent perovskite single-junction solar cells with different interlayers are compared. The device stack contains glass/ITO/SnO$_2$/"triple-cation" perovskite/Spiro-OMeTAD/MoOx/*buffer layer*/ITO, with "triple cation" perovskite being the $Cs_{0.05}(FA_{0.83}MA_{0.17})_{0.95}Pb(I_{0.83}Br_{0.17})_3$ composition as utilized before. Respective layer thicknesses amount to 1.1 mm/150 nm/25 nm/

600 nm/150 nm/25 nm/ *buffer*/150 nm. Representative J-V curves under illumination through the glass substrate are illustrated in Figure 4.19.

Figure 4.19 a) depicts the solar cell characteristics for ALD SnO_2 interlayers between MoOx and ITO that are characterized by different thicknesses. For less than 17 cycles of ALD, the device performance is substantially deteriorated. This might be attributed to distorted growth kinetics of SnO_2 and surface cleaning processes during the first few ALD cycles, as observed before for various material combinations.[299, 300] 17 cycles of ALD, which is expected to yield around 2 nm of SnO_2, instead allows high V_{OC} values up to 1.14 V as compared to around 1.05 V for the reference solar cell without SnO_2 buffer layer. Yet, an overall higher series resistance leads to rather low FF around 50%, as compared to ~60% in the reverse scan of the reference device. Hysteresis is strongly reduced for the given scan rate of 333 mV/s, but the MPP stabilizes around 1% absolute lower as compared to without SnO_2 interlayer (11.5% PCE without, 10.5% PCE with 17 cycles of SnO_2 as interlayer, see Figure S 15 in chapter 7.3).

More deposition cycles (20 or 25) and thus thicker SnO_2 interlayers further reduce the FF and increase the series resistance of the resulting solar cells. As high FF above 75% with up to 20 nm thick SnO_2 ALD buffer layers have been shown before by our group in *p-i-n* type perovskite solar cells[22, 216], conductivity of SnO_2 is not expected to be a limiting parameter here. Instead, the pronounced sensitivity on the SnO_2 thickness, might imply an energetic tunneling barrier to cause the FF decrease.[202] MoOx is assumed to possess a higher electron affinity and work function than ITO and an even larger electron affinity than the ionization energy of Spiro-OMeTAD (from UPS results in chapters 4.1.2, 4.2 and ref[301]). Thus electrons are expected to flow from the ITO to the lower lying MoOx conduction band and recombine with holes from the HTM at the MoOx/Spiro-OMeTAD interface. Introducing SnO_2 interlayers with a presumably lower electron affinity than the ITO, implied by UPS measurements in chapter 4.1.2, would therefore induce an energetic barrier between the MoOx and the ITO. However, further investigations are necessary to elucidate the detailed energy alignment at the contact utilized here.

Figure 4.19 b) on the other hand compares the performance metrics for MoOx/ITO nanoparticle/ITO layer stack when differently sonicated ITO nanoparticles form the buffer layer. As compared to the reference without nanoparticle layer, a significant series resistance increase is detected, resulting in a very poor FF. The modest lateral conductivity even requires an additional Ag back contact atop the ITO to extract reasonable J-V characteristics. Still, the FF is significantly lower than in the reference device without a buffer between MoOx and ITO and without a metal back contact. The large ITO agglomerates thus seem to hamper both vertical as well as lateral charge transport across the top contact. On the other hand, ITO nanoparticle buffer layers from dispersion sonicated for a longer period of 1 hour, leading to smaller agglomerates and higher coverage, are capable to enhance the overall performance and even reduce hysteresis for the given scan speed of 333 mV/s as compared to the solar cell without buffer layer. The reason for the reduced hysteresis is difficult to originate, but the ITO nanoparticles might improve charge collection across the top contact (in agreement to better FF) which could in turn reduce charge accumulation at the perovskite surfaces and thus hysteresis.[181]

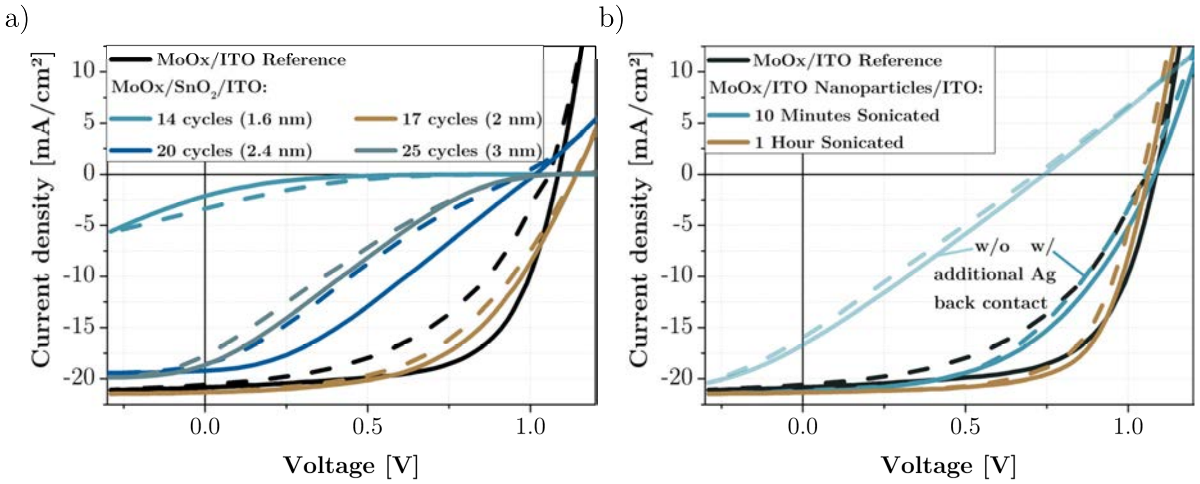

Figure 4.19: Representative current density-voltage characteristics of different buffer layers in a MoOx/buffer/ITO top contact stack of semi-transparent perovskite single junction solar cells illuminated through the glass/ETM side. a) Solar cells with 14, 17, 20 and 25 cycles of atomic layer deposited SnO_2 as buffer (expected layer thicknesses of 1.8, 2, 2.5 and 3 nm, respectively). b) Devices with ITO nanoparticles from 10 minutes and 1 hour sonicated dispersions as buffer. The sparse lateral conductivity of the top contact when utilizing 10 minutes sonicated nanoparticle dispersions requires deposition of an additional Ag back contact.

Therefore, the interlayers achieving increased transmittance of the top electrode stack such as 2 nm thick ALD SnO_2 or buffer layers from agglomerated ITO nanoparticle dispersions compensate this optical improvements by reduced electrical performance of resulting solar cells. The one hour sonicated ITO nanoparticles as interlayer between MoOx and ITO on the other hand even decrease transmittance of the layer stack, but slightly improved the PCE of semi-transparent solar cells when illuminated through the glass/ETM side first. For 0° incidence angle sputtering of the initial 5-10 nm of ITO, no change in device performance as compared to commonly prepared devices has been observed (see Figure S 11 in appendix chapter 7.3). The MoOx/ITO interface therefore seems to be electrically unaltered by the low angle sputter deposition while reducing the parasitic absorption of the stack by around 25%.

Based on the findings generated from the semitransparent single junction solar cells summarized above, tandem solar cells with SHJ/ITO/SnO_2/"triple cation" perovskite/Spiro-OMeTAD/MoOx/*buffer*/ITO architecture were prepared and analyzed. Due to the reduced electrical device performance for SnO_2 and large agglomerate ITO nanoparticles as interlayers, only small agglomerate ITO nanoparticles were investigated as buffer layers. Differences between the single- and two-junction architecture thereby arise in film processing and device designs. Mainly the perovskite absorber crystallization is drastically accelerated upon thermal annealing on 250 mm thin Si bottom cells as compared to the 1.1 mm thick glass substrates for semi-transparent cells. Besides, the active area of the tandem device is more than six times larger than for single-junction cells (1 cm^2 versus 0.16 cm^2), which poses higher demands on the homogeneity of the layers.

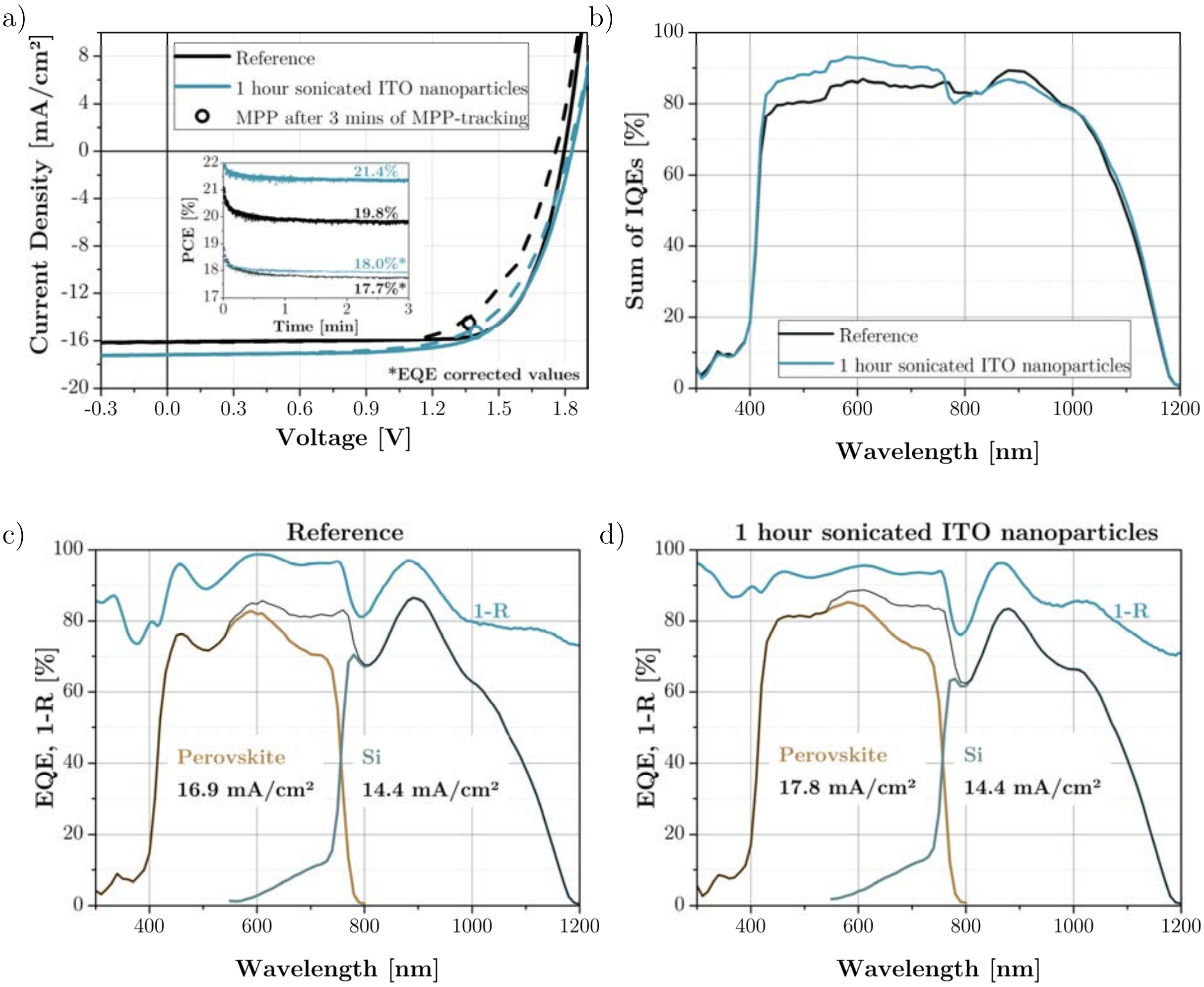

Figure 4.20: a) Current-voltage measurements under illumination in forward ($V_{start}<V_{end}$, dashed lines) and reverse ($V_{start}<V_{end}$, solid lines) scan direction of monolithic perovskite-silicon heterojunction tandem solar cells with and without one hour sonicated ITO nanoparticles between MoOx and ITO in the top electrode stack. Maximum power point (MPP) tracking and EQE_{PV}-corrected MPP values are given in the inset. b) Sum of sub cell IQE_{PV} values for the two tandem solar cells from a). EQE_{PV} and integrated current densities for both sub cells as well as sum of the sub cell EQE_{PV} values (black line) and 1-reflection of the monolithic tandem devices c) without or d) with one hour sonicated ITO nanoparticles between MoOx and ITO in the top electrode stack.

Figure 4.20 a) shows the JV-curves of the two tandem solar cells with and without one hour sonicated ITO nanoparticle buffer layer between MoOx and ITO. As depicted, current-voltage hysteresis is again smaller for the device with the ITO nanoparticles, and even V_{OC} and J_{SC} are slightly larger (1.83 V and 17.2 mA/cm^2 with ITO nanoparticles as compared to 1.80 V and 16.1 mA/cm^2 without interlayer). This results in a stabilized power output in MPP tracking of 21.4% with the nanoparticles, as compared to 19.8% without. However, EQE_{PV} measurements reveal significantly lower integrated J_{SC} values for the Si-bottom cell of 14.4 mA/cm^2 (Figure 4.20 c) and d). This would in both cases limit the J_{SC} of the tandem solar cell to this value, and reduce the power outputs to 18.0 and 17.7%, respectively. Differences between integrated J_{SC} from EQE_{PV} and measured value under one sun illumination can thereby originate e.g. in spectral variations between the setups. The herein used LED based sun simulator was found recently to show non-stability in the near-infrared region above 1000 nm, which can lead to a large mismatch between the calibrated reference cell and the tested tandem device.

Surprisingly, the perovskite sub cell EQE_{PV} is drastically improved by the ITO nanoparticles, raising the integrated J_{SC} from 16.9 to 17.8 mA/cm^2 (Figure 4.20 c) and d). As reflection is even slightly higher across the wavelength range of perovskite absorption, this increase in top cell J_{SC} on addition of ITO nanoparticles is related to an enhanced IQE_{PV} (Figure 4.20 d). Considering the parasitic absorption induced by ITO nanoparticles for wavelengths above 400 nm, as shown in Figure 4.17 b), the raised IQE_{PV} is most likely attributed to an improved photon-to-electron conversion efficiency of the perovskite absorber or enhanced charge collection in the device. Possibly, the ITO nanoparticles are required as an additional sputter protection layer for the Spiro-OMeTAD and/or the perovskite layer. IQE_{PV} in the Si absorption regime, however, is slightly lower upon utilization of the ITO nanoparticle interlayer, most probably due to the raised parasitic absorption. Note, that integrated currents from the Si sub cell EQE_{PV} are still similar in both cases (14.4 mA/cm^2), because of differences in the interference and reflection patterns.

Parasitic absorption of the nanoparticles yet is less of an impairment here as compared to the overall high internal losses for both tandem devices with IQE_{PV} values of around 80-90%. For the shown devices, the largest contributions to parasitic absorption losses, according to simulations with GenPro4 and optical data of the ITO deposited in this sputter run, arise from a strongly absorptive ITO and the Spiro-OMeTAD top contact (Figure S 12 in appendix 7.3). The reduced transmittance of the ITO in this sputter run might stem from cross-contamination of residuals from previously deposited In_2O_3:Zn in the system. Pre-conditioning of the sputter setup by depositing 10-20 nm of ITO prior to inserting the samples recently turned out to resolve this issue (also see Figure S 13 in appendix 7.3).

This underlines the necessity but also the complexity of achieving high transparency for all materials in the top layer stack of tandem solar cells. In summary, one hour sonicated ITO nanoparticle dispersions with small agglomerates do not improve the optics but are confirmed in tandem solar cells to reduce hysteresis and enhance the overall PCE. Alternatively, low incidence angle deposition of the top TCO was shown to increase the transmittance of the MoOx/ITO contact by around 25%. To further enhance light harvesting of the tandem device, the following chapter focuses on replacing the strongly absorptive Spiro-OMeTAD with a more transparent hole selective contact.

4.3.3 Perovskite Top Cell: Alternative Hole Transport Materials (Region II)

Spiro-OMeTAD is the archetypal HTM in *n-i-p* single-junction PSCs and allowed excellent device efficiencies around 22%. As introduced before, dopants are needed to promote oxidization and sufficient conductivity of the HTM.[26, 278] However, doped Spiro-OMeTAD shows strong absorption below 450 nm and further peaks from oxidized states around 500, 700 and 1000 nm wavelengths.[302] Besides, the small molecule-based HTM typically requires layer thicknesses between 150 and 300 nm.[21, 212, 213] When illuminating a solar cell through Spiro-OMeTAD, as in *n-i-p* perovskite-Si tandem devices, this is expected to cause high losses around 2.5 mA/cm^2 under one-sun illumination even for optimized layer thicknesses.[24, 173]

Alternatively, more transparent HTMs were demonstrated in *n-i-p* single junction PSCs, such as the wide band gap metal oxides NiO[303], $CuGaO_2$[304] or CuSCN[267, 305] or the organic *p*-type polymeric semiconductor PTAA[26, 153]. The latter two, CuSCN and PTAA, even allowed high device efficiencies >20% and thus might be promising alternative HTMs for tandem integration.[153, 267] CuSCN is a low-temperature, solution processable semiconductor with large band gaps up to 3.9 eV and hole mobilities around 10^{-2} cm^2/Vs.[296, 306] Besides, the *p*-type polymer PTAA provides an optical band gap of around 3.0 eV[307] and hole mobilities in its pristine form of around 10^{-3} cm^2/Vs[308]. It has been used as ≤10 nm thin, undoped HTM in above 21% efficient *p-i-n* type PSCs.[224] Further, doped PTAA as around 50 nm thick capping layer hole contact in mesoporous *n-i-p* type devices enabled PCEs >22%.[153] Finally, also the PEDOT/Spiro-OMeTAD mixtures introduced in chapter 4.2 allow a significant reduction of the amount of Spiro-OMeTAD in the HTM. 25 wt.-% concentration of the small molecule in the mixed dispersion is chosen here for tandem application, as it yields high PCEs in single-junction devices while providing a rather low Spiro-OMeTAD concentration. However, the highly conductive PEDOT in the mixed HTM also raises pronounced parasitic absorption losses over the complete absorption range of the perovskite-Si tandem solar cell, as further discussed below.

This section therefore aims towards realistic estimation of the potential gains in optics and performances of monolithic perovskite-SHJ tandem solar cells by replacing Spiro-OMeTAD with the aforementioned alternative HTMs, which have not been implemented into monolithic perovskite/silicon tandem solar cells before. The estimations are based on a combination of experimental results and optical simulations. They are oriented at the herein produced perovskite solar cells, meaning the so called “triple cation” perovskite absorber with a band gap around 1.64 eV and SnO_2 as the electron contact. The more robust SnO_2, similar to chapter 4.2, is chosen here as model *n*-type contact instead of the TiO_2/PCBM double-layer contact, due to the high solubility of fullerenes in the dimethyl formamide solvent of the “triple cation” perovskite solution, as discussed before.

Optical properties of the HTMs

A prerequisite to allow optical simulations and compare the optical properties of the various examined HTMs is knowledge about their complex refractive indices. For Spiro-OMeTAD and PTAA, these metrics were aquired from Löper et al.[240] and Santbergen et al.[234], respectively. Further, for CuSCN and PEDOT/Spiro-OMeTAD mixtures, they were determined from their reflectance and transmittance by the APCSA software as described in chapter 3.2.9. While the optical data for Spiro-OMeTAD have been successfully used before in simulations by our group[24, 173], reflectance and transmittance measurements of PTAA, PEDOT/Spiro-OMeTAD mixtures and CuSCN thin films on glass can well be reproduced by optical simulations with the complex refractive indices obtained here (Figure 4.21 a). Note that the experimentally determined absorption of PTAA around 500 nm is slightly lower as compared to simulation with literature optical data. This implies that the herein measured film is less oxidized than expected in simulations, as this wavelength region is attributed to absorption from oxidized states in PTAA.[307]

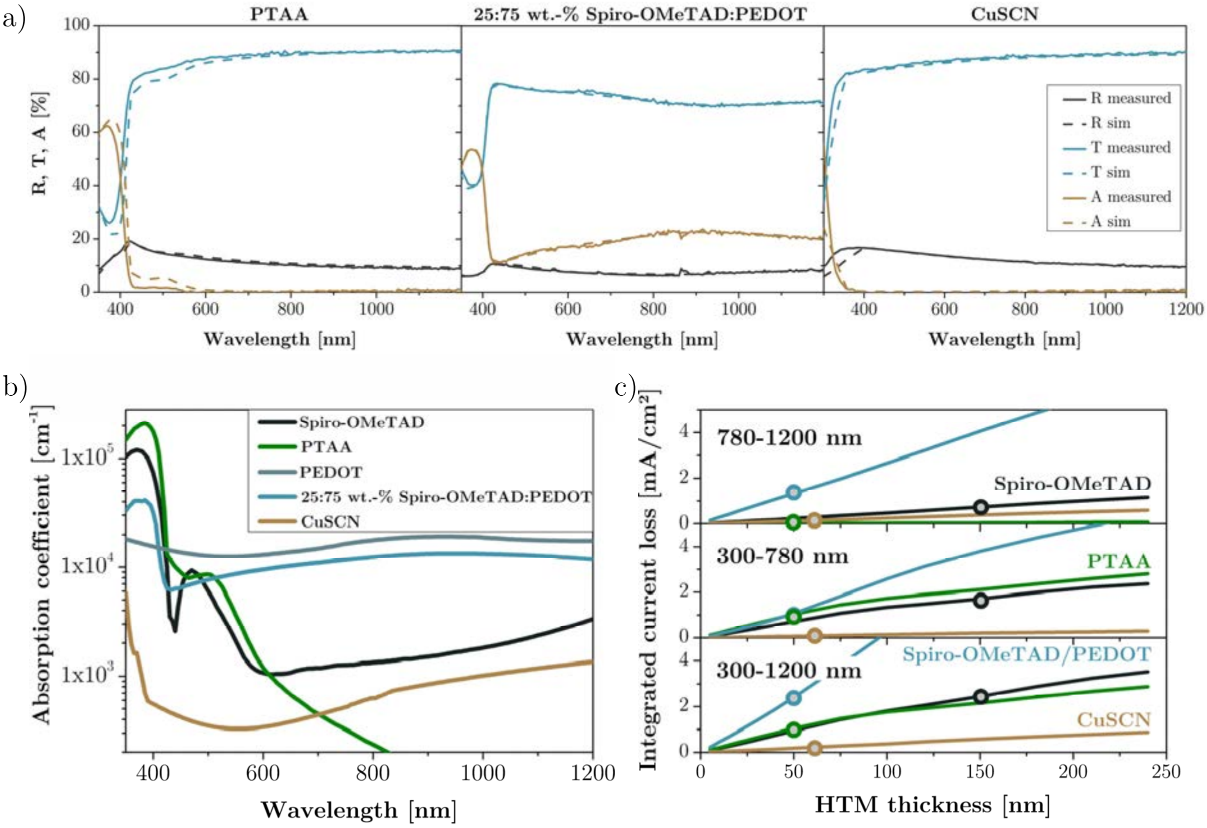

Figure 4.21: a) Experimentally determined and simulated reflectance (R) and transmittance (T) as well as absorptance (A) from 1-R-T for thin films of PTAA, 25:75 wt.-% Spiro-OMeTAD/PEDOT mixtures and CuSCN on glass. b) Absorption coefficients of Spiro-OMeTAD, PTAA, Spiro-OMeTAD/PEDOT mixtures and CuSCN determined from the extinction coefficients utilized here for optical simulations. c) Integrated current losses in monolithic perovskite-Si tandem solar cells arising from parasitic absorption in the different HTMs depending on their thickness. Values are determined by optical simulations of a back textured SHJ bottom and a perovskite top cell comprising ITO/SnO_2/Perovskite/HTM/MoOx/ITO/LiF with 20/23/615/HTM/25/105/140 nm thicknesses, respectively. Absorption losses are further depicted for the complete wavelength range as well as individually for the absorption regimes of perovskite (~300-780) and Si (~780-1200 nm). Circles mark the optimized HTM thicknesses of 150 nm, 50 nm, 50 nm and 60 nm for Spiro-OMeTAD, PTAA, 25:75 wt.-% Spiro-OMeTAD/PEDOT mixtures and CuSCN, respectively, as further elucidated below.

Absorption coefficients α can further be calculated from the complex refractive indices according to $\alpha(\lambda)=4 \cdot \pi \cdot k(\lambda)/\lambda$ where k is the extinction coefficient, and are illustrated for the different HTMs in Figure 4.21 b).[37] The depiction reaffirms the aforementioned strong absorption of doped Spiro-OMeTAD below 450 nm, around 500 nm, and for longer wavelengths as well as over the complete wavelength range for the water-free PEDOT dispersion introduced in chapter 4.2

(Clevios P SB5 SCA726-1). Blending 25 wt.-% dopant free Spiro-OMeTAD into the PEDOT formulation dilutes the polymer in the resulting film, which lowers absorptance in the long wavelength regime as compared to pure PEDOT. The same accounts for Spiro-OMeTAD absorption below 450 nm in the mixed HTM, as the absorption coefficient at peak intensity around 380 nm is only about a third (34.7%) of the value for doped Spiro-OMeTAD. Further, absorption from oxidized states of Spiro-OMeTAD around 500 nm is not apparent in the dopant-free Spiro-OMeTAD/PEDOT mixed HTM. PTAA on the other hand strongly absorbs below 450 nm wavelengths, even more than Spiro-OMeTAD, but provides high transmittance in the longer-wavelength range. Finally, CuSCN possesses superior optical properties with negligible absorption over the complete spectrum due to its large band gap.

The dependence of parasitic absorption losses of the different HTMs in perovskite-SHJ tandem solar cells on their thickness is exemplarily shown according to optical simulations in Figure 4.21 c). Circles further represent the ideal thickness of each HTM, as further elucidated below (150 nm for Spiro-OMeTAD, 60 nm for CuSCN and 50 nm for PTAA and PEDOT/Spiro-OMeTAD mixtures). Spiro-OMeTAD thereby suffers as expected from severe absorption losses, distributed with around two thirds in the perovskite and one third in the Si related absorption regime. For the assumed device architecture and ideal HTM thicknesses, PEDOT/Spiro-OMeTAD mixtures are expected to cause slightly lower absorption losses over the complete spectrum as compared to Spiro-OMeTAD, but the highest parasitic absorption of all examined HTMs for the Si bottom cell. PTAA, in contrast, is essentially transparent for the SHJ sub cell but raises around 1 mA/cm^2 of deficit for the perovskite top cell. Completing, CuSCN reaffirms its superior optical properties as it is expected to impair the incident light only by 0.2 mA/cm^2. To evaluate the impact of the different HTMs in more detail, constraints of the top cell contact are determined in the following.

HTM thickness determination

The first constraint concerns the respective HTM thicknesses for the different materials. When integrating them in tandem solar cells, the HTMs are supposed to be as thin as possible and thick as necessary to still provide complete surface coverage and benign electrical functionality but minimal parasitic absorption. Solution prepared films of the small molecule Spiro-OMeTAD yet suffer from high pinhole densities[297] and thus require layer thicknesses of few hundred nanometers to ensure sufficient perovskite surface coverage. So far reported monolithic tandem devices with *n-i-p* perovskite top cell architecture utilized >200 nm Spiro-OMeTAD layers as HTM.[21, 212, 213] Here, thickness variations of the different materials in opaque single-junction PSCs allow to determine the respective optimum values. Note, that per HTM, 3-12 different devices were prepared. As shown in Figure 4.22 a), the ideal layer thickness for Spiro-OMeTAD amounts to around 150 nm, with a slight drop in V_{OC} as compared to thicker films, but an overall high efficiency due to better FF for thinner layers (also see Figure S 16 in appendix 7.3).

For the polymer PTAA, layers as thin as 50 nm are reported to adequately cover the perovskite surface in *n-i-p* type single-junction solar cells.[26, 153] As depicted in Figure 4.22 b), peak efficiency is here achieved as well for 50 nm of PTAA, with slightly lower PCEs for 40 nm and a marked drop in V_{OC} and PCE for 30 and 20 nm (Figure 4.22 b). As the reduction of parasitic absorption from 50 to 40 nm of the polymer is negligible (0.04 mA/cm^2 from simulations), the thicker value is selected as the target for tandem integration. Also for PEDOT/Spiro-OMeTAD mixtures, 50 nm appears to be the optimum HTM thickness (Figure 4.22 c). It still allows PCEs and V_{OC} values close to the 100 nm thick layers, as standardly used in opaque cells, but reduces parasitic absorption on illumination trough the HTM by ~2.8 mA/cm², according to simulations. Finally, CuSCN has been deployed in PSCs before with thicknesses of 60-130 nm. For the parameter range examined here, 60 nm thick layers of CuSCN as HTM revealed the best device performance as depicted in Figure 4.22 d) and is thus chosen for tandem application.

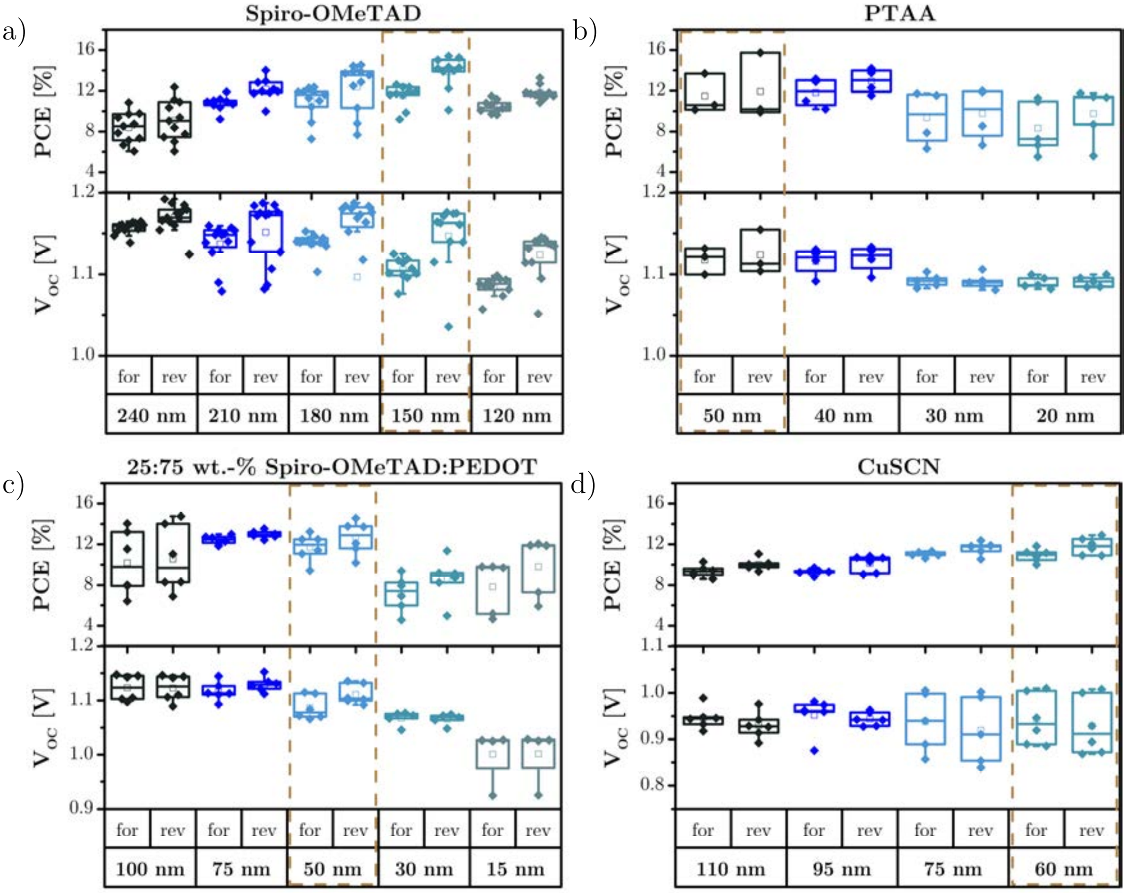

Figure 4.22: FF and V_{OC} values in boxplot diagrams for forward ($V_{Start}<V_{End}$) and reverse ($V_{Start}>V_{End}$) current-voltage scans of opaque *n-i-p* single junction perovskite solar cells with a) Spiro-OMeTAD, b) PTAA c) 25:75 wt.-% Spiro-OMeTAD:PEDOT and d) CuSCN layers of different thicknesses as HTM. 3-12 samples were evaluated per HTM, void squares represent the arithmetic average values and beige rectangles mark the selected layer thicknesses of the respective HTMs for tandem solar cells. The remaining parameters J_{SC} and FF are presented in Figure S 16.

Sputter protection layer thickness determination

The HTMs investigated here therefore not only differ by their material properties, e.g. polymeric versus small molecule structure, but also in their surface coverage and optimum layer thicknesses. As a result, also the sputter resilience of the selective contact can vary between the HTMs. Therefore, the minimum MoOx layer thickness required to protect the respective HTM during ITO sputter deposition is determined in the following. Around 6 semi-transparent solar cells were analyzed each with 0, 5, 15 and 25 nm thick MoOx evaporated on the different HTMs prior to sputtering 150 nm of ITO atop. Along with them, opaque reference devices with gold back electrode were processed for every hole contact, to allow assessment of the sputter induced damage.

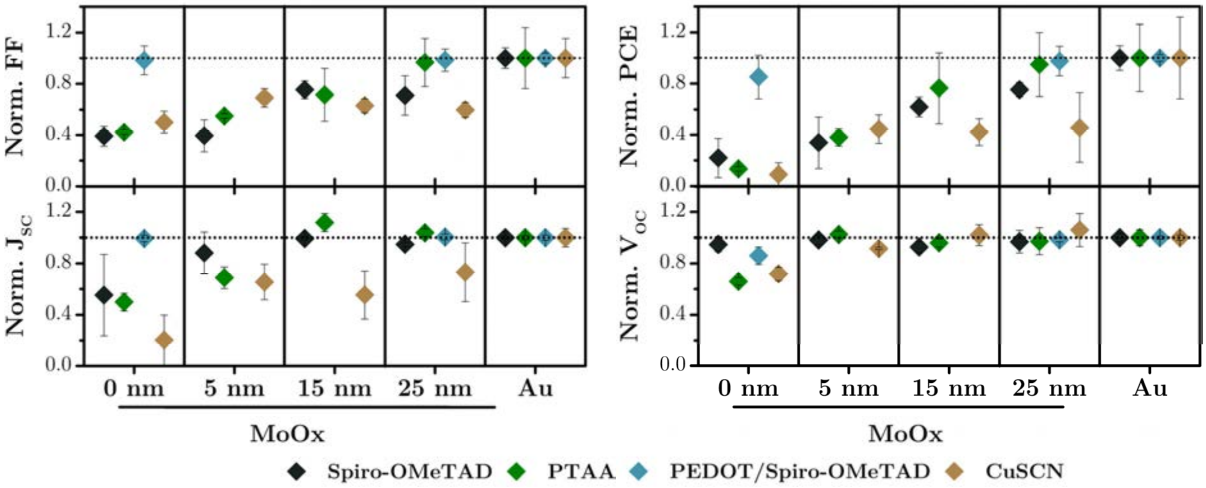

Figure 4.23: Current-voltage parameters overview of reverse scans (V_{Start}>V_{End}) for semi-transparent solar cells with top contacts, illuminated through the glass/n-type contact/perovskite side. Metrics are displayed for different HTMs and MoOx thicknesses in the HTM/MoOx/ITO top contact stack, as well as opaque reference devices with gold electrode. The parameters J_{SC}, FF, V_{OC} and PCE are normalized to the average value of the gold reference solar cell for each HTM. Standard deviations are given for around 6 devices per HTM. Note that for 25:75 wt-% Spiro-OMeTAD:PEDOT mixtures (labeled as PEDOT/Spiro-OMeTAD) only 0 and 25 nm of MoOx buffer layers were investigated along with the gold reference. Absolute values can be found in appendix 7.3.

Depicted in Figure 4.23 are the corresponding average J-V parameters from reverse scans (V_{Start}>V_{End}) of the different solar cells under illumination, normalized to the gold reference device of the respective HTM. As presented, for all HTMs utilized here, 25 nm of MoOx are sufficient to provide sputter protection during ITO deposition. Further, layers of 25:75 wt.-% Spiro-OMeTAD:PEDOT mixtures provide the highest sputter resilience. For this HTM, devices without MoOx still performed at around 85% of the reference device performance in average, owing to a slight deterioration in V_{OC} only. Besides that, semi-transparent solar cells with CuSCN as HTM performed for all MoOx thicknesses considerably worse than their opaque references. While the V_{OC} is even slightly enhanced for 25 nm of MoOx, FF and even J_{SC} substantially drop by around 50 and 75%, respectively. As similar was observed for the FF in opaque solar cells with CuSCN/MoOx/Au top contact (Figure S 20 in appendix, chapter 7.3), this decline cannot exclusively be attributed to sputter damage from ITO deposition. Instead, the CuSCN/MoOx interface appears to result in a poor contact. Finally, Figure 4.23 indicates that sputter induced damage most severely affects the device parameters FF and J_{SC}, both declining by around 50% on average when no MoOx layer is used. Solar cells with 150 nm thick Spiro-OMeTAD exemplarily still achieve V_{OC} values on direct ITO deposition comparable to the reference devices. This suggests that rather charge transport in the HTM than the perovskite absorber or the perovskite/Spiro-OMeTAD interface is affected in this case by the sputter process.

Monolithic tandem solar cell

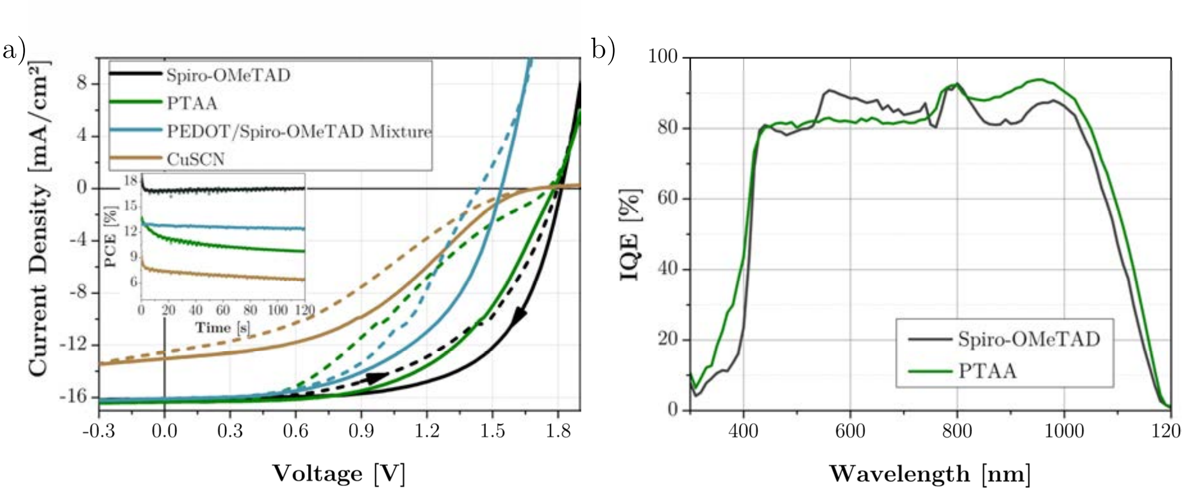

Figure 4.24: a) Current-voltage characteristics of monolithic perovskite-SHJ tandem solar cells under illumination in forward ($V_{Start}<V_{End}$) and reverse ($V_{Start}>V_{End}$) scan direction and maximum power point track in the inset. The devices thereby employed different hole selective contacts in the perovskite top cell: Spiro-OMeTAD, PTAA, 25:75 wt.-% Spiro-OMeTAD:PEDOT mixtures and CuSCN. b) IQE_{PV} of the monolithic perovskite-SHJ tandem solar cells with Spiro-OMeTAD or PTAA as perovskite hole selective contact achieving the highest EQE_{PV} and IQE_{PV} values in this study. Corresponding J-V and EQE_{PV} curves are depicted in the appendix, Figure S 22. Note, that these samples differ from the solar cells shown in a).

The different HTMs were finally employed in monolithic perovskite-SHJ tandem solar cells. The general device architecture is SHJ/ITO/SnO_2/”triple-cation” perovskite/HTM/MoOx/ITO/LiF. Corresponding J-V characteristics for devices with Spiro-OMeTAD, PTAA, PEDOT/Spiro-OMeTAD mixtures or CuSCN as respective HTMs are depicted in Figure 4.24 a). Spiro-OMeTAD achieved high V_{OC} values up to 1.82 V, which correlates well with an expected bottom cell V_{OC} of around 0.7 V and a top cell V_{OC} of 1.1-1.15 V. It is close to the 1.83 V achieved with the ITO nanoparticles in the previous chapter and among the highest values realized so far in perovskite-SHJ tandem solar cells of any device architecture. PTAA obtained slightly lower V_{OC} values around 1.77 V and FF (56% in reverse san) but 0.2 mA/cm² higher J_{SC} values as compared to Spiro-OMeTAD (tabulated values in Table 4.2). The EQE_{PV} values of the solar cells, depicted in Figure S 21 in the appendix chapter 7.3, again do not match the currents in JV, presumably similar to the previous chapter due to spectral mismatch of the LED based sun simulator. Yet, EQE_{PV} confirms the trend in J_{SC} with a 0.4 mA/cm² higher integrated photocurrent for the device with PTAA. While the MPP for Spiro-OMeTAD stabilized at 17.3%, the MPP for PTAA was constantly decreasing to below 10% after five minutes. This effect has been observed as well in chapter 4.1 for metal oxide ETMs with presumably slow charge extraction. The decreasing MPP over time together with the low FF might indicate poor charge collection by the PTAA, possibly related to insufficient doping of the polymer. Therefore further optimization of the doping procedure might be necessary, e.g. by adjusting the post-deposition treatment of the films with longer storage in dry air before further processing of the top electrode. Tandem devices with CuSCN again suffered from poor FF and low J_{SC} values, similar to what has been observed in single-junction solar cells upon deposition of MoOx on CuSCN. The diminished performance is therefore most likely attributable to the MoOx/CuSCN interface. Monolithic devices with

PEDOT/Spiro-OMeTAD as HTM on the other hand revealed rather low V_{OC} values (around 1.5 V), leading to stabilized efficiencies at 12.4%. Here, the transition to the larger area of the tandem solar cell with 1 cm^2 as compared to 0.16 cm^2 in single-junction solar cells might require further considerations.

Comparing the tandem solar cells achieving the highest IQE_{PV} values in this study with Spiro-OMeTAD and PTAA as HTMs, highlights the optical potential of the polymer (corresponding EQE_{PV} curves are shown in appendix, Figure S 22). The parasitic absorption is reduced by around 5-10% absolute in the long wavelength regime above 800 nm and for short wavelengths below 400 nm. Between 500 and 800 nm, surprisingly, IQE_{PV} is larger for the solar cell with Spiro-OMeTAD as compared to the device with PTAA as HTM. This might however also be attributed to non-optical origins such as differences in the perovskite absorber quality and thus in internal photon-to-electron conversion efficiencies. In order to elucidate the optical potential of the different HTMs in more detail, optical simulations are performed in the following.

Table 4.2: Current-voltage parameters under illumination in forward and reverse scan direction for the devices shown in Figure 4.24 a).

HTM	***Scan Direction***	***J_{SC} [mA/cm²]***	***V_{OC} [V]***	***FF [%]***	***PCE [%]***
Spiro-OMeTAD	*forward*	16.1	1.80	53.5	15.51
	reverse	16.1	1.82	64.3	18.81
PTAA	*forward*	16.3	1.76	36.1	10.34
	reverse	16.3	1.78	56.1	16.32
PEDOT/Spiro-OMeTAD	*forward*	16.1	1.44	52.1	12.1
	reverse	16.1	1.54	54.4	13.5
CuSCN	*forward*	16.3	1.17	27.6	5.26
	reverse	16.3	1.44	44.7	10.53

Optical simulations

The previous results and considerations revealed realistic constraints of the individual top contact layer stacks and different HTMs that could potentially be utilized. With that a more accurate analysis of the achievable efficiency and thus a detailed loss analyses can be drawn in the following, serving as guideline for future development. To validate the capacity of the optical simulations performed here, experimentally determined reflection and EQE_{PV} measurements of initial perovskite-SHJ tandem solar cells with different HTMs are shown to be well reproduced (Figure 4.25) by the simulation. Layer thicknesses in simulations of around 500-530, 21, 105 and 140 nm for perovskite, MoOx, ITO and LiF, respectively, as well as 160 nm for Spiro-OMeTAD and 50 nm for PEDOT/Spiro-OMeTAD mixtures are in line with the layer thicknesses extracted from cross-section SEM images (Figure S 24, chapter 7.3). Less pronounced interferences observed in the experiment for wavelengths below 780 nm can be attributed to a certain roughness of the top contact, predominantly induced by the perovskite surface, which in simulations is assumed as perfectly planar. These differences are well pronounced for the tandems containing Spiro-

OMeTAD. Indeed, the investigated devices are covered with 1 hour sonicated, small agglomerates of ITO nanoparticles as introduced in chapter 4.3.2. The surface is therefore distinctly roughened, as can be seen in the SEM images (Figure S 24, chapter 7.3). Besides, the IQE_{PV} of the perovskite sub cell is lower than expected from simulation, which can as well be attributed to the increased parasitic absorption by ITO nanoparticles in the short wavelength regime, shown before. In addition to underestimated parasitic absorption, also non-unity charge collection might cause a lower EQE_{PV} for the perovskite top-cell, especially as the simulated absorption to measured EQE_{PV} is relatively independent of the photon energy. The Si absorption in contrast shows consistent curves between measurement and experiment. Further, the general characteristics of the interference patterns are well reproduced by the optical simulations.

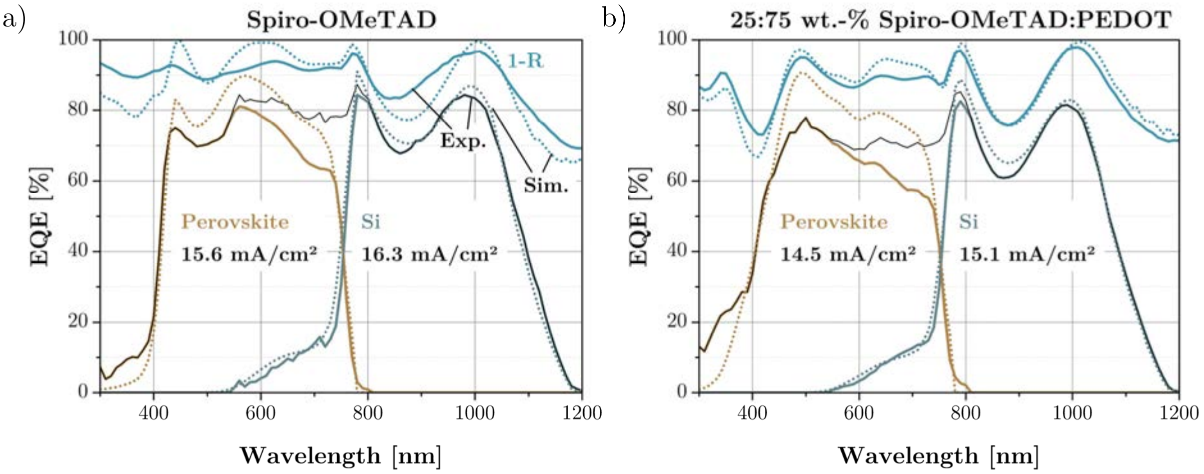

Figure 4.25: Experimentally determined reflection and EQE_{PV} measurements of monolithic perovskite-silicon heterojunction tandem solar cells with a) Spiro-OMeTAD and b) PEDOT/Spiro-OMeTAD mixtures as top cell HTM, compared to characteristics reproduced by optical simulations. Solid lines display the experimental results, dotted lines the simulated values. The black line further represents the sum of both measured sub cell EQE_{PV}. Given values state the integrated short-circuit current density of the actually measured EQE_{PV} responses.

The comparison between simulation and experiment allows to confidently perform layer thickness optimizations for the top contact to determine the maximum achievable J_{SC} in monolithic perovskite-SHJ tandem solar cells for the different HTMs with reasonable estimates. According to the previous experimental results, layer thicknesses for MoOx, Spiro-OMeTAD, PTAA, PEDOT/Spiro-OMeTAD mixtures and CuSCN are set to 25, 150, 50, 50 and 60 nm, respectively. Further, the perovskite, ITO and LiF thickness were varied in 10 nm steps in the ranges of 250-450 nm, 80-140 nm and 90-150 nm, respectively, to determine the optically optimized parameters. The complete tandem device architecture utilized in the optical simulations is depicted in Figure 4.26 a). The results are summarized in Table 4.3 and absorption in the different layers is displayed in Figure 4.26 b) for the different HTMs. Front electrode thereby comprises absorption in LiF (negligible), ITO and MoOx (typically 0.2 mA/cm² as no sputter damage induced parasitic absorption is assumed here), other losses occur in the back ITO and Ag, a-Si and ITO tunnel recombination junction layers.

The optical simulations reveal that perovskite-SHJ tandem solar cells with the herein used perovskite band gap of 1.64 eV and back textured SHJ bottom cells can achieve a maximum J_{SC}

of 17.4 mA/cm² for Spiro-OMeTAD as top cell HTM. This is slightly lower than found in a previous, comparable study by Jäger et al.[24] for planar perovskite-SHJ tandem solar cells (17.6 mA/cm²). However, the previous study utilized highly transparent ITO layers and essentially neglected parasitic absorption at the rear contact. Here, reported optical data of ITO[239] are used which accurately reproduce the absorption of herein deposited thin films (Figure S 23). Further, plasmonic absorption in the rear contact becomes more relevant for textured back surfaces, and is reproduced in the simulations by assuming a more absorptive ITO layer instead of the ZnO:Al, utilized in the real device. The validity of this approach is shown by the well matching EQE_{PV} results for the Si bottom cell shown in Figure 4.25. The achievable J_{SC} values determined here thus present a more conservative estimation as compared to the previous report[24], yet at higher practical feasibility. Indeed, experimentally realized values in this architecture are so far considerably lower than the herein determined limits, with highest tandem J_{SC} values around 16.5 mA/cm².[215] Besides, the general trends in maximum J_{SC} for alternative HTMs still hold, as simulated losses in the front and rear contacts are rather similar in all cases.

Table 4.3: Minimum and maximum layer thicknesses for optical simulations as well as optimum values determined to achieve the maximum J_{SC} in perovskite-silicon heterojunction tandem solar cells with Spiro-OMeTAD, PTAA, 25:75 wt.-% Spiro-OMeTAD:PEDOT mixtures or CuSCN as top cell HTM. Resulting J_{SC} and estimated tandem solar cell PCE values are given for the different HTMs as well as the relative change of the parameters as compared to the Spiro-OMeTAD reference HTM. PCEs are estimated with tandem solar cell V_{OC} values of 1.854, 1.854, 1.864 and 1.814 V comprising Spiro-OMeTAD, PTAA, PEDOT/Spiro-OMeTAD mixtures or CuSCN as top cell HTM, respectively. FF is assumed in all cases to amount to 80%. Detailed explanations are given in the text.

	Min	*Max*	*Spiro-OMeTAD*	*PTAA*	*PEDOT/Spiro-OMeTAD*	*CuSCN*
LiF [nm]	90	150	110	100	100	100
ITO [nm]	80	140	140	100	100	100
Perovskite [nm]	250	450	400	380	340	330
J_{SC} max [mA/cm²]	-	-	17.4	17.9	17.2	18.4
$\Delta J_{SC,Spiro\text{-}OMeTAD}$	-	-	0%	+2.9%	-1.1%	+5.7%
Tandem PCE [%]	-	-	25.8	26.5	25.5	26.4
$\Delta PCE_{Spiro\text{-}OMeTAD}$	-	-	0	+2.9%	-0.6%	+3.5%

Regarding the alternative HTMs, the highest J_{SC} value in monolithic tandem devices can be achieved with CuSCN as hole contact (18.4 mA/cm²), followed by PTAA (17.9 mA/cm²) and PEDOT/Spiro-OMeTAD mixtures (17.2 mA/cm²). This represents a maximum relative increase in J_{SC} of 5.7% for CuSCN as compared to Spiro-OMeTAD as HTM. The corresponding reflection and absorption spectra for optimized tandem solar cells employing Spiro-OMeTAD and CuSCN are displayed in Figure 4.26 c), and for all other HTMs in Figure S 26. Further, Figure 4.26 b) highlights that in in all cases, reflection imposes the largest loss mechanism for the tandem solar cells with 5.5-6 mA/cm². Also, the front ITO with absorption of 1.5-1.9 mA/cm² provides potential for further improvements. Besides that, PEDOT/Spiro-OMeTAD mixtures are expected to cause parasitic losses comparable to doped Spiro-OMeTAD in optimized devices around 2.6 mA/cm^2. In contrast, PTAA and CuSCN successfully remedy absorption in the HTM and reduce the integrated loss to 1.1 and 0.3 mA/cm^2, respectively.

However, the different HTMs also alter the electric properties of the perovskite top cell. Spiro-OMeTAD[26, 117] and PTAA[153] were shown in PSCs to allow potential losses between the band gap energy and $e \cdot V_{OC}$ as low around 0.4 eV. Further, the passivating effect of mixed PEDOT/Spiro-OMeTAD layers even allows to outperform the potential loss induced by doped Spiro-OMeTAD films on perovskite surfaces, as shown in chapter 4.2. On the other hand, the best performing PSCs with CuSCN hole contacts achieved a maximum V_{OC} of only 1.11 V in literature with an average 40 mV lower value as compared to reference devices employing Spiro-OMeTAD.[267] The perovskite top cell comprising Spiro-OMeTAD is estimated to realistically achieve open circuit voltages of 1.15 V in tandem configuration, as this has been realized here already for semi-transparent solar cells (Figure S 25). V_{OC} values of 1.15 V for PTAA, 1.16 V for PEDOT/Spiro-OMeTAD mixtures as well as 1.11 V for CuSCN as HTMs of the perovskite sub cell can accordingly well be assumed. The Si bottom cell used here further delivers 725 mV of V_{OC} under STC, which are expected to drop in the tandem device to around 704 mV due to shading by the top cell, as seen by equation (2.8) in chapter 2.1.3.[24] Finally, assuming an optimized FF in the tandem solar cell of 80% in all cases which is a high but realistic value[173] allows to estimate the maximum PCE for each perovskite HTM.

Following the previous considerations, the optimized tandem solar cell efficiencies amount to 25.8%, 26.5%, 25.6% and 26.7% for Spiro-OMeTAD, PTAA, PEDOT/Spiro-OMeTAD mixtures as well as CuSCN as HTM of the perovskite top cell, respectively. Regarding the reference device with Spiro-OMeTAD as top cell HTM, this represents a maximum relative increase in PCE of 3.5% for CuSCN and a slightly lower improvement (2.9%) for PTAA as top cell HTM. PEDOT/Spiro-OMeTAD mixtures as top cell HTM instead slightly decrease the achievable efficiency in tandem solar cells by 0.6% relative to the reference architecture.

As expected from its high transmittance, CuSCN is revealed to enable the lowest optical losses. However, the expected gain in PCE as compared to PTAA is only around 0.2% absolute due to higher potential losses. Besides, the experimental results imply an electrically disrupted CuSCN/MoOx interface, which causes low FF on device level. This further impedes realization of high efficiencies in monolithic tandem solar cells. Therefore, PTAA is the most promising HTM of the investigated materials to replace Spiro-OMeTAD as top cell HTM in tandem application and increase the device efficiencies by around 0.7% absolute or 2.9% relative. The most efficient four-terminal tandem device with a *n-i-p* type perovskite top cell as well utilized PTAA as the HTM, which is in line to the optical advantages presented here.[210]

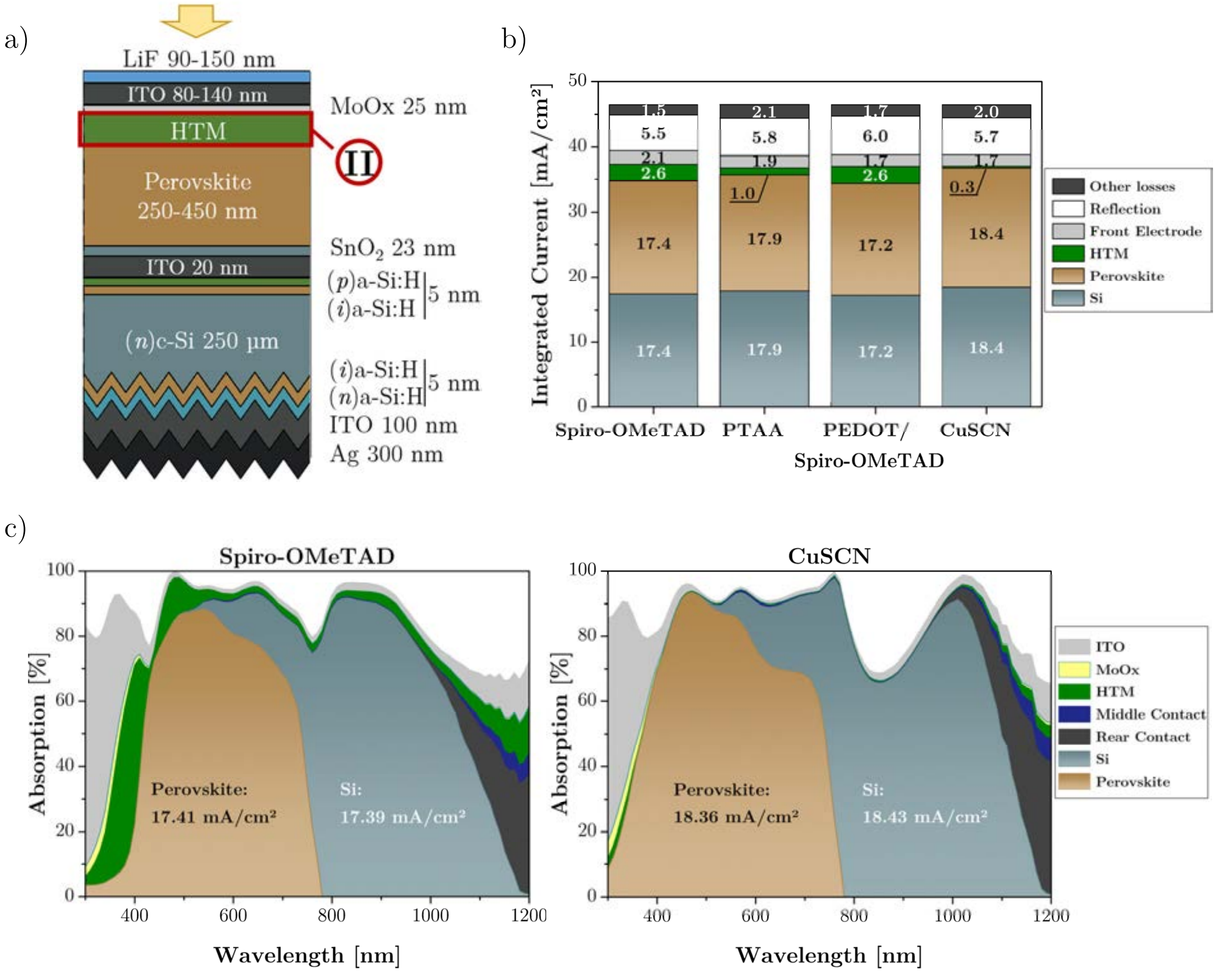

Figure 4.26: a) Schematic device architecture and corresponding layer thicknesses used for optical simulations. The altered HTMs in region II are Spiro-OMeTAD, PTAA, 25:75 wt.-% Spiro-OMeTAD:PEDOT mixtures and CuSCN with thicknesses of 150 nm, 50 nm, 50 nm and 60 nm, respectively. b) Integrated absorption under AM1.5G illumination for the different layers in tandem solar cells with different perovskite HTMs. c) Spectral absorption profiles for optimized monolithic perovskite-silicon heterojunction solar cells with the top cell comprising Spiro-OMeTAD (left) and CuSCN (right) as *p*-type contact.

Further optical optimization potentials

In summary, monolithic perovskite-SHJ tandem solar cells with *n-i-p* type perovskite top cells are highly desirable. For perovskite single-junctions, the highest efficiencies have been achieved so far in *n-i-p* geometry. Also the SHJ bottom cell was reported to perform best in front emitter on *n*-type wafer configuration, as *p*-type wafers tend to suffer from pronounced surface recombination and front emitters can outperform rear emitter SHJ due to improved charge transport on the stronger illumination of the a-Si.[195] The high V_{OC} values up to 1.83 V realized here in tandem solar cells exceed the values reported so far for monolithic perovskite-silicon tandem solar cells and underline the potential of this architecture.

However, even for CuSCN as the most transparent HTM in the presented comparison, the maximum achievable J_{SC} according to simulations is lower than already realized values for monolithic tandem solar cells with a *p-i-n* perovskite top cell architecture, in the following also called “inverted” architecture. Bush et al. achieved integrated J_{SC} values from EQE_{PV} of

18.9 mA/cm² in the perovskite and 18.5 mA/cm² in the Si sub cell for an absorber of similar band gap.[107] The difference here originates from two main points. First, Bush et al. enhanced the infrared absorption of the SHJ bottom cell by introducing silicon nanoparticles between the rear metal and ITO to successfully reduce plasmonic absorption. Second, reflection losses for the tandem device by Bush et al. amount to only 4.8 mA/cm². For the herein investigated “regular” tandem devices with *n-i-p* type top cells instead, optical simulations revealed that more than 10% of the achievable current, or around 5.5 mA/cm², is lost by reflection. Figure 4.27 a) depicts the spectral refractive indices of the different layers throughout the device stack of a “regular” monolithic tandem comprising Spiro-OMeTAD. Further, Figure 4.27 b) displays the similar dependence but for all investigated HTMs and for a single wavelength of 850 nm. Obviously, there is poor index matching between MoOx, the HTM and perovskite which enhances reflection losses. C_{60} on the other hand, typically used as top selective contact in “inverted” tandem solar cells, has a refractive index of around 2 and matches well between ITO (n≈1.9 at 850 nm) and perovskite (n≈2.3 at 850 nm). Replacing 50 nm of PTAA in “regular” tandem devices with 20 nm of C_{60}, while keeping all remaining layers identical, reduces reflection, according to optical simulations, by 1.3 mA/cm² from 5.7 to 4.4 mA/cm². Therefore, another desirable material property for an alternative HTM towards higher J_{SC} values in “regular” monolithic tandems is a refractive index around 2.

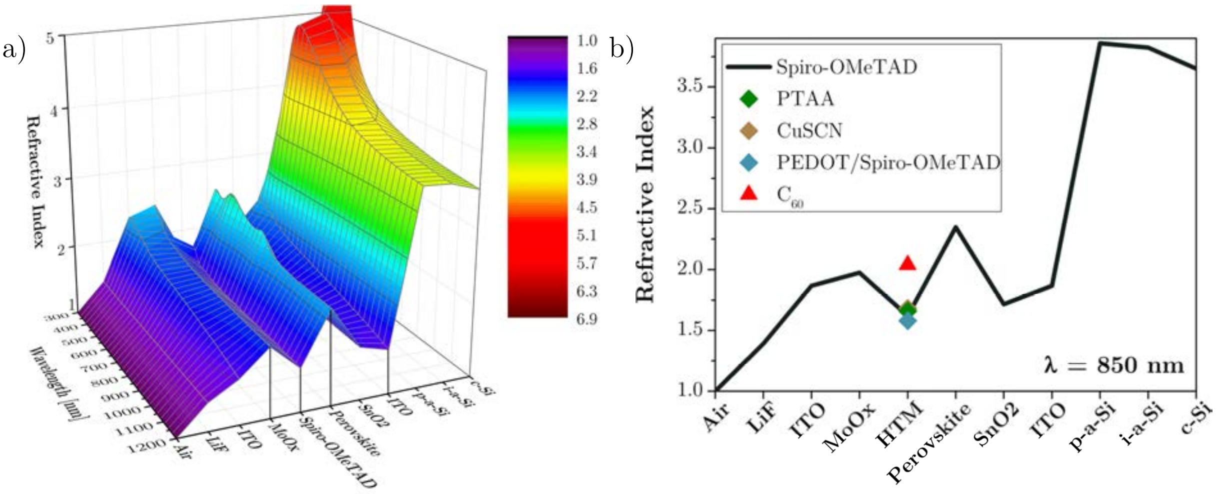

Figure 4.27: Refractive indices throughout the layer stack of a monolithic perovskite-silicon heterojunction tandem solar cell from top electrode to Si absorber. a) Spectrally resolved with Spiro-OMeTAD as top cell HTM and b) for a single wavelength of 850 nm and given refractive indices of all HTMs investigated in this chapter.

The second origin of Fresnel reflection in regular tandems distinguishable in Figure 4.27 is the transition from the middle ITO to (*p*)a-Si:H, with an increase in refractive index from 1.9 to 3.9 at 850 nm wavelength. Replacing the (*p*)a-Si:H layer by a *p*-type nanocrystalline silicon oxide with tunable refractive index between 2.0 and 2.7 can significantly mediate reflection losses from this interface by around 1.5 mA/cm², as shown before for “inverted” tandem stacks.[309, 310]

Alternatively, more effective light management schemes could resolve reflection losses and enhance the light absorption. As an example, adhesive textured foils without the necessity of an index matching liquid have been applied very recently in our group on top of “inverted” perovskite-silicon tandem solar cells.[216] As a result, reflection was reduced from 6.1 to 2.5 mA/cm^2 and efficiency raised from 23.4 to 25.5%.

Besides, the experimentally realized TCO front contact with optical properties comparing well to Zhang et al.[239] induces losses of 1.5-1.8 mA/cm^2. Utilizing instead a highly transparent TCO[220], similar to simulations by Jäger et al.[24], would reduce parasitic absorption in the ITO by around two thirds. An alternative TCO with higher mobility and thus less required carrier density and with that free carrier absorption is In_2O_3:H.[178] However In_2O_3:H needs to be crystallized for best optoelectronic properties at 160°C which would degrade the perovskite top cell. Thus other high mobility TCO materials or reduced crystallization temperatures need to be developed.

Further, the herein used mixtures of PEDOT and Spiro-OMeTAD are based on a highly conductive PEDOT formulation with strong parasitic absorption. This PEDOT could potentially be exchanged by a less conductive but more transparent formulation. In turn, this could reduce parasitic absorption losses in the hole contact and might enable higher PCE values as compared to tandem solar cells with Spiro-OMeTAD as HTM.

Assuming instead PTAA as top contact HTM with reduced reflections of 2.5 mA/cm^2, as demonstrated for "inverted" tandems with the adhesive light-management foil, and reduced front ITO absorption by another 1 mA/cm^2 could allow 2.1 mA/cm^2 higher tandem J_{SC} values, which would result in PCE values of 29.7%. Reducing the rear contact absorption to below 1 mA/cm^2, as demonstrated by Bush et al.[311], could further increase the J_{SC} by around 0.5 mA/cm^2 and push the PCE to 30.4% and above.

Further efficiency gains are achievable by band gap tuning of the perovskite absorber. The spectral absorption profiles in Figure 4.26 clearly highlight that absorption in Si above the band gap energy of the perovskite absorber is necessary to achieve current matching of the two sub cells. This of course counteracts the approach to minimize thermalization losses, and thus reduces the overall PCE potential. Band gap tuning of the perovskite absorber towards higher energies is therefore necessary to resolve this limitation.

4.3.4 Conclusions

Two scientifically important options to optically improve *n-i-p* type perovskite-SHJ tandem solar cells have been evaluated here and were summarized in chapters 4.3.2 and 4.3.3. First, reduction of MoOx during sputter deposition of ITO is shown to significantly raise absorption losses of this layer stack as compared to the expected absorption from simulations. Interlayers of around 2 or 3 nm thick SnO_2 or ITO nanoparticles successfully mitigate this effect. While most of the interlayers however suffered from poor charge transport and diminished fill factors, 2 nm of SnO_2 revealed a reduction in current-voltage hysteresis, increased V_{OC} values and a reduced PCE by only 1% absolute as compared to a device without interlayer. Further, buffer layers of small ITO nanoparticle agglomerates which did not improve the optical properties, yet enhanced the device performance and as well reduced hysteresis. Applying the nanoparticles in monolithic perovskite-silicon tandem solar cells achieved high open circuit voltages of 1.83 V, and an enhanced perovskite top cell EQE_{PV} as compared to a device without interlayer. This results in an improved efficiency of 21.4% with ITO nanoparticles interlayer as compared to 19.8% without, or 18.0 and 17.7%, respectively, when referencing to the integrated J_{SC} value from EQE_{PV} measurements. Alternatively, ITO deposition at low incidence angles and high deposition rates is identified to alleviate chemical reduction of the MoOx, mitigating around 50% of the absorption increase in standardly deposited MoOx/ITO stacks. Further studies might reveal if combining small agglomerate ITO nanoparticles as buffer layer underneath low angle deposited ITO allows to improve both the transparency of the top electrode stack and the performance of the tandem solar cells.

Second, potential replacements of the Spiro-OMeTAD [2,2‘7,7‘-tetrakis(N,N-di-p-methoxyphenylamin)-9,9‘-spirobifluoren] hole transport material (HTM) were investigated to reduce parasitic absorption in perovskite-silicon heterojunction tandem solar cells. PTAA [poly(triaryl amine)], mixtures of PEDOT [poly(3,4-ethylenedioxythiophene)] and Spiro-OMeTAD as well as CuSCN were evaluated as promising materials. Optical properties of the different HTMs were acquired and revealed superior transmittance for CuSCN, as well as for PTAA in longer wavelength regimes. The highly conductive PEDOT in contrast is shown to suffer from distinct absorption over a wide spectrum. Next, experimental results in single-junction perovskite solar cells (PSCs) revealed optimized layer thicknesses of the HTMs of 150 nm, 50 nm, 50 nm and 60 nm for Spiro-OMeTAD, PTAA, PEDOT/Spiro-OMeTAD and CuSCN, respectively. The thinner optimized thicknesses for the polymeric HTMs also helped to reduce parasitic absorption as compared to Spiro-OMeTAD layers. Further, 25 nm of MoOx were found in semi-transparent PSCs to be sufficient for all HTMs to provide sputter protection of the organic HTM materials during ITO deposition. Finally, initial experimental results of monolithic tandem solar cells revealed the best electronic properties when employing Spiro-OMeTAD as HTMs. CuSCN further suffered from strong charge extraction barriers which were attributed to the CuSCN/MoOx interface. PTAA and PEDOT/Spiro-OMeTAD seem to require further optimization of the doping procedure and the homogeneity of the layer deposition, respectively. However, tandem devices with PTAA as HTM achieved higher J_{SC} (0.2 mA/cm^2) and EQE_{PV} values (>0.4 mA/cm^2) for both sub cells as compared to devices with Spiro-OMeTAD, thereby proving higher transmittance of the top contact. To evaluate the performance potential of monolithic tandem solar cells with the different HTMs in more detail, optical simulations were performed.

The experimental results were optically well reproduced by simulations taking measured thicknesses and optical constants into account. This validation and the knowledge on boundary conditions such as optimized thicknesses per HTM allowed to determine realistic estimates of the maximum achievable J_{SC} in monolithic perovskite-silicon heterojunction solar cells employing the different HTMs. The results revealed a potential reduction of the parasitic absorption in the HTM by 90% from 2.6 to 0.3 mA/cm^2 and a gain in tandem J_{SC} from 17.4 to 18.4 mA/cm^2 by replacing Spiro-OMeTAD with CuSCN. However, even the best reported solar cells with CuSCN as HTM obtained around 40 mV lower V_{OC} values as compared to devices with Spiro-OMeTAD. As a result, the expected maximum PCE for tandem solar cells with CuSCN as HTM amounts to 26.7%, 0.2% and 0.9% absolute higher than for PTAA (26.5%) and Spiro-OMeTAD (25.8%), respectively. Tandem devices with PEDOT/Spiro-OMeTAD mixtures on the other hand achieve slightly lower maximum J_{SC} values due to higher reflection losses in the optimized devices. Consequently, also the achievable efficiency was reduced to 25.6%, a relative loss of 0.6% as compared to devices with Spiro-OMeTAD.

Realization of the highest tandem device efficiencies with CuSCN as top cell HTM however appears difficult to implement, as the CuSCN/MoOx interface is shown here, both in single-junction and tandem solar cells, as inferior for charge collection. Therefore, PTAA is uncovered here as the most promising material to replace Spiro-OMeTAD in tandem solar cells, with an expected reduction in parasitic absorption of the HTM by 60% and a relative increase in J_{SC} and PCE by 2.9%. It has further been shown, that reflection imposes the largest optical loss in herein investigated monolithic tandem solar cells. Two main origins of these reflection losses were identified: first, the low refractive indices of the utilized HTMs, all around 1.6, were shown to cause considerable Fresnel reflections. Utilizing a different HTM with higher refractive index might be difficult, as only few materials have achieved >20% efficiencies so far in *n-i-p* type perovskite single junction devices. Second, the ITO/(*p*)a-Si:H tunnel recombination junction between the sub cells introduces an abrupt increase of the refractive index (n) from around 2 to around 4. Replacing the a-Si with nanocrystalline silicon oxide of n=2.0-2.7 could provide better index matching here. Besides, additional light management schemes such as applying textured foils at the top contact might be a promising approach to enhance light harvesting in tandem solar cells. Following these guidelines and reducing parasitic absorption losses in the front ITO and rear electrode allows enhanced efficiencies of above 30% in monolithic tandem solar cells.

5. Conclusions and Outlook

This thesis was motivated by the promising potential of the perovskite/silicon tandem solar cell technology to achieve high efficiencies of 30% and above, which attracted significant interest in recent years from both research and academia. The work aimed at establishing efficient low-temperature processed charge selective contacts for perovskite solar cells and to understand respective changes in interface and material (or contact) properties and their impact on device performances on both the single junction and tandem level. Deposition temperatures below 200°C further allow implementation of silicon heterojunction (SHJ) bottom cells into monolithic tandem devices, which have lately shown the highest efficiencies in silicon photovoltaics.

To develop test structures for contact material analysis, deposition routines from solution were developed and integrated in planar *n-i-p* type solar cells, following the superstrate layer configuration: glass/ITO/n-type contact/perovskite/p-type contact/Au. The presented results for a variety of different contact materials, also employing new contact materials, emphasize how charge selective contacts govern the device performance in perovskite photovoltaics. Non-radiative recombination losses at both the *n*- and *p*-type selective contacts are revealed in this work to not only amplify current-voltage hysteresis but also determine the open circuit voltages (V_{OC}) in perovskite solar cells. Suppressing non-radiative recombination losses at the perovskite/selective contact interfaces therefore is identified as a key strategy for further gains in device efficiency.

A second important issue in perovskite-SHJ tandem solar cells with *n-i-p* type top cell is the *p*-type contact/molybdenum oxide (MoOx)/ITO top layer stack, through which light enters the device. High optical transmittance therefore is another substantial requirement for these contact layers. It was underlined here, that careful consideration of the MoOx/ITO interface and replacing the standardly employed *p*-type contact Spiro-OMeTAD [2,2‘7,7‘-tetrakis(N,N-di-p-methoxyphenylamin)-9,9‘-spirobifluoren] with more transparent hole transport materials (HTM) are important measures to reduce parasitic absorption losses and increase the tandem solar cell efficiency. Further, substantial reflection losses of tandem devices with *n-i-p* type top cells were revealed, due to poor refractive index matching between the HTMs and the adjacent layers. Utilizing higher refractive index materials as HTM or employing additional light-management schemes is therefore required. The presented results can serve as design guidelines for further development of monolithic perovskite tandem solar cell efficiencies to above 30%.

5.1 Double-Layer Selective Contacts for Improved Device Performance and Reduced Hysteresis

The best performing perovskite solar cells (PSCs) to date employ high-temperature sintered mesoporous TiO_2 as electron contact, which are complex in processing and renders them incompatible with SHJ devices. To identify promising alternatives towards monolithic tandem integration, chapter 4.1 presented a comparative study of different low-temperature deposited *n*-type selective contacts in planar *n-i-p* type PSCs. The metal oxides TiO_2, SnO_2, and fullerenes C_{60}, PCBM (phenyl-C_{60}-butyric acid methyl ester), ICMA (indene-C_{60} monoadduct) as well as double-layers of metal oxide/PCBM were examined as potential electron transport materials

(ETMs). Scanning electron microscopy images and surface photovoltage measurements revealed comparable absorber morphologies and qualities on all ETMs except TiO_2, where a stronger influence of defect states, possibly from TiO_2, was observed. The profound comparison of absorber qualities on different ETMs was shown here for the first time in PSCs, and allowed to directly correlate the device performance and photocurrent hysteresis over a broad range of scan speeds to the respective contact properties.

For solar cells with single-layer ETMs, fullerenes outperformed the metal oxide ETMs with faster electron extraction, implied by transient photoluminescence, less pronounced hysteresis and higher power outputs stabilizing closer to the reverse J-V curve. However, only their combination in double-layer ETM structures led to negligible photocurrent hysteresis and highest device efficiencies up to 18.0% stabilized. J—V measurements correlated the significant performance enhancements for TiO_2/PCBM double-layer ETMs to strongly reduced recombination losses. The combination of materials thereby allows to merge good charge extraction with high selectivity at the interface. Three beneficial effects of the double- as compared to PCBM single-layer ETMs were proposed: (i) increased shunt resistance, (ii) improved hole blocking by the additional wide band gap metal oxide, and (iii) decreased charge transport losses due to an energetically more favorable contact. Claims (ii) and (iii) were also supported by photoelectron spectroscopy (UPS) measurements.

TiO_2/PCBM therefore represent a promising *n*-type contact for monolithic perovskite-SHJ tandem solar cells. This comparative study further highlights the necessity to reduce interface recombination in PSCs and confirms double-layer selective contacts as a universal approach to establish efficient and highly selective contacts. In line with this, more recent works have utilized planar double-layer ETMs of TiO_2/SnO_2 in 21.1% efficient *n-i-p*[158] or of LiF/C_{60} in close to 21% efficient *p-i-n* type PSCs[29], both being amongst the highest values reported so far for the respective device architectures.

5.2 PEDOT/Spiro-OMeTAD Mixtures as Passivating Hole Contact

Doped Spiro-OMeTAD is the most commonly used hole transport material (HTM) in *n-i-p* type perovskite solar cells and achieved high efficiencies around 22%.[26, 152] Yet, its dopants were found to enhance non-radiative recombination at the perovskite interface and limit the V_{OC} in PSCs.[257] Thus, mixtures of dopant-free Spiro-OMeTAD and water-free PEDOT were employed in this study for the first time as HTM in PSCs. Lateral conductivities of these mixed HTM layers were found to be similar to doped Spiro-OMeTAD films. UPS studies on thin films of Spiro-OMeTAD and PEDOT revealed a superposition of the energetic states of the two pure species which excludes perfect vertical phase segregation of the two species.

Remarkably, water-free PEDOT was found to suppress non-radiative recombination at the top perovskite interface. Time-resolved and absolute photoluminescence (PL) measurements revealed enhanced PL lifetimes and quasi-Fermi level splitting (QFLS) when PEDOT or PEDOT/Spiro-OMeTAD mixtures were coated on perovskite absorbers. High QFLS of 1.24 eV were realized for perovskite/HTM stacks and allowed high V_{OC} values of up to 1.19 V in complete solar cells. This exceeded V_{OC} values in devices with doped Spiro-OMeTAD as HTM in this study and represents the lowest potential loss reported so far for perovskite solar cells comprising PEDOT as HTM.

Blending dopant-free Spiro-OMeTAD into the PEDOT and optimizing the HTM deposition moreover enhanced charge extraction at the perovskite/HTM interface. Fill factors (FF) of the resulting solar cells increased from 65% to above 70% and consequently PCEs up to 16.8% stabilized efficiency were achieved. The presented study thereby demonstrates, that HTMs (or ETMs) can combine the functionalities of efficient charge selective contacts and surface passivation layers. This dual capability has not been shown this way before in perovskite photovoltaics and represents a compelling strategy for further efficiency gains of this technology.

5.3 Optical Optimizations of the Top Contact in Perovskite-Si Tandem Solar Cells

The top electrode stack in monolithic perovskite-SHJ tandem solar cells comprises the layer sequence of *p*-type contact/MoOx/ITO. Two main aspects within this layer sequence were identified, analyzed and optimized. First, the chemical reduction of MoOx during sputter deposition of ITO is shown to raise the parasitic absorption of the overall front contact layer stack. Interlayers of around 2 or 3 nm thick SnO_2 prepared by atomic layer deposition or ITO nanoparticles successfully mitigate this effect. However, most of the MoOx/interlayer/ITO interfaces suffer from poor charge transport properties and low fill factors in perovskite solar cells. Only 2 nm of SnO_2 obtained reasonable device efficiencies, yet still 1% absolute lower than a device without interlayer. Instead, static ITO deposition at low incidence angles avoids the reduction of MoOx to a certain extent, mitigating around 50% of the absorption increase for standardly deposited MoOx/ITO stacks. Besides, small agglomerates of ITO nanoparticles as buffer layers are shown to improve the device performance in monolithic perovskite-silicon tandem solar cells from 19.8 to 21.4% in current-voltage measurements at high open circuit voltages of 1.83 V.

Second, alternative hole transport material (HTM) are investigated to replace the strongly absorptive Spiro-OMeTAD in tandem solar cells. PTAA[153] [poly(triaryl amine)], mixtures of PEDOT [poly(3,4-ethylenedioxythiophene)] and Spiro-OMeTAD as well as CuSCN[267] achieved high efficiencies in PSCs and were thus evaluated as promising materials. Optically, superior transmittance was revealed for CuSCN, as well as for PTAA in longer wavelength regimes, whereas PEDOT shows stronger absorption over a wide spectral range. First, the minimum necessary thicknesses of the HTMs and the MoOx layer in single-junction PSCs were experimentally determined. Next, initial monolithic tandem solar cells with the different HTMs revealed highest electrical performance for Spiro-OMeTAD as HTM and lower FF and V_{OC} values for solar cells with the remaining HTMs. However, for PTAA as HTM, a raise in device J_{SC} and EQE_{PV} for both sub cells was realized, proving an increased transmittance of the top contact.

Following the experimentally determined layer constraints, optical simulations were further performed after their successful validation by comparison to the experiment. Tandem solar cells with PEDOT/Spiro-OMeTAD mixtures as HTM are expected to obtain 1.1% lower optimum J_{SC} values and 0.6% reduced efficiencies relative to devices employing doped Spiro-OMeTAD. Instead, replacing Spiro-OMeTAD with CuSCN in tandem solar cells revealed the largest enhancement in J_{SC} by 5.7% relative. Yet, CuSCN is expected to suffer from lower V_{OC} values[267], and the CuSCN/MoOx interface is shown here to achieve poor charge extraction. PTAA on the other hand provides a 60% reduction of the HTM absorption and an increase in J_{SC} of 2.9% (to 17.9 mA/cm^2) relative to devices with Spiro-OMeTAD as HTM. As also good interface properties can be assumed[153], the optimum PCE is expected to rise from 25.8 to 26.5% when replacing Spiro-OMeTAD with PTAA. The polymer therefore represents the most promising alternative p-type contact of the examined materials for tandem solar cells with *n-i-p* type perovskite top cell. Finally, large reflection losses above 5 mA/cm^2 have been identified as severe problem of this tandem architecture, arising partially from the low refractive indices of the HTMs. Therefore, along with a transition to PTAA as HTM, improved light management schemes are required, e.g. by textured foils at the top electrode. When enabling reduced parasitic absorption losses in the front ITO and rear contact, tandem PCE values above 30% are shown to be realistically achievable.

5.4 Outlook

This work clearly underlines the importance of the interfaces between absorber and selective contact layers in perovskite solar cells. It was shown that suppression of interface recombination losses is vital in this technology. Suppressing surface recombination has also been a major obstacle in the last decades in Si photovoltaics and lead to the development of the SHJ cell utilized here. The basic concept of the SHJ cell matches surprisingly well with the mechanisms observed here for the double-layer contact structure or the PEDOT/Spiro-OMeTAD mixtures. An intrinsic amorphous silicon layer with a low defect density at the interface provides minimized surface recombination at the absorber interface, while doped layers of amorphous silicon establish selective charge extraction. For the double-layer ETM, PCBM provided a good interface to the absorber while the additional metal oxide increased the selectivity of the contact. For PEDOT/Spiro-OMeTAD mixtures, on the other hand, both beneficial effects of reduced surface recombination and selective charge extraction were achieved by deposition from a single dispersion. The success of the SHJ architecture in Si photovoltaics suggests that advancing this concept in perovskite photovoltaics can be a key to further efficiency gains. Finding suitable surface passivation layers which still allow efficient charge extraction, either by themselves or supported by an additional selective material, should therefore be of essential interest for future research.

Further, the results presented here enable to draw advanced considerations towards future improvements in the herein utilized monolithic perovskite-SHJ tandem solar cell. Parasitic absorption in Spiro-OMeTAD as top selective contact was shown to impose around 25% of the overall optical losses. Replacing it with more transparent materials while maintaining the electrical performance allows an increase in PCE by above 3% relative. Besides, the MoOx/ITO top contact utilized here was identified to impose severe absorption losses. Higher mobility TCOs such as In_2O_3:H require less carrier densities for similar conductivities and thus could reduce free-carrier absorption occurring at higher wavelengths.[312] Alternatively, MoOx could also be replaced by a more transparent and robust buffer layer, such as the wide band gap NiO e.g. deposited by low-temperature ALD.[299] Also, a less invasive deposition method of the top electrode might resolve the necessity of a sputter protection layer completely.

Moreover, reflection was identified as the major optical loss mechanism in monolithic tandem solar cells with planar *n-i-p* type perovskite cell. Realizing efficient HTMs with a refractive index around 2 would help to reduce Fresnel reflections at the top contact stack. Highest efficiencies on a long-term scale might though be achieved on fully textured Si bottom cells, due to their excellent anti-reflection and light trapping properties. This poses the challenging task to conformal deposit the complete perovskite top cell on the pyramidal Si surface. Yet, a proof of this concept was recently demonstrated for *p-i-n* type devices in perovskite-SHJ tandem solar cells[214] and might serve as an example for the *n-i-p* architecture.

The conclusions derived in this work might therefore pave the way to further develop the perovskite technology and promote device performances both in perovskite single- as well as in monolithic perovskite-SHJ tandem solar cells.

6. Bibliography

[1] U.S. Energy Information Adinistration, *January 2018 Monthly Energy Review*, vol. 0035, no. July. 2018.

[2] ISE Fraunhofer, “Photovoltaics Report,” 2018.

[3] OCDE & IEA, “Market Report Series: Renewables 2017, analysis and forecast to 2022,” *Exec. Summ.*, p. 10, 2017.

[4] N. Christidis, G. S. Jones, and P. A. Stott, “Dramatically increasing chance of extremely hot summers since the 2003 European heatwave,” *Nat. Clim. Chang.*, vol. 5, no. 1, pp. 46–50, 2015.

[5] A. F. Imbery, K. Friedrich, S. Haeseler, C. Koppe, W. Janssen, and P. Bissolli, “Vorläufiger Rückblick auf den Sommer 2018 – eine Bilanz extremer Wetterereignisse,” *DWD*, pp. 1–8, 2018.

[6] International Energy Agency, “Key World Energy Statistics,” 2017.

[7] ITRPV, “International Technology Roadmap for Photovoltaic—,” vol. 9, no. March, 2017.

[8] C. Kost, T. Schlegl, and F. Ise, “Stromgestehungskosten Erneuerbare Energien,” 2018.

[9] M. A. Green, Y. Hishikawa, E. D. Dunlop, D. H. Levi, J. Hohl-Ebinger, and A. W. Y. Ho-Baillie, “Solar cell efficiency tables (version 51),” *Prog. Photovoltaics Res. Appl.*, vol. 26, no. 1, pp. 3–12, Jan. 2018.

[10] P. Würfel and U. Würfel, *Physics of Solar Cells - From Principles To Advanced Concepts*, vol. 3. Weinheim, Germany: Wiley-VCH Verlag GmbH, 2016.

[11] L. C. Hirst and N. J. Ekins-Daukes, “Fundamental losses in solar cells,” *Prog. Photovoltaics Res. Appl.*, vol. 19, no. 3, pp. 286–293, May 2011.

[12] T. Kirchartz and U. Rau, “What Makes a Good Solar Cell?,” *Adv. Energy Mater.*, vol. 1703385, p. 1703385, Mar. 2018.

[13] T. Leijtens, K. A. Bush, R. Prasanna, and M. D. McGehee, “Opportunities and challenges for tandem solar cells using metal halide perovskite semiconductors,” *Nat. Energy*, 2018.

[14] U. W. Paetzold *et al.*, “Scalable Perovskite/CIGS Thin-Film Solar Module with Power Conversion Efficiency of 17.8%,” *J. Mater. Chem. A*, 2017.

[15] Oxford Photovoltaics, “Oxford PV acquires thin-film development line for perovskite scale-up,” 2016. [Online]. Available: http://www.oxfordpv.com/News/20161114-Oxford-PV-acquires-thin-film-development-line-for-perovskite-scale-up.

[16] A. Kojima, K. Teshima, Y. Shirai, and T. Miyasaka, “Organometal Halide Perovskites as Visible-Light Sensitizers for Photovoltaic Cells,” *J. Am. Chem. Soc.*, vol. 131, no. 17, pp. 6050–6051, May 2009.

[17] Z. Xiao, R. A. Kerner, L. Zhao, K. M. Lee, T.-W. Koh, and B. P. Rand, “Efficient Perovskite LEDs Featuring Nanometer Sized Crystallites,” in *Light, Energy and the Environment*, 2017, p. SM4C.3.

[18] National Renewable Energy Laboratory, “Efficiency Chart,” 2018. [Online]. Available:

https://www.nrel.gov/pv/assets/images/efficiency-chart.png.

[19] M. Taguchi *et al.*, “24.7% Record Efficiency HIT Solar Cell on Thin Silicon Wafer,” *IEEE J. Photovoltaics*, vol. 4, no. 1, pp. 96–99, Jan. 2014.

[20] Z. C. Holman, A. Descoeudres, S. De Wolf, and C. Ballif, “Record Infrared Internal Quantum Efficiency in Silicon Heterojunction Solar Cells With Dielectric/Metal Rear Reflectors,” *IEEE J. Photovoltaics*, vol. 3, no. 4, pp. 1243–1249, Oct. 2013.

[21] S. Albrecht *et al.*, “Monolithic perovskite/silicon-heterojunction tandem solar cells processed at low temperature,” *Energy Environ. Sci.*, vol. 9, no. 1, pp. 81–88, 2016.

[22] E. Köhnen, M. Jost, A. Al Ashouri, and S. Albrecht, “25% monolithic perovskite/silicon heterojunction tandem solar cell,” *unpublsihed Work*.

[23] Oxford Photovoltaics, “Oxford PV sets world record for perovskite solar cell,” 2018. [Online]. Available: https://www.oxfordpv.com/news/oxford-pv-sets-world-record-perovskite-solar-cell.

[24] K. Jäger, L. Korte, B. Rech, and S. Albrecht, “Numerical optical optimization of monolithic planar perovskite-silicon tandem solar cells with regular and inverted device architectures,” *Opt. Express*, vol. 25, no. 12, p. A473, Jun. 2017.

[25] M. T. Hörantner and H. J. Snaith, “Predicting and optimising the energy yield of perovskite-on-silicon tandem solar cells under real world conditions,” *Energy Environ. Sci.*, vol. 10, no. 9, pp. 1983–1993, 2017.

[26] M. Saliba *et al.*, “Incorporation of rubidium cations into perovskite solar cells improves photovoltaic performance,” *Science*, vol. 354, no. 6309, pp. 206–209, Oct. 2016.

[27] N. J. Jeon *et al.*, “A fluorene-terminated hole-transporting material for highly efficient and stable perovskite solar cells,” *Nat. Energy*, Jul. 2018.

[28] Y. Yang *et al.*, “Top and bottom surfaces limit carrier lifetime in lead iodide perovskite films,” *Nat. Energy*, vol. 2, no. 2, p. 16207, Jan. 2017.

[29] M. Stolterfoht *et al.*, “Visualization and suppression of interfacial recombination for high-efficiency large-area pin perovskite solar cells,” *Nat. Energy*, Jul. 2018.

[30] L. Kegelmann *et al.*, “It Takes Two to Tango—Double-Layer Selective Contacts in Perovskite Solar Cells for Improved Device Performance and Reduced Hysteresis,” *ACS Appl. Mater. Interfaces*, vol. 9, no. 20, pp. 17245–17255, May 2017.

[31] H. E. Hans-Günther Wagemann, *Photovoltaik Solarstrahlung und Halbleitereigenschaften, Solarzellenkonzepte und Aufgaben*. Wiesbaden: B.G. Teubner Verlag, 2007.

[32] P. V Foukal, *Solar Astrophysics*. Weinheim, Germany: Wiley-VCH Verlag GmbH, 2004.

[33] M. Hosenuzzaman, N. A. Rahim, J. Selvaraj, M. Hasanuzzaman, A. B. M. A. Malek, and A. Nahar, “Global prospects, progress, policies, and environmental impact of solar photovoltaic power generation,” *Renew. Sustain. Energy Rev.*, vol. 41, pp. 284–297, Jan. 2015.

[34] A. E. Becquerel, “Memoire sur les Effects d’Electriques Produits Sous l’Influence des Rayons Solaires,” *Comptes Rendus l’Academie des Sci.*, vol. 9, pp. 561–567, 1839.

[35] C. E. Fritts, “On the fritts selenium cells and batteries,” *J. Franklin Inst.*, vol. 119, no. 3, pp. 221–232, 1885.

[36] R. S. Ohl, “Light-Sensitive Electric Device Including Silicon,” 2,443,542, 1948.

[37] T. Dittrich, *Materials Concepts for Solar Cells.* IMPERIAL COLLEGE PRESS, 2014.

[38] American Society for Testing and Materials, “Reference Solar Spectral Irradiance: Air Mass Zero.” NREL, Golden, CO, 2018.

[39] American Society for Testing and Materials, “Reference Solar Spectral Irradiance: Air Mass 1.5.” NREL, Golden, CO, 2018.

[40] A. M. A. Leguy *et al.*, “Experimental and theoretical optical properties of methylammonium lead halide perovskites,” *Nanoscale*, vol. 8, no. 12, pp. 6317–6327, 2016.

[41] M. L. Cohen and J. R. Chelikowsky, *Electronic Structure and Optical Properties of Semiconductors*, vol. 75, no. 2. Berlin, Heidelberg: Springer Berlin Heidelberg, 1989.

[42] M. A. Green and M. J. Keevers, “Optical properties of intrinsic silicon at 300 K,” *Prog. Photovoltaics Res. Appl.*, vol. 3, no. 3, pp. 189–192, 1995.

[43] J. A. Guerra *et al.*, “Determination of the complex refractive index and optical bandgap of CH 3 NH 3 PbI 3 thin films,” *J. Appl. Phys.*, vol. 121, no. 17, p. 173104, May 2017.

[44] S. M. Sze and K. K. Ng, *Physics of Semiconductor Devices.* Hoboken, NJ, USA: John Wiley & Sons, Inc., 2006.

[45] S. Torabi *et al.*, “Strategy for Enhancing the Dielectric Constant of Organic Semiconductors Without Sacrificing Charge Carrier Mobility and Solubility,” *Adv. Funct. Mater.*, vol. 25, no. 1, pp. 150–157, Jan. 2015.

[46] T. M. Burke and M. D. McGehee, “How High Local Charge Carrier Mobility and an Energy Cascade in a Three-Phase Bulk Heterojunction Enable >90% Quantum Efficiency,” *Adv. Mater.*, vol. 26, no. 12, pp. 1923–1928, Mar. 2014.

[47] Q. Lin, A. Armin, R. C. R. Nagiri, P. L. Burn, and P. Meredith, “Electro-optics of perovskite solar cells,” *Nat. Photonics*, vol. 9, no. 2, pp. 106–112, Feb. 2015.

[48] Y. Yang, M. Yang, Z. Li, R. Crisp, K. Zhu, and M. C. Beard, “Comparison of Recombination Dynamics in CH 3 NH 3 PbBr 3 and CH 3 NH 3 PbI 3 Perovskite Films: Influence of Exciton Binding Energy,” *J. Phys. Chem. Lett.*, vol. 6, no. 23, pp. 4688–4692, Dec. 2015.

[49] Y. Chen *et al.*, “Extended carrier lifetimes and diffusion in hybrid perovskites revealed by Hall effect and photoconductivity measurements,” *Nat. Commun.*, vol. 7, p. 12253, Aug. 2016.

[50] Q. Dong *et al.*, “Electron-hole diffusion lengths >175 m in solution-grown CH3NH3PbI3 single crystals,” *Science*, vol. 347, no. 6225, pp. 967–970, Feb. 2015.

[51] U. Würfel, A. Cuevas, and P. Würfel, “Charge Carrier Separation in Solar Cells,” *IEEE J. Photovoltaics*, vol. 5, no. 1, pp. 461–469, Jan. 2015.

[52] W. Tress, “Perovskite Solar Cells on the Way to Their Radiative Efficiency Limit - Insights Into a Success Story of High Open-Circuit Voltage and Low Recombination,”

Adv. Energy Mater., vol. 7, no. 14, p. 1602358, Jul. 2017.

[53] P. Würfel, *Physik der Solarzellen*, vol. 2. 2000.

[54] F. Staub, T. Kirchartz, K. Bittkau, and U. Rau, “Manipulating the Net Radiative Recombination Rate in Lead Halide Perovskite Films by Modification of Light Outcoupling,” *J. Phys. Chem. Lett.*, vol. 8, no. 20, pp. 5084–5090, Oct. 2017.

[55] U. Strauss, W. W. Rühle, and K. Köhler, “Auger recombination in intrinsic GaAs,” *Appl. Phys. Lett.*, vol. 62, no. 1, pp. 55–57, Jan. 1993.

[56] W. Shockley and W. T. Read, “Statistics of the Recombination of Holes and Electrons,” *Phys. Rev.*, vol. 87, no. 46, pp. 835–842, 1952.

[57] R. N. Hall, “Electron-Hole Recombination in Germanium,” *Phys. Rev.*, vol. 87, no. 2, pp. 387–387, Jul. 1952.

[58] A. G. Aberle, “Surface passivation of crystalline silicon solar cells: a review,” *Prog. Photovoltaics Res. Appl.*, vol. 8, no. 5, pp. 473–487, Sep. 2000.

[59] R. J. Nelson and R. G. Sobers, “Minority-carrier lifetimes and internal quantum efficiency of surface-free GaAs,” *J. Appl. Phys.*, vol. 49, no. 12, pp. 6103–6108, Dec. 1978.

[60] D. W. deQuilettes *et al.*, “Photoluminescence Lifetimes Exceeding 8 μs and Quantum Yields Exceeding 30% in Hybrid Perovskite Thin Films by Ligand Passivation,” *ACS Energy Lett.*, vol. 1, no. 2, pp. 438–444, Aug. 2016.

[61] H. Tan *et al.*, “Efficient and stable solution-processed planar perovskite solar cells via contact passivation,” *Science*, vol. 355, no. 6326, pp. 722–726, Feb. 2017.

[62] Y. Bi, E. M. Hutter, Y. Fang, Q. Dong, J. Huang, and T. J. Savenije, “Charge Carrier Lifetimes Exceeding 15 Microseconds in Methylammonium Lead Iodide Single Crystals,” *J. Phys. Chem. Lett.*, vol. 7, no. 5, pp. 923–928, Feb. 2016.

[63] K. Tvingstedt *et al.*, “Radiative efficiency of lead iodide based perovskite solar cells,” *Sci. Rep.*, vol. 4, no. 1, p. 6071, May 2015.

[64] M. A. Green, “Accuracy of analytical expressions for solar cell fill factors,” *Sol. Cells*, vol. 7, no. 3, pp. 337–340, Dec. 1982.

[65] G. Kirchhoff, “Ueber das Verhältniss zwischen dem Emissionsvermögen und dem Absorptionsvermögen der Körper für Wärme und Licht,” *Ann. der Phys. und Chemie*, vol. 185, no. 2, pp. 275–301, 1860.

[66] W. Shockley and H. J. Queisser, “Detailed Balance Limit of Efficiency of p-n Junction Solar Cells,” *J. Appl. Phys.*, vol. 32, no. 3, pp. 510–519, Mar. 1961.

[67] S. Rühle, “Tabulated values of the Shockley–Queisser limit for single junction solar cells,” *Sol. Energy*, vol. 130, pp. 139–147, Jun. 2016.

[68] R. Sheng *et al.*, “Four-Terminal Tandem Solar Cells Using CH3NH3PbBr3 by Spectrum Splitting,” *J. Phys. Chem. Lett.*, vol. 6, no. 19, pp. 3931–3934, Oct. 2015.

[69] J. C. Jimeno *et al.*, “A 3 Terminal Parallel Connected Silicon Tandem Solar Cell,” *Energy Procedia*, vol. 92, pp. 644–651, Aug. 2016.

[70] S. Hui, “Conductivity and stability of SrVO3 and mixed perovskites at low oxygen partial

pressures," *Solid State Ionics*, vol. 143, no. 3–4, pp. 275–283, Jul. 2001.

[71] D. B. Mitzi, C. A. Feild, W. T. A. Harrison, and A. M. Guloy, "Conducting tin halides with a layered organic-based perovskite structure," *Nature*, vol. 369, no. 6480, pp. 467–469, Jun. 1994.

[72] H. Jin, S. H. Rhim, J. Im, and A. J. Freeman, "Topological Oxide Insulator in Cubic Perovskite Structure," *Sci. Rep.*, vol. 3, no. 1, p. 1651, Dec. 2013.

[73] M. R. Filip and F. Giustino, "The geometric blueprint of perovskites," *Proc. Natl. Acad. Sci.*, vol. 115, no. 21, pp. 5397–5402, May 2018.

[74] G. Rose, "Ueber einige neue Mineralien des Urals," *J. für Prakt. Chemie*, vol. 19, no. 1, pp. 459–468, 1840.

[75] H. L. Wells, "On the caesium- and the potassium-lead halides," *Am. J. Sci.*, vol. s3-45, no. 266, pp. 121–134, Feb. 1893.

[76] D. Weber, "(x = 0-3), ein Sn (II) -System mit kubischer Perowskitstruktur," *Zeitschrift für Naturforsch.*, vol. 33b, pp. 862–865, 1978.

[77] C. R. Kagan, D. B. Mitzi, and C. D. Dimitrakopoulos, "Organic-Inorganic Hybrid Materials as Semiconducting Channels in Thin-Film Field-Effect Transistors," *Science*, vol. 286, no. 5441, pp. 945–947, Oct. 1999.

[78] K. Chondroudis and D. B. Mitzi, "Electroluminescence from an Organic−Inorganic Perovskite Incorporating a Quaterthiophene Dye within Lead Halide Perovskite Layers," *Chem. Mater.*, vol. 11, no. 11, pp. 3028–3030, Nov. 1999.

[79] T. Ibn-Mohammed *et al.*, "Perovskite solar cells: An integrated hybrid lifecycle assessment and review in comparison with other photovoltaic technologies," *Renew. Sustain. Energy Rev.*, vol. 80, no. December, pp. 1321–1344, Dec. 2017.

[80] H. Zhu *et al.*, "Lead halide perovskite nanowire lasers with low lasing thresholds and high quality factors," *Nat. Mater.*, vol. 14, no. 6, pp. 636–642, Jun. 2015.

[81] Y. C. Kim *et al.*, "Printable organometallic perovskite enables large-area, low-dose X-ray imaging," *Nature*, vol. 550, no. 7674, pp. 87–91, Oct. 2017.

[82] D. Weber, "CH3NH3PbX3, ein Pb(II)-System mit kubischer Perowskitstruktur / CH3NH3PbX3, a Pb(II)-System with Cubic Perovskite Structure," *Zeitschrift für Naturforsch. B*, vol. 33, no. 12, pp. 1443–1445, Jan. 1978.

[83] A. Walsh, "Principles of Chemical Bonding and Band Gap Engineering in Hybrid Organic–Inorganic Halide Perovskites," *J. Phys. Chem. C*, vol. 119, no. 11, pp. 5755–5760, Mar. 2015.

[84] J. Even *et al.*, "Solid-State Physics Perspective on Hybrid Perovskite Semiconductors," *J. Phys. Chem. C*, vol. 119, no. 19, pp. 10161–10177, May 2015.

[85] V. M. Goldschmidt, "Die Gesetze der Krystallochemie," *Naturwissenschaften*, vol. 14, no. 21, pp. 477–485, 1926.

[86] M.-C. Wu, W.-C. Chen, S.-H. Chan, and W.-F. Su, "The effect of strontium and barium doping on perovskite-structured energy materials for photovoltaic applications," *Appl.*

Surf. Sci., vol. 429, pp. 9–15, Jan. 2018.

[87] Z. Li, M. Yang, J.-S. Park, S.-H. Wei, J. Berry, and K. Zhu, “Stabilizing Perovskite Structures by Tuning Tolerance Factor: Formation of Formamidinium and Cesium Lead Iodide Solid-State Alloys,” *Chem. Mater.*, p. acs.chemmater.5b04107, Dec. 2015.

[88] K. Korshunova, L. Winterfeld, W. J. D. Beenken, and E. Runge, “Thermodynamic stability of mixed Pb:Sn methyl-ammonium halide perovskites,” *Phys. status solidi*, vol. 253, no. 10, pp. 1907–1915, Oct. 2016.

[89] T. A. Tyson, W. Gao, Y. S. Chen, S. Ghose, and Y. Yan, “Large thermal motion in Halide Perovskites,” *Sci. Rep.*, vol. 7, no. 1, pp. 1–10, 2017.

[90] C. Eames, J. M. Frost, P. R. F. Barnes, B. C. O’Regan, A. Walsh, and M. S. Islam, “Ionic transport in hybrid lead iodide perovskite solar cells,” *Nat. Commun.*, vol. 6, no. May, p. 7497, 2015.

[91] Y. Yuan and J. Huang, “Ion Migration in Organometal Trihalide Perovskite and Its Impact to Photovoltaic Efficiency and Stability,” 2015.

[92] F. H. Taylor, J. Buckeridge, and C. R. A. Catlow, “Defects and Oxide Ion Migration in the Solid Oxide Fuel Cell Cathode Material LaFeO3,” *Chem. Mater.*, vol. 28, no. 22, pp. 8210–8220, Nov. 2016.

[93] B. Hailegnaw, S. Kirmayer, E. Edri, G. Hodes, and D. Cahen, “Rain on methylammonium lead iodide based perovskites: Possible environmental effects of perovskite solar cells,” *J. Phys. Chem. Lett.*, vol. 6, no. 9, pp. 1543–1547, 2015.

[94] A. H. Slavney, T. Hu, A. M. Lindenberg, and H. I. Karunadasa, “A Bismuth-Halide Double Perovskite with Long Carrier Recombination Lifetime for Photovoltaic Applications,” *J. Am. Chem. Soc.*, vol. 138, no. 7, pp. 2138–2141, Feb. 2016.

[95] Y. Bekenstein *et al.*, “The Making and Breaking of Lead-Free Double Perovskite Nanocrystals of Cesium Silver–Bismuth Halide Compositions,” *Nano Lett.*, vol. 18, no. 6, pp. 3502–3508, Jun. 2018.

[96] A. Buin *et al.*, “Materials Processing Routes to Trap-Free Halide Perovskites,” *Nano Lett.*, vol. 14, no. 11, pp. 6281–6286, Nov. 2014.

[97] B. Conings *et al.*, “Intrinsic Thermal Instability of Methylammonium Lead Trihalide Perovskite,” *Adv. Energy Mater.*, vol. 5, no. 15, p. 1500477, Aug. 2015.

[98] A. Leguy *et al.*, “The reversible hydration of CH3NH3PbI3 in films, single crystals and solar cells,” *Chem. Mater.*, vol. 27, no. 9, pp. 3397–3407, Apr. 2015.

[99] G. Niu, W. Li, F. Meng, L. Wang, H. Dong, and Y. Qiu, “Study on the stability of CH3NH3PbI3 films and the effect of post-modification by aluminum oxide in all-solid-state hybrid solar cells,” *J. Mater. Chem. A*, vol. 2, no. 3, pp. 705–710, 2014.

[100] K. Domanski *et al.*, “Not All That Glitters Is Gold: Metal-Migration-Induced Degradation in Perovskite Solar Cells,” *ACS Nano*, vol. 10, no. 6, pp. 6306–6314, Jun. 2016.

[101] F. Lang *et al.*, “Radiation Hardness and Self-Healing of Perovskite Solar Cells,” *Adv. Mater.*, vol. 28, no. 39, pp. 8726–8731, 2016.

[102] D. R. Ceratti *et al.*, “Self-Healing Inside APbBr 3 Halide Perovskite Crystals,” *Adv. Mater.*, vol. 30, no. 10, p. 1706273, Mar. 2018.

[103] F. Bella *et al.*, “Improving efficiency and stability of perovskite solar cells with photocurable fluoropolymers,” *Science*, vol. 354, no. 6309, pp. 203–206, Oct. 2016.

[104] M. Jung, T. J. Shin, J. Seo, G. Kim, and S. Il Seok, “Structural features and their functions in surfactant-armoured methylammonium lead iodide perovskites for highly efficient and stable solar cells,” *Energy Environ. Sci.*, pp. 0–9, 2018.

[105] K. O. Brinkmann *et al.*, “Suppressed decomposition of organometal halide perovskites by impermeable electron-extraction layers in inverted solar cells,” *Nat. Commun.*, vol. 8, p. 13938, Jan. 2017.

[106] J.-P. Correa-Baena *et al.*, “Promises and challenges of perovskite solar cells,” *Science*, vol. 358, no. 6364, pp. 739–744, Nov. 2017.

[107] K. A. Bush *et al.*, “23.6%-efficient monolithic perovskite/silicon tandem solar cells with improved stability,” *Nat. Energy*, vol. 2, no. February, p. 17009, Feb. 2017.

[108] Z. Wang *et al.*, “High irradiance performance of metal halide perovskites for concentrator photovoltaics,” *Nat. Energy*, Aug. 2018.

[109] P. P. Boix, S. Agarwala, T. M. Koh, N. Mathews, and S. G. Mhaisalkar, “Perovskite Solar Cells: Beyond Methylammonium Lead Iodide,” *J. Phys. Chem. Lett.*, vol. 6, no. 5, pp. 898–907, Mar. 2015.

[110] G. Grancini *et al.*, “One-Year stable perovskite solar cells by 2D/3D interface engineering,” *Nat. Commun.*, vol. 8, p. 15684, Jun. 2017.

[111] W.-J. Yin, J.-H. Yang, J. Kang, Y. Yan, and S.-H. Wei, “Halide perovskite materials for solar cells: a theoretical review,” *J. Mater. Chem. A*, vol. 3, pp. 8926–8942, 2015.

[112] S. De Wolf *et al.*, “Organometallic Halide Perovskites: Sharp Optical Absorption Edge and Its Relation to Photovoltaic Performance,” *J. Phys. Chem. Lett.*, vol. 5, no. 6, pp. 1035–1039, Mar. 2014.

[113] C. M. Wolff, F. Zu, A. Paulke, L. P. Toro, N. Koch, and D. Neher, “Reduced Interface-Mediated Recombination for High Open-Circuit Voltages in CH 3 NH 3 PbI 3 Solar Cells,” *Adv. Mater.*, vol. 29, no. 28, p. 1700159, Jul. 2017.

[114] S. R. Johnson and T. Tiedje, “Temperature dependence of the Urbach edge in GaAs,” *J. Appl. Phys.*, vol. 78, no. 9, pp. 5609–5613, Nov. 1995.

[115] A. D. Wright, R. L. Milot, G. E. Eperon, H. J. Snaith, M. B. Johnston, and L. M. Herz, “Band-Tail Recombination in Hybrid Lead Iodide Perovskite,” *Adv. Funct. Mater.*, vol. 27, no. 29, p. 1700860, Aug. 2017.

[116] D. Meggiolaro *et al.*, “Iodine chemistry determines the defect tolerance of lead-halide perovskites,” *Energy Environ. Sci.*, vol. 11, no. 3, pp. 702–713, 2018.

[117] M. Abdi-Jalebi *et al.*, “Maximizing and stabilizing luminescence from halide perovskites with potassium passivation,” *Nature*, vol. 555, no. 7697, pp. 497–501, Mar. 2018.

[118] H. Zhu *et al.*, “Screening in Crystalline Liquids Protects Energetic Carriers in Hybrid

Perovskites," *Science*, vol. 353, no. in press, 2016.

[119] F. Ambrosio, J. Wiktor, F. De Angelis, and A. Pasquarello, "Origin of Low Electron-Hole Recombination Rate in Metal Halide Perovskites," *Energy Environ. Sci.*, pp. 25–29, 2017.

[120] M. Kim, J. Im, A. J. Freeman, J. Ihm, and H. Jin, "Switchable S = 1/2 and J = 1/2 Rashba bands in ferroelectric halide perovskites," *Proc. Natl. Acad. Sci.*, vol. 111, no. 19, pp. 6900–6904, May 2014.

[121] C. L. Davies *et al.*, "Bimolecular recombination in methylammonium lead triiodide perovskite is an inverse absorption process," *Nat. Commun.*, vol. 9, no. 1, p. 293, Dec. 2018.

[122] W. van Roosbroeck and W. Shockley, "Photon-Radiative Recombination of Electrons and Holes in Germanium," *Phys. Rev.*, vol. 94, no. 6, pp. 1558–1560, Jun. 1954.

[123] T. W. Crothers *et al.*, "Photon Reabsorption Masks Intrinsic Bimolecular Charge-Carrier Recombination in CH 3 NH 3 PbI 3 Perovskite," *Nano Lett.*, vol. 17, no. 9, pp. 5782–5789, Sep. 2017.

[124] M. B. Johnston and L. M. Herz, "Hybrid Perovskites for Photovoltaics: Charge-Carrier Recombination, Diffusion, and Radiative Efficiencies," *Acc. Chem. Res.*, vol. 49, no. 1, pp. 146–154, Jan. 2016.

[125] L. M. Herz, "Charge-Carrier Mobilities in Metal Halide Perovskites: Fundamental Mechanisms and Limits," *ACS Energy Lett.*, vol. 2, no. 7, pp. 1539–1548, Jul. 2017.

[126] M. Karakus, S. A. Jensen, F. D'Angelo, D. Turchinovich, M. Bonn, and E. Cánovas, "Phonon–Electron Scattering Limits Free Charge Mobility in Methylammonium Lead Iodide Perovskites," *J. Phys. Chem. Lett.*, vol. 6, no. 24, pp. 4991–4996, Dec. 2015.

[127] A. D. Wright *et al.*, "Electron–phonon coupling in hybrid lead halide perovskites," *Nat. Commun.*, vol. 7, no. May, May 2016.

[128] L. M. Pazos-Outon *et al.*, "Photon recycling in lead iodide perovskite solar cells," *Science*, vol. 351, no. 6280, pp. 1430–1433, Mar. 2016.

[129] E. T. Hoke, D. J. Slotcavage, E. R. Dohner, A. R. Bowring, H. I. Karunadasa, and M. D. McGehee, "Reversible photo-induced trap formation in mixed-halide hybrid perovskites for photovoltaics," *Chem. Sci.*, vol. 6, no. 1, pp. 613–617, 2015.

[130] P. Fedeli *et al.*, "Influence of the Synthetic Procedures on the Structural and Optical Properties of Mixed-Halide (Br, I) Perovskite Films," *J. Phys. Chem. C*, vol. 119, no. 37, pp. 21304–21313, Sep. 2015.

[131] J. T. Jacobsson *et al.*, "An exploration of the compositional space for mixed lead halogen perovskites for high efficiency devices," *Energy Environ. Sci.*, 2016.

[132] R. J. Sutton *et al.*, "Bandgap-Tunable Cesium Lead Halide Perovskites with High Thermal Stability for Efficient Solar Cells," *Adv. Energy Mater.*, vol. 6, no. 8, p. 1502458, Apr. 2016.

[133] R. E. Beal *et al.*, "Cesium lead halide perovskites with improved stability for tandem solar cells," *J. Phys. Chem. Lett.*, pp. 746–751, Feb. 2016.

[134] D. P. McMeekin *et al.*, “A mixed-cation lead mixed-halide perovskite absorber for tandem solar cells,” *Science*, vol. 351, no. 6269, pp. 151–155, Jan. 2016.

[135] W. Rehman *et al.*, “Photovoltaic mixed-cation lead mixed-halide perovskites: links between crystallinity, photo-stability and electronic properties,” *Energy Environ. Sci.*, vol. 10, no. 1, pp. 361–369, 2017.

[136] G. E. Eperon *et al.*, “Perovskite-perovskite tandem photovoltaics with optimized band gaps,” *Science*, vol. 354, no. 6314, pp. 861–865, Nov. 2016.

[137] E. L. Unger, L. Kegelmann, K. Suchan, D. Sörell, L. Korte, and S. Albrecht, “Roadmap and roadblocks for the band gap tunability of metal halide perovskites,” *J. Mater. Chem. A*, 2017.

[138] G. Maculan *et al.*, “CH3NH3PbCl3 Single Crystals: Inverse Temperature Crystallization and Visible-Blind UV-Photodetector,” *J. Phys. Chem. Lett.*, vol. 6, no. 19, pp. 3781–3786, Oct. 2015.

[139] C. G. Bischak *et al.*, “Origin of Reversible Photoinduced Phase Separation in Hybrid Perovskites,” *Nano Lett.*, vol. 17, no. 2, pp. 1028–1033, Feb. 2017.

[140] F. Brivio, C. Caetano, and A. Walsh, “Thermodynamic Origin of Photoinstability in the CH 3 NH 3 Pb(I 1− x Br x) 3 Hybrid Halide Perovskite Alloy,” *J. Phys. Chem. Lett.*, vol. 7, no. 6, pp. 1083–1087, Mar. 2016.

[141] H.-S. Kim *et al.*, “Lead Iodide Perovskite Sensitized All-Solid-State Submicron Thin Film Mesoscopic Solar Cell with Efficiency Exceeding 9%,” *Sci. Rep.*, vol. 2, no. 1, p. 591, Dec. 2012.

[142] M. M. Lee, J. Teuscher, T. Miyasaka, T. N. Murakami, and H. J. Snaith, “Efficient hybrid solar cells based on meso-superstructured organometal halide perovskites.,” *Science*, vol. 338, no. 6107, pp. 643–7, Nov. 2012.

[143] H. Tian, B. Xu, H. Chen, E. M. J. Johansson, and G. Boschloo, “Solid-State Perovskite-Sensitized p-Type Mesoporous Nickel Oxide Solar Cells,” *ChemSusChem*, vol. 7, no. 8, pp. 2150–2153, Aug. 2014.

[144] K.-C. Wang *et al.*, “p-type Mesoscopic Nickel Oxide/Organometallic Perovskite Heterojunction Solar Cells,” *Sci. Rep.*, vol. 4, no. 1, p. 4756, May 2015.

[145] E. H. Anaraki *et al.*, “Highly efficient and stable planar perovskite solar cells by solution-processed tin oxide,” *Energy Environ. Sci.*, vol. 9, pp. 3128–3134, 2016.

[146] Q. Wang, Q. Dong, T. Li, A. Gruverman, and J. Huang, “Thin Insulating Tunneling Contacts for Efficient and Water-Resistant Perovskite Solar Cells,” *Adv. Mater.*, vol. 28, no. 31, pp. 6734–6739, Aug. 2016.

[147] C. Bi, Q. Wang, Y. Shao, Y. Yuan, Z. Xiao, and J. Huang, “Non-wetting surface-driven high-aspect-ratio crystalline grain growth for efficient hybrid perovskite solar cells.,” *Nat. Commun.*, vol. 6, p. 7747, Jan. 2015.

[148] X. Zheng *et al.*, “Defect passivation in hybrid perovskite solar cells using quaternary ammonium halide anions and cations,” *Nat. Energy*, vol. 2, no. 7, p. 17102, Jun. 2017.

[149] D. Luo *et al.*, “Enhanced photovoltage for inverted planar heterojunction perovskite solar

cells," *Science*, vol. 360, no. 6396, pp. 1442–1446, Jun. 2018.

[150] C. Momblona *et al.*, "Efficient vacuum deposited p-i-n and n-i-p perovskite solar cells employing doped charge transport layers," *Energy Environ. Sci.*, vol. 9, no. 11, pp. 3456–3463, 2016.

[151] D. Bi *et al.*, "Polymer-templated nucleation and crystal growth of perovskite films for solar cells with efficiency greater than 21%," *Nat. Energy*, vol. 1, no. September, p. 16142, 2016.

[152] M. Saliba *et al.*, "Cesium-containing triple cation perovskite solar cells: improved stability, reproducibility and high efficiency," *Energy Environ. Sci.*, vol. 9, no. 6, pp. 1989–1997, 2016.

[153] W. S. Yang *et al.*, "Iodide management in formamidinium-lead-halide–based perovskite layers for efficient solar cells," *Science*, vol. 356, no. 6345, pp. 1376–1379, Jun. 2017.

[154] D. Zhao *et al.*, "Low-bandgap mixed tin–lead iodide perovskite absorbers with long carrier lifetimes for all-perovskite tandem solar cells," *Nat. Energy*, vol. 2, no. March, p. 17018, 2017.

[155] L. Meng, J. You, T. F. Guo, and Y. Yang, "Recent Advances in the Inverted Planar Structure of Perovskite Solar Cells," *Acc. Chem. Res.*, vol. 49, no. 1, pp. 155–165, 2016.

[156] H.-S. Kim *et al.*, "Control of I – V Hysteresis in CH 3 NH 3 PbI 3 Perovskite Solar Cell," *J. Phys. Chem. Lett.*, vol. 6, no. 22, pp. 4633–4639, Nov. 2015.

[157] K. Wojciechowski *et al.*, "Heterojunction Modification for Highly Efficient Organic–Inorganic Perovskite Solar Cells," *ACS Nano*, vol. 8, no. 12, pp. 12701–12709, Dec. 2014.

[158] S. Song *et al.*, "Systematically Optimized Bilayered Electron Transport Layer for Highly Efficient Planar Perovskite Solar Cells (η = 21.1%)," *ACS Energy Lett.*, pp. 2667–2673, 2017.

[159] Q. Jiang *et al.*, "Planar-Structure Perovskite Solar Cells with Efficiency beyond 21%," *Adv. Mater.*, vol. 29, no. 46, p. 1703852, Dec. 2017.

[160] C. Chen *et al.*, "Effect of BCP buffer layer on eliminating charge accumulation for high performance of inverted perovskite solar cells," *RSC Adv.*, vol. 7, no. 57, pp. 35819–35826, 2017.

[161] J. P. Correa Baena *et al.*, "Highly efficient planar perovskite solar cells through band alignment engineering," *Energy Environ. Sci.*, vol. 8, pp. 2928–2934, 2015.

[162] Y. He, H. Y. Chen, J. Hou, and Y. Li, "Indene - C60 bisadduct: A new acceptor for high-performance polymer solar cells," *J. Am. Chem. Soc.*, vol. 132, no. 4, pp. 1377–1382, 2010.

[163] N. Ishiyama, M. Kubo, T. Kaji, and M. Hiramoto, "Doping-based control of the energetic structure of photovoltaic co-deposited films," *Appl. Phys. Lett.*, vol. 99, no. 13, pp. 1–5, 2011.

[164] R. Nakanishi, A. Nogimura, R. Eguchi, and K. Kanai, "Electronic structure of fullerene derivatives in organic photovoltaics," *Org. Electron.*, vol. 15, no. 11, pp. 2912–2921, 2014.

[165] M. G. Helander, M. T. Greiner, Z. B. Wang, W. M. Tang, and Z. H. Lu, "Work function

of fluorine doped tin oxide," *J. Vac. Sci. Technol. A Vacuum, Surfaces, Film.*, vol. 29, no. 1, p. 011019, Jan. 2011.

[166] Y. Ogomi *et al.*, "CH3NH3SnxPb(1–x)I3 Perovskite Solar Cells Covering up to 1060 nm," *J. Phys. Chem. Lett.*, vol. 5, no. 6, pp. 1004–1011, 2014.

[167] J. Liu *et al.*, "Employing PEDOT as the p-Type Charge Collection Layer in Regular Organic–Inorganic Perovskite Solar Cells," *J. Phys. Chem. Lett.*, vol. 6, no. 9, pp. 1666–1673, May 2015.

[168] Y. Shao, Y. Yuan, and J. Huang, "Correlation of energy disorder and open-circuit voltage in hybrid perovskite solar cells," *Nat. Energy*, vol. 1, no. 1, p. 15001, Jan. 2016.

[169] A. Shit and A. K. Nandi, "Interface engineering of hybrid perovskite solar cells with poly(3-thiophene acetic acid) under ambient conditions," *Phys. Chem. Chem. Phys.*, vol. 18, no. 15, pp. 10182–10190, 2016.

[170] J. Rumble, *CRC Handbook for Chemistry and Physics*, 98th ed. CRC Press, 2017.

[171] M. A. Green, "Radiative efficiency of state-of-the-art photovoltaic cells," *Prog. Photovoltaics Res. Appl.*, vol. 20, no. 4, pp. 472–476, Jun. 2012.

[172] C. Tao *et al.*, "17.6% stabilized efficiency in low-temperature processed planar perovskite solar cells," *Energy Environ. Sci.*, vol. 8, no. 8, pp. 2365–2370, 2015.

[173] S. Albrecht *et al.*, "Towards optical optimization of planar monolithic perovskite/silicon-heterojunction tandem solar cells," *J. Opt. (United Kingdom)*, vol. 18, no. 6, pp. 1–10, 2016.

[174] Y. Deng, E. Peng, Y. Shao, Z. Xiao, Q. Dong, and J. Huang, "Scalable fabrication of efficient organolead trihalide perovskite solar cells with doctor-bladed," *Energy Environ. Sci.*, 2015.

[175] G. Cotella *et al.*, "One-step deposition by slot-die coating of mixed lead halide perovskite for photovoltaic applications," *Sol. Energy Mater. Sol. Cells*, vol. 159, pp. 362–369, Jan. 2017.

[176] C. Liang *et al.*, "One-Step Inkjet Printed Perovskite in Air for Efficient Light Harvesting (Solar RRL 22018)," *Sol. RRL*, vol. 2, no. 2, p. 1770150, Feb. 2018.

[177] J. H. Heo, M. H. Lee, H. J. Han, B. R. Patil, J. S. Yu, and S. H. Im, "Highly efficient low temperature solution processable planar type CH3NH3PbI3 perovskite flexible solar cells," *J. Mater. Chem. A*, vol. 4, no. 5, pp. 1572–1578, 2016.

[178] J. Werner *et al.*, "Efficient Near-Infrared-Transparent Perovskite Solar Cells Enabling Direct Comparison of 4-Terminal and Monolithic Perovskite/Silicon Tandem Cells," *ACS Energy Lett.*, vol. 1, no. 2, pp. 474–480, Aug. 2016.

[179] F. Lang *et al.*, "Perovskite Solar Cells with Large-Area CVD-Graphene for Tandem Solar Cells," *J. Phys. Chem. Lett.*, vol. 6, no. 14, pp. 2745–2750, Jul. 2015.

[180] E. L. Unger *et al.*, "Hysteresis and transient behavior in current–voltage measurements of hybrid-perovskite absorber solar cells," *Energy Environ. Sci.*, vol. 7, no. 11, pp. 3690–3698, Aug. 2014.

[181] S. van Reenen, M. Kemerink, and H. J. Snaith, “Modeling Anomalous Hysteresis in Perovskite Solar Cells,” *J. Phys. Chem. Lett.*, vol. 6, no. 19, pp. 3808–3814, Oct. 2015.

[182] M. T. Neukom, S. Züfle, E. Knapp, M. Makha, R. Hany, and B. Ruhstaller, “Why perovskite solar cells with high efficiency show small IV-curve hysteresis,” *Sol. Energy Mater. Sol. Cells*, vol. 169, no. May, pp. 159–166, Sep. 2017.

[183] Y. Shao, Z. Xiao, C. Bi, Y. Yuan, and J. Huang, “Origin and elimination of photocurrent hysteresis by fullerene passivation in CH3NH3PbI3 planar heterojunction solar cells,” *Nat. Commun.*, vol. 5, p. 5784, Dec. 2014.

[184] S. Meloni *et al.*, “Ionic polarization-induced current–voltage hysteresis in CH3NH3PbX3 perovskite solar cells,” *Nat. Commun.*, vol. 7, no. May 2015, p. 10334, Feb. 2016.

[185] I. Zarazua, J. Bisquert, and G. Garcia-Belmonte, “Light-Induced Space-Charge Accumulation Zone as Photovoltaic Mechanism in Perovskite Solar Cells,” *J. Phys. Chem. Lett.*, vol. 7, no. 3, pp. 525–528, Feb. 2016.

[186] W. Tress, N. Marinova, T. Moehl, S. M. Zakeeruddin, M. K. Nazeeruddin, and M. Grätzel, “Understanding the rate-dependent J–V hysteresis, slow time component, and aging in CH 3 NH 3 PbI 3 perovskite solar cells: the role of a compensated electric field,” *Energy Environ. Sci.*, vol. 8, no. 3, pp. 995–1004, Jan. 2015.

[187] J. Xu *et al.*, “Perovskite–fullerene hybrid materials suppress hysteresis in planar diodes,” *Nat. Commun.*, vol. 6, no. 1, p. 7081, Dec. 2015.

[188] S. Weber *et al.*, “How the Formation of Interfacial Charge Causes Hysteresis in Perovskite Solar Cells,” *Energy Environ. Sci.*, 2018.

[189] D. M. Chapin, C. S. Fuller, and G. L. Pearson, “A New Silicon p-n Junction Photocell for Converting Solar Radiation into Electrical Power,” *J. Appl. Phys.*, vol. 25, no. 5, pp. 676–677, May 1954.

[190] W. Fuhs, K. Niemann, and J. Stuke, “Heterojunctions of Amorphous Silicon and Silicon Single Crystals,” in *TETRAHEDRALLY BONDED AMORPHOUS SEMICONDUCTORS: International Conference*, 1974, pp. 345–350.

[191] K. Wakisaka *et al.*, “More than 16% solar cells with a new ‘HIT’ (doped a-Si/nondoped a-Si/crystalline Si) structure,” in *The Conference Record of the Twenty-Second IEEE Photovoltaic Specialists Conference - 1991*, 2011, pp. 887–892.

[192] K. Yoshikawa *et al.*, “Silicon heterojunction solar cell with interdigitated back contacts for a photoconversion efficiency over 26%,” *Nat. Energy*, vol. 2, no. 5, p. 17032, Mar. 2017.

[193] R. A. Street, *Hydrogenated amorphous silicon.* Cambridge: Cambridge University Press, 1991.

[194] K. Fukutani *et al.*, “Band gap tuning of a-Si:H from 1.55 eV to 2.10 eV by intentionally promoting structural relaxation,” *J. Non. Cryst. Solids*, vol. 227–230, no. PART 1, pp. 63–67, 1998.

[195] S. De Wolf, A. Descoeudres, Z. C. Holman, and C. Ballif, “High-efficiency Silicon Heterojunction Solar Cells: A Review,” *Green*, vol. 2, pp. 1–18, Jan. 2012.

[196] L. Korte, E. Conrad, H. Angermann, R. Stangl, and M. Schmidt, “Advances in a-Si:H/c-

Si heterojunction solar cell fabrication and characterization," *Sol. Energy Mater. Sol. Cells*, vol. 93, no. 6–7, pp. 905–910, Jun. 2009.

[197] P. Campbell and M. A. Green, "Light trapping properties of pyramidally textured surfaces," *J. Appl. Phys.*, vol. 62, no. 1, pp. 243–249, Jul. 1987.

[198] S. De Wolf and M. Kondo, "Abruptness of a-Si:H/c-Si interface revealed by carrier lifetime measurements," *Appl. Phys. Lett.*, vol. 90, no. 4, p. 042111, 2007.

[199] Z. C. Holman *et al.*, "Infrared light management in high-efficiency silicon heterojunction and rear-passivated solar cells," *J. Appl. Phys.*, vol. 113, no. 1, p. 013107, Jan. 2013.

[200] R. Varache, C. Leendertz, M. E. Gueunier-Farret, J. Haschke, D. Muñoz, and L. Korte, "Investigation of selective junctions using a newly developed tunnel current model for solar cell applications," *Sol. Energy Mater. Sol. Cells*, vol. 141, pp. 14–23, Oct. 2015.

[201] M. Rahmouni, A. Datta, P. Chatterjee, J. Damon-Lacoste, C. Ballif, and P. Roca i Cabarrocas, "Carrier transport and sensitivity issues in heterojunction with intrinsic thin layer solar cells on N-type crystalline silicon: A computer simulation study," *J. Appl. Phys.*, vol. 107, no. 5, p. 054521, Mar. 2010.

[202] M. W. M. van Cleef, R. E. I. Schropp, and F. A. Rubinelli, "Significance of tunneling in p+ amorphous silicon carbide n crystalline silicon heterojunction solar cells," *Appl. Phys. Lett.*, vol. 73, no. 18, pp. 2609–2611, Nov. 1998.

[203] Sunpower, "X-Series Residential Solar Panels SunPower Residential Solar Panels Engineered for Peace of Mind X-Series," 2016. [Online]. Available: https://us.sunpower.com/sites/sunpower/files/media-library/data-sheets/ds-x22-series-360-residential-solar-panels.pdf. [Accessed: 17-Jun-2018].

[204] S. Essig *et al.*, "Raising the one-sun conversion efficiency of III–V/Si solar cells to 32.8% for two junctions and 35.9% for three junctions," *Nat. Energy*, vol. 2, no. 9, p. 17144, Aug. 2017.

[205] P. Löper *et al.*, "Organic–inorganic halide perovskite/crystalline silicon four-terminal tandem solar cells," *Phys. Chem. Chem. Phys.*, vol. 17, no. 3, pp. 1619–1629, Nov. 2015.

[206] C. D. Bailie *et al.*, "Semi-transparent perovskite solar cells for tandems with silicon and CIGS," *Energy Environ. Sci.*, vol. 8, no. 3, pp. 956–963, 2015.

[207] J. Werner *et al.*, "Sputtered rear electrode with broadband transparency for perovskite solar cells," *Sol. Energy Mater. Sol. Cells*, vol. 141, pp. 407–413, Oct. 2015.

[208] T. Duong *et al.*, "Semitransparent Perovskite Solar Cell With Sputtered Front and Rear Electrodes for a Four-Terminal Tandem," *IEEE J. Photovoltaics*, vol. 6, no. 3, pp. 679–687, May 2016.

[209] B. Chen *et al.*, "Efficient Semitransparent Perovskite Solar Cells for 23.0%-Efficiency Perovskite/Silicon Four-Terminal Tandem Cells," *Adv. Energy Mater.*, p. 1601128, 2016.

[210] T. Duong *et al.*, "Rubidium Multication Perovskite with Optimized Bandgap for Perovskite-Silicon Tandem with over 26% Efficiency," *Adv. Energy Mater.*, vol. 7, no. 14, p. 1700228, Jul. 2017.

[211] C. O. Ramírez Quiroz *et al.*, "Balancing electrical and optical losses for efficient Si-

perovskite 4-terminal solar cells with solution processed percolation electrodes.," *J. Mater. Chem. A*, 2018.

[212] J. P. Mailoa *et al.*, "A 2-terminal perovskite/silicon multijunction solar cell enabled by a silicon tunnel junction," *Appl. Phys. Lett.*, vol. 106, no. 12, p. 121105, 2015.

[213] J. Werner *et al.*, "Efficient Monolithic Perovskite/Silicon Tandem Solar cell with Cell Area greater than 1 cm^2," *J. Phys. Chem. Lett.*, vol. 7, no. 1, pp. 161–166, Jan. 2016.

[214] F. Sahli *et al.*, "Fully textured monolithic perovskite/silicon tandem solar cells with 25.2% power conversion efficiency," *Nat. Mater.*, Jun. 2018.

[215] F. Sahli *et al.*, "Improved Optics in Monolithic Perovskite/Silicon Tandem Solar Cells with a Nanocrystalline Silicon Recombination Junction," *Adv. Energy Mater.*, vol. 1701609, p. 1701609, Oct. 2017.

[216] M. Jošt *et al.*, "Textured interfaces for high energy yield in monolithic perovskite/silicon tandem solar cells," *Prep.*, 2018.

[217] B. C. Duck *et al.*, "Energy yield potential of perovskite-silicon tandem devices," in *2016 IEEE 43rd Photovoltaic Specialists Conference (PVSC)*, 2016, vol. 2016–Novem, pp. 1624–1629.

[218] K. Wojciechowski, M. Saliba, T. Leijtens, A. Abate, and H. J. Snaith, "Sub-150 °C processed meso-superstructured perovskite solar cells with enhanced efficiency," *Energy Environ. Sci.*, vol. 7, no. 3, pp. 1142–1147, 2014.

[219] N. J. Jeon, J. H. Noh, Y. C. Kim, W. S. Yang, S. Ryu, and S. Il Seok, "Solvent engineering for high-performance inorganic-organic hybrid perovskite solar cells.," *Nat. Mater.*, vol. 13, no. September, pp. 897–903, Jul. 2014.

[220] S. Kirner *et al.*, "The Influence of ITO Dopant Density on J-V Characteristics of Silicon Heterojunction Solar Cells: Experiments and Simulations," *Energy Procedia*, vol. 77, pp. 725–732, Aug. 2015.

[221] J. Halme, P. Vahermaa, K. Miettunen, and P. Lund, "Device Physics of Dye Solar Cells," *Adv. Mater.*, vol. 22, no. 35, pp. E210–E234, Sep. 2010.

[222] I. Riedel *et al.*, "Polymer solar cells with novel fullerene-based acceptor," *Thin Solid Films*, vol. 451–452, pp. 43–47, Mar. 2004.

[223] J. Szmytkowski, "The influence of the thickness, recombination and space charge on the loss of photocurrent in organic semiconductors: an analytical model," *J. Phys. D. Appl. Phys.*, vol. 40, no. 11, pp. 3352–3357, Jun. 2007.

[224] M. Stolterfoht *et al.*, "Approaching the fill factor Shockley–Queisser limit in stable, dopant-free triple cation perovskite solar cells," *Energy Environ. Sci.*, vol. 10, no. 6, pp. 1530–1539, 2017.

[225] J. Gilot, M. M. Wienk, and R. A. J. Janssen, "Measuring the External Quantum Efficiency of Two-Terminal Polymer Tandem Solar Cells," *Adv. Funct. Mater.*, vol. 20, no. 22, pp. 3904–3911, Nov. 2010.

[226] A. Redinger, S. Kretzschmar, and T. Unold, "Quantitative PL imaging of thin film solar cells — Potential and pitfalls," in *2016 IEEE 43rd Photovoltaic Specialists Conference*

(PVSC), 2016, pp. 3559–3562.

[227] J. M. Hollas, *Moderne Methoden in der Spektroskopie*. Braunschweig/Wiesbaden: Friedr. Vieweg & Sohn Verlagsgesellschaft mbH, 1995.

[228] J. Rubio-Zuazo and G. R. Castro, "Information depth determination for hard X-ray photoelectron spectroscopy up to 15 keV photoelectron kinetic energy," *Surf. Interface Anal.*, vol. 40, no. 11, pp. 1438–1443, Nov. 2008.

[229] G. Ertl and J. Küppers, *Low Energy Electrons and Surface Chemistry*. Weinheim, Germany: Verlag Chemie, 1974.

[230] L. Korte, *Die elektronische Struktur des Silizium-Heterostruktur-Kontakts*. Marburg: Philipps-Universität Marburg, 2006.

[231] M. Wojdyr, "Fityk : a general-purpose peak fitting program," *J. Appl. Crystallogr.*, vol. 43, no. 5, pp. 1126–1128, Oct. 2010.

[232] D. Rugar and P. Hansma, "Atomic Force Microscopy," no. October, 1990.

[233] JEOL - Serving Advanced Technology, "Scanning Electron Microscope A To Z," p. 32, 2006.

[234] R. Santbergen *et al.*, "Minimizing optical losses in monolithic perovskite/c-Si tandem solar cells with a flat top cell," *Opt. Express*, vol. 24, no. 18, p. A1288, Sep. 2016.

[235] R. Siegel, "Net radiation method for transmission through partially transparent plates," *Sol. Energy*, vol. 15, no. 3, pp. 273–276, 1973.

[236] R. Santbergen, A. H. M. Smets, and M. Zeman, *Optical model for multilayer structures with coherent, partly coherent and incoherent layers*, vol. 21, no. S2. 2013.

[237] R. Santbergen, "Manual for solar cell optical simulation software : GenPro4," no. February, 2016.

[238] H. H. Li, "Refractive index of alkaline earth halides and its wavelength and temperature derivatives," *J. Phys. Chem. Ref. Data*, vol. 9, no. 1, pp. 161–290, Jan. 1980.

[239] D. Zhang *et al.*, "Design and fabrication of a SiOx/ITO double-layer anti-reflective coating for heterojunction silicon solar cells," *Sol. Energy Mater. Sol. Cells*, vol. 117, pp. 132–138, Oct. 2013.

[240] M. Filipič *et al.*, "CH3NH3PbI3 perovskite / silicon tandem solar cells: characterization based optical simulations," *Opt. Express*, vol. 23, no. 7, p. A263, Apr. 2015.

[241] S. Albrecht *et al.*, "Efficient hybrid inorganic/organic tandem solar cells with tailored recombination contacts," *Sol. Energy Mater. Sol. Cells*, vol. 127, pp. 157–162, Aug. 2014.

[242] J. A. Sap, O. Isabella, K. Jäger, and M. Zeman, "Extraction of optical properties of flat and surface-textured transparent conductive oxide films in a broad wavelength range," *Thin Solid Films*, vol. 520, no. 3, pp. 1096–1101, 2011.

[243] P. B. Johnson and R. W. Christy, "Optical constants of the noble metals," *Phys. Rev. B*, vol. 6, no. 12, pp. 4370–4379, 1972.

[244] M. Gohlke, "Documentation of the APCSA Program," *Tech. Rep.*, pp. 1–6, 2014.

[245] B. Harbecke, “Coherent and incoherent reflection and transmission of multilayer structures,” *Appl. Phys. B*, vol. 39, no. 3, pp. 165–170, 1986.

[246] A. D. Rakić, J. M. Elazar, and A. B. Djurišić, “Acceptance-probability-controlled simulated annealing: A method for modeling the optical constants of solids,” *Phys. Rev. E*, vol. 52, no. 6, pp. 6862–6867, Dec. 1995.

[247] W. Ke *et al.*, “Low-Temperature solution-processed tin oxide as an alternative electron transporting layer for efficient perovskite solar cells,” *J. Am. Chem. Soc.*, vol. 137, no. 21, pp. 6730–6733, 2015.

[248] T. Hu *et al.*, “Indium-Free Perovskite Solar Cells Enabled by Impermeable Tin-Oxide Electron Extraction Layers,” *Adv. Mater.*, vol. 29, no. 27, pp. 1–9, 2017.

[249] W. Ke *et al.*, “Cooperative tin oxide fullerene electron selective layers for high-performance planar perovskite solar cells,” *J. Mater. Chem. A*, vol. 4, no. 37, pp. 14276–14283, 2016.

[250] S. Albrecht *et al.*, “On the Efficiency of Charge Transfer State Splitting in Polymer:Fullerene Solar Cells,” *Adv. Mater.*, vol. 26, no. 16, pp. 2533–2539, Apr. 2014.

[251] Y. Zhou, O. S. Game, S. Pang, and N. P. Padture, “Microstructures of Organometal Trihalide Perovskites for Solar Cells: Their Evolution from Solutions and Characterization,” *J. Phys. Chem. Lett.*, vol. 6, no. 23, pp. 4827–4839, Dec. 2015.

[252] H. Minemawari *et al.*, “Inkjet printing of single-crystal films,” *Nature*, vol. 475, no. 7356, pp. 364–367, 2011.

[253] A. Abrusci, S. D. Stranks, P. Docampo, H.-L. L. Yip, A. K.-Y. Y. Jen, and H. J. Snaith, “High-performance perovskite-polymer hybrid solar cells via electronic coupling with fullerene monolayers,” *Nano Lett.*, vol. 13, no. 7, pp. 3124–3128, Jun. 2013.

[254] T. J. Jacobsson *et al.*, “Unreacted PbI 2 as a Double-Edged Sword for Enhancing the Performance of Perovskite Solar Cells,” *J. Am. Chem. Soc.*, vol. 138, no. 32, pp. 10331–10343, Aug. 2016.

[255] Y. Fang, C. Bi, D. Wang, and J. Huang, “The Functions of Fullerenes in Hybrid Perovskite Solar Cells,” *ACS Energy Lett.*, pp. 782–794, Mar. 2017.

[256] Y. Wu *et al.*, “Perovskite solar cells with 18.21% efficiency and area over 1 cm2 fabricated by heterojunction engineering,” *Nat. Energy*, vol. 1, no. 11, p. 16148, Sep. 2016.

[257] J.-P. Correa-Baena *et al.*, “Identifying and suppressing interfacial recombination to achieve high open-circuit voltage in perovskite solar cells,” *Energy Environ. Sci.*, vol. 10, no. 5, pp. 1207–1212, 2017.

[258] P. Zhao, B. J. Kim, and H. S. Jung, “Passivation in perovskite solar cells: A review,” *Mater. Today Energy*, vol. 7, pp. 267–286, Mar. 2018.

[259] P.-L. Qin *et al.*, “Stable and Efficient Organo-Metal Halide Hybrid Perovskite Solar Cells via π-Conjugated Lewis Base Polymer Induced Trap Passivation and Charge Extraction,” *Adv. Mater.*, vol. 30, no. 12, p. 1706126, Mar. 2018.

[260] Q. Zeng *et al.*, “Polymer-Passivated Inorganic Cesium Lead Mixed-Halide Perovskites for Stable and Efficient Solar Cells with High Open-Circuit Voltage over 1.3 V,” *Adv. Mater.*, vol. 30, no. 9, p. 1705393, Mar. 2018.

[261] J. Peng *et al.*, "Interface passivation using ultrathin polymer–fullerene films for high-efficiency perovskite solar cells with negligible hysteresis," *Energy Environ. Sci.*, vol. 10, no. 8, pp. 1792–1800, 2017.

[262] P. Ganesan *et al.*, "A simple spiro-type hole transporting material for efficient perovskite solar cells," *Energy Environ. Sci.*, vol. 8, no. 7, pp. 1986–1991, 2015.

[263] I. Lee, J. H. Yun, H. J. Son, and T.-S. Kim, "Accelerated Degradation Due to Weakened Adhesion from Li-TFSI Additives in Perovskite Solar Cells," *ACS Appl. Mater. Interfaces*, vol. 9, no. 8, pp. 7029–7035, Mar. 2017.

[264] Z. H. Bakr, Q. Wali, A. Fakharuddin, L. Schmidt-Mende, T. M. Brown, and R. Jose, "Advances in hole transport materials engineering for stable and efficient perovskite solar cells," *Nano Energy*, vol. 34, no. November 2016, pp. 271–305, Apr. 2017.

[265] A. Magomedov *et al.*, "Amorphous Hole-Transporting Material based on 2,2′-Bis-substituted 1,1′-Biphenyl Scaffold for Application in Perovskite Solar Cells," *Chem. - An Asian J.*, vol. 12, no. 9, pp. 958–962, May 2017.

[266] W. Zhou, Z. Wen, and P. Gao, "Less is More: Dopant-Free Hole Transporting Materials for High-Efficiency Perovskite Solar Cells," *Adv. Energy Mater.*, vol. 8, no. 9, p. 1702512, Mar. 2018.

[267] N. Arora *et al.*, "Perovskite solar cells with CuSCN hole extraction layers yield stabilized efficiencies greater than 20 %," vol. 5655, no. September, pp. 1–9, 2017.

[268] Y. Hou *et al.*, "Inverted, Environmentally Stable Perovskite Solar Cell with a Novel Low-Cost and Water-Free PEDOT Hole-Extraction Layer," *Adv. Energy Mater.*, vol. 5, no. 15, p. 1500543, Aug. 2015.

[269] D. Koushik *et al.*, "Atomic Layer Deposition Enabled Perovskite/PEDOT Solar Cells in a Regular n-i-p Architectural Design," *Adv. Mater. Interfaces*, vol. 4, no. 18, p. 1700043, Sep. 2017.

[270] J.-H. Yu, C.-H. Lee, H.-I. Joh, J.-S. Yeo, and S.-I. Na, "Synergetic effects of solution-processable fluorinated graphene and PEDOT as a hole-transporting layer for highly efficient and stable normal-structure perovskite solar cells," *Nanoscale*, vol. 9, no. 44, pp. 17167–17173, 2017.

[271] C.-Y. Chang, B.-C. Tsai, and Y.-C. Hsiao, "Efficient and Stable Vacuum-Free-Processed Perovskite Solar Cells Enabled by a Robust Solution-Processed Hole Transport Layer," *ChemSusChem*, vol. 10, no. 9, pp. 1981–1988, May 2017.

[272] K. Tvingstedt *et al.*, "Removing Leakage and Surface Recombination in Planar Perovskite Solar Cells," *ACS Energy Lett.*, vol. 2, no. 2, pp. 424–430, Feb. 2017.

[273] Q. Xue *et al.*, "Efficient and Stable Perovskite Solar Cells via Dual Functionalization of Dopamine Semiquinone Radical with Improved Trap Passivation Capabilities," *Adv. Funct. Mater.*, vol. 1707444, p. 1707444, Mar. 2018.

[274] J. H. Heo, H. J. Han, D. Kim, T. K. Ahn, and S. H. Im, "Hysteresis-less inverted CH 3 NH 3 PbI 3 planar perovskite hybrid solar cells with 18.1% power conversion efficiency," *Energy Environ. Sci.*, vol. 8, no. 5, pp. 1602–1608, 2015.

[275] H. Kim, K.-G. Lim, and T.-W. Lee, “Planar heterojunction organometal halide perovskite solar cells: roles of interfacial layers,” *Energy Environ. Sci.*, vol. 9, no. 1, pp. 12–30, 2016.

[276] B. J. Moon, G.-Y. Lee, M. J. Im, S. Song, and T. Park, “In situ modulation of the vertical distribution in a blend of P3HT and PC60BM via the addition of a composition gradient inducer,” *Nanoscale*, vol. 6, no. 4, p. 2440, 2014.

[277] G.-W. Kim, G. Kang, M. Malekshahi Byranvand, G.-Y. Lee, and T. Park, “Gradated Mixed Hole Transport Layer in a Perovskite Solar Cell: Improving Moisture Stability and Efficiency,” *ACS Appl. Mater. Interfaces*, vol. 9, no. 33, pp. 27720–27726, Aug. 2017.

[278] W. H. Nguyen, C. D. Bailie, E. L. Unger, and M. D. McGehee, “Enhancing the hole-conductivity of spiro-OMeTAD without oxygen or lithium salts by using spiro(TFSI)$_2$ in perovskite and dye-sensitized solar cells.,” *J. Am. Chem. Soc.*, vol. 136, no. 31, pp. 10996–1001, Aug. 2014.

[279] N. Koch, A. Elschner, J. P. Rabe, and R. L. Johnson, “Work Function Independent Hole-Injection Barriers Between Pentacene and Conducting Polymers,” *Adv. Mater.*, vol. 17, no. 3, pp. 330–335, Feb. 2005.

[280] D. J. D. Moet, P. de Bruyn, and P. W. M. Blom, “High work function transparent middle electrode for organic tandem solar cells,” *Appl. Phys. Lett.*, vol. 96, no. 15, p. 153504, Apr. 2010.

[281] I. Lange, J. C. Blakesley, J. Frisch, A. Vollmer, N. Koch, and D. Neher, “Band Bending in Conjugated Polymer Layers,” *Phys. Rev. Lett.*, vol. 106, no. 21, p. 216402, May 2011.

[282] S. Jäckle *et al.*, “Junction formation and current transport mechanisms in hybrid n-Si/PEDOT:PSS solar cells,” *Sci. Rep.*, vol. 5, no. 1, p. 13008, Oct. 2015.

[283] J. Kim, A. Kanwat, H.-M. Kim, and J. Jang, “Solution processed polymer light emitting diode with vanadium-oxide doped PEDOT:PSS,” *Phys. status solidi*, vol. 212, no. 3, pp. 640–645, Mar. 2015.

[284] A. Krishna *et al.*, “Novel hole transporting materials based on triptycene core for high efficiency mesoscopic perovskite solar cells,” *Chem. Sci.*, vol. 5, no. 7, pp. 2702–2709, May 2014.

[285] D. B. Khadka, Y. Shirai, M. Yanagida, J. W. Ryan, and K. Miyano, “Exploring the effects of interfacial carrier transport layers on device performance and optoelectronic properties of planar perovskite solar cells,” *J. Mater. Chem. C*, vol. 5, no. 34, pp. 8819–8827, 2017.

[286] Y. Hou *et al.*, “Suppression of Hysteresis Effects in Organohalide Perovskite Solar Cells,” *Adv. Mater. Interfaces*, vol. 4, no. 11, p. 1700007, Jun. 2017.

[287] P. Würfel and W. Ruppel, “The chemical potential of luminescent radiation,” *J. Lumin.*, vol. 24–25, no. PART 2, pp. 925–928, Nov. 1981.

[288] W. Tress, N. Marinova, O. Inganäs, M. K. Nazeeruddin, S. M. Zakeeruddin, and M. Graetzel, “Predicting the Open-Circuit Voltage of CH 3 NH 3 PbI 3 Perovskite Solar Cells Using Electroluminescence and Photovoltaic Quantum Efficiency Spectra: the Role of Radiative and Non-Radiative Recombination,” *Adv. Energy Mater.*, vol. 5, no. 3, p. 1400812, Feb. 2015.

[289] Z. Yu, Y. Xia, D. Du, and J. Ouyang, "PEDOT:PSS Films with Metallic Conductivity through a Treatment with Common Organic Solutions of Organic Salts and Their Application as a Transparent Electrode of Polymer Solar Cells," *ACS Appl. Mater. Interfaces*, vol. 8, no. 18, pp. 11629–11638, 2016.

[290] G. Greczynski, T. Kugler, and W. . Salaneck, "Characterization of the PEDOT-PSS system by means of X-ray and ultraviolet photoelectron spectroscopy," *Thin Solid Films*, vol. 354, no. 1–2, pp. 129–135, Oct. 1999.

[291] D. Zielke *et al.*, "Large-Area PEDOT:PSS/c-Si Heterojunction Solar Cells With Screen-Printed Metal Contacts," *Sol. RRL*, vol. 2, no. 3, p. 1700191, Mar. 2018.

[292] W. Kong, T. Ding, G. Bi, and H. Wu, "Optical characterizations of the surface states in hybrid lead–halide perovskites," *Phys. Chem. Chem. Phys.*, vol. 18, no. 18, pp. 12626–12632, 2016.

[293] J. Werner *et al.*, "Parasitic Absorption Reduction in Metal Oxide-Based Transparent Electrodes: Application in Perovskite Solar Cells," *ACS Appl. Mater. Interfaces*, vol. 8, no. 27, pp. 17260–17267, Jul. 2016.

[294] T. J. Driscoll, L. D. McCormick, and W. C. Lederer, "Altered Layer Formation and Sputtering Yields for 5keV Ar+ Bombardment of MoO3 and WO3," *Surf. Sci.*, vol. 187, pp. 539–558, 1987.

[295] A. Descoeudres *et al.*, "Silicon Heterojunction solar cells on n- and p- type wafers with efficiencies above 20%," *27th Eur. Photovolt. Sol. Energy Conf. Exhib.*, pp. 646–651, 2012.

[296] N. Wijeyasinghe *et al.*, "Copper(I) Thiocyanate (CuSCN) Hole-Transport Layers Processed from Aqueous Precursor Solutions and Their Application in Thin-Film Transistors and Highly Efficient Organic and Organometal Halide Perovskite Solar Cells," *Adv. Funct. Mater.*, vol. 27, no. 35, p. 1701818, Sep. 2017.

[297] Z. Hawash, L. K. Ono, S. R. Raga, M. V. Lee, and Y. Qi, "Air-Exposure Induced Dopant Redistribution and Energy Level Shifts in Spin-Coated Spiro-MeOTAD Films," *Chem. Mater.*, vol. 27, no. 2, pp. 562–569, Jan. 2015.

[298] J. Choi and L. T. Thompson, "XPS study of as-prepared and reduced molybdenum oxides," vol. 93, pp. 143–149, 1996.

[299] V. Zardetto *et al.*, "Atomic layer deposition for perovskite solar cells: research status, opportunities and challenges," *Sustain. Energy Fuels*, vol. 1, no. 1, pp. 30–55, 2017.

[300] M. Tallarida, K. Kukli, M. Michling, M. Ritala, M. Leskelä, and D. Schmeisser, "Substrate Reactivity Effects in the Atomic Layer Deposition of Aluminum Oxide from Trimethylaluminum on Ruthenium," *Chem. Mater.*, vol. 23, no. 13, pp. 3159–3168, Jul. 2011.

[301] J. C. Bernède *et al.*, "XPS study of the band alignment at ITO/oxide (n-type MoO3 or p-type NiO) interface," *Phys. status solidi*, vol. 209, no. 7, pp. 1291–1297, Jul. 2012.

[302] S. Fantacci, F. De Angelis, M. K. Nazeeruddin, and M. Grätzel, "Electronic and Optical Properties of the Spiro-MeOTAD Hole Conductor in Its Neutral and Oxidized Forms: A DFT/TDDFT Investigation," *J. Phys. Chem. C*, vol. 115, no. 46, pp. 23126–23133, Nov.

2011.

[303] Z. Liu *et al.*, “Nickel oxide nanoparticles for efficient hole transport in p-i-n and n-i-p perovskite solar cells,” *J. Mater. Chem. A*, vol. 5, no. 14, pp. 6597–6605, 2017.

[304] H. Zhang, H. Wang, W. Chen, and A. K.-Y. Jen, “CuGaO2: A Promising Inorganic Hole-Transporting Material for Highly Efficient and Stable Perovskite Solar Cells,” *Adv. Mater.*, p. 1604984, 2016.

[305] M. Jung *et al.*, “Thermal Stability of CuSCN Hole Conductor-Based Perovskite Solar Cells,” *ChemSusChem*, vol. 9, no. 18, pp. 2592–2596, Sep. 2016.

[306] J. E. Jaffe, T. C. Kaspar, T. C. Droubay, T. Varga, M. E. Bowden, and G. J. Exarhos, “Electronic and Defect Structures of CuSCN,” *J. Phys. Chem. C*, vol. 114, no. 19, pp. 9111–9117, May 2010.

[307] J. Endres *et al.*, “Electronic structure of the CsPbBr 3 /polytriarylamine (PTAA) system,” *J. Appl. Phys.*, vol. 121, no. 3, p. 035304, Jan. 2017.

[308] Z. Yu and L. Sun, “Recent Progress on Hole-Transporting Materials for Emerging Organometal Halide Perovskite Solar Cells,” *Adv. Energy Mater.*, vol. 5, no. 12, p. 1500213, Jun. 2015.

[309] L. Mazzarella *et al.*, “Infrared photocurrent management in monolithic perovskite/silicon heterojunction tandem solar cells by using a nanocrystalline silicon oxide interlayer,” *Opt. Express*, vol. 26, no. 10, p. A487, May 2018.

[310] K. Bittkau, T. Kirchartz, and U. Rau, “Optical design of spectrally selective interlayers for perovskite/silicon heterojunction tandem solar cells,” *Opt. Express*, vol. 26, no. 18, p. A750, Sep. 2018.

[311] K. A. Bush *et al.*, “Minimizing Current and Voltage Losses to Reach 25% Efficient Monolithic Two-Terminal Perovskite–Silicon Tandem Solar Cells,” *ACS Energy Lett.*, pp. 2173–2180, Aug. 2018.

[312] T. Wahl, J. Hanisch, S. Meier, M. Schultes, and E. Ahlswede, “Sputtered indium zinc oxide rear electrodes for inverted semitransparent perovskite solar cells without using a protective buffer layer,” *Org. Electron. physics, Mater. Appl.*, vol. 54, no. September 2017, pp. 48–53, 2018.

[313] A. Czudek *et al.*, “Dynamic maximum power point tracking (dynaMPP) algorithm for characterization of lead halide perovskite solar cells,” *Unpubl. Work*, 2018.

7. Appendix

7.1 Scientific Appendix to Chapter 4.1

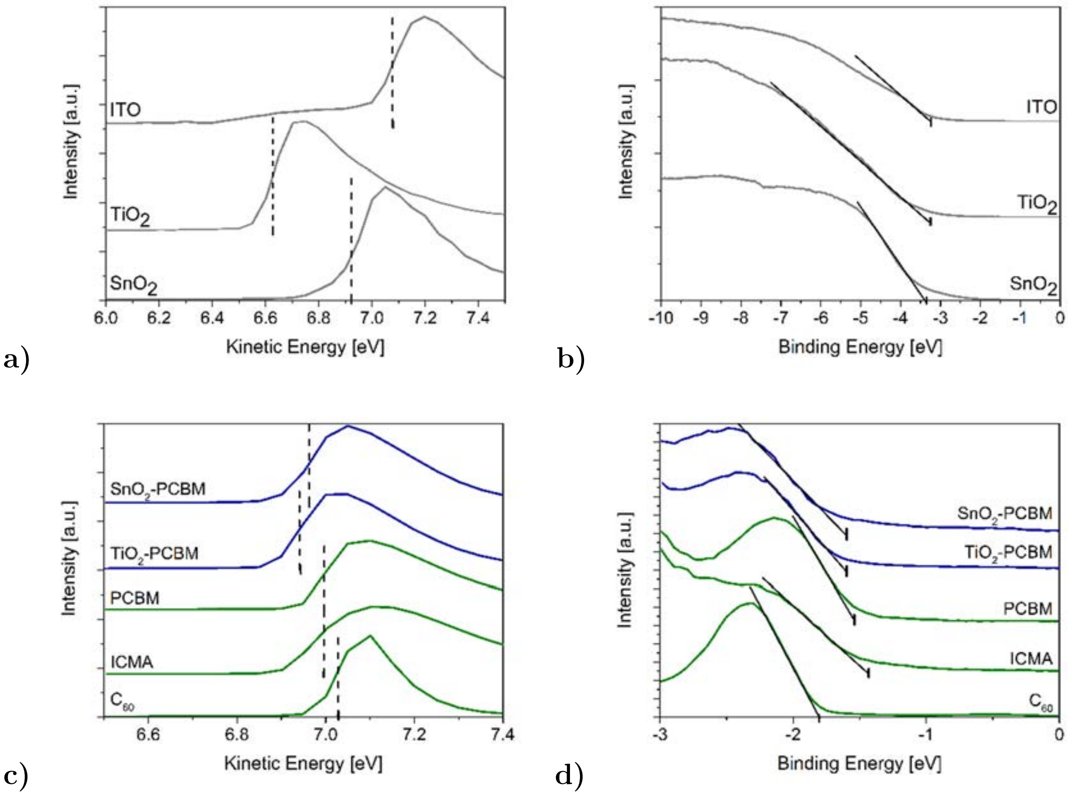

Figure S1. UPS measurements to determine (a) the secondary electron cut-off (SECO) and (b) the Fermi-edge of the metal oxides. (c) and (d) present the respective characteristics for organic single- and double-layer ETMs.

ETM	Work function from SECO	Fermi Edge	Ionization potential
ITO	-4.6 eV	-3.2 eV	-7.8 eV
TiO_2	-4.1 eV	-3.2 eV	-7.3 eV
SnO_2	-4.45 eV	-3.35 eV	-7.8 eV
ICMA	-4.5 eV	-1.45 eV	-5.95 eV
C_{60}	-4.55 eV	-1.8 eV	-6.35 eV
PCBM	-4.5 eV	-1.55 eV	-6.05 eV
SnO_2-PCBM	-4.45 eV	-1.65 eV	-6.1 eV
TiO_2-PCBM	-4.45 eV	-1.65 eV	-6.1 eV

Table S1. Work function and Fermi edge energies corresponding to Figure S1 as well as resulting ionization potentials.

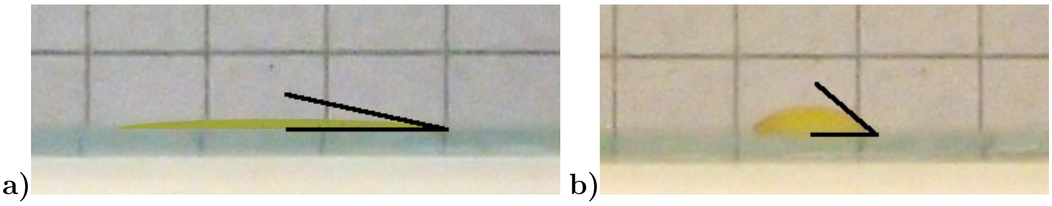

Figure S2. Droplets of 10 µl of the perovskite precursor solution on (a) glass/ITO/TiO_2 and (b) glass/ITO/PCBM.

Table S 2: Root-mean-square (RMS) values of the surface roughness of different ETMs on ITO determined by atomic force microscopy.

Surface Roughness	ITO	TiO2	SnO2	C60	PCBM	SnO2-PCBM	TiO2-PCBM
RMS [nm]	3	3	3	16	4	2	2

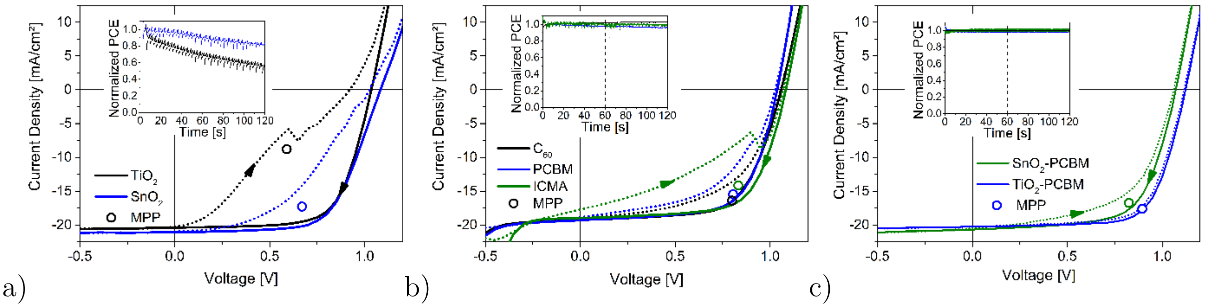

Figure S3. Current density-voltage (J-V) characteristics under illumination and maximum power points (MPP) after 60 s MPP tracking of perovskite solar cells with (a) TiO_2 or SnO_2 and (b) ICMA, C60 or PCBM as single-layer ETM. Corresponding curves for devices with a double-layer ETM structure of SnO_2/PCBM and TiO_2/PCBM are depicted in panel (c). The insets show maximum power point tracking measurements of the solar cells.

The kinks in different forward J-V curves at current densities around 6 mA/cm² are a reproducible phenomenon ascribed to the measurement. The Keithley source-meter unit is set to automatically adjust the sensitivity of the current measurement during J-V scans. The mentioned current density of around 6 mA/cm² relates for a 0.16 cm² cell to 1 mA and therefore is the threshold for the source-meter to adjust sensitivity from the 10 to 1 mA range. This autoranging function however causes a slight delay of the J-V scan and leaves the device in an unclear bias condition during the range change. As a result, the transient dynamics in the device are influenced which leads to a slight change in the observed hysteresis at this voltage step.

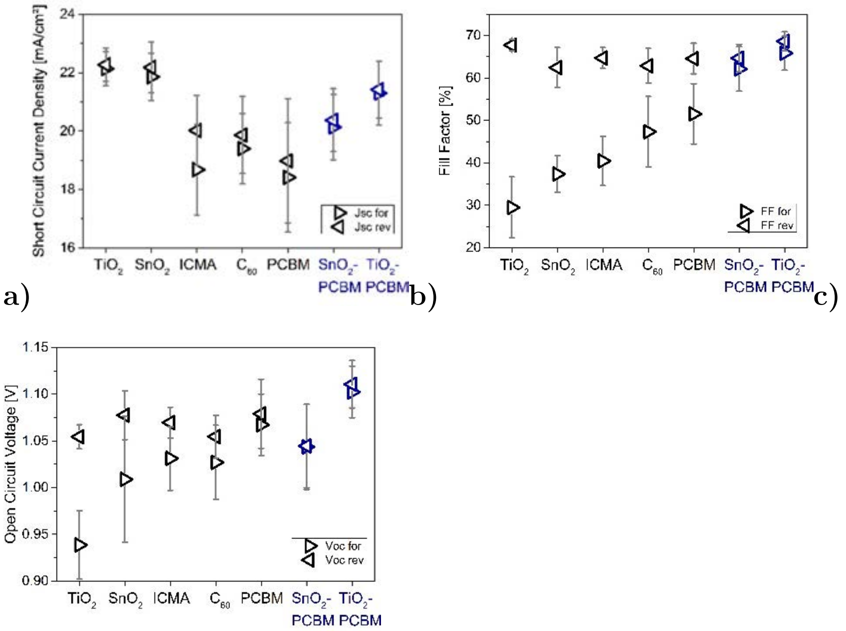

Figure S4. Parameters (a) J_{SC}, (b) fill factor and (c) V_{OC} averaged separately for forward and reverse scans at 1666 mV/s sweep rate for perovskite solar cells under illumination with different ETMs averaged over all devices.

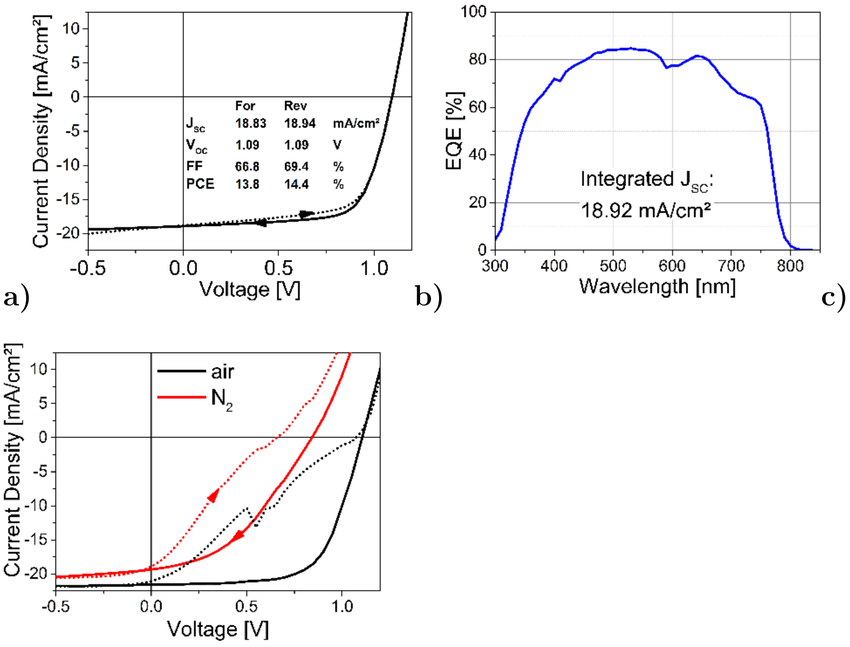

Figure S5. (a) J-V-curve measured in N_2 atmosphere and 1666 mV/s scan speed corresponding to the champion device shown in Figure 4.4 (b). (b) Respective external quantum efficiency also determined in N_2 atmosphere. (c) J-V-measurements of a TiO_2 single-layer ETM device in air and N_2 atmosphere, both at 1666 mV/s.

The J-V-curves of devices measured in N_2 atmosphere differed strongly from those obtained in air. As an example, Figure 4.4 (b) and Figure S5 (a) show J-V-curves of the same device, measured on the same day but in air and N_2 respectively. As the external quantum efficiency (EQE_{PV}) measurement was performed in N_2 (Figure S5 (b)), we were able to confirm the J_{SC}

value of the corresponding J-V-scan (Figure S5 (a)). As the reduction of J_{SC} in N_2 compared to measurements in air is reversible and was observed more pronounced for devices incorporating metal oxides (Figure S5 (c)), we suggest that oxygen in the environment plays an important role in this device architecture for the Spiro-OMeTAD hole and the metal oxide electron selective layers.

7.2 Scientific Appendix to Chapter 4.2

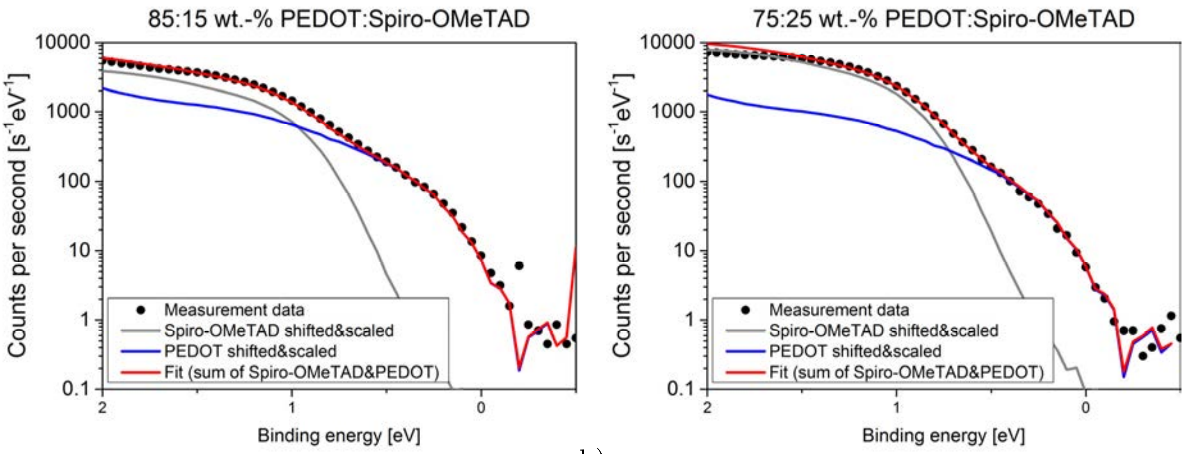

a) b)

Figure S 6: Ultraviolet photoelectron spectroscopy measurements of a) 85:15 wt.-% and b) 75:25 wt.-% PEDOT:Spiro-OMeTAD mixtures and fits to the measurements consisting of the scaled and binding-energy shifted spectra of pure PEDOT and Spiro-OMeTAD.

Fits to the photoelectron spectroscopy measurement data of PEDOT/Spiro-OMeTAD mixed films in Figure S 6 were determined by sums of the scaled spectra of pure PEDOT and Spiro-OMeTAD layers. Besides, they are shifted along the binding energy axis according to the differences in work functions between the pure materials and the blends. The fits were calculated according to:

$$Y_{fit}(E) = c_{PEDOT} \cdot Y_{PEDOT}(E - \Delta_{PEDOT}) + c_{Spiro-OMeTAD} \cdot Y_{Spiro-OMeTAD}(E - \Delta_{Spiro-OMeTAD}),$$

with:

	c_{PEDOT}	Δ_{PEDOT}	$c_{Spiro-OMeTAD}$	$\Delta_{Spiro-OMeTAD}$
85:15 wt.-% PEDOT:Spiro-OMeTAD	0.939	-0.04 eV	0.037	-0.13 eV
75:25 wt.-% PEDOT:Spiro-OMeTAD	0.757	-0.06 eV	0.074	-0.09 eV

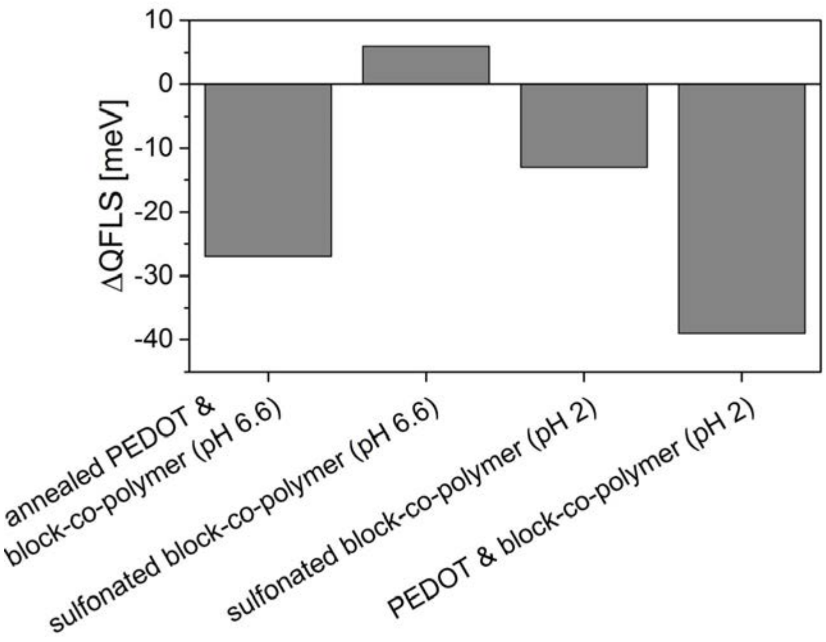

Figure S 7: Deviation of the quasi-Fermi level splitting (QFLS) for different layers in a glass/perovskite/HTM stack referred to the regular, non-annealed and pH-neutralized PEDOT HTM as a reference.

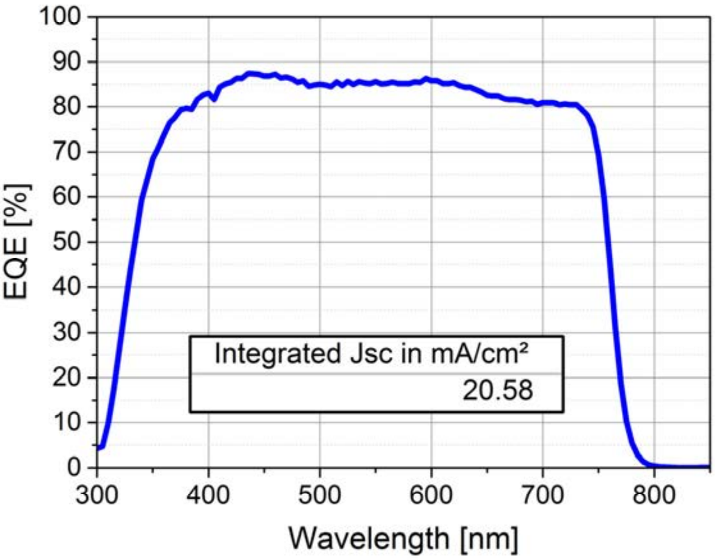

Figure S 8: Exemplary external quantum efficiency measurement for a perovskite solar cell with post-deposition annealed 75:25 wt.-% PEDOT:Spiro-OMeTAD mixture as HTM.

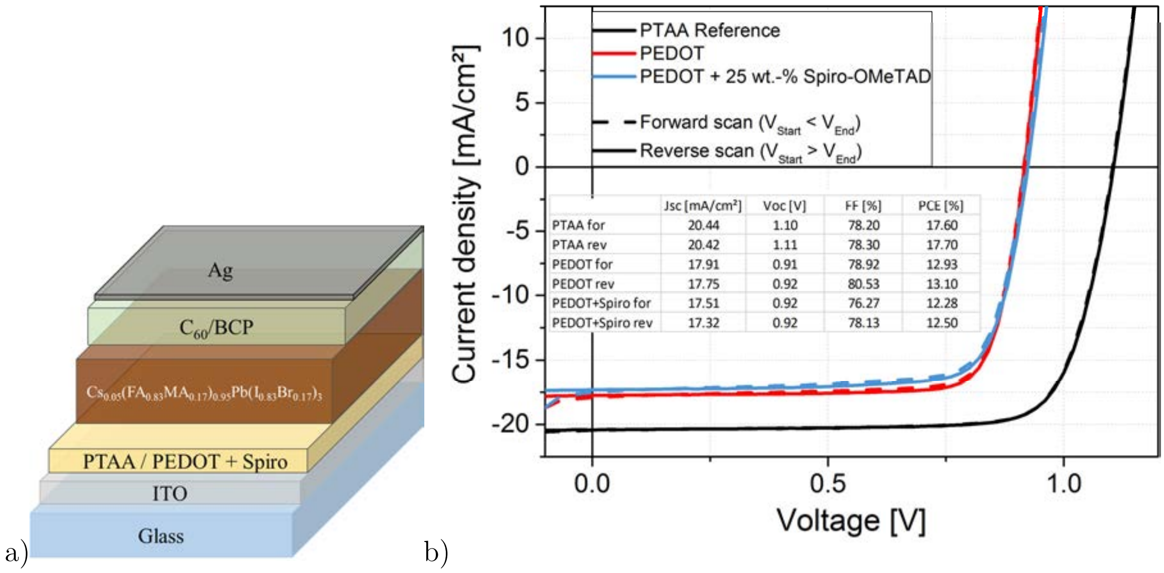

	Jsc [mA/cm²]	Voc [V]	FF [%]	PCE [%]
PTAA for	20.44	1.10	78.20	17.60
PTAA rev	20.42	1.11	78.30	17.70
PEDOT for	17.91	0.91	78.92	12.93
PEDOT rev	17.75	0.92	80.53	13.10
PEDOT+Spiro for	17.51	0.92	76.27	12.28
PEDOT+Spiro rev	17.32	0.92	78.13	12.50

Figure S 9: a) Layer stack of the herein produced planar p-i-n perovskite solar cells with PTAA, water-free PEDOT or mixtures of water-free PEDOT and dopant-free Spiro-OMeTAD as HTM. b) Forward and reverse current-voltage characteristics and solar cell parameters of the resulting devices.

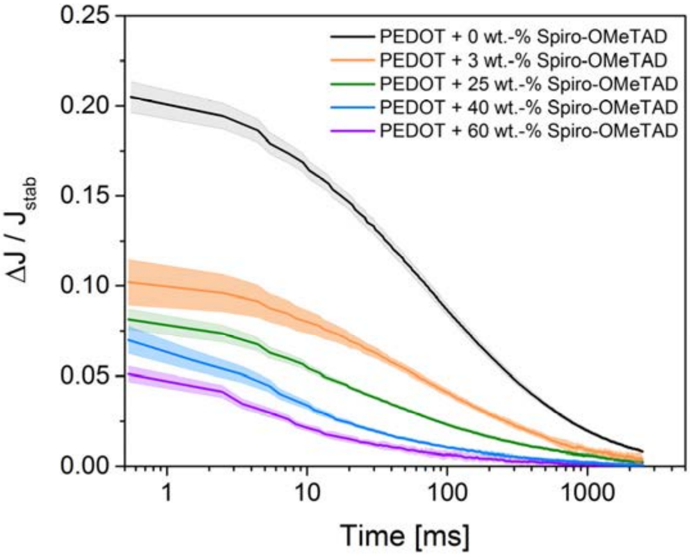

Figure S 10: Hysteresis analysis according to Czudek et al.[313] for perovskite solar cells with water-free PEDOT as HTM as well as different amounts of dopant-free Spiro-OMeTAD added to the PEDOT.

Hysteresis analysis was performed, based on a perturb-and-observe algorithm, similar to the MPP tracking as described in the experimentals section. The external voltage applied to each solar cell under illumination was modulated by V_{MPP} +/- 50 mV in 2.5 s time intervals and the subsequent transient current responses following each voltage perturbation were recorded. The ΔJ displayed in Figure S 10 represents the difference in the current density at time t after perturbation referenced to the stabilized current density at MPP. Hence, the amplitude of ΔJ is proportional to the transient response of the solar cell and is larger for devices with more pronounced J-V hysteresis.[313]

Table S 3: Thin film thicknesses for undiluted mixtures of PEDOT and Spiro-OMeTAD on glass.

wt.-% PEDOT	wt-% Spiro-OMeTAD	Layer thickness on glass [nm]
100	0%	150
97	3%	160
85	15%	180
75	25%	200
60	40%	250
50	50%	270

7.3 Scientific Appendix to Chapter 4.3

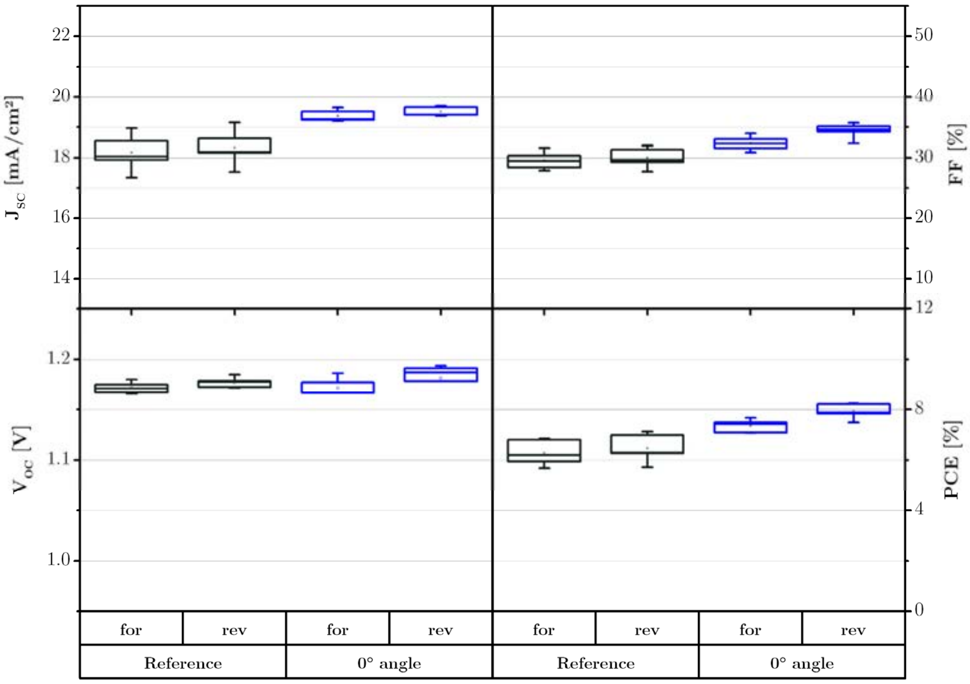

Figure S 11: Current-voltage characteristics in forward and reverse scan direction under illumination for semi-transparent solar cells with MoOx/ITO top contact. ITO was either sputtered as usual (reference) or with pre-deposition of the initial 10 nm at low incidence sputter angle (0° angle).

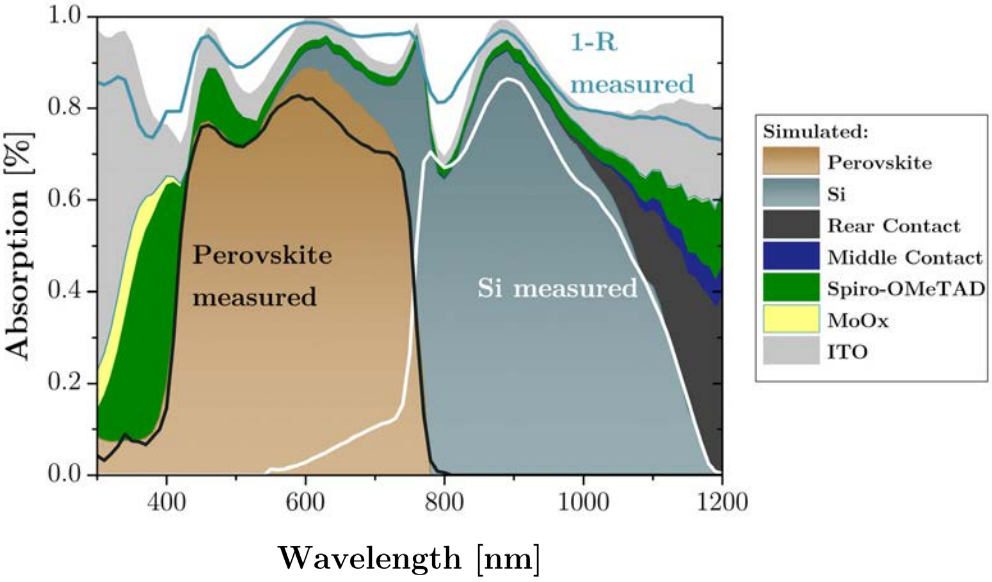

Figure S 12: Optical simulations with GenPro4 compared to actually measured $\mathrm{EQE_{PV}}$ of the Si and perovskite sub cell as well as 1-reflection for the tandem solar cell depicted in Figure 4.20.

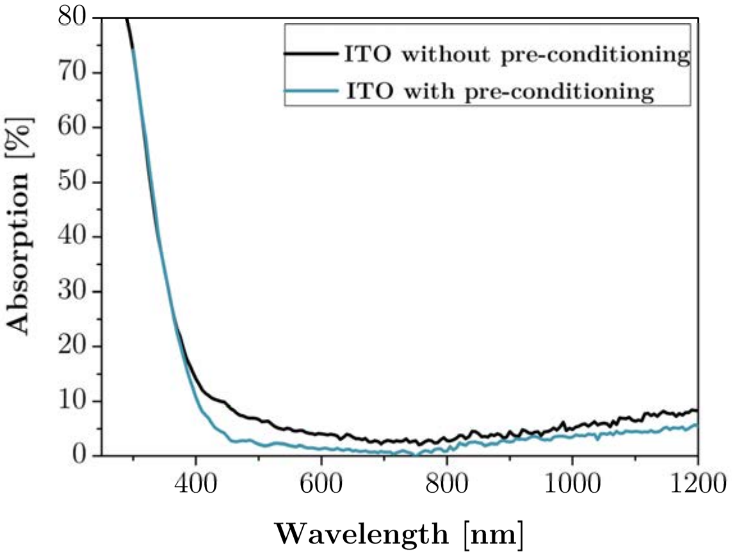

Figure S 13: Absorptance of different ITO layers, both around 100 nm thick, either with or without pre-conditioning of the sputter system by initial ITO deposition prior to inserting the samples.

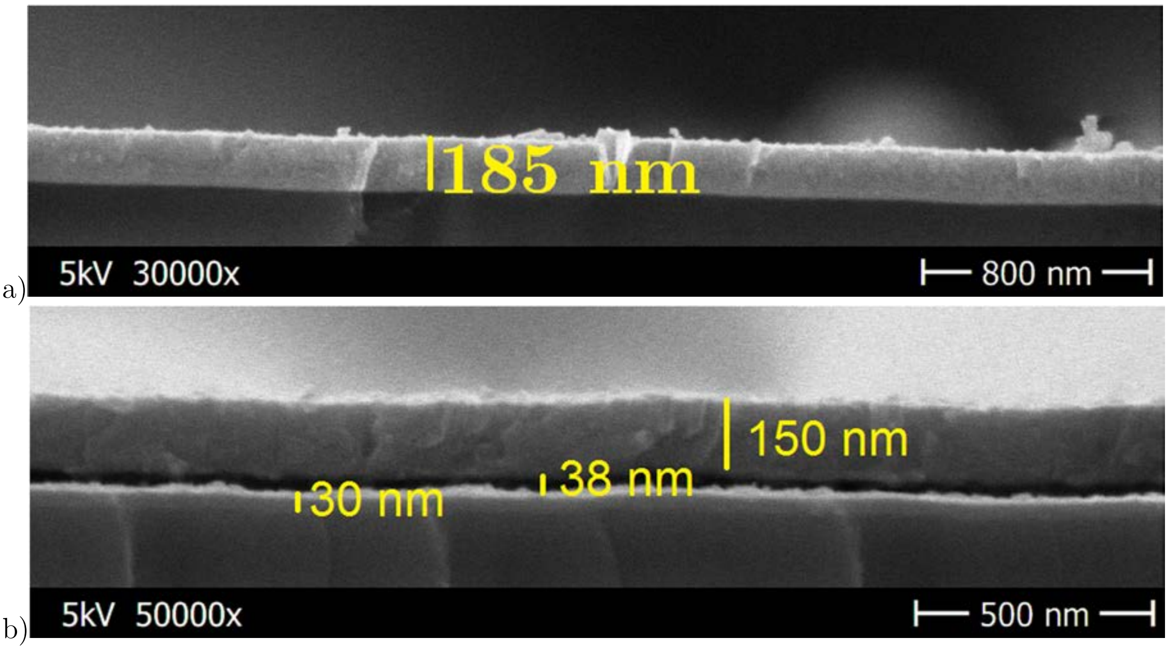

Figure S 14: Scanning electron microscopy images of glass/MoOx/buffer/ITO layer stacks with buffer being a) ITO nanoparticles spin coated at 4000 rpm and b) CuSCN prepared by spin coating. The thickness comparison reveals no contribution of ITO nanoparticles to the overall layer stack thickness (~185 nm), which is instead similar to the sum of the individual ITO (~150 nm) and MoOx (~30 nm) thicknesses as determined in b). Note, that CuSCN has been initially examined here as a buffer layer to protect the MoOx during the ITO sputter process but has not been further investigated due to the expected low electron mobility of CuSCN.

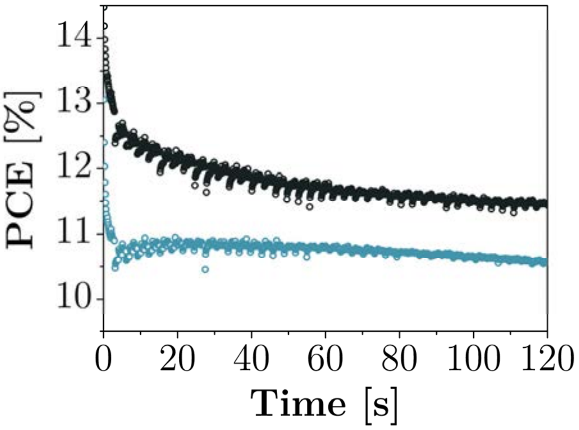

Figure S 15: Maximum power point tracking of semi-transparent perovskite single junction solar cells with MoOx/ITO (black) and MoOx/17 cycles SnO_2 ALD/ITO (blue) as top contacts.

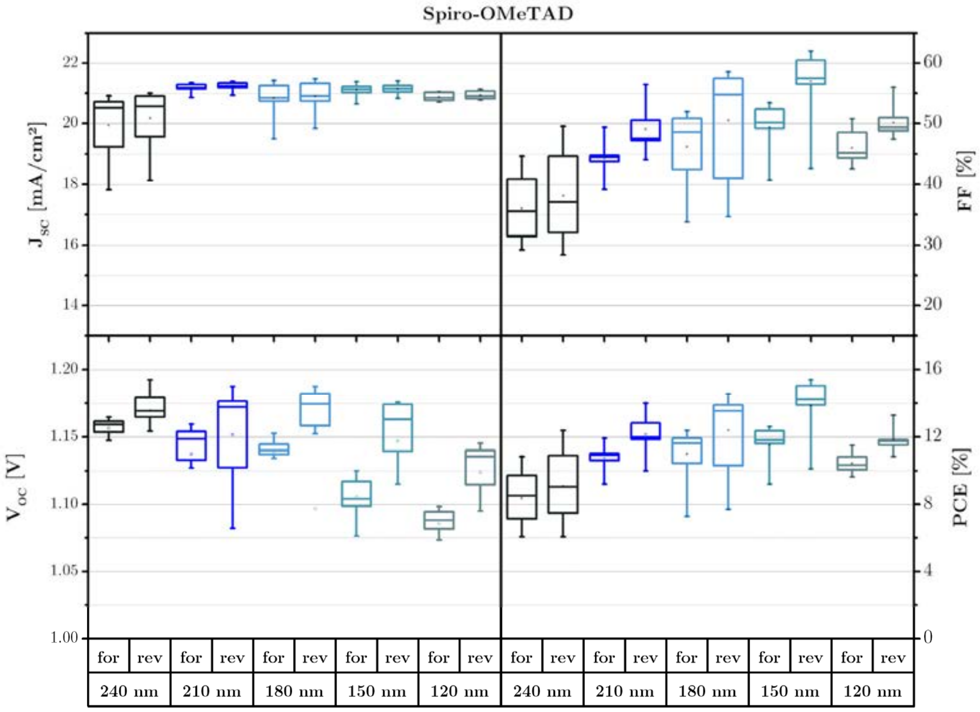

Figure S 16: Boxplot diagrams of current-voltage scan parameters in forward ($V_{Start}<V_{End}$) and reverse ($V_{Start}>V_{End}$) direction for perovskite single junction solar cells with Spiro-OMeTAD of different thicknesses as HTM, corresponding to Figure 4.23 a). Void squares mark the arithmetic average values.

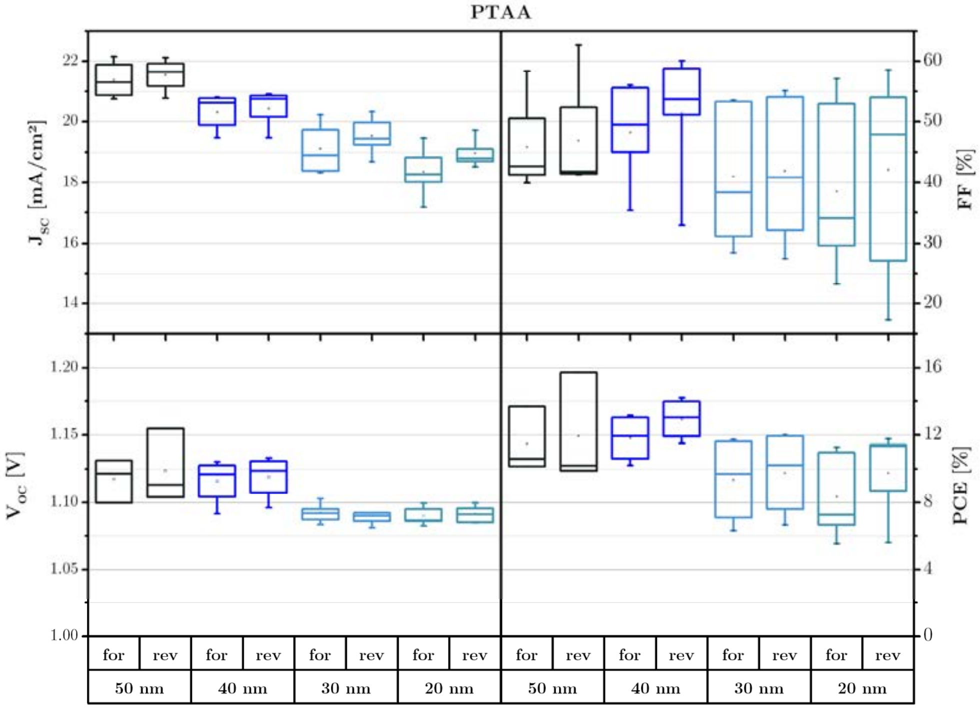

Figure S 17: Boxplot diagrams of current-voltage scan parameters in forward ($V_{Start}<V_{End}$) and reverse ($V_{Start}>V_{End}$) direction for perovskite single junction solar cells with PTAA of different thicknesses as HTM, corresponding to Figure 4.23 b). Void squares mark the arithmetic average values.

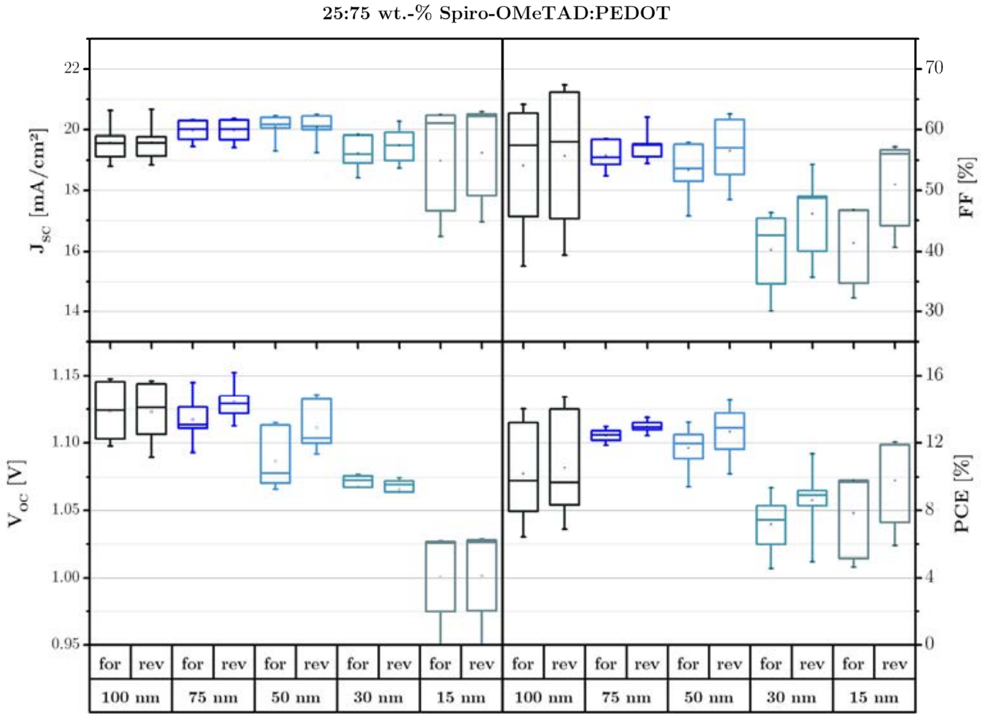

Figure S 18 Boxplot diagrams of current-voltage scan parameters in forward ($V_{Start}<V_{End}$) and reverse ($V_{Start}>V_{End}$) direction for perovskite single junction solar cells with 25:75 wt.-% Spiro-OMeTAD:PEDOT mixtures of different thicknesses as HTM, corresponding to Figure 4.23 c). Void squares mark the arithmetic average values.

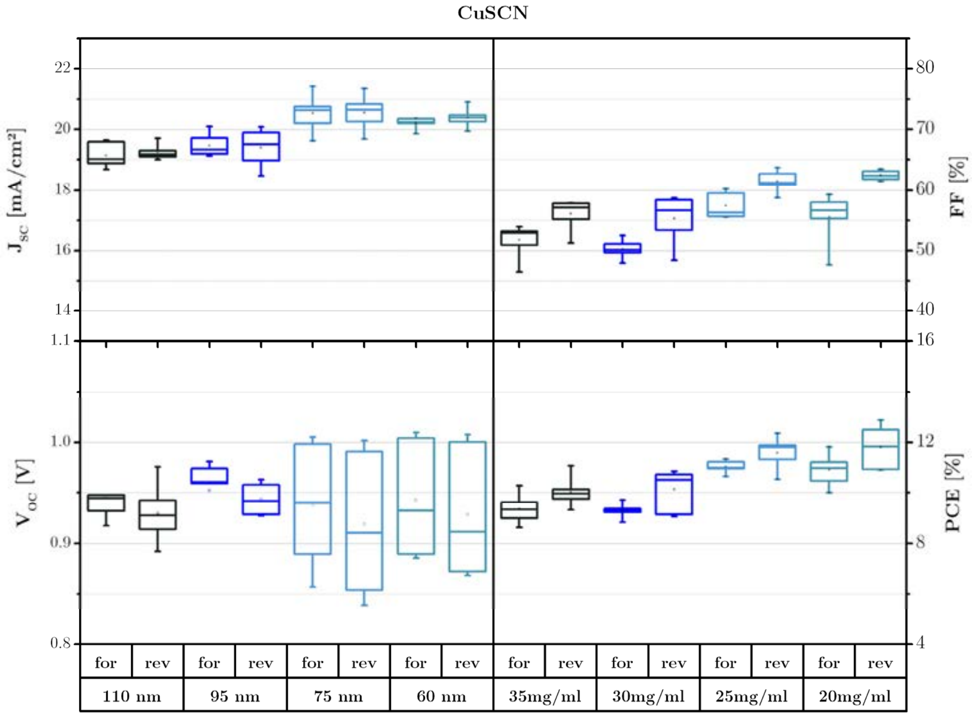

Figure S 19 Boxplot diagrams of current-voltage scan parameters in forward ($V_{Start}<V_{End}$) and reverse ($V_{Start}>V_{End}$) direction for perovskite single junction solar cells with CuSCN of different thicknesses as HTM, corresponding to Figure 4.23 d). Void squares mark the arithmetic average values.

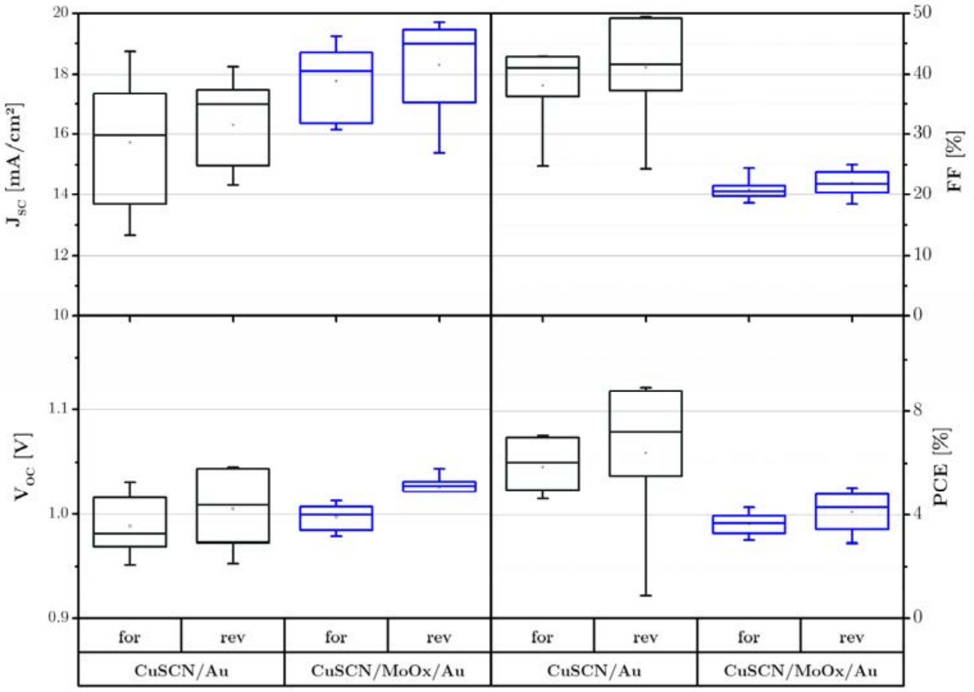

Figure S 20: Device parameters for current-voltage scans in forward ($V_{Start}<V_{End}$) and reverse ($V_{Start}>V_{End}$) direction of opaque single-junction solar cells with layer sequence glass/ITO/SnO_2/"triple cation" perovskite/CuSCN(/MoOx)/Au under illumination (black: only Au as top electrode, blue: MoOx/Au as top electrode).

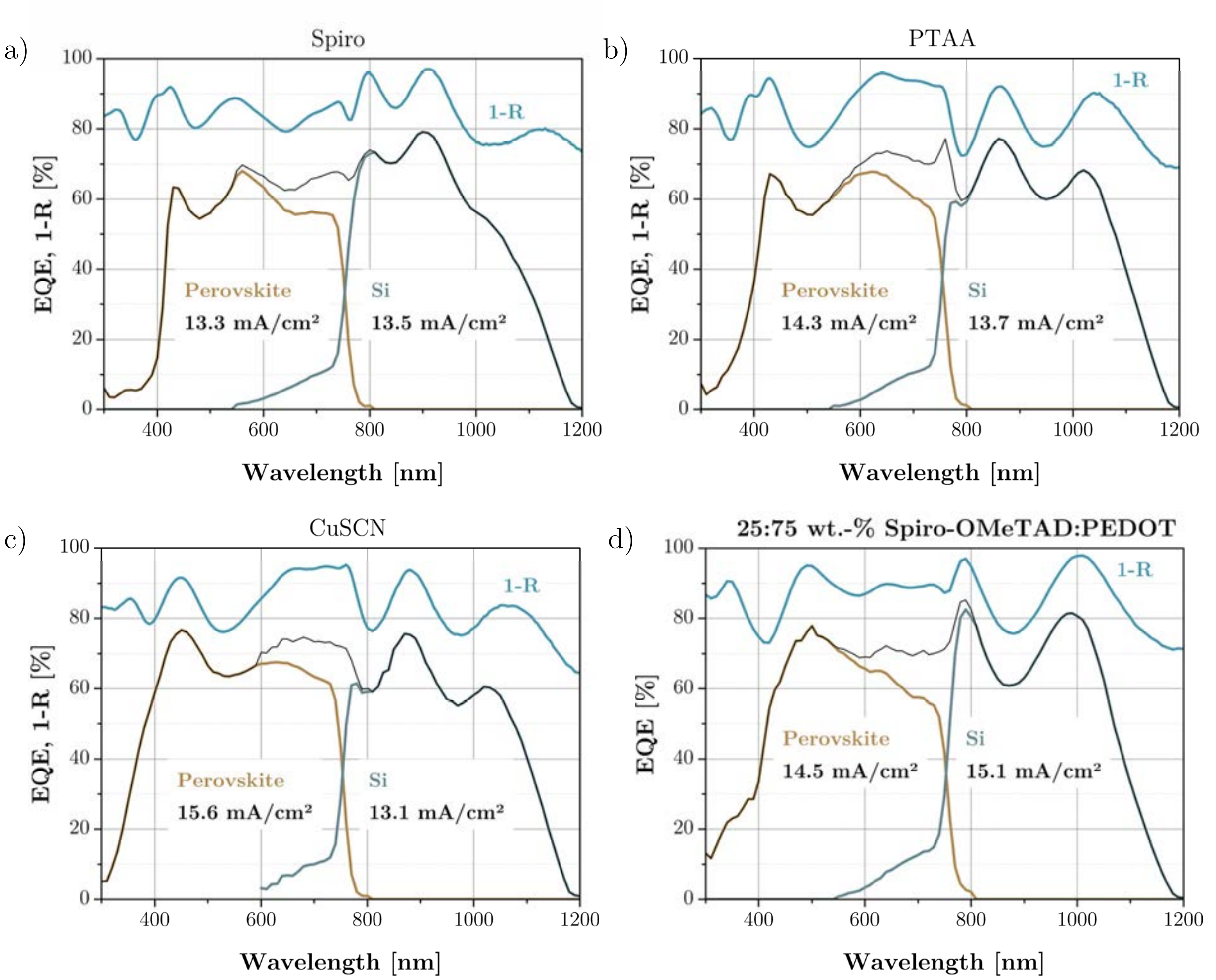

Figure S 21: EQE$_{PV}$ and 1-reflection measurements of monolithic perovskite-silicon heterojunction tandem solar cells with a) Spiro-OMeTAD, b) PTAA, c) CuSCN and d) PEDOT/Spiro-OMeTAD mixtures as HTMs. The depicted EQE$_{PV}$ measurements correspond to the devices shown in Figure 4.24 a).

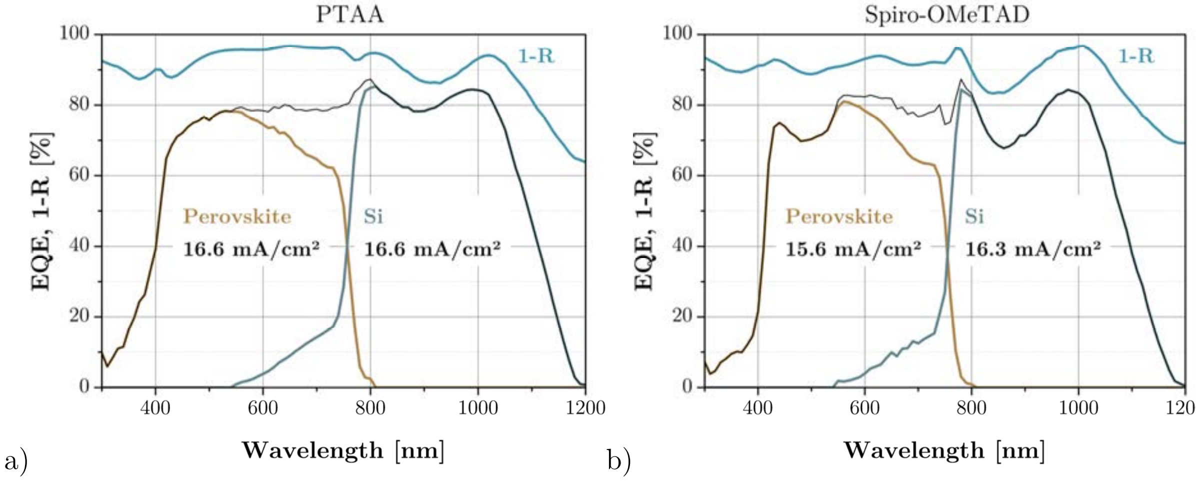

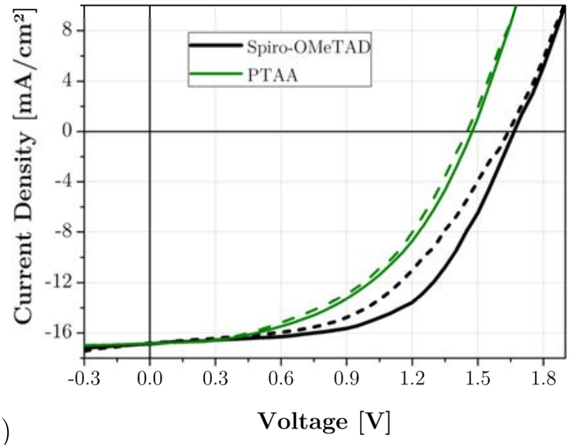

c)

Figure S 22: EQE$_{PV}$ measurements of the devices presented in Figure 4.24 b) with a) PTAA and b) Spiro-OMeTAD as HTM as well as c) corresponding J-V characteristics under illumination.

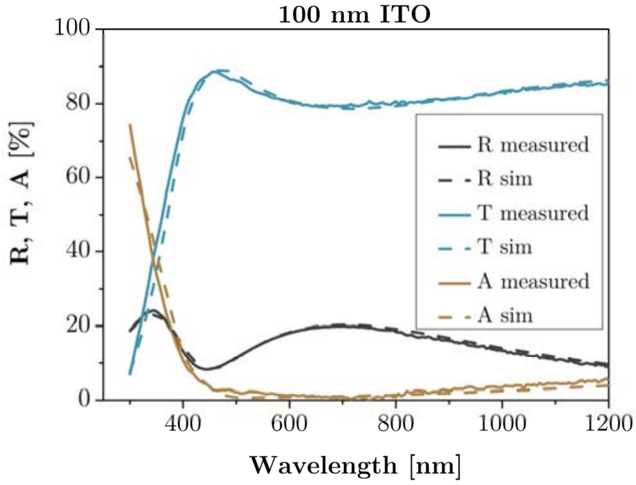

Figure S 23: Experimentally determined reflection and transmission characteristics of 100 nm ITO on glass compared to simulated results with optical data aquired from Zhang et al.[239] Absorption is calculated from 1-reflection-transmission.

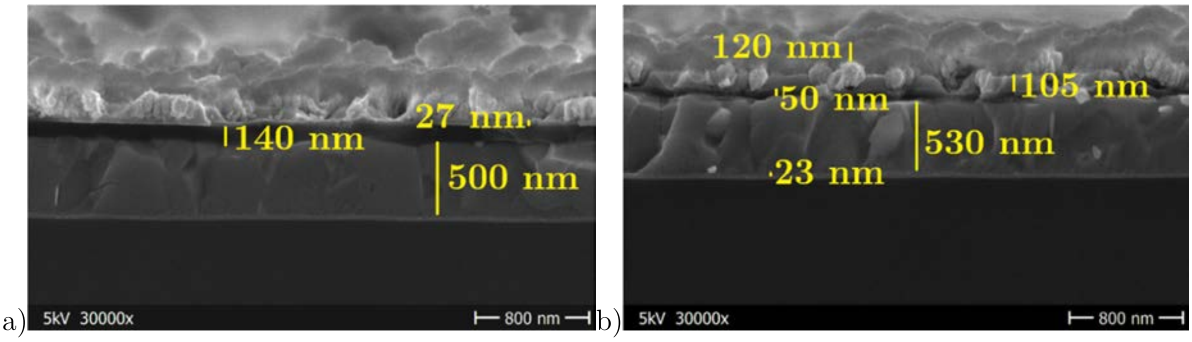

Figure S 24: Cross-section scanning electron microscopy images of perovskite top cells with a) Spiro-OMeTAD and b) PTAA as HTM in perovskite-silicon tandem solar cells. Determined layer thicknesses are 27 nm for MoOx, 140 nm for Spiro-OMeTAD, a) 500 nm and b) 530 nm for the perovskite absorber,

120 nm for LiF coating, 105 nm for ITO, 50 nm for PTAA and 23 nm for SnO_2. Note, that the textured surface stems from 1 hour sonicated ITO nanoparticles, which were coated between MoOx and ITO.

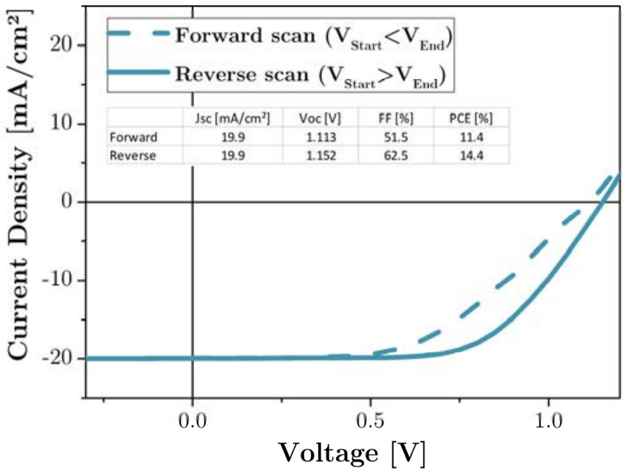

	Jsc [mA/cm²]	Voc [V]	FF [%]	PCE [%]
Forward	19.9	1.113	51.5	11.4
Reverse	19.9	1.152	62.5	14.4

Figure S 25: Current-voltage characteristics of a semi-transparent perovksite solar cell with Spiro-OMeTAD as hole contact.

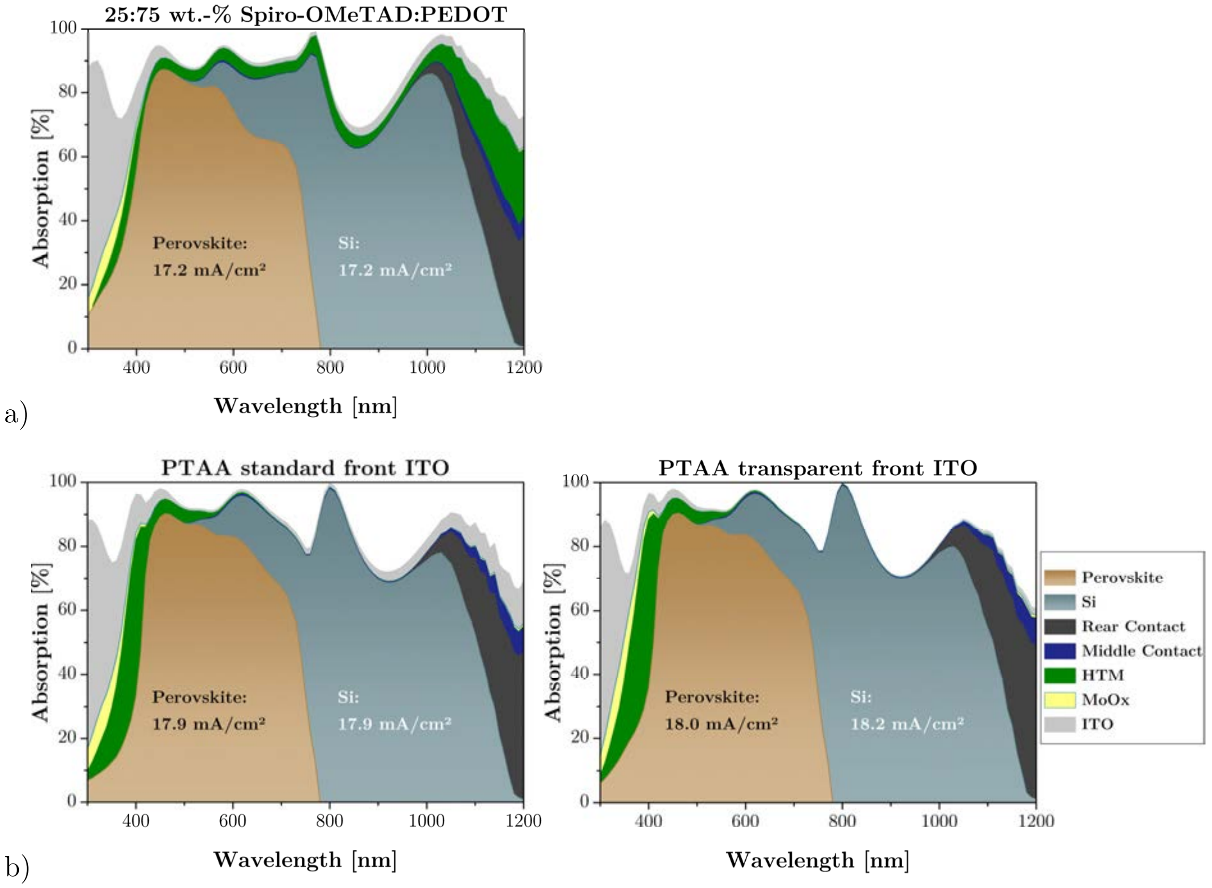

Figure S 26: Spectral absorption profiles for optimized monolithic perovskite-silicon heterojunction solar cells with the top cell comprising a) 25:75 wt.-% Spiro-OMeTAD:PEDOT mixtures or b) PTAA as *p*-type contact with optical data for the ITO electrode following (left) ref.[239] or (right) ref.[220].

7.4 List of Publications and Conference Contributions

Manuscripts in the framework of this thesis:

It Takes Two To Tango – Double-layer Selective Contacts in Perovskite Solar Cells for Improved Device Performance and Reduced Hysteresis
L. Kegelmann, C.M. Wolff, C.A. Omondi, F. Lang, E.L. Unger, L. Korte, T. Dittrich, D. Neher, B. Rech, S. Albrecht
ACS Applied Materials&Interfaces (2017), vol. 9 (20), pp. 17245-17255.

Mixtures of Dopant-Free Spiro-OMeTAD and Water-Free PEDOT as a Passivating Hole Contact in Perovskite Solar Cells
L. Kegelmann, P. Tockhorn, C.M. Wolff, J.A. Márquez, L. Korte, T. Unold, W. Lövenich, D. Neher, B. Rech and S. Albrecht
ACS Applied Materials&Interfaces (2019), vol. 11 (9), pp. 9172–9181.

Roadmap and roadblocks for the band gap tunability of metal halide perovskites
E.L. Unger, L. Kegelmann, K. Suchan, D. Sörell, L. Korte, S. Albrecht
Journal of Materials Chemistry A (2017), vol 5 (23), pp. 11401-11409

Room temperature atomic layer deposited Al_2O_3 improves perovskite solar cells efficiency over time
M. Kot, L. Kegelmann, P. Kus, N. Tsud, I. Matolinova, S. Albrecht, V. Matolin, D. Schmeisser
ChemSusChem (2018), accepted manuscript, doi: 10.1002/cssc.201801434

Efficient light management by textured nanoimprinted layers for perovskite solar cells
M. Jošt, S. Albrecht, L. Kegelmann, C.M. Wolff, F. Lang, B. Lipovšek, J. Krč, L. Korte, D. Neher, B. Rech, M. Topič
ACS Photonics, 2017, 4 (5), pp 1232–1239

Determination of the complex refractive index and optical bandgap of $CH_3NH_3PbI_3$ thin films
J.A. Guerra, A. Tejada, L. Korte, L. Kegelmann, J.A. Töfflinger, S. Albrecht, B. Rech, R. Weingärtner
Journal of Applied Physics (2017), 121, 173104

Monolithic perovskite/silicon-heterojunction tandem solar cells processed at low temperature
S. Albrecht, M. Saliba, J.P. Correa Baena, F. Lang, L. Kegelmann, M. Mews, L. Steier, A. Abate, J. Rappich, L. Korte, R. Schlatmann, M.K. Nazeeruddin, A. Hagfeldt, M. Grätzel, B. Rech
Energy & Environmental Sciences (2016), vol 9 (1), pp. 81-88

Oral conference contributions:

Double-layer charge selective contacts in perovskite solar cells for improved device performance and reduced hysteresis
L. Kegelmann, C.M. Wolff, C.A. Omondi, L. Korte, T. Dittrich, D. Neher, B. Rech, S. Albrecht
Hybrid & Organic Photovoltaics 2017
Lausanne, Switzerland, 21.05.2017 - 24.05.2017 (2017)

Double-layer charge selective contacts in perovskite solar cells as a key to improved efficiency and reduced hysteresis effects
L. Kegelmann, C.M. Wolff, C.A. Omondi, L. Korte, T. Dittrich, D. Neher, B. Rech, S. Albrecht
DPG Frühjahrstagung 2017
Dresden, 20.03.2017 - 24.03.2017 (2017)

Passivating perovskite surfaces by mixtures of PEDOT and dopant-free Spiro-OMeTAD
L. Kegelmann, C.M. Wolff, J.A. Márquez, P. Tockhorn, L. Korte, T. Unold, D. Neher, B. Rech, S. Albrecht
DPG Frühjahrstagung 2018
Berlin, 11.03.2018 - 16.03.2018 (2018)

Poster conference contributions:

Perovskite absorber and device characteristics for different low-temperature processed electron transport materials
L. Kegelmann, S. Albrecht, L. Korte, D. Neher, B. Rech
ABXPV - International Conference on Perovskite Thin Film Photovoltaics
Barcelona, Spanien, 03.03.2016 - 04.03.2016 (2016)

Reducing hysteresis in regular planar perovskite solar cells by interlayers between the cathode and the electron selective material
L. Kegelmann, S. Albrecht, L. Korte, B. Rech, D. Neher
Perovskite Solar Cells and Optoelectronics
Genova, Italy, 26.09.2016 - 28.09.2016 (2016)

Mixtures of PEDOT and dopant-free Spiro-OMeTAD as hole selective contact in regular perovskite solar cells
L. Kegelmann, C.M. Wolff, P. Tockhorn, L. Korte, D. Neher, B. Rech, S. Albrecht
Perovskite Solar Cells and Optoelectronics
Oxford, Great Britain, 18.09.2017 - 20.09.2017 (2017)

Mixtures of PEDOT and dopant-free Spiro-OMeTAD as passivating hole contact in regular perovskite solar cells
L. Kegelmann, C.M. Wolff, P. Tockhorn, L. Korte, D. Neher, B. Rech, S. Albrecht
HEST-PV
Rehovot, Israel, 24.10.2017 - 24.10.2017 (2017)

7.5 List of Symbols and Abbreviations

Abbreviations

AFM	Atomic force microscope
ALD	Atomic layer deposition
AM	Air mass
APLY	Absolute photoluminescence yield
BCP	Bathocuproine
BOS	Balance-of-system
c-Si	Crystalline silicon
CBZ	Chlorobenzene
CVD	Chemical vapor deposition
a-Si	Amorphous silicon
DMF	Dimethyl formamide
DMSO	Dimethyl sulfoxide
DSSC	Dye sensitized solar cells
ETM	Electron transport material
$\boldsymbol{EQE_{EL}}$	External electron-to-photon conversion efficiency
$\boldsymbol{EQE_{PV}}$	Spectral photon-to-electron conversion efficiency
FA	Formamidinium $HC(NH_2)_2$
FF	Fill factor
FK209	Tris(bis(trifluoromethylsulfonyl)imide)
FTO	Flourine doped tin oxide, SnO_2:F
HOMO	Highes occupied molecular orbital
HTM	Hole transport material
IE	Ionization energy
ICMA	1',4'-Dihydro-naphtho[2,'3':1,2][5,6]fullerene-C_{60}
ITO	Tin doped indium oxide, In_2O_3:Sn
$\boldsymbol{IQE_{PV}}$	Internal quantum
LED	Light emitting diode
LiTFSI	Bis(trifluoromethane) sulfonimide lithium salt
LUMO	Lowest unoccupied molecular orbital

MA	Methylammonium CH_3NH_3
MoOx	Molybdenum oxide
MPP	Maximum power point
OPV	Organic photovoltaics
PCBM	phenyl-C_{60}-butyric acid methyl ester
PCE	Power conversion efficiency
PEDOT	poly(3,4-ethylenedioxythiophene)
PL	Photoluminescence
PSC	Perovskite solar cell
PSS	Polystyrene sulfonate
PTAA	poly(triaryl amine)
PV	Photovoltaics
QFLS	Quasi-Fermi level splitting
SECO	Secondary electron cut-off
SEM	Scanning electron microscopy
SHJ	Silicon heterojunction
Spiro-OMeTAD	2,2',7,7'-tetrakis(N,N-di-p-methoxyphenylamine)-9,9'-spirobifluoren
SPV	Surface Photovoltage
SRH	Shockley-Read-Hall
STC	Standard test conditions
TCO	Transparent conductive oxide
TRPL	Transient photoluminescence
UPS	Ultraviolet photoelectron spectroscopy
UV	Ultraviolet
WF	Work function
XPS	X-ray photoelectron spectroscopy

Symbols

α	Absorption coefficient
AM1.5G	Solar spectrum under standard test conditions
β	Radiatice recombination rate constant

$\mathbf{c}$	Speed of light 299,792,458 m·s^{-1}
$\mathbf{d_{BE}}$	Distance between the Sun (regarded as black body) and Earth 1.5·10^{8} km
$\mathbf{e}$	Elementary charge 1.60217662·10^{-19} C
$\mathbf{E_b}$	Binding energy
$\mathbf{E_C}$	Conduction band energy
$\mathbf{E_F}$, $\mathbf{E_{F,e}}$, $\mathbf{E_{F,h}}$	Fermi energy level, electron and hole quasi-Fermi level energies
$\mathbf{E_g}$	Band gap energy
$\mathbf{E_\lambda}$	Spectral irradiance
$\mathbf{E_{Photon}}$	Photon energy
$\mathbf{E_T}$	Tail slope parameter from SPV measurements
$\boldsymbol{\eta}_\mathbf{q}$	Photon-to-electron conversion efficiency
$\mathbf{E_{kin}}$	Kinetic energy
$\mathbf{E_V}$	Valence band energy
$\mathbf{G}$	Generation rate
$\mathbf{h}$	Planck constant 6.62607004·10^{-34} m^{2}·kg·s^{-1}
$\mathbf{H}$	Hysteresis index
$\mathbf{I}$	Current
$\mathbf{I_i}$	Interstitial iodine
$\mathbf{I_0}$	Reverse dark saturation current
$\mathbf{I_{SC}}$	Short-circuit current
$\mathbf{J}$	Current-density
$\mathbf{J_{SC}}$	Short-circuit current density
$\mathbf{k}$	Extinction coefficient
$\mathbf{k_B}$	Boltzmann constant 1.38064852·10^{-23} m^{2}·kg·s^{-2}·K^{-1}
$\mathbf{L_\lambda}$	Spectral radiance
$\boldsymbol{\lambda}$	wavelength
$\boldsymbol{\mu}$	Charge carrier mobility
$\mathbf{MA_i}$	Methylammonium interstitials
$\mathbf{N}$	Complex refractive index
$\mathbf{n}$	refractive index
$\boldsymbol{n}$	Electron density
$\boldsymbol{\nu}$	Photon frequency

$\mathbf{n}_{\mathbf{id}}$	Diode ideality factor
$\boldsymbol{n_0}$	Intrinsic charge carrier density
$\boldsymbol{p}$	Hole density
$\boldsymbol{\Phi}$	Photon flux
$\mathbf{P}_{\mathbf{light}}$	Incident light intensity
$\mathbf{R}$	Reflectance
$\boldsymbol{R}$	Resistance
$\mathbf{r}_{\mathbf{i}}$	Ionic radii
$\mathbf{R}_{\mathbf{rad}}$	Radiative recombination rate
$\mathbf{R}_{\mathbf{S}}$	Series resistance
$\mathbf{R}_{\mathbf{P}}$	Parallel resistance
$\mathbf{r}_{\mathbf{BB}}$	Radius of a black body (radius of the sun $6.95\cdot10^5$ km)
$\mathbf{s}_{\mathbf{n,p}}$	Electron and hole surface recombination velocity
$\boldsymbol{\tau}$	Charge carrier lifetime
$\mathbf{T}$	Transmittance
$\boldsymbol{T}$	Temperature
$\mathbf{t}$	Goldschmidt tolerance factor
$\mathbf{V}$	Voltage
$\mathbf{V}_{\mathbf{OC}}$	Open circuit voltage
$\mathbf{V}_{\mathbf{Pb}}$	Lead vacancy
$\mathbf{Y}_{\mathbf{PL}}$	PL yield

7.6 Acknowledgements

Although the sun does not always shine, even in photovoltaics research, all the great experiences during the last three years at HZB and in the HyPerCells graduate school clearly outshine the frustrating days. All this would not have been possible without the help and support of so many people and I am sincerely grateful to every one of you. I would like to thank a few people in particular:

My biggest gratitude to my doctor father **Dieter Neher** for wise guidelines, good ideas and for critically reading the thesis and the publications which have emerged from it. Just as much, I am deeply thankful for all the support and trust in me from **Bernd Rech**, who triggered and strongly pushed perovskite research at HZB, making this PhD project possible. I further acknowledge Dieter, Bernd as well as **Thomas Unold** for initiating the HyPerCells graduate school, which provided the stipend for my thesis.

Additionally, I would like to thank **Prof. Dr. Emil List-Kratochvil** for being the co-examiner of this dissertation.

Undoubtedly most patronizing for this work were the invaluable efforts of **Steve Albrecht**. Your encouraging, unlimited assistance since the first day you arrived at HZB, all the instructive discussions, tireless proof-readings and great advices make you a true mentor. Thank you for all of that.

Furthermore many thanks to **Lars Korte, Thomas Dittrich** and **Eva Unger** for inspiring input, always open doors, paramount roof-top barbeques and for taking me on to the most astonishing business travel to the Weizmann Institute and Ben-Gurion University in Israel!

Thank you to the HZB and the HyPerCells graduate school in general for enabling countless memorable activities, such as conferences in Barcelona, Lausanne or Oxford, sports events like the B2Run and the AirfieldRun, or Christmas parties and PhD retreats. All these events, as well as the daily work, however, would not have been half as enjoyable without all the splendid colleagues and friends I got to know on this journey! Thank you all for fruitful discussions and lots of fun, **Felix, Ganna, Mathias Mews, Oleksandra** (also for SNL, carpool karaoke and a daily dose of charming sarcasm), **Eike, Amran, Moni, Hagen** (also for squash battles and Vulcano Fizz supplies), **Steffen, Shannon,** the musketeers **Caro** (party queen and best graph advisor ever), **Kati** and **Aniela** as well as my snooze-bro **Aboma** for proof-reading, loads of funny stories and the best Sweden-trip I could imagine! Special thanks also go out to **Ula** and **Christian** for profound scientific exchange, critical reading of my work and especially all the good times we've had together over the last three years (so many good concerts, bar evenings, retreats, …)! A big compliment also to **Daniel Meza** for organizing plenty of wonderful PhD-students events and enabling one of our greatest birthday parties! Of course, I must not forget the helping hands of **Marion Krusche, Carola Klimm, Carola Ferber** and **Thomas Lußky**.

The sincerest tschuppla, tschuppla, tschuppla to all members of THE office. **Marko, Philipp, Marcel, Artiom** (thanks for the CuSCN series) and **Paul**! To not burst the limits here, I will just mention a few of the memories that will stay: Karaoke, Mini Golf, flossing, sweets-shall-not-pass (didn’t work at all), bathrobe retreats, Nerf-gun challenges, Slovenia-excursions, schocken&Ha-Lo photo sessions, Bamberger diplomas, WC3, hot-air-fryer dinners, berlin beer tests, Umsteiger, Ako su to samu bile lazi, and countless others.

Finally, I would like to express the deepest thanks to my dearest **Theresa** for her unfailing support, even when I left to Berlin, her patience and indulgence when I dedicated my time to this thesis instead of holidays together, and her encouragement and happiness in stressful times. No less, I am grateful to my **family** for the immeasurable care during my entire life, opening up so many opportunities for me and allowing me to come this far in the first place!

7.7 Thesis Declaration

I, Lukas Kegelmann, hereby certify that this thesis has been written by me, that it is the record of work carried out by me, and that I did not use source material or aids other than those mentioned. The work has not been submitted to any other University.

Place/Date Signature